[illegible]
IN 34-CR
242525

P-166

INVESTIGATION OF TURBULENT FLOW IN HIGHLY CURVED DUCTS WITH APPLICATION TO TURBOMACHINERY COMPONENTS

Final Report for Research Contract NAG 3-624

Principal Investigator J.A.C. Humphrey

Research Assistant M.P. Arnal

Department of Mechanical Engineering
University of California, Berkeley

(NASA-CR-186060) INVESTIGATION OF TURBULENT FLOW IN HIGHLY CURVED DUCTS WITH APPLICATION TO TURBOMACHINERY COMPONENTS Final Report (California Univ.) 166 p
CSCL 20D
N90-12392
Unclas
G3/34 0242525

NUMERICAL CALCULATION OF TURBULENT FLOW IN PASSAGE THROUGH A 90° BEND OF SQUARE CROSS SECTION

M.P. Arnal and J.A.C. Humphrey

Department of Mechanical Engineering
University of California, Berkeley

ABSTRACT

Numerical predictions have been performed using a semi-elliptic calculation procedure for the case of turbulent flow in passage through a 90° bend of square cross section. Two versions of the isotropic turbulent viscosity two equation $k-\varepsilon$ model were used. One (WFM) employs the logarithmic law-of-the-wall relation and the notion of equilibrium flow to set all the necessary boundary conditions at the first grid point adjacent to a solid wall. The other (VDM) employs Prandtl's original mixing length formulation, in conjunction with Van Driest's semi-empirical relation for the mixing length, to calculate the turbulent viscosity in the near wall regions of the flow. In this case, boundary conditions for k and ε, required to calculate these quantities in the core of the flow, are obtained by matching the mixing length and Reynolds number model formulations in an overlapping region of the flow near the walls. In both cases the results obtained show an improvement over earlier calculations using an elliptic numerical procedure. This is attributed to the finer grids possible in the present work. Of the two models, the VDM formulation shows better overall conformity with the mean flow measurements. Neither model reproduces well the details of the stress distribution as a result of the implied isotropic turbulent viscosity.

Table of Contents

ACKNOWLEDGEMENTS 1
LIST OF FIGURES 2
NOMENCLATURE 9
1. INTRODUCTION 13
  1.1. The Problem Considered 13
  1.2. Previous Work 14
  1.3. Objectives of the Work 15
  1.4. Outline 16
2. MEAN FLOW EQUATIONS AND THE TURBULENCE MODEL 17
  2.1. Introduction 17
  2.2. Governing equations and the problem of closure 17
  2.3. The Turbulence Model 19
  2.4. Boundary Conditions 20
  2.5. Summary of the Equations 26
3. THE NUMERICAL PROCEDURE 31
  3.1. Introduction 31
  3.2. Semi-elliptic flows 31
  3.3. Finite Differencing Procedures 33
    3.3.1. Treatment of Boundary Conditions 35
  3.4. The Solution Algorithm 38
4. TEST CASES AND DISCUSSION 44
  4.1. Introduction 44
  4.2. Laminar flows 44
  4.3. Turbulent flows 46
  4.4. Conclusions 53
5. RESULTS AND DISCUSSION 55
  5.1. Introduction 55
  5.2. Results 57
  5.3. Discussion 66
6. CONCLUSIONS 69
  Appendix A: The QUICK scheme formulation 70
  A.1 The problem of interest 70
  A.2 Formulation 70
    A.2.1 Grid arrangement 70

A.2.2 Finite difference approximation of the convective term(s) 71
A.2.3 Quadratic upstream interpolation 71
A.2.4 Implementation of QUICK scheme in variable density flows 74
A.2.5 Treatment of boundary nodes 77
References 78
Figures 81

ACKNOWLEDGEMENTS

This study was funded by NASA Lewis through two Research Grant Awards (NAG 3-624 and NAG 3-735). The authors are grateful to this agency for their support. Special thanks go to Dr. Peter Sockol of NASA Lewis who took a special interest in the work. The study has proceeded in close collaboration with Professor B.E. Lauder and his group at the University of Manchester, Institute of Science and Technology. In particular, we are grateful to Dr. H. Iacovides (UMIST) and Dr. W.M. To (UCB) for their technical support, especially during the initiation of the investigation.

LIST OF FIGURES

Figure 1.1. Flow pattern of the secondary motion in a curved duct of square cross-section, r_i and r_o are the inner- and outer- curved wall radii, respectively.

Figure 1.2. Schematic of test section from Humphrey et al. [1981] showing dimensions, coordinate system and velocity components of the flow. $R^* = (r-r_i)/(r_o-r_i)$ is the non-dimensional radial position in the bend.

Figure 2.1. Coordinate system for boundary condition definitions. The boundary is either a wall or symmetry plane.

Figure 2.2. Duct geometry, showing coordinate system and velocity components. (a) Straight duct. (b) Curved duct.

Figure 2.3. Illustration of the mixing length region, interface and core flow region in the VDM formulation.

Figure 3.1. Main grid node control volume.

Figure 3.2. Velocity node control volume.

Figure 3.3. Control volume for intergration of the general ϕ-variable transport equation.

Figure 4.1. Centerline velocity for developing laminar flow in a 2D straight channel, Re=300. Comparison with Schlichting [1979] boundary layer predictions and McDonald et al. [1972] fully elliptic predictions.

Figure 4.2. Velocity profiles for developing laminar flow in a 2D straight channel, Re=300. (a) Comparison with Schlichting [1979] boundary layer predictions. (b) Comparison with McDonald et al. [1972] fully elliptic predictions.

Figure 4.3. Centerline velocity for developing laminar flow in a square duct, Re=200. Comparison with data of Goldstein and Kreid [1967].

Figure 4.4. Velocity profiles for developing laminar flow in a square duct, Re=200. Comparison with data of Goldstein and Kreid [1967].

Figure 4.5. Variation of streamwise friction coefficient c_f, with number of nodes in a cross-stream direction. Straight duct laminar flow.

Figure 4.6. Mean velocity profile for fully developed turbulent channel flow, Re=110,000. Comparison of predictions using VDM with Laufer [1950] data.

Figure 4.7. Turbulent kinetic energy profile for fully developed turbulent channel flow, Re=110,000. Comparison of predictions using VDM with Laufer [1950] data.

Figure 4.8. Turbulent shear stress profile for fully developed turbulent channel flow, Re=110,000. Comparison of predictions using VDM with Laufer [1950] data.

Figure 4.9. Mean velocity profile for fully developed turbulent channel flow, Re=110,000. Comparison of predictions using WFM (standard constants) with Laufer [1950] data.

Figure 4.10. Turbulent kinetic energy profile for fully developed turbulent channel flow, Re=110,000. Comparison of predictions using WFM (standard constants) with Laufer [1950] data.

Figure 4.11. Turbulent shear stress profile for fully developed turbulent channel flow, Re=110,000. Comparison of predictions using WFM (standard constants) with Laufer [1950] data.

Figure 4.12. Turbulent shear stress profile for fully developed turbulent channel flow, Re=110,000. Comparison of predictions using WFM (Laufer's constants) with Laufer [1950] data.

Figure 4.13. Mean velocity profile for fully developed turbulent channel flow, Re=110,000. Comparison of predictions using WFM (standard constants) and VDM with interface region at $y^+ \approx 10$.

Figure 4.14. Turbulent kinetic energy profile for fully developed turbulent channel flow, Re=110,000. Comparison of predictions using WFM (standard constants) and VDM with interface region at $y^+ \approx 10$.

Figure 4.15. Energy dissipation profile for fully developed turbulent channel flow, Re=110,000. Comparison of predictions using WFM (standard constants) and VDM with interface region at $y^+ \approx 10$.

Figure 4.16. Eddy diffusivity (μ_e) profile for fully developed turbulent channel flow, Re=110,000. Comparison of predictions using WFM (standard constants) and VDM with interface region at $y^+ \approx 10$.

Figure 4.17. Mean velocity profile for fully developed turbulent channel flow, Re=110,000. Comparison of predictions using WFM (standard constants) and VDM with interface region at $y^+ \approx 25$.

Figure 4.18. Turbulent kinetic energy profile for fully developed turbulent channel flow, Re=110,000. Comparison of predictions using WFM (standard constants) and VDM with interface region at $y^+ \approx 25$.

Figure 4.19. Energy dissipation profile for fully developed turbulent channel flow, Re=110,000. Comparison of predictions using WFM (standard constants) and VDM with interface region at $y^+ \approx 25$.

Figure 4.20. Eddy diffusivity (μ_e) profile for fully developed turbulent channel flow, Re=110,000. Comparison of predictions using WFM (standard constants) and VDM with interface region at $y^+ \approx 25$.

Figure 4.21. Centerline velocity for developing turbulent duct flow, Re=40,000. Comparison of predictions using WFM in the near wall region with Melling [1975] data.

Figure 4.22. Centerline velocity for developing turbulent duct flow, Re=40,000. Comparison of predictions using VDM in the near wall region with Melling [1975] data.

Figure 4.23. Centerline turbulence intensity for developing turbulent duct flow, Re=40,000. Comparison of predictions using WFM in the near wall region with Melling [1975] data.

Figure 4.24. Centerline turbulence intensity for developing turbulent duct flow, Re=40,000. Comparison of predictions using VDM in the near wall region with Melling [1975] data.

Figure 4.25. Contours of U_x/U_{cl} for fully developed turbulent duct flow, Re=40,000. Comparison of predictions using VDM (lower left) and WFM (upper right) with data of Melling [1975].

Figure 4.26. Cross-stream profiles of U_x/U_b for fully developed turbulent duct flow, Re=40,000. (a) $z/D_h = 0.5$. (b) $z/D_h = 0.25$. Comparison of predictions with data of Melling [1975].

Figure 4.27. Contours of $\tilde{u}/U_{cl}$ for fully developed turbulent duct flow, Re=40,000. Comparison of predictions using VDM (lower left) and WFM (upper right) with data of Melling [1975].

Figure 4.28. Cross-stream profiles of $\tilde{u}/U_{cl}\times10^2$ for fully developed turbulent duct flow, Re=40,000. (a) $z/D_h = 0.5$. (b) $z/D_h = 0.25$. Comparison of predictions with data of Melling [1975].

Figure 5.1. Grid arrangement for curved duct calculations.

Figure 5.2. Contours of U_θ/U_b for turbulent bend flow, $x/D_h = -2.5$. Comparison of predictions using VDM with data of Humphrey [1977].

Figure 5.3. Contours of U_θ/U_b for turbulent bend flow, $x/D_h = -2.5$. Comparison of predictions using WFM with data of Humphrey [1977].

Figure 5.4. Radial profiles of U_θ/U_b for turbulent bend flow, $x/D_h = -2.5$. (a) $z/D_h = 0.5$. (b) $z/D_h = 0.25$. Comparison of predictions with data of Humphrey [1977].

Figure 5.5. Contours of $\tilde{u}/U_b\times10^2$ for turbulent bend flow, $x/D_h = -2.5$. Comparison of predictions using VDM with data of Humphrey [1977].

Figure 5.6. Contours of $\tilde{u}/U_b\times10^2$ for turbulent bend flow, $x/D_h = -2.5$. Comparison of predictions using WFM with data of Humphrey [1977].

Figure 5.7. Radial profiles of $\tilde{u}/U_b\times10^2$ for turbulent bend flow, $x/D_h = -2.5$. (a) $z/D_h = 0.5$. (b) $z/D_h = 0.25$. Comparison of predictions with data of Humphrey [1977].

Figure 5.8. Contours of turbulent dissipation, $\varepsilon\nu/U_b^4\times10^6$ for turbulent bend flow, $x/D_h = -2.5$. Comparison of predictions using (a) WFM and (b) VDM.

Figure 5.9. Contours of U_θ/U_b for turbulent bend flow, $\theta = 0°$. Comparison of predictions using VDM with data of Humphrey [1977].

Figure 5.10. Contours of U_θ/U_b for turbulent bend flow, $\theta = 0°$. Comparison of predictions using WFM with data of Humphrey [1977].

Figure 5.11. Radial profiles of U_θ/U_b for turbulent bend flow, $\theta = 0°$. (a) $z/D_h = 0.5$. (b) $z/D_h = 0.25$. Comparison of predictions with data of Humphrey [1977].

Figure 5.12. Contours of $\tilde{u}/U_b\times10^2$ for turbulent bend flow, $\theta = 0°$. Comparison of predictions using VDM with data of Humphrey [1977].

Figure 5.13. Contours of $\tilde{u}/U_b\times10^2$ for turbulent bend flow, $\theta = 0°$. Comparison of predictions using WFM with data of Humphrey [1977].

Figure 5.14. Radial profiles of $\tilde{u}/U_b \times 10^2$ for turbulent bend flow, $\theta = 0°$. (a) $z/D_h = 0.5$. (b) $z/D_h = 0.25$. Comparison of predictions with data of Humphrey [1977].

Figure 5.15. Cross-stream velocity vector plot for turbulent bend flow, $\theta = 0°$. Comparison of predictions using (a) VDM and (b) WFM.

Figure 5.16. Contours of turbulent dissipation, $\varepsilon\nu/U_b^4 \times 10^6$ for turbulent bend flow, $\theta = 0°$. Comparison of predictions using (a) WFM and (b) VDM.

Figure 5.17. Contours of U_θ/U_b for turbulent bend flow, $\theta = 45°$. Comparison of predictions using VDM with data of Humphrey [1977].

Figure 5.18. Contours of U_θ/U_b for turbulent bend flow, $\theta = 45°$. Comparison of predictions using WFM with data of Humphrey [1977].

Figure 5.19. Radial profiles of U_θ/U_b for turbulent bend flow, $\theta = 45°$. (a) $z/D_h = 0.5$. (b) $z/D_h = 0.25$. Comparison of predictions with data of Humphrey [1977] and predictions of Humphrey et al. [1981].

Figure 5.20. Contours of $\tilde{u}/U_b \times 10^2$ for turbulent bend flow, $\theta = 45°$. Comparison of predictions using VDM with data of Humphrey [1977].

Figure 5.21. Contours of $\tilde{u}/U_b \times 10^2$ for turbulent bend flow, $\theta = 45°$. Comparison of predictions using WFM with data of Humphrey [1977].

Figure 5.22. Radial profiles of $\tilde{u}/U_b \times 10^2$ for turbulent bend flow, $\theta = 45°$. (a) $z/D_h = 0.5$. (b) $z/D_h = 0.25$. Comparison of predictions with data of Humphrey [1977].

Figure 5.23. Cross-stream velocity vector plot for turbulent bend flow, $\theta = 45°$. Comparison of predictions using (a) VDM and (b) WFM.

Figure 5.24. Contours of turbulent dissipation, $\varepsilon\nu/U_b^4 \times 10^6$ for turbulent bend flow, $\theta = 45°$. Comparison of predictions using (a) WFM and (b) VDM.

Figure 5.25. Contours of U_θ/U_b for turbulent bend flow, $\theta = 71°$. Comparison of predictions using VDM with data of Humphrey [1977].

Figure 5.26. Contours of U_θ/U_b for turbulent bend flow, $\theta = 71°$. Comparison of predictions using WFM with data of Humphrey [1977].

Figure 5.27. Radial profiles of U_θ/U_b for turbulent bend flow, $\theta = 71°$. (a) $z/D_h = 0.5$. (b) $z/D_h = 0.25$. Comparison of predictions with data of Humphrey [1977].

Figure 5.28. Contours of $\tilde{u}/U_b \times 10^2$ for turbulent bend flow, $\theta = 71°$. Comparison of predictions using VDM with data of Humphrey [1977].

Figure 5.29. Contours of $\tilde{u}/U_b \times 10^2$ for turbulent bend flow, $\theta = 71°$. Comparison of predictions using WFM with data of Humphrey [1977].

Figure 5.30. Radial profiles of $\tilde{u}/U_b \times 10^2$ for turbulent bend flow, $\theta = 71°$. (a) $z/D_h = 0.5$. (b) $z/D_h = 0.25$. Comparison of predictions with data of Humphrey [1977].

Figure 5.31. Cross-stream velocity vector plot for turbulent bend flow, $\theta = 71°$. Comparison of predictions using (a) VDM and (b) WFM.

Figure 5.32. Contours of turbulent dissipation, $\epsilon\nu/U_b^4 \times 10^6$ for turbulent bend flow, $\theta = 71°$. Comparison of predictions using (a) WFM and (b) VDM.

Figure 5.33. Contours of U_θ/U_b for turbulent bend flow, $\theta = 90°$. Comparison of predictions using VDM with data of Humphrey [1977].

Figure 5.34. Contours of U_θ/U_b for turbulent bend flow, $\theta = 90°$. Comparison of predictions using WFM with data of Humphrey [1977].

Figure 5.35. Radial profiles of U_θ/U_b for turbulent bend flow, $\theta = 90°$. (a) $z/D_h = 0.5$. (b) $z/D_h = 0.25$. Comparison of predictions with data of Humphrey [1977] and predictions of Humphrey et al. [1981].

Figure 5.36. Contours of $\tilde{u}/U_b \times 10^2$ for turbulent bend flow, $\theta = 90°$. Comparison of predictions using VDM with data of Humphrey [1977].

Figure 5.37. Contours of $\tilde{u}/U_b \times 10^2$ for turbulent bend flow, $\theta = 90°$. Comparison of predictions using WFM with data of Humphrey [1977].

Figure 5.38. Radial profiles of $\tilde{u}/U_b \times 10^2$ for turbulent bend flow, $\theta = 90°$. (a) $z/D_h = 0.5$. (b) $z/D_h = 0.25$. Comparison of predictions with data of Humphrey [1977].

Figure 5.39. Cross-stream velocity vector plot for turbulent bend flow, $\theta = 90°$. Comparison of predictions using (a) VDM and (b) WFM.

Figure 5.40. Contours of turbulent dissipation, $\varepsilon\nu/U_b^4\times10^6$ for turbulent bend flow, $\theta = 90°$. Comparison of predictions using (a) WFM and (b) VDM.

Figure 5.41. Wall pressure coefficient on the symmetry plane of a 90° curved duct, Re=40,000. Comparison of calculations using Van Driest model in the near wall region with wall function model.

Figure 5.42. Friction coefficient on the symmetry plane of a 90° curved duct, Re=40,000. Comparison of calculations using Van Driest model in the near wall region with wall function model.

Figure A.1. Control volume for the property node.

Figure A.2. Control volume for the velocity node.

Figure A.3. Boundary node for a scalar or velocity component parallel to the boundary.

Figure A.4. Boundary node for a velocity component perpendicular to the boundary.

NOMENCLATURE

a	coefficient in finite difference equation 3.3
A	area, perpendicular to the velocity in the difference equations 3.6, 3.7
A^+	non-dimensional empirical constant in equation 2.20
c_f	$\equiv \tau_w/(\frac{1}{2}\rho U_b^2)$, friction coefficient
c_p	$\equiv \Delta p/(\frac{1}{2}\rho U_b^2)$, pressure coefficient
c_μ	= 0.09, proportionality constant in the definition of turbulent diffusivity
C_j	j = e, w, n, s, u, d; convection coefficients in discretized equation 3.2
$C_{\varepsilon 1}$	constant in ε-transport equation 2.29
$C_{\varepsilon 2}$	constant in ε-transport equation 2.29
d	half channel height in two-dimensional channel flow
dU	$\equiv$ A/a, velocity coefficient in velocity correction equation 3.7
D_j	j = e, w, n, s; diffusion coefficients in discretized equation 3.2
D_h	hydraulic diameter
De	$\equiv (D_h/2R_c)^{1/2} \cdot$Re, Dean number
E	roughness parameter in the turbulent law of the wall equation 2.12
k	time-averaged kinetic energy of turbulence
l_c	characteristic length in defining μ_t
l_{eff}	effective distance from the wall in the Van Driest model exponent. Used in corner regions in duct flows, equation 4.3
l_m	mixing length
p	pressure
p_t	$\equiv p+(2/3)\rho k$, turbulent pressure term
p'	pressure correction term, in equation 3.5
p^*	guessed, best estimate pressure, equation 3.5
P	velocity strain rate term in definition of ν_t, equation 2.21

P_k	production of kinetic energy
r, θ, z	cylindrical coordinates for curved ducts
r_i	inner radius of curvature in a curved duct
r_o	outer radius of curvature in a curved duct
R_c	mean radius of curvature in a curved duct
R^*	$\equiv(r-r_i)/(r_o-r_i)$, non-dimensional radial position in a curved duct
Re	$\equiv\rho U_b D_h/\mu$, duct Reynolds number
Re_c	$\equiv\rho U\,\Delta x/\mu$, cell Reynolds number
S_P	coefficient of the linear term in the source, S_ϕ
S_U	constant coefficient in the source, S_ϕ
S_ϕ	source term in ϕ-transport equation, equation 3.1
u	fluctuating velocity
u_c	characteristic velocity in defining the turbulent diffusivity, μ_t
$\tilde{u}$	$\equiv(\overline{u^2})^{1/2}$, root mean square of the fluctuating velocity, u
U	mean velocity
U_{cl}	mean velocity at the duct centerline
U_τ	$\equiv(\tau_w/\rho)^{1/2}$, wall friction velocity
U^+	$\equiv U/U_\tau$, non-dimensional velocity
x, y, z	Cartesian coordinate system for straight ducts and channels
y^+	$\equiv yU_\tau/\nu$, non-dimensional distance from a wall

Greek

α	under-relaxation factor in equation 3.10
Γ	diffusion coefficient in ϕ-transport equation 3.10
Δr	finite difference approximation to dr
ΔU	finite difference approximation to dU
ΔV	finite difference approximation to dV

Δx	finite difference approximation to dx
Δy	finite difference approximation to dy
Δz	finite difference approximation to dz
$\Delta \theta$	finite difference approximation to $d\theta$
ε	time-averaged dissipation of kinetic energy of turbulence
θ	tangential direction in cylindrical coordinates
κ	Von Karman constant in turbulent law-of-the-wall, equation 2.12
μ	dynamic viscosity
μ_e	$\equiv \mu + \mu_t$, effective diffusivity
μ_{num}	numerical diffusion
μ_t	turbulent diffusivity
ν	$\equiv \mu / \rho$, kinematic viscosity
ν_t	$\equiv \mu_t / \rho$, kinematic turbulent diffusivity
ξ	angle between velocity vector and coordinate direction, equation 5.2
ρ	density
σ_k	turbulent Prandtl/Schmidt number for k
σ_ε	turbulent Prandtl/Schmidt number for ε
τ_{res}	resultant wall shear stress in duct flows
τ_w	wall shear stress
ϕ	generalized scalar variable in transport equation 3.1
ψ	angle between resultant shear stress and coordinate direction, equation 2.18

Subscripts

b	bulk
d	downstream boundary of P-cell
e	east boundary of P-cell
E	east node

i	interface
n	north boundary of P-cell
N	north node
o	wall value
P	P-node
r	radial direction
s	south boundary of P-cell
S	south node
u	upstream boundary of P-cell
w	west boundary of P-cell
W	west node
x	streamwise direction (Cartesian coordinates)
y	cross-stream direction
z	second cross-stream direction
θ	streamwise direction (cylindrical coordinates)

Superscripts

n	new
o	old
$-$	time-averaged
$\rightarrow$	vector

1. INTRODUCTION

1.1. The Problem Considered

Over the years, the flow in curved ducts has been studied extensively, both numerically and experimentally over the years. It has been focussed on because of its academic interest and industrial importance. The three-dimensional nature of the flow field provides a challenge to the computational fluid dynamicist both in the laminar and turbulent regimes. The turbulent flow field also provides a challenging test case for turbulence models.

The basic flow field is characterized by an imbalance between the pressure force (directed radially inward) and the centrifugal force (directed radially outward) acting on the fluid as it moves around a curved duct or bend. In the core of the flow the centripetal acceleration overcomes the radial pressure gradient creating a cross-stream flow perpendicular to the main flow direction. This flow is from the inner radius convex wall to the outer radius concave wall. Near the side walls, the centrifugal force acting on the fluid in the boundary layers is overcome by the radial pressure force, creating a cross-stream flow in this region that is directed from the outer radius wall towards the inner radius wall. The resulting secondary motion in the curved duct cross-section is shown schematically in Figure 1.1. This secondary motion acts to distort the symmetry of the the streamwise velocity field, which provides a the challenge to any numerical procedure used to predict the flow, particularly in the turbulent regime.

The objective of this work is to model the turbulent flow in a passage through a 90° bend of square cross-section. In particular, the semi-elliptic solution procedure developed by Pratap and Spalding [1975] and used by Chang and Humphrey [1983] and Iacovides and Launder [1985] is applied together with modifications to the standard $k-\varepsilon$ model of turbulence. The specific problem selected is the turbulent flow in a 90° bend with straight tangents upstream and downstream of the bend. The bend radius and geometrical configuration are those of the test section described by Humphrey et al. [1981] and shown in Figure 1.2. This flow configuration has a variety of industrial applications, ranging from the flow of air in ducts in buildings, to coal transport in power plants. The study of this flow also sheds light on the complex motions occurring in turbomachinery.

1.2. Previous Work

The literature dealing with curved ducts and pipes is extensive and covers more than 50 years of experimental and theoretical work. An extensive survey of the important work done prior to 1977 is provided by Humphrey [1977]. A more recent review of work done since 1977 is given by Chang et al. [1983]. Some of the significant numerical work on curved duct flows and on applications of the semi-elliptic calculation procedure are reviewed below.

Curved duct turbulent flow calculations were made by Humphrey et al. [1981] for a 90° bend using a three-dimensional elliptic code. In general, good agreement with their experiments was obtained up to the 45° plane in the bend. Beyond 45°, there were significant discrepancies between the predicted and measured results.

Calculations of laminar and turbulent flow in curved pipes were reported by Patankar et al. [1974,1975]. Here, a parabolic calculation scheme was used in order to reduce computer storage requirements. The parabolic approach effectively limits the applicability of the calculation procedure to gently curved pipes and ducts with no streamwise recirculation.

The parabolic code was extended by Pratap and Spalding [1976] to allow for the elliptic nature of the pressure field in curved ducts and pipes with smaller radii of curvature. In the partially parabolic procedure proposed by them, the pressure field alone is stored as a three-dimensional array. The velocity components and scalars are stored as two-dimensional arrays which are overwritten as the calculation domain is traversed. The flow field is marched through several times and the pressure field is updated, until some predetermined convergence criterion is met.

This partially parabolic solution procedure was first applied by Pratap [1975] to curved ducts to study the fluid mechanics and heat transfer of laminar flows in such configurations. The procedure was extended to include turbulent flows in curved ducts, first by Patankar et al. [1975] and later by Chang et al. [1983] and Rhie [1983]. In the study by Chang et al., comparisons were made between the measurements made by the authors in a 180° bend and calculations using the partially parabolic solution method. In the study by Rhie, comparisons were made between the numerical results of the author and the experiments of Stanitz et al. [1953] for the case of subsonic compressible flow in an accelerating rectangular elbow. In both cases the agreement between measurements and predictions was best in the first 45° of the bend. After the 45° plane, the agreement was qualitative at best. For the turbulent calculations the boundary conditions were imposed using the wall function approach, which minimizes the number of grid points needed in the near wall region.

In addition to the applications to curved ducts, the partially parabolic or semi-elliptic procedure has also been applied to flows in curved pipes, to a turbulent jet in a cross-stream (Bergeles et al. [1978]) and to other three-dimensional duct flows. For the flows in curved pipes in particular, a great deal of work relevant to the present effort has been done by Iacovides [1986]. The author used a higher order differencing scheme (QUICK) and applied several techniques designed to stabilize and speed the convergence of the calculation procedure. Many of these techniques have been incorporated in the present code for predicting turbulent flows in curved ducts.

From this review of theoretical curved duct studies it becomes apparent that there is a place for further work in this area. The lack of quantitative agreement between experiments and calculations beyond the 45° plane, and the use of wall functions in the near wall region which introduce inaccuracies, are areas which need further attention.

1.3. Objectives of the Work

There are two primary objectives which the current study addresses:

1) to evaluate the semi-elliptic calculation procedure as a way of predicting the complex turbulent flows which occur in curved ducts with small radii of curvature, and

2) to achieve better agreement between predictions of such flows and the experimental data.

To this end the treatment of the near wall region was evaluated and an alternative to the wall function approach was studied. Several techniques designed to improve the convergence rates and improve the accuracy of the final results were also evaluated.

1.4. Outline

The next four sections describe the present study in detail. In section 2 the equations solved by the calculation procedure are summarized and distinctive features of the specific turbulence model used are described. To this end, some space is devoted to developing the treatment for the near wall region which is incorporated into the boundary conditions. Section 3 is devoted to a discussion of the numerical procedure used to calculate turbulent curved duct flows. A brief description of the semi-elliptic calculation technique is given, followed by a detailed account of the finite differencing scheme and the specific implementation of the boundary conditions. Finally, the solution algorithm is reviewed.

Both the semi-elliptic numerical procedure and the turbulence model were examined and compared with experimental or analytical data when possible. The results of the testing, summarized in section 4, demonstrate what can and cannot be expected from the predictions. They show the limitations of the calculation scheme, and enable one to properly interpret the results of the final calculations.

In section 5 the results of the calculations of the 90° bend are presented. Two sets of calculations are provided and compared with the experimental data of Humphrey [1977]. In one set of calculations the standard wall function approach is used in the near wall region. In the second set of calculations a Van Driest low Reynolds number model is used to treat the wall region.

Lastly, in section 6 some conclusions are drawn and specific recommendations are made for future numerical work in this area.

2. MEAN FLOW EQUATIONS AND THE TURBULENCE MODEL

2.1. Introduction

This section summarizes the mean flow equations governing the flow in curved ducts. The problem of closure for the set of equations is discussed. The standard $k-\varepsilon$ model is briefly described before the derivation of the near wall treatment. Both the wall function approach and the Van Driest model for wall bounded flows are presented. The final equations which are solved, including all the modeled terms, are given at the close of the section.

2.2. Governing equations and the problem of closure

In deriving the governing mean flow equations for flows in curved ducts the practice first proposed by O. Reynolds [1895] is followed. The field variables are decomposed into their mean and fluctuating components and substituted into the governing equations in cylindrical coordinates. The resulting equations are time averaged and yield the following for a statistically stationary turbulent flow:

Continuity:

$$\frac{1}{r}\frac{\partial}{\partial r}(\rho r U_r) + \frac{1}{r}\frac{\partial}{\partial \theta}(\rho U_\theta) + \frac{\partial}{\partial z}(\rho U_z) = 0 \qquad (2.1)$$

Momentum:

r-momentum:

$$\frac{1}{r}\frac{\partial}{\partial r}(\rho r U_r U_r) + \frac{1}{r}\frac{\partial}{\partial \theta}(\rho U_\theta U_r) + \frac{\partial}{\partial z}(\rho U_z U_r) - \frac{\rho U_\theta^2}{r} = - \frac{\partial p}{\partial r} \qquad (2.2)$$

$$+ \frac{1}{r}\frac{\partial}{\partial r}\left(\mu r\frac{\partial U_r}{\partial r}\right) + \frac{1}{r}\frac{\partial}{\partial \theta}\left(\frac{\mu}{r}\frac{\partial U_r}{\partial \theta}\right) + \frac{\partial}{\partial z}\left(\mu\frac{\partial U_r}{\partial z}\right) - \frac{\mu}{r}\left(\frac{U_r}{r} + \frac{2}{r}\frac{\partial U_\theta}{\partial \theta}\right)$$

$$+ \frac{\partial}{\partial z}\left(-\rho\overline{u_r u_z}\right) + \frac{1}{r}\frac{\partial}{\partial r}\left(-\rho r\overline{u_r u_\theta}\right) + \frac{1}{r}\frac{\partial}{\partial \theta}\left(-\rho\overline{u_r u_\theta}\right) + \rho\frac{\overline{u_\theta u_\theta}}{r}$$

θ-momentum:

$$\frac{1}{r}\frac{\partial}{\partial r}(\rho r U_r U_\theta) + \frac{1}{r}\frac{\partial}{\partial \theta}(\rho U_\theta U_\theta) + \frac{\partial}{\partial z}(\rho U_z U_\theta) + \frac{\rho U_r U_\theta}{r} = -\frac{1}{r}\frac{\partial p}{\partial \theta} \tag{2.3}$$

$$+ \frac{1}{r}\frac{\partial}{\partial r}\left(\mu r\frac{\partial U_\theta}{\partial r}\right) + \frac{1}{r}\frac{\partial}{\partial \theta}\left(\mu\frac{1}{r}\frac{\partial U_\theta}{\partial \theta}\right) + \frac{\partial}{\partial z}\left(\mu\frac{\partial U_\theta}{\partial z}\right) - \frac{\mu}{r}\left(\frac{U_\theta}{r} - \frac{2}{r}\frac{\partial U_r}{\partial \theta}\right)$$

$$+ \frac{\partial}{\partial z}\left(-\rho\overline{u_\theta u_z}\right) + \frac{1}{r}\frac{\partial}{\partial r}\left(-\rho r\overline{u_r u_\theta}\right) + \frac{1}{r}\frac{\partial}{\partial \theta}\left(-\rho\overline{u_\theta u_\theta}\right) - \rho\frac{\overline{u_r u_\theta}}{r}$$

z-momentum:

$$\frac{1}{r}\frac{\partial}{\partial r}(\rho r U_r U_z) + \frac{1}{r}\frac{\partial}{\partial \theta}(\rho U_\theta U_z) + \frac{\partial}{\partial z}(\rho U_z U_z) = -\frac{\partial p}{\partial z} \tag{2.4}$$

$$+ \frac{1}{r}\frac{\partial}{\partial r}\left(\mu r\frac{\partial U_z}{\partial r}\right) + \frac{1}{r}\frac{\partial}{\partial \theta}\left(\frac{\mu}{r}\frac{\partial U_z}{\partial \theta}\right) + \frac{\partial}{\partial z}\left(\mu\frac{\partial U_z}{\partial z}\right)$$

$$+ \frac{1}{r}\frac{\partial}{\partial r}\left(-\rho r\overline{u_r u_z}\right) + \frac{1}{r}\frac{\partial}{\partial \theta}\left(-\rho\overline{u_\theta u_z}\right) + \frac{\partial}{\partial z}\left(-\rho\overline{u_z u_z}\right)$$

In the above equations the upper and lower case u's stand for mean and fluctuating velocities, respectively, and p is the mean pressure. The bars denote time averaging of the correlation terms, ρ is the fluid density, and μ is the dynamic viscosity.

The presence of the correlation stress terms, which are additional unknowns in the above equations, means that a direct solution of the equations is impossible. These terms require additional expressions or equations in order to make the set of equations and boundary conditions a well-posed problem. This is known as the closure problem in turbulence and is the reason for using turbulence models in solving such flows.

2.3. The Turbulence Model

The turbulence model used in the present work is essentially the high Reynolds number version of the $k-\varepsilon$ model, see Rodi [1980], with some modifications to incorporate boundary conditions. The closure problem is treated via a Boussinesq assumption, which defines an isotropic turbulent diffusivity, μ_t, and uses it to relate the turbulent stresses to the mean rate of strain tensor. In cylindrical coordinates the six unknown turbulent stresses can be expressed as:

$$-\rho\overline{u_r u_r} = \mu_t\left(2\frac{\partial U_r}{\partial r}\right) - \frac{2}{3}\rho k \tag{2.5}$$

$$-\rho\overline{u_\theta u_\theta} = \mu_t\left(\frac{2}{r}\frac{\partial U_\theta}{\partial \theta} + 2\frac{U_r}{r}\right) - \frac{2}{3}\rho k \tag{2.6}$$

$$-\rho\overline{u_z u_z} = \mu_t\left(2\frac{\partial U_z}{\partial z}\right) - \frac{2}{3}\rho k \tag{2.7}$$

$$-\rho\overline{u_r u_\theta} = \mu_t\left(\frac{1}{r}\frac{\partial U_r}{\partial \theta} + \frac{\partial U_\theta}{\partial r} - \frac{U_\theta}{r}\right) \tag{2.8}$$

$$-\rho\overline{u_r u_z} = \mu_t\left(\frac{\partial U_z}{\partial r} + \frac{\partial U_r}{\partial z}\right) \tag{2.9}$$

$$-\rho\overline{u_\theta u_z} = \mu_t\left(\frac{1}{r}\frac{\partial U_z}{\partial \theta} + \frac{\partial U_\theta}{\partial z}\right) \tag{2.10}$$

These relations are similar to the constitutive relations for the stress tensor of an incompressible Newtonian fluid. The additional term $\frac{2}{3}\rho k$ is included in order to assure that the definition of the turbulent kinetic energy remains unchanged for incompressible flow:

$$k = \frac{1}{2}(\overline{u_r u_r} + \overline{u_\theta u_\theta} + \overline{u_z u_z}). \tag{2.11}$$

The closure problem is now reduced to finding an expression for the distribution of the turbulent viscosity. This is done by relating the turbulent viscosity to a local velocity and length scale:

$$\mu_t \propto \rho u_c l_c$$

where u_c and l_c are the appropriate velocity and length scales. For turbulent flows away from wall boundaries, the appropriate velocity scale is $k^{1/2}$, where k is the turbulent kinetic energy. The length scale used is $l_c = k^{3/2}/\varepsilon$, where ε is the dissipation of turbulent kinetic energy.

The distribution of k and ε are determined by solving their respective transport equations with the associated boundary conditions. Both of these equations can be derived but contain many terms which must be modeled. A complete description of the derivation of the k and ε equations and the modeling of the various terms which appear in them is given in Launder and Spalding [1974] and Rodi [1980]. The equations themselves with the modeled terms are given at the end of this section.

2.4. Boundary Conditions

In this section the treatment of the boundary regions is described and various modeling assumptions are given. First, the standard wall function approach (hereafter referred to as WFM) is explained, then the alternative Van Driest low Reynolds number model (hereafter referred to as VDM) is given.

Wall Functions

Wall functions are introduced to avoid having to resolve regions of very steep gradients of velocity and turbulence quantities which occur near fixed walls. Instead of applying boundary conditions at the wall, conditions are effectively fixed at a point near the wall in the flow field. This point is numerical fixed so as to be in the inertial sublayer region ($30 < y^+ < 200$). The influence of the wall on the flow is modeled through setting the boundary conditions at this point. In the following, the two-dimensional case is derived with reference to Figure 2.1. The extension to three dimensions will then be outlined for the curved duct.

For the velocity component parallel to the wall, the logarithmic law of the wall is assumed to be valid in the inertial sublayer region. The velocity is related to the perpendicular distance from the wall according to:

$$U_x^+ = \frac{1}{\kappa}\ln(Ey^+) \tag{2.12}$$

where $E = 9.793$ and the Von Karman constant $\kappa = 0.4187$. In equation 2.12, U_x^+ and y^+ are the mean velocity and distance from the wall in wall coordinates and are defined as:

$$U_x^+ = \frac{U_x}{U_\tau} \qquad y^+ = \frac{yU_\tau}{\nu}$$

where U_τ is the shear velocity, $U_\tau = \sqrt{\tau_w/\rho}$.

For the turbulent kinetic energy, local equilibrium is assumed to hold, and so the production of turbulent kinetic energy is equal to the dissipation. This is not unreasonable since the convection and diffusion of the Reynolds stresses can be shown to be small in this region near the wall. Therefore, it is assumed that

$$-\overline{u_x u_y}\frac{dU_x}{dy} = \varepsilon \tag{2.13}$$

The Reynolds stress is related to the mean velocity gradient and the turbulent viscosity is expressed in terms of the velocity and length scales from the $k-\varepsilon$ model:

$$-\overline{u_x u_y} = \nu_t\frac{dU_x}{dy} \qquad \nu_t = c_\mu\frac{k^2}{\varepsilon} \tag{2.14}$$

where c_μ is the constant of proportionality. Combining equations 2.13 and 2.14 and recalling that the shear stress in the inertial sublayer is approximately equal to the wall shear stress gives:

$$\left(\nu_t\frac{dU_x}{dy}\right)^2 = \left(\frac{\tau_w}{\rho}\right)^2 = \nu_t\varepsilon = c_\mu k^2 \tag{2.15}$$

After collecting terms and recalling the definition of the shear velocity U_τ, the boundary condition for the turbulent kinetic energy k, in terms of U_τ and the proportionality constant

c_μ is obtained:

$$k = \frac{U_\tau^2}{c_\mu^{1/2}} \tag{2.16}$$

For the dissipation ε, the equilibrium assumption is made again and the Reynolds stress is expressed in terms of the wall shear stress:

$$-\overline{u_x u_y}\frac{dU_x}{dy} = \frac{\tau_w}{\rho}\frac{dU_x}{dy} = \varepsilon$$

The velocity gradient is determined from the log law of the wall as:

$$U_x^+ = \frac{1}{\kappa}\ln(Ey^+) \qquad \frac{dU_x}{dy} = \frac{U_\tau^2}{\nu}\frac{dU_x^+}{dy^+} = \frac{U_\tau^2}{\nu}\frac{1}{\kappa y^+}$$

Combining the above expressions for ε and dU_x/dy gives the boundary condition for the dissipation of kinetic energy ε in terms of the wall shear velocity, the Von Karman constant and the fixed perpendicular distance from the wall:

$$\varepsilon = \frac{U_\tau^3}{\kappa y} \tag{2.17}$$

In three-dimensional flows such as those in curved ducts the wall function approach is very similar. Figure 2.2 illustrates the basic geometry, coordinate system and velocity components for straight and curved ducts. The shear velocity, U_τ is based on the resultant wall shear stress, τ_{res} where,

$$\tau_{res} = \sqrt{\tau_{w1}^2 + \tau_{w2}^2}$$

since in general, the resultant shear stress is no longer aligned with one of the three coordinate directions. In the above equation the subscripts, 1 and 2 refer to the two shear stress components parallel to the wall surface. For example, referring to Figure 2.2(a), the resultant shear stress on a wall in the $x-z$ plane would be determined by τ_{wx} and τ_{wy}, the shear stresses on the wall due to the $x-$ and $z-$velocity components respectively. The non-dimensional wall distance and velocity magnitude are defined as before:

$$y^+ = \frac{yU_\tau}{\nu} \qquad \frac{(\vec{U}\cdot\vec{U})^{1/2}}{U_\tau} = \frac{1}{\kappa}\ln(Ey^+)$$

where $U_\tau = \sqrt{\tau_{res}/\rho}$ and $\vec{U}$ is the velocity vector parallel to the wall.

The velocity must now be separated into components in the coordinate directions to apply the boundary conditions. Referring to Figure 2.2(a), there are two velocity components, U_x and U_z parallel to the walls in the $x-z$ plane. The boundary conditions at either of these walls are:

$$\frac{U_x}{U_\tau} = \frac{1}{\kappa}\ln(Ey^+)\cos\psi$$

$$\frac{U_z}{U_\tau} = \frac{1}{\kappa}\ln(Ey^+)\sin\psi \tag{2.18}$$

$$U_y = 0$$

where ψ is the angle between the resultant wall shear stress and the streamwise (x) direction and y^+ is the non-dimensional distance from the side wall. Note that the boundary conditions for the components parallel to the wall are similar to equation 2.12 for the two-dimensional case. For the curved duct the treatment of the boundary conditions is similar for the radial and side walls. The conditions for the turbulence quantities k and ε are the same as those given in equations 2.16 and 2.17 with the shear velocity, U_τ calculated from the resultant wall shear stress, τ_{res}. The specifics of how equations 2.16, 2.17 and 2.18 are incorporated into the numerical scheme, and further details about the governing relations for the wall function approach can be found in Gosman and Ideriah [1976].

The Van Driest Model

In the derivation of the turbulence model following Prandtl [1925], the eddy viscosity ν_t was assumed proportional to a local length and velocity scale. For the $k-\varepsilon$ model these scales are combined to give the expressions in equation 2.14. Prandtl originally proposed a simpler and less general mixing length model for which the expressions for the length and velocity scales for boundary layers are:

$$l_c = l_m \tag{2.19}$$

$$u_c = l_m \left[2 \left(\frac{\partial U_x}{\partial y} + \frac{\partial U_y}{\partial x} \right)^2 \right]^{1/2}$$

where the coordinates and velocities refer to Figure 2.1. These are combined to form the turbulent diffusivity, ν_t:

$$\nu_t = l_m^2 \left[2 \left(\frac{\partial U}{\partial y} + \frac{\partial V}{\partial x} \right)^2 \right]^{1/2}$$

For the case of a fully developed turbulent boundary layer flow the mixing length is proportional to the perpendicular distance from the wall:

$$l_m = \kappa y$$

where κ is the von Karman constant.

In shear layers and two-dimensional boundary layers the mixing length model actually performs reasonably well in predicting features of the flow. The problem in applying the model to more complex flows lies in determining the appropriate distribution of the local length scale, l_c. Van Driest [1956] modified the form of the mixing length to account for wall damping effects. Following his arguments and the analogy to Stokes second problem, the following length is obtained:

$$l_m = \kappa y \left(1 - \exp\left(-\frac{y^+}{A^+} \right) \right) \tag{2.20}$$

where A^+ is an empirical constant determined to be $A^+ = 26$ for a two dimensional boundary layer on a flat plate, and κ is the Von Karman constant.

Using the mixing length model in the near wall region makes it possible to account for the wall's influence on the core flow directly instead of relying on the wall functions. The wall functions lump all of the wall influence into the boundary conditions which are fixed in the flow field rather than at the wall as is most appropriate. In the region near the wall the mixing length model is used to determine the eddy viscosity distribution. In the core of the flow the standard $k-\varepsilon$ model is used. In an interface region between the two, the two models are matched (see Figure 2.3). The determination of this interface region provides the boundary conditions for the k and ε equations. For the velocities, the boundary conditions are set at the wall by assuming that a laminar sublayer exists in this region.

To summarize, the additional relations needed for the Van Driest low Reynolds number model are:

$$\nu_t = l_m^2 \left[2 \left(\frac{\partial U_x}{\partial y} + \frac{\partial U_y}{\partial x} \right)^2 \right]^{1/2}$$

$$l_m = \kappa y \left(1 - e^{-y^+/A^+} \right) \qquad \frac{y^+}{A^+} = \frac{y^+}{26} = \frac{yU_\tau}{26\nu} \tag{2.21}$$

$$U_\tau = \left(\frac{\tau_w}{\rho} \right)^{1/2} \qquad \tau_w = \mu \frac{\Delta U}{\Delta y}$$

These relations form a complete set of equations for calculating the wall modified turbulent viscosity in the near wall regions. No transport equations are solved for k and ε in these regions. In the core of the flow the standard high Reynolds number version (hereafter known as HRE) of the $k-\varepsilon$ model is used to calculate ν_t. As mentioned above, the boundary conditions needed for calculating k and ε in the core of the flow are applied in the interface region, where the mixing length and the $k-\varepsilon$ models are both assumed to apply in determining ν_t. Thus, at the interface,

$$\nu_t = l_m^2 P^{1/2} \qquad \nu_t = c_\mu \frac{k^2}{\varepsilon} \tag{2.22}$$

where

$$P = 2 \left(\frac{\partial U_x}{\partial y} + \frac{\partial U_y}{\partial x} \right)^2 .$$

In the overlap region the turbulence production is assumed to balance dissipation: $\nu_t P = \varepsilon$. Combining this relation with equations 2.22 yields expressions for k and ε in the interface region in terms of mixing length values:

$$k_i = \frac{\nu_t^2}{c_\mu^{1/2} l_m^2} = \frac{l_m^2 P}{c_\mu^{1/2}} \tag{2.23}$$

$$\varepsilon_i = \frac{c_\mu k_i^2}{\nu_t} = l_m^2 P^{3/2} \tag{2.24}$$

The subscript i stands for the interfacial values of the quantities in question. These relations are then used to form boundary conditions for the standard $k-\varepsilon$ model which is assumed to hold in the core of the flow. The position of the overlap region is determined empirically to be $y^+ \approx 10-15$.

2.5. Summary of the Equations

In this section the equations which are used to obtain the turbulent flow field in curved ducts are summarized. The equations contain all the terms and constants as they are modeled in the numerical scheme. (The constants are taken from Launder and Spalding [1974].) The boundary conditions which result from the two methods of modeling the near wall region are also summarized.

Continuity:

$$\frac{1}{r}\frac{\partial}{\partial r}(\rho r U_r) + \frac{1}{r}\frac{\partial}{\partial \theta}(\rho U_\theta) + \frac{\partial}{\partial z}(\rho U_z) = 0 \tag{2.25}$$

Momentum:

r-momentum:

$$\frac{1}{r}\frac{\partial}{\partial r}(\rho r U_r U_r) + \frac{1}{r}\frac{\partial}{\partial \theta}(\rho U_\theta U_r) + \frac{\partial}{\partial z}(\rho U_z U_r) - \frac{\rho U_\theta^2}{r} = -\frac{\partial p_t}{\partial r} \tag{2.26}$$

$$+ \frac{1}{r}\frac{\partial}{\partial r}\left(\mu_e r \frac{\partial U_r}{\partial r}\right) + \underline{\frac{1}{r}\frac{\partial}{\partial \theta}\left(\mu_e \frac{\partial U_r}{r\partial \theta}\right)} + \frac{\partial}{\partial z}\left(\mu_e \frac{\partial U_r}{\partial z}\right)$$

$$- \frac{\mu_e}{r}\left(\frac{U_r}{r} + \underline{\frac{2}{r}\frac{\partial U_\theta}{\partial \theta}}\right) + \frac{\partial}{\partial z}\left(\mu_t \frac{\partial U_z}{\partial r}\right) + \frac{1}{r}\frac{\partial}{\partial r}\left(\mu_t r \frac{\partial U_r}{\partial r}\right)$$

$$+ \underline{\frac{1}{r}\frac{\partial}{\partial \theta}\left(\mu_t \frac{\partial U_\theta}{\partial r}\right)} - \underline{\frac{1}{r}\frac{\partial}{\partial \theta}\left(\mu_t \frac{U_\theta}{r}\right)} - \mu_t \frac{U_r}{r^2}$$

θ-momentum:

$$\frac{1}{r}\frac{\partial}{\partial r}(\rho r U_r U_\theta) + \frac{1}{r}\frac{\partial}{\partial \theta}(\rho U_\theta U_\theta) + \frac{\partial}{\partial z}(\rho U_z U_\theta) + \frac{\rho U_r U_\theta}{r} = -\frac{1}{r}\frac{\partial p_t}{\partial \theta} \tag{2.27}$$

$$+ \frac{1}{r}\frac{\partial}{\partial r}\left(\mu_e r \frac{\partial U_\theta}{\partial r}\right) + \underline{\frac{1}{r}\frac{\partial}{\partial \theta}\left(\mu_e \frac{1}{r}\frac{\partial U_\theta}{\partial \theta}\right)} + \frac{\partial}{\partial z}\left(\mu_e \frac{\partial U_\theta}{\partial z}\right)$$

$$- \frac{\mu_e}{r}\left(\frac{U_\theta}{r} - \frac{2}{r}\frac{\partial U_r}{\partial \theta}\right) + \frac{\partial}{\partial z}\left(\mu_t \frac{1}{r}\frac{\partial U_z}{\partial \theta}\right) + \frac{\partial}{\partial r}\left(\mu_t \frac{1}{r}\frac{\partial U_r}{\partial \theta}\right)$$

$$+ \underline{\frac{1}{r}\frac{\partial}{\partial \theta}\left(\mu_t \frac{1}{r}\frac{\partial U_\theta}{\partial \theta}\right)} + \frac{2}{r}\frac{\partial}{\partial \theta}\left(\mu_t \frac{U_r}{r}\right) - \frac{\partial}{\partial r}\left(\mu_t \frac{U_\theta}{r}\right) + \frac{\mu_t}{r}\left(\frac{\partial U_\theta}{\partial r} - \frac{U_\theta}{r}\right)$$

z-momentum:

$$\frac{1}{r}\frac{\partial}{\partial r}(\rho r U_r U_z) + \frac{1}{r}\frac{\partial}{\partial \theta}(\rho U_\theta U_z) + \frac{\partial}{\partial z}(\rho U_z U_z) = -\frac{\partial p_t}{\partial z} \tag{2.28}$$

$$+ \frac{1}{r}\frac{\partial}{\partial r}\left(\mu_e r \frac{\partial U_z}{\partial r}\right) + \underline{\frac{1}{r}\frac{\partial}{\partial \theta}\left(\mu_e \frac{\partial U_z}{r \partial \theta}\right)} + \frac{\partial}{\partial z}\left(\mu_e \frac{\partial U_z}{\partial z}\right)$$

$$+ \frac{1}{r}\frac{\partial}{\partial r}\left(\mu_t r \frac{\partial U_r}{\partial z}\right) + \frac{1}{r}\frac{\partial}{\partial \theta}\left(\mu_t \frac{\partial U_\theta}{\partial z}\right) + \frac{\partial}{\partial z}\left(\mu_t \frac{\partial U_z}{\partial z}\right)$$

k-equation:

$$\frac{1}{r}\frac{\partial}{\partial r}(\rho r U_r k) + \frac{1}{r}\frac{\partial}{\partial \theta}(\rho U_\theta k) + \frac{\partial}{\partial z}(\rho U_z k) = \rho P_k - \rho \varepsilon \tag{2.29}$$

$$+\frac{1}{r}\frac{\partial}{\partial r}\left[\left(\mu+\frac{\mu_t}{\sigma_k}\right)r\frac{\partial k}{\partial r}\right]+\underline{\frac{1}{r}\frac{\partial}{\partial\theta}\left[\left(\mu+\frac{\mu_t}{\sigma_k}\right)\frac{1}{r}\frac{\partial k}{\partial\theta}\right]}+\frac{\partial}{\partial z}\left[\left(\mu+\frac{\mu_t}{\sigma_k}\right)\frac{\partial k}{\partial z}\right]$$

ε-equation:

$$\frac{1}{r}\frac{\partial}{\partial r}(\rho r U_r\varepsilon)+\frac{1}{r}\frac{\partial}{\partial\theta}(\rho U_\theta\varepsilon)+\frac{\partial}{\partial z}(\rho U_z\varepsilon)=C_{\varepsilon 1}\rho\frac{\varepsilon}{k}P_k-C_{\varepsilon 2}\rho\frac{\varepsilon^2}{k} \tag{2.30}$$

$$+\frac{1}{r}\frac{\partial}{\partial r}\left[\left(\mu+\frac{\mu_t}{\sigma_\varepsilon}\right)r\frac{\partial\varepsilon}{\partial r}\right]+\underline{\frac{1}{r}\frac{\partial}{\partial\theta}\left[\left(\mu+\frac{\mu_t}{\sigma_\varepsilon}\right)\frac{1}{r}\frac{\partial\varepsilon}{\partial\theta}\right]}+\frac{\partial}{\partial z}\left[\left(\mu+\frac{\mu_t}{\sigma_\varepsilon}\right)\frac{\partial\varepsilon}{\partial z}\right]$$

where

$$\mu_e=\mu_t+\mu \qquad \mu_t=\rho c_\mu\frac{k^2}{\varepsilon} \qquad c_\mu=0.09 \qquad C_{\varepsilon 1}=1.44 \qquad C_{\varepsilon 2}=1.92$$

$$\sigma_k=1.0 \qquad \sigma_\varepsilon=1.3 \qquad p_t=p+\frac{2}{3}\rho\,k$$

$$P_k=\frac{\mu_t}{\rho}\left\{2\left[\left(\frac{\partial U_r}{\partial r}\right)^2+\left(\frac{1}{r}\frac{\partial U_\theta}{\partial\theta}\right)^2+\left(\frac{\partial U_z}{\partial z}\right)^2-\frac{U_\theta}{r}\left(\frac{1}{r}\frac{\partial U_r}{\partial\theta}+\frac{\partial U_\theta}{\partial r}\right)\right.\right.$$

$$+\frac{U_r}{r}\left(\frac{U_r}{r}+\frac{2}{r}\frac{\partial U_\theta}{\partial\theta}\right)+\left(\frac{1}{r}\frac{\partial U_r}{\partial\theta}\cdot\frac{\partial U_\theta}{\partial r}+\frac{1}{r}\frac{\partial U_z}{\partial\theta}\cdot\frac{\partial U_\theta}{\partial z}\right)$$

$$\left.+\left(\frac{\partial U_r}{\partial z}\cdot\frac{\partial U_z}{\partial r}\right)\right]+\left(\frac{U_\theta}{r}\right)^2+\left(\frac{\partial U_\theta}{\partial r}\right)^2+\left(\frac{\partial U_\theta}{\partial z}\right)^2+\left(\frac{1}{r}\frac{\partial U_r}{\partial\theta}\right)^2$$

$$\left.+\left(\frac{\partial U_r}{\partial z}\right)^2+\left(\frac{\partial U_z}{\partial r}\right)^2+\left(\frac{1}{r}\frac{\partial U_z}{\partial\theta}\right)^2\right\}$$

Boundary Conditions

For the purpose of defining the boundary conditions the coordinates and velocities are shown in Figure 2.1. Note that the definitions are for a x-y coordinate system shown with U_x and U_y, the velocity components parallel and perpendicular to the boundary, respectively.

Wall Function Approach

Velocities

(a) Symmetry plane $\dfrac{\partial U_x}{\partial y} = 0 \qquad U_y = 0$

(b) Wall $U_y = 0 \qquad U_x = \dfrac{U_\tau}{\kappa} \ln(Ey^+)$

Turbulent kinetic energy

(a) Symmetry plane $\dfrac{\partial k}{\partial y} = 0$

(b) Wall $k_o = \dfrac{U_\tau^2}{c_\mu^{1/2}}$

Energy dissipation

(a) Symmetry plane $\dfrac{\partial \varepsilon}{\partial y} = 0$

(b) Wall $\varepsilon_o = \dfrac{U_\tau^3}{\kappa y}$

Van Driest Model

Velocities

(a) Symmetry plane $\dfrac{\partial U_x}{\partial y} = 0 \qquad U_y = 0$

(b) Wall $U_y = 0 \qquad U_x = 0$

Turbulent kinetic energy

(a) Symmetry plane $\dfrac{\partial k}{\partial y} = 0$

(b) Interface $k_i = \dfrac{l_m^2 P}{c_\mu^{1/2}}$

Energy dissipation

(a) Symmetry plane $\dfrac{\partial \varepsilon}{\partial y} = 0$

(b) Interface $\varepsilon_i = l_m^{1/2} P^{3/2}$

where

$$l_m = \kappa y \left(1 - \exp\left(- \frac{y^+}{A^+} \right) \right)$$

and

$$P = 2 \left(\frac{\partial U_x}{\partial y} + \frac{\partial U_y}{\partial x} \right)^2$$

This completes the review of the various aspects of the turbulence model and the transformation of the governing equations to a set of equations and boundary conditions which can be solved numerically.

3. THE NUMERICAL PROCEDURE

3.1. Introduction

The results presented in this report were all obtained with a modified three-dimensional version of the TEACH code developed at Imperial College [1976]. The modifications in the calculation procedure were made by Chang and Humphrey [1983] along the lines proposed by Pratap [1975], and take advantage of the semi-elliptic nature of strongly curved duct flows. The modifications and validation of the numerical procedure are fully described in Chang and Humphrey [1983]. In the following section a general description of semi-elliptic flows is presented. In section 3.3 the finite difference procedure is described and in section 3.4 the solution algorithm is summarized.

3.2. Semi-elliptic flows

Strictly speaking, all subsonic flows are elliptic in nature. Physically, this means that a change of conditions at any point in the flow field can influence the conditions at any other point. The information can be transmitted from one point to the other by molecular diffusion, convection or pressure waves in the fluid. In order to obtain a mathematical solution to such a problem, boundary conditions for all the dependent variables must be specified on all boundaries of the flow field. From a computational point of view such problems are often time consuming and expensive to solve. Fortunately, simplifying approximations to the equations and boundary conditions can often be made for the problem of interest. These give rise to two further classes of fluid flow problems, the parabolic flow and the semi-elliptic (partially-parabolic) flow.

In a parabolic flow one assumes that convection is the only means of transport in the main flow direction. Such problems do not require boundary conditions for the flow variables on the downstream boundary. Computationally, such flows can be solved using marching techniques with a large saving of computer storage and time. At any time in the solution procedure, values for the dependent variables are needed only at the previously calculated step in order to calculate the unknowns at the next downstream location. For three-dimensional problems the dependent variables are stored in two-dimensional arrays rather than in the three-dimensional arrays required in the counterpart elliptic problem. Examples of such flows include boundary layers, thin shear layers, steady pipe flows and mildly curved duct flows.

The semi-elliptic or partially-parabolic flows, as one might expect, are flows which have some characteristics of both elliptic and parabolic flows. Transport in the main flow direction is assumed to be by convection only, with molecular diffusion being neglected. However, changes in the downstream flow can influence the upstream flow behavior through the pressure field which is treated elliptically. The solution procedure for semi-elliptic problems is similar to that for parabolic problems. Boundary conditions for the dependent variables are not required in the downstream direction and such problems can also be solved using marching techniques.

The distinction between the two types of problems lies in the treatment of the pressure field. In a parabolic problem the pressure is treated like any other dependent variable, determined at any point by its value at the immediate upstream plane. In a semi-elliptic problem the pressure is treated as an elliptic variable field. This means that the pressure at any one location is dependent on the value at every other location in the flow field. So, for a three-dimensional semi-elliptic problem, the pressure must be stored as a three-dimensional array while all the other variables can be stored as two-dimensional arrays. Also, time-marching through the flow field once only is no longer sufficient to determine the values of the flow field variables, since the downstream locations would have no effect on the upstream values. Instead, the solution is determined iteratively by marching through the field several times and updating the pressure field at each iteration.

The semi-elliptic treatment essentially extends the range of flow problems which can be solved using cost effective marching techniques. Among the flow geometries which can be effectively handled are strongly curved duct flows (with no streamwise recirculation) and jet flows in a cross-stream.

3.3. Finite Differencing Procedures

As a result of treating the flow field in curved ducts as a semi-elliptic problem, the terms which are underlined in the governing equations given in chapter 2 can be neglected. Each of the equations can then be written in the same general form given below as a transport equation for the general variable ϕ:

$$\frac{1}{r}\frac{\partial}{\partial r}(\rho r U_r \phi) + \frac{1}{r}\frac{\partial}{\partial \theta}(\rho U_\theta \phi) + \frac{\partial}{\partial z}(\rho U_z \phi) = \frac{1}{r}\frac{\partial}{\partial r}\left(r\Gamma\frac{\partial \phi}{\partial r}\right) + \frac{\partial}{\partial z}\left(\Gamma\frac{\partial \phi}{\partial z}\right) + S_\phi \qquad (3.1)$$

where Γ is the diffusion coefficient for ϕ and S_ϕ is the source term for ϕ, which contains all the remaining terms.

The discretization of the general transport equation is done as in the TEACH family of programs, see Gosman and Ideriah [1976]. A staggered grid system is set up in which the main grid nodes are the storage locations for the pressure and other scalar fields such as the turbulent kinetic energy, k, dissipation, ε, density, ρ, and viscosity, μ (control volume shown in Figure 3.1). The velocity components are stored at points midway between the main grid nodes (control volume shown in Figure 3.2). The treatment of the streamwise velocity is modified in the semi-elliptic procedure. In order to march through the flow field, it is convenient to locate the streamwise velocity a half-step ahead of the main grid node rather than behind as is the case in the elliptic version. This grid system enhances the stability of the solution procedure and minimizes the amount of interpolation necessary in performing the calculations.

To obtain the finite difference form of the general transport equation, equation 3.1 is integrated over the control volume for ϕ shown in Figure 3.3. Using central differencing for the diffusion terms and leaving the convection terms unspecified for the moment, the discretized form of equation 3.1 becomes:

$$\begin{aligned} &C_e\phi_e - C_w\phi_w + C_n\phi_n - C_s\phi_s + C_d\phi_d - C_u\phi_u = \qquad (3.2)\\ &\qquad D_e(\phi_E - \phi_P) - D_w(\phi_P - \phi_W) + D_n(\phi_N - \phi_P) - D_s(\phi_P - \phi_S) + \overline{S_\phi}\Delta V \end{aligned}$$

where $C_e = (r\Delta r\Delta\theta)_e(\rho U_z)_e$; $C_w = (r\Delta r\Delta\theta)_w(\rho U_z)_w$

$$C_n = (r\,\Delta z\,\Delta\theta)_n(\rho U_r)_n \quad ; \qquad C_s = (r\,\Delta z\,\Delta\theta)_s(\rho U_r)_s$$

$$C_d = (\Delta r\,\Delta z)_d(\rho U_\theta)_d \quad ; \qquad C_u = (\Delta r\,\Delta z)_u(\rho U_\theta)_u$$

$$D_e = \left.\frac{r\,\Delta r\,\Delta\theta}{\Delta z}\right|_e \Gamma_e \quad ; \qquad D_w = \left.\frac{r\,\Delta r\,\Delta\theta}{\Delta z}\right|_w \Gamma_w$$

$$D_n = \left.\frac{r\,\Delta r\,\Delta\theta}{\Delta r}\right|_n \Gamma_n \quad ; \qquad D_s = \left.\frac{r\,\Delta r\,\Delta\theta}{\Delta r}\right|_s \Gamma_s$$

$$\Delta V = r\,\Delta r\,\Delta\theta\,\Delta z \quad ; \qquad \overline{S_\phi} = \frac{1}{\Delta V}\int S_\phi\, r\, dr\, d\theta\, dz$$

where all the subscripts refer to Figure 3.3.

As is the practice in TEACH type programs the source term is linearized as $\overline{S_\phi} = S_U + S_P\phi_P$. This practice proves to be beneficial in adding stability to the solution procedure and is fully described in Patankar [1980]. The accuracy of the solution and stability of the numerical procedure have proven to be very sensitive to the prescription of the ϕ's in the convective terms at the control volume interfaces. A summary of the differencing schemes used in the present study is given next.

For the ϕ's at the upstream and downstream locations (ϕ_u, ϕ_d), upwind differencing was always used for the calculations presented in this report. In this scheme the values for the ϕ's are given as $\phi_d = \phi_P$ and $\phi_u = \phi_P^o$ where ϕ_P^o is the value of ϕ_P at the neighboring upstream location, (or, the "old" ϕ_P-value). This differencing method is in keeping with the assumptions made for marching through the flow field in semi-elliptic problems.

For the ϕ's at the cross-stream locations (ϕ_n, ϕ_s, ϕ_e, ϕ_w) the hybrid differencing method was used for the calculations presented. This scheme, which was first proposed by Spalding [1972], is based on an approximation to the exact solution of the one-dimensional convection-diffusion equation. Depending on the local control volume Peclet number either a central-differencing or upwind-downwind differencing approximation is made. Details of the specific use of the hybrid scheme are given in Chang and Humphrey [1983]. What is important to note is that the scheme results in a very stable form of the difference equations. The drawback to the this scheme is that it is only first order accurate in regions where convection dominates. This leads to the possibility of serious errors in the solution due to numerical diffusion which makes the evaluation of turbulence models more difficult.

For these reasons as well as others, the higher order quadratic-upwind scheme (QUICK) first proposed by Leonard [1979] has come into increasing usage. The details of this differencing scheme as it is used by our research group are summarized by S. L. Yuan in Appendix A. While all of the calculations presented in the report were done using the hybrid differencing scheme, it is proposed to incorporate the QUICK scheme into the program in future work. The advantages to be gained from reduced numerical diffusion far outweigh the disadvantages of potential stability problems which can result from careless use of the quadratic differencing.

After the form of the difference scheme is determined, the interface values of ϕ can be determined in terms of the values of ϕ at the main grid nodes (P,N,S,E,W). The difference equation 3.2 can then be written in the following form for the general field variable, ϕ:

$$a_P \phi_P = \sum_{n=1}^{4} a_n \phi_n + S_U \tag{3.3}$$

where the a_n's are coefficients of the ϕ_n's and are determined by the local convective and diffusive coefficients of equation 3.2. Details of how the coefficients are determined are given in Patankar [1980] for the hybrid scheme as well as several others.

3.3.1. Treatment of Boundary Conditions

This section presents the incorporation of the boundary conditions into the numerical procedure. There are four different types of boundaries which occur in the calculation of straight and curved ducts: the inlet, wall, symmetry plane and outlet. For each type of boundary a numerical treatment must be determined for the three velocity components as well as for the turbulence quantities, k and ε. The numerical representation of the boundary conditions must reproduce faithfully the exact mathematical formulation (as given in section 2.5) in order to obtain as accurate a solution of the flow field as possible.

With reference to Figure 1.2, at the inlet plane of a straight channel or duct, a plug flow profile is prescribed for both the laminar and turbulent cases. The streamwise velocity component is set to the bulk velocity and the cross-stream velocities are set to zero. For turbulent flow in a straight channel, empirical profiles for the turbulent kinetic energy and dissipation are given. These profiles are due to Coles and Hirst [1968] and are for turbulent flow past a flat plate. For the straight duct the profile for the turbulent kinetic energy is set to 0.045% of the main flow kinetic energy. This corresponds to a turbulence intensity of approximately 1.2%. The inlet value of k was chosen to be small compared to final fully developed values which in duct flows. Estimates of the turbulent kinetic energy distribution in duct flows were determined using experimental values for the wall shear stress and a semi-empirical equation relating the shear stress coefficient to the duct Reynolds number. From Kays and Crawford [1980] for $3\times10^4 < \mathrm{Re} < 10^6$:

$$\frac{c_f}{2} = 0.023\mathrm{Re}^{-0.2}$$

where

$$\frac{c_f}{2} = \frac{\tau_w}{\rho U_b^2}$$

is the shear stress coefficient. This is related to the shear velocity, U_τ as

$$\frac{U_\tau^2}{U_b^2} = \frac{\tau_w}{\rho U_b^2} = 0.023\mathrm{Re}^{-0.2}.$$

For a duct Reynolds number of Re = 40,000, this corresponds to

$$U_\tau^2 \approx 0.0028 U_b^2.$$

In fully developed duct flows, the value of k^+ $(= k/U_\tau^2)$ is known to vary between approximately 1.0 at the centerline and a maximum of 3.5 near the wall (see e.g. Laufer [1954]). Combining the above relations for the turbulent kinetic energy k, and the shear velocity U_τ, gives estimates of the bounds on the expected k-profile:

$$0.0028 < \frac{k}{U_b^2} < 0.0070$$

The inlet profile of k was chosen to be less than 20% of the expected centerline value for fully developed flow so that incoming turbulence would not significantly affect the flow development in the duct. The dissipation profile is prescribed by setting

$$\varepsilon = \frac{c_\mu^{3/4}\, k^{3/2}}{l_m} \tag{3.4}$$

where l_m is the mixing length determined from a generalization of Nikuradse's straight pipe formula for square ducts by Chang and Humphrey [1983]. For the inlet conditions to the curved duct, the fully developed outlet profiles of the velocity components and turbulence quantities from the straight duct calculations are used. The flow in the straight duct calculations was assumed to be fully developed when the profiles of the velocities and turbulence quantities did not change in the streamwise direction. These calculations are discussed further in the section on test cases. The profiles are computed using either wall functions (WFM) or the Van Driest model (VDM) in the near wall region depending on which is to be used in the curved duct calculations.

At the symmetry plane of the duct or channel, the velocity perpendicular to the symmetry plane is set to zero as well as the normal gradient of the remaining two velocity components and all other scalar quantities.

At the walls, the boundary conditions depend on which turbulence model is used in the near wall region. When the WFM formulation is used the boundary conditions are specified near the wall rather than at the wall, as outlined in section 2.4. The grid point nearest the wall is assumed to lie in a region where the logarithmic law of the wall holds. It is further assumed that the turbulence is in a state of local equilibrium (production of kinetic energy = dissipation, $P_k = \varepsilon$). With these assumptions the boundary conditions for the three velocity components and the turbulence quantities, k and ε, can be set as given in section 2.5.

When the VDM formulation is used in the near wall region the zero velocity boundary condition is applied at the wall for the three velocity components. The boundary conditions for k and ε are set at the interface between the region where the Van Driest model (VDM) applies and that where the high Reynolds number model (HRE) applies. In the interfacial region it is assumed that the turbulence is in local equilibrium and that both the Van Driest and standard k-ε models are valid. With these assumptions the conditions for k and ε at the interface given in section 2.5 can be derived.

Finally, the conditions at the outlet plane are those of a fully developed flow. In this situation the normal gradients of all the dependent variables are set to zero. In all of the cases examined these conditions yielded satisfactory results and provided few problems with stability or convergence.

3.4. The Solution Algorithm

The code developed by Chang and Humphrey [1983] has been substantially modified in order to obtain the results reported here. The semi-elliptic procedure proposed by Pratap [1975] was used with several modifications suggested by Iacovides [1986]. In the semi-elliptic solution procedure the basic strategy can be summarized as follows. All the dependent variables (U_θ, U_r, U_z, k, ε, etc.) with the exception of the pressure are stored as two-dimensional arrays and continuously updated. The pressure field alone is stored as a three-dimensional array covering the entire flow field. The solution domain is swept through using a plane-by-plane marching technique until a converged solution is obtained. At each step in the marching procedure the sequence begins with the computation of the three velocity components at the current plane. The respective momentum equations are solved using the upstream station values from the current sweep for the velocities and the current plane values of the previous sweep for the pressure. A pressure correction equation is then solved and the current plane velocity field is corrected to satisfy continuity. The current plane pressure field is also updated through the pressure correction equation. Lastly the transport equations of the turbulence quantities are solved. The sequence is then repeated at the next downstream station until the entire flow field has been traversed. This makes up one pass through the flow field. Generally, several passes are required to obtain a converged solution.

The procedure of correcting the current plane velocity and pressure fields to satisfy continuity is part of the SIMPLE algorithm of Patankar and Spalding [1972]. The algorithm was introduced with reference to parabolic flows and extended to elliptic flows;

Patankar [1980]. It is the standard pressure solver used in the TEACH type elliptic codes. It has also been used with some modifications in the semi-elliptic calculations of Pratap [1975], Chang et al. [1983] and Iacovides [1986]. The algorithm is briefly summarized here. The dependent variables are assumed to take the form of equations 3.5:

$$p = p^* + p' \tag{3.5}$$

$$U = U^* + U'$$

where the superscripts (*) and (′) refer to the estimated values and the correction terms, respectively. The procedure begins with a guessed pressure field, p^*. Discretized momentum equations are solved to give a "starred" velocity field. For example, the equation for the velocity at the east boundary of the P-cell would be:

$$a_e U_e^* = \sum_{n=1}^{4} a_n U_n^* + S_U + (p_P^* - p_E^*) A_e \tag{3.6}$$

where the subscripts in equation 3.6 refer to Figure 3.2, A_e is the perpendicular control volume area and the rest of the terms are the same as before. Note also, that equation 3.6 is in the form of equation 3.3. The resulting velocity field satisfies the momentum equations subject to the guessed pressure field, p^*. A pressure correction equation derived from the continuity equation (see Patankar [1980], for details) is then solved to give a pressure correction field, p'. The "starred" pressure and velocity fields are then corrected to satisfy continuity. The velocity and pressure corrections are related as follows:

$$U_e' = \frac{A_e}{a_e}(p_P' - p_E') = dU_e \cdot (p_P' - p_E') \tag{3.7}$$

where the subscripts refer again to Figure 3.2. This simplified relation between the pressure and velocity corrections is approximate and only true as the two corrections approach zero. The resulting corrected velocity field will, in general no longer satisfy the momentum equations. A number of iterations are therefore necessary to obtain a velocity field which satisfies both the momentum and continuity equations.

The algorithm is uncomplicated and has been applied to a wide variety of problems with success. Nevertheless the use of the simplified pressure-velocity correction relation decreases the stability of the numerical procedure. This is especially noticeable in applications of the algorithm to the semi-elliptic calculations, since the pressure field carries all of the information concerning the flow from one sweep to the next. Instabilities in the pressure field can be passed to the velocity field through the correction equation. The new velocity field is then in turn used to update the pressure field. The instabilities in the original pressure field can then possibly be amplified in the updated version.

One of the techniques suggested by Pratap [1975] to speed convergence and add stability to semi-elliptic calculations is the downstream bulk pressure correction. It is particularly helpful in semi-elliptic calculations of flows which are more elliptic than parabolic, such as the curved duct flow examined in this study. A bulk pressure correction term is calculated in an analogous way to the local pressure correction term used in SIMPLE. This correction term is based on an overall mass imbalance at each plane rather than a local mass imbalance. A corresponding bulk velocity correction term for the streamwise velocity is also calculated. The correction terms are determined from the following:

$$p_b{}' = \frac{\sum\sum \rho U_\theta \Delta r \Delta z - \sum\sum \rho U_b \Delta r \Delta z}{\sum\sum \rho d U_\theta \cdot \Delta r \Delta z} \tag{3.8}$$

$$U_\theta{}' = \frac{\sum\sum \rho U_\theta \Delta r \Delta z - \sum\sum \rho U_b \Delta r \Delta z}{\sum\sum \rho \Delta r \Delta z}$$

The pressure correction is applied to the pressures at each downstream plane. The velocity correction is applied to the current plane streamwise velocity field. Pratap [1975] found that the use of the bulk pressure correction increased the convergence rate by up to 5 times, in the mildly curved pipe flows he examined.

Several additional improvements, suggested by Iacovides [1986], have been incorporated in the present code for making the calculations of the 90° curved bend. They have been found to stabilize the calculation procedure and improve the convergence rates of the calculations reported here.

The plane-by-plane solution of the local pressure correction equation mentioned in connection with the SIMPLE algorithm can lead to instability in the procedure when applied to flows which are strongly elliptic in nature. At a given plane in the marching sequence, the downstream velocity field is unknown so the corresponding pressure correction term, p_d must be set to zero. The local streamwise (θ) velocity correction equation then becomes:

$$U_\theta{}' = dU_\theta \cdot p_P{}' \tag{3.9}$$

$$U_\theta = U_\theta^* + dU_\theta \cdot p_P{}' .$$

At the beginning of the iteration process this expression can lead to physically improper velocity corrections which can, in turn, destabilize the numerical procedure. For example, consider the flow in the entry region of the curved duct near the outer radius wall where the streamwise pressure gradient is positive. As this region is approached the velocity correction equation will accelerate the velocities since $p_P{}'$ and therefore the velocity correction, $U_\theta{}'$ will be positive. Just the opposite situation will occur in a region where the pressure gradient is negative. As suggested by Bergeles et al. [1978] and Iacovides [1986] this source of instability can be avoided by leaving the streamwise velocity uncorrected during a given sweep. The local correction is indirectly applied in the succeeding sweep when the updated pressure field (which has been corrected) is used. Continuity is still satisfied locally because the bulk pressure correction is applied to the streamwise velocity component (equation 3.8). This modification will affect how the final solution is approached but not the solution itself. It will remain unaffected since the p' terms all go to zero as the converged solution is approached.

In the semi-elliptic calculation procedure, solving the momentum equations at the current plane requires the use of upstream values of the velocities to evaluate the convection coefficients (the C's in equation 3.2) and source terms. This clearly will be a source of error in the final results although the error may be small if the flow field changes slowly from one cross-stream plane to the next. For the case where significant changes in the flow field occur within the spacing of successive cross-stream planes, grid refinement in the streamwise direction can resolve the flow domain more accurately. For reasons of cost and storage limitations it is not always possible to add the additional planes necessary in the streamwise direction. Even with grid refinement this source of inaccuracy can not be completely eliminated. However, the inaccuracy can be removed by performing additional in-step iterations at the current plane which can be added as the converged solution is approached. When the current plane velocities have been determined the momentum equations are solved again using the new velocities to determine the convective coefficients and source terms. This practice has been followed in the present study. It was suggested by Iacovides [1986] who found significant improvements in the resolution of the cross-stream velocities in his curved pipe calculations. In practice, 2 to 3 iterations per plane were found to be sufficient in the present calculations. As pointed out by Iacovides, the number of iterations necessary to determine a velocity field at the current plane which does not change with additional iterations (fully converged) will depend on the Reynolds number, streamwise grid resolution and the bend radius.

Finally, the subject of under-relaxation must be considered. In a fully elliptic calculation procedure it is possible and often beneficial to under-relax the momentum equations and transport equations for the turbulence quantities. The use of an under-relaxation factor is useful in stabilizing the iterative procedure, particularly in solving the non-linear momentum equations. However, in a marching type procedure such as the semi-elliptic method, the relationship between the new variable value to be calculated ϕ^n and old value upon which it is based, ϕ^o is no longer the same. In an elliptic calculation procedure the entire variable field is stored and the value of any variable is related to its previous iteration value via:

$$\frac{a_P}{\alpha}\phi_P^n = \sum_{n=1}^{4} a_n \phi_n^n + S_U + (1-\alpha)\frac{a_P}{\alpha}\phi_P^o \tag{3.10}$$

where the subscripts are the same as in equation 3.3, the superscripts refer to "new" and "old" values and α is the under-relaxation factor such that $0 \leq \alpha \leq 1$. The derivation of equation 3.10 can be found in Patankar [1980]. Note that the spatial location of the old and new values of ϕ are the same so that, as the converged solution is approached, the difference between the two will go to zero. This is not the case in a marching type solution procedure. In this situation the value of the new variable is related to its value at the previous plane in the marching sequence. Because in a completely converged solution the field variables at different spatial locations will not usually be the same, the under-relaxation factor in equation 3.10 must be set equal to one for the final sweep of all the transport equations solved for the dependent variables. In the initial stages of the calculation the under-relaxation factor is often less than one to add stability to the solution procedure. The solution procedure in the present case generally started with under-relaxation factors of 0.5 which were raised gradually after a stable pressure and velocity field were established. The local and bulk pressure correction equations are the only exceptions. They may have under-relaxation factors less than one throughout the calculation procedure since they are both approximate. However, as the correction terms which they determine will go to zero for the final converged solution, no errors will result from the under-relaxation.

In summary, the principal features of the semi-elliptic calculation procedure are as follows:

(1) The pressure field is stored as a three-dimensional array for the entire flow field. It is assigned an initial guessed value for the first pass and is updated on each succeeding pass through the calculation domain.

(2) A solution is obtained by marching through the flow domain along the main flow direction as many times as necessary in order to satisfy the preset convergence criteria.

(3) The momentum equations and equations of transport for k and ϵ are solved at each cross-section in a pass through the flow field. The dependent variables are stored temporarily as two-dimensional arrays at the current computing station. Because of this practice the non-linear convective terms in the momentum equations are linearized with respect to their values at the previous (upstream) station.

(4) The pressure and velocity fields are corrected at each station using a modified version of the SIMPLE algorithm. Details of the SIMPLE solution algorithm can be found in Patankar [1980].

(5) The finite difference equations are solved at each cross-section using a line by line iterative procedure, the tridiagonal matrix algorithm.

(6) A solution is taken as converged when all the corrections to the pressure field fall below a predetermined value set at the start of a calculation run.

4. TEST CASES AND DISCUSSION

4.1. Introduction

The modifications to the semi-elliptic procedure which were discussed in the previous section, were incorporated into the code of Chang and Humphrey [1983]. Prior to embarking on the calculations with which this study is concerned, several preliminary tests of the calculation procedure were made. There were two purposes in making these initial test runs. First, it was necessary to check that alterations in the coding were correctly implemented. Second, it was important to compare the results of this numerical procedure with other calculations and experimental data to quantify the accuracy which could be expected. Laminar flows were used for the comparisons, so that errors due to the numerical procedure could be separated from errors due to the turbulence model. The test cases consisted of developing flow in a two-dimensional straight channel and in a square straight duct. As a final test, the turbulence models were evaluated by comparison with experimental data of two well documented turbulent flows, the fully developed channel flow of Laufer [1956] and the developing flow in a straight duct of Melling [1975]. This permitted quantifying the extent to which the predictions and the experimental data could be expected to agree. In addition to the tests reported here, the basic semi-elliptic procedure of Chang and Humphrey [1983] has been extensively tested against a variety of flows by the authors.

In the next section the laminar flow calculations will be described. The turbulent flow test cases are considered in section 4.3. Some concluding remarks about the performance of the numerical procedure are given in the final section of this chapter.

4.2. Laminar flows

The two cases which were chosen for the evaluation of the numerical procedure were the developing laminar flow in a straight channel and the developing laminar flow in a straight duct. The laminar flow in a straight duct has been studied numerically and analytically by a number of researchers. Calculations using the present numerical procedure were compared with the predictions of Schlichting [1979] using the boundary layer equations, and of McDonald et al. [1972] using a fully elliptic procedure. The developing centerline velocity is shown in Figure 4.1, and profiles of the streamwise velocity at various stations downstream are given in Figure 4.2. It will be noted that the agreement with the fully elliptic predictions of McDonald et al. is much better than that with the parabolic predictions of Schlichting. This is due primarily to the fact that the semi-elliptic procedure allows for the cross-stream pressure gradient and velocity which exist in the early development of the channel flow, which are neglected in the parabolic procedure. As a result, the parabolic procedure predicts a centerline velocity development which is too fast at first and shows the maximum velocity always occurring at the centerline at each downstream position in the development region. The results of the semi-elliptic procedure predict an initially slower development of the centerline velocity. In the early development region, the maximum velocity occurs between the channel wall and symmetry plane ($y/d = 0.4$, $x/d = 1.0$). This is in agreement with the elliptic predictions of McDonald et al. [1972]. The departure of the semi-elliptic predictions from those of the fully elliptic procedure in the first hydraulic diameter is due to the omission of the streamwise diffusion terms in the semi-elliptic formulation. This leads to a maximum discrepancy in the predictions of $\leq 4\%$ at $x/d = 1$, when compared with the exact elliptic predictions. The semi-elliptic calculations were performed on a uniform 20×60 grid, with 20 nodes in the cross-stream direction and 60 streamwise positions. The results compare well with the exact elliptic calculations which were done on a 21×201 grid. Preliminary coarse grid calculations were carried out on a uniform 15×40 grid. The results showed a shorter development length which was the result of numerical diffusion in the calculation.

The predictions of the developing laminar flow in a square duct using the semi-elliptic code compare very well with the experimental results for Re = 200 (Figure 4.3). The deviation from the measured values is $\leq 2\%$. The agreement between measurements and predictions of the velocity profiles in the development region is also good (Figure 4.4). As with the channel flow predictions, the maximum error occurs in the first hydraulic diameter where the streamwise diffusion of momentum is significant in determining the velocity profile. Nevertheless, even in this region the departure from the measured velocities is $\leq 2.5\%$. Because of the symmetry of the flow in both cross-stream (y,z) directions, calculations could have been made in one quadrant of the cross-stream plane. However, the present calculations were made taking advantage of only one plane of symmetry (z-direction) in order to check the symmetry of the calculation procedure. Plots of the results from the two quadrants were identical.

The calculations were done on a uniform $20 \times 40 \times 50$ ($z \times y \times x$) grid with 50 planes in the streamwise (x) direction. The grid resolution in the streamwise direction was determined experimentally so that the development length did not vary as the number of streamwise planes increased. Two streamwise planes per hydraulic diameter were found to give sufficient resolution of the streamwise flow variation. The cross-stream grid distribution was determined by plotting the wall shear stress on the symmetry plane as a function of the number of nodes in the z- or y-direction. The results for two streamwise locations are shown in Figure 4.5. The grid used to produce the results shown in Figure 4.2-4.4 corresponds to 20 nodes between the wall and plane of symmetry (z- or y-direction).

4.3. Turbulent flows

The test cases for turbulent flow provided a check for the two turbulence model formulations used in the present study. The test cases served to characterize the models and give some idea of their capabilities and limitations. As mentioned in Chapter 2 the models differed in their treatment of the near wall region and both used the standard $k-\varepsilon$ model (HRE) in regions away from solid boundaries. In this section the two models will be compared and contrasted in their ability to predict the features of the turbulent shear flow in a two-dimensional channel and in a square duct. The model which uses wall functions in the near wall region will be referred to as WFM and that which uses the Van Driest mixing length model will be referred to as VDM.

Two-dimensional channel flow. The fully developed turbulent flow in a large aspect ratio channel has been experimentally characterized by Laufer [1950]. This study has often been used to characterize turbulence models because of the abundance of detailed data provided for this relatively simple flow.

In the present study both the VDM and WFM formulations were used to predict the flow. Comparisons with Laufer's data are shown in Figures 4.6-4.12. Further comparisons of the two models are given in Figures 4.13-4.20 where the effect of the log law-of-the-wall constants in the WFM is shown. The results were obtained using a 34×240 grid for the VDM and a 24×240 grid for the WFM with 240 positions in the streamwise direction. The grid distribution was non-uniform in the cross-stream direction and uniform in the flow direction. The flow was assumed to be numerically fully developed when the changes in the velocity profile and the profiles of k and ε showed no variation further downstream. Additionally, the streamwise pressure gradient and predicted wall shear stresses remained constant.

The 240 positions in the streamwise direction correspond to nearly $50D_h$, which is much longer than the distance necessary to obtain fully developed profiles in the experimental case ($\approx 20D_h$). It is known that turbulence profiles in the $k-\varepsilon$ model develop more slowly in numerical calculations than experimentally. This was true in the present study also, regardless of which model was used in the near wall region. The difference in development length is also related to the different inlet profiles used in the present numerical study and Laufer's experimental investigation. Laufer used screens and a contracting channel upstream of the measurement stations. He also did not characterize the inlet plane, so it was not possible to reproduce the development region numerically. The streamwise grid spacing was chosen so that the marching procedure would be stable. Additional nodes in the cross-stream direction did not significantly change the streamwise velocity profile or distribution of k and ε. However, the profiles of velocity and turbulence quantities were strongly influenced by the placement of the near wall nodes.

In Figures 4.6-4.8 the predictions using the VDM are compared with Laufer's [1950] data. The predictions were made with the overlap region between the standard $k-\varepsilon$ model (HRE) and the VDM located at $y^+ \approx 10$ in dimensionless wall coordinates. This seemed to give the best results for the duct flows which were the focus of the study, but leads to some discrepancies in the channel flow predictions. It will be seen later that locating the overlap region too far into the flow can lead to serious discrepancies when the VDM is used. Figure 4.6 compares the experimentally measured mean velocity profile with the predicted values. The agreement is good, with the error being everywhere less than 3%. However, the mean velocity profile proved to be the least sensitive variable to model differences. Figures 4.7 and 4.8 show the predicted profiles of the turbulent kinetic energy and Reynolds shear stress ($\overline{u_x u_y}$) compared with the experimental results. In both cases the predicted results are too high, although they show the correct trends.

Figures 4.9-4.11 show the predicted profiles of velocity, kinetic energy, and shear stress using the WFM in the near wall region. In these figures the standard constants in the law-of-the-wall are used (equation 2.12, with κ and E as given). In general, the agreement of the predictions with Laufer's results is similar to that obtained using the VDM. The discrepancy in the mean velocity profile is a little greater ($\leq 5\%$) using the WFM.

The predicted results of the turbulent kinetic energy and Reynolds shear stress using the WFM formulation are also higher than the experimental results. The magnitude of the overprediction is similar for the VDM and the WFM except very near the wall. Here, the WFM shows an unrealistic peak for both the k- and $\overline{u_x u_y}$- profiles. This is partly due to accounting for the entire influence of the wall at the single grid node closest to the wall. Adjusting the near wall values of k and ε (and hence, μ_t) through the boundary conditions given in equations 2.16 and 2.17 will determine the distribution of the turbulent viscosity in the rest of the flow. This means that the distribution of the turbulence quantities is determined at least in part by the log law-of-the-wall constants κ and E since they are used to determine the wall shear τ_w and hence the shear velocity, U_τ. Figure 4.12 shows the effect on the Reynolds stress distribution of using Laufer's [1950] recommended constants (E = 6.27, κ = 0.334) in the WFM formulation. The agreement away from the wall is quite good. However, this is not surprising since the predictions assume law-of-the-wall behavior and Laufer's constants were chosen to fit the data. Essentially, the predictions show that the fit is a good one.

The constants which Laufer determined experimentally differ greatly from those recommended by Rodi [1980] and others and which are most commonly used. Therefore, the more widely accepted values given in equation 2.12 are used in the WFM throughout this study.

The overprediction of the turbulence quantities in the core of the flow by both model formulations is due, in part, to assumptions implicit in the models themselves. The $k-\varepsilon$ model assumes local isotropy of the normal stresses when, in fact, the streamwise fluctuations in the channel flow are up to five times greater than the cross-stream fluctuations. This is certain to affect both the predicted k-profile as well as the $\overline{u_x u_y}$-profile, which is related to the kinetic energy through the Boussinesq assumption (equation 2.14).

Figures 4.13-4.16 and 4.17-4.20 compare results obtained with the VDM formulation with those obtained using the WFM formulation (and standard constants). The first set of four figures gives the profiles obtained when the overlap region between the VDM and HRE regions is located at $y^+ \approx 10$. It will be seen that the agreement obtained for the velocity profile and the k- and ε- profiles is fairly close. The agreement of the profiles of the turbulence quantities yields agreement in the profile of the effective eddy viscosity shown in Figure 4.16. In contrast with this close agreement between predictions using the two model formulations, the differences in Figures 4.17-4.20 are larger. The VDM predictions in this case were made by fixing the overlap region between the near wall and the core flow at $y^+ \approx 25$. The mean velocity profile in Figure 4.17 shows the least sensitivity to this change, although the discrepancies are larger than those in Figure 4.13. Figures 4.18-4.20 show large differences in the profiles of k and ε and in the resulting effective eddy viscosity profile. Locating the near wall/core overlap region too far from the wall can be seen to have a significant effect on determining the distribution of the turbulence quantities, and hence on the effective turbulent transport properties. Additional tests with the overlap region located still further from the wall region led to further discrepancies in the turbulence quantity profiles. As a result of these comparisons, prior to making the detailed curved duct calculations using the VDM, some preliminary coarse grid calculations were made to determine the grid positions in wall coordinates. The overlap region was then chosen to occur in the region $y^+ \approx 10-15$.

Developing flow in a square duct. Figures 4.21-4.28 show comparison of calculated results with the experiments of Melling [1975]. The calculations were conducted in one half-plane of the duct cross-section to take advantage of a plane of symmetry in the geometrical configuration. Calculations could have been performed in one quadrant of the duct since there are actually two planes of symmetry in straight duct flow. This was not done since the resulting fully developed duct profiles were to be used as the inlet flow for the curved duct calculations where there is only one plane of symmetry. As in the straight channel calculations the profiles were determined to be fully developed when they exhibited no further change in the streamwise direction. Further, the streamwise pressure gradient and wall shear stress were constant.

The calculations were performed either on a non-uniform $25 \times 50 \times 40$ ($z \times y \times x$) grid for the VDM formulation or a non-uniform $20 \times 40 \times 40$ ($z \times y \times x$) grid for the WFM formulation. The 40 planes in the streamwise (x) direction corresponded to approximately $25D_h$, which was not enough to yield a fully developed solution. The outlet profile was therefore used as an inlet profile and another $25D_h$ were calculated in the streamwise direction. This process was continued until no changes were observed in the profiles of velocity and the turbulence quantities. The grid distribution was determined from the preliminary turbulent channel flow calculation where the significant flow features were found to be well resolved.

The development of the centerline velocity for the WFM and VDM calculations are compared with Melling's [1975] data in Figures 4.21 and 4.22, respectively. The development of the streamwise turbulence intensity, is shown for the WFM and VDM calculations in Figures 4.23 and 4.24. The turbulence intensity was determined from the $k-\varepsilon$ model and is related to the root mean square of the velocity fluctuations, $\tilde{u}$. If local isotropy is assumed, then the r.m.s. velocity is

$$\tilde{u} = \sqrt{\overline{u^2}} = \left(\frac{2}{3} k \right)^{1/2} \tag{4.1}$$

The turbulence intensity is determined either as a percentage of the bulk velocity, U_b or the centerline velocity, U_{cl} as in Melling's experiments:

$$\text{Intensity} = \frac{\tilde{u}}{U_{cl}} \cdot 100 \tag{4.2}$$

Because of the isotropic viscosity assumption, all three components of the calculate turbulence intensity are identical. Comparisons with Melling's data are made with the measured streamwise turbulence intensity.

Melling had a smooth square contraction upstream of the duct and used a boundary layer trip at the duct entrance. Because he used a boundary layer trip in his experiments, the initial conditions are difficult to reproduce numerically. Instead a virtual origin for the calculations is determined by adjusting the axial location of the experimental profiles so that they agree with predictions at some initial position. In this case the virtual origin was determined to be about $6D_h$ upstream of the trip. The profiles in Figures 4.21-4.24 have been adjusted to account for this experimental virtual origin.

The development length of turbulent duct flow in a square cross-section duct varies between $85D_h$ and $140D_h$ depending on the inlet conditions, according to Demuren and Rodi [1984]. Although the basic features of the fully developed duct flow are present in Melling's measurements at the last streamwise measurement position, an additional 40-50 hydraulic diameters would be necessary to obtain a truly fully developed flow. Even at the final downstream measurement position (36.8 D_h from the entrance) the flow was far from being fully developed. Melling [1975] mentioned that the centerline velocity and turbulence intensity were still changing at the final measurement station, although the changes observed were small. For the WFM calculations (Figure 4.21) the development length was approximately $70D_h$, while for the VDM calculations (Figure 4.22) the length was a little longer, approximately $90D_h$. These values compare well with those determined by Demuren and Rodi [1984]. It is clear from the figures that the experimental profiles do not exhibit as large a variation in the centerline velocity and turbulence intensity as the calculations show.

There is a noticeable overshoot in the predicted profiles of velocity and turbulence intensity using either of the model formulations (the "hump" in the Figures). A similar overshoot was noted by Melling in the experimental study, although much smaller in magnitude and occurring earlier in the development region. This was due to a redistribution of the momentum in the duct by the Reynolds stress driven secondary motion. In the numerical calculations this type of secondary motion will not occur because of the assumed isotropy of the eddy diffusivity term, ν_t. However, a redistribution of momentum by means of the turbulent diffusion probably does influence the centerline profiles of velocity and turbulence intensity. For example, the turbulence intensity profiles of Figures 4.23 and 4.24 show a much longer development length before the turbulence intensity starts to increase. This could be explained by the transport due to turbulent diffusion being underpredicted in the initial development region of the duct. This would account for the longer length over which the centerline velocity increases, since the low value of k at the centerline would lead to less mixing in this region. When the centerline turbulence intensity increases in both model formulations there is an accompanying decrease in the centerline velocity.

Figure 4.25 compares experimental and numerical contours of the streamwise velocity for fully developed flow in a square duct. The experimental results are from Melling's [1975] study, at the final downstream measurement plane. As mentioned earlier the experimental profiles still showed evidence of further downstream development, but the changes were small ($\leq 1\%$). The bulging in the experimental contours towards the duct corners are due to the stress driven secondary motion referred to above. These "bulges" do not show up in either of the predictions because of the isotropic eddy diffusivity assumption of both model formulations. Figure 4.26 shows the streamwise velocity profile at two cross-stream positions. The profiles were taken at the symmetry plane ($z/D_h = 0.5$) and midway between the symmetry plane and duct wall ($z/D_h = 0.25$). The profiles indicate the symmetry which exists in the flow both experimentally and numerically. There is little difference in the predicted results using either model formulation, the agreement being to within 1%. The discrepancies between the measured and predicted profiles are due primarily to the absence of stress driven secondary motion in both calculation schemes. This secondary motion results in a flatter velocity profile in the core of the duct flow and steeper velocity gradients in the corners than predicted.

Figures 4.27 and 4.28 show similar contour and profile comparisons for the streamwise turbulence intensity. The "bulging" towards corners is sharper than that occurring in the velocity contours and again does not show up in the computations.

The VDM calculation shows a higher turbulence intensity in the core of the flow and not as sharp a drop-off in the corners as the WFM predictions. The flatter profile in the corner regions in the VDM results is likely due to the corner treatment in calculating the eddy viscosity for the mixing length model. In the mixing length region (see Figure 2.3), the distance from the wall (y) used in equations 2.21, is an effective length determined from:

$$l_{eff} = \left(\frac{z^2 y^2}{z^2 + y^2} \right)^{1/2} \tag{4.3}$$

where z and y are perpendicular distances from the neighboring walls. Far from a second wall, this reduces to $l_{eff} \approx z$ or $l_{eff} \approx y$, depending on which wall is nearest. In a corner region where $z \approx y$, equation 4.3 gives $l_{eff} \approx z/\sqrt{2}$. This in turn gives a smaller mixing length, which results in a lower estimate of the eddy diffusivity and a flatter profile of the turbulence intensity. The effect of the corner treatment is not limited to the mixing length region but is also felt in the HRE core region through the boundary conditions for k and ε in the overlap region. This can be seen in the contours of Figure 4.27 and the profiles of Figure 4.28. In the latter figure, a comparison of the predicted profiles using the VDM formulation in (a) and (b) shows a flatter profile in (b) which is located halfway between the second wall and the symmetry plane. A comparison of the profiles predicted in Figure 4.28 shows that the VDM formulation predicts a turbulence intensity about 1% higher than the corresponding WFM predictions throughout the core of the flow. Only in the near wall region does the WFM prediction of $\tilde{u}/U_{cl}$ exceed that of the VDM predictions. The peaks which occur in the predictions using the WFM are a result of the log law-of-the-wall boundary conditions (equation 2.18) used in the near wall region for this formulation. They lead to steep gradients of k in this region which are not supported by the experimental data.

4.4. Conclusions

The semi-elliptic calculation procedure has proved to be numerically accurate in predicting the developing laminar flows presented in this chapter. It has also been shown to be stably applicable for turbulent flow calculations. Here, where numerical discrepancies exist with experimental results, they are due to deficiencies in the turbulence models arising from the assumption of an isotropic viscosity.

The two model formulations have been compared with the straight channel and duct flows. The strong dependen of the WFM calculations on the log law-of-the-wall constants was demonstrated. Both model formulations do a god job of predicting the mean velocity fields. Differences exist in the prediction of the turbulent kinetic energy field. The WFM calculations show peaks near the bounding walls which are not experimentally supported. The VDM predictions of the turbulent duct flow show flatter profiles of $\tilde{u}$ in the corner regions due to the corner treatment used in this formulation. Neither model predicts the contour bulging of mean and turbulence quantities in the corner region, which are due to the anisotropic Reynolds stress distribution in the duct flow.

5. RESULTS AND DISCUSSION

5.1. Introduction

Predictions of the turbulent flow in a 90° bend are presented in this section. The calculations were performed using the two equation $k-\varepsilon$ model in the core of the flow and either wall functions (WFM) or the Van Driest mixing length model (VDM) in the near wall region. As was mentioned in the previous section the isotropic viscosity assumption prevents the prediction of the stress-driven secondary motion that occurs in straight duct turbulent flow. However, in a bend one expects the much larger pressure-centrifugal force driven secondary motion to exceed, by a large amount, the stress-driven motion that is dominant in straight duct flows. Therefore, the assumption of an isotropic viscosity may be less critical to resolving the main features of the bend flow. The calculations were made using the semi-elliptic code described above, employing 65 planes in the streamwise direction. There were 45 planes used to resolve the flow in the bend itself, and 10 planes to resolve the flow in each of the straight duct tangents. The streamwise planes were distributed uniformly, every 2° in the bend. This distribution was sufficient to resolve the steady state structures appearing in the bend. A contracting grid was used in the streamwise direction in the upstream tangent while an expanding grid was used in the downstream tangent. This meant that the greatest resolution in the tangents occurred where they joined the 90° bend. In the cross-stream planes a non-uniform 20×40 ($z \times r$) grid was used for the WFM calculations and a non-uniform 25×50 ($z \times r$) grid for the VDM calculations. This grid distribution corresponds to that used to make the straight duct turbulent calculations discussed in the previous section. The grids are shown in Figure 5.1.

Much of the testing of the code discussed in Chapter 4 was done on the campus IBM 3090 main-frame computer. The final production runs for the curved duct calculations were performed on a CRAY-XMP supercomputer. The calculations of the 90° bend proved to be prone to instabilities in the pressure field even when using all of the stabilizing techniques discussed in Chapter 3. This is most likely due to the strongly elliptic nature of the flow field in a bend with a small radius of curvature. The calculations for both model formulations required 400 passes to obtain a converged solution. For the WFM predictions this amounted to approximately 50 minutes of CRAY time. The VDM calculations required 90 minutes of CRAY time because of the larger grid used.

The flow calculated is meant to conform as closely as possible to the measurements made in a 90° bend by Humphrey [1977]. The flow Reynolds number and bend geometry were fixed in the calculation scheme to agree with the experimental values. For all quantities, the calculated fully developed straight duct flow profiles discussed in the previous section were used as inlet conditions in the upstream tangent. The upstream and downstream tangents of the bend are $4.2D_h$ and $4.8D_h$ in length respectively, in the calculations. At the outlet plane of the downstream tangent a constant pressure gradient condition was set. The calculations were performed in one symmetrical half of the duct cross-section to take advantage of the symmetry which exists in the axial (z) direction.

Comparisons of the predictions with the measurements are given at 5 stations in the streamwise direction ($x/D_h = -2.5$, $\theta = 0°, 45°, 71°, 90°$). For each station comparisons are shown of the mean streamwise velocity (U_θ) and turbulence intensity ($\tilde{u}/U_b$) as contours. Profiles of both U_θ and $\tilde{u}/U_b$ at two axial positions ($z/D_h = 0.25, 0.5$) are also given to provide a more quantitative comparison with the measurements. The axial positions correspond to the symmetry plane ($z/D_h = 0.5$), and a position halfway between the wall and symmetry plane ($z/D_h = 0.25$). Contour plots of the predicted values of ε, the dissipation of turbulent kinetic energy, are also given. Since there is no experimental data available for this quantity, the results due to the two model formulations are compared with each other. Finally, vector plots of the cross-stream velocity field predicted using both model formulations are compared with each other. In each plane the vectors are scaled with the maximum cross-stream velocity in that plane. The largest vectors will correspond then to the regions of strongest secondary flow.

In the next section a summary is given for the numerical results of each of the five stations. In section 5.3 a discussion of the results is provided. Some concluding remarks are provided in the final section of this chapter.

5.2. Results

Upstream tangent (x/D_h = −2.5). The numerical results at this position in the upstream tangent are not noticeably different from the fully developed profiles used as the inlet condition at x/D_h = −5. Figures 5.2-5.4 show no observable departure from symmetry in the longitudinal mean velocity contours and profiles. The experimental symmetry about R^* = 0.5 is observable in the predictions using both turbulence model formulations. As in the straight duct calculations of chapter 4, no bulging in the velocity contours in the duct corners occurs in the predictions. The predictions due to both model formulations agree with each other to within 2% over the entire cross-stream plane.

Figures 5.5-5.7 show the corresponding contour plots and profiles for the turbulence intensity. Here, the turbulence intensity has been calculated as a percentage of the bulk velocity U_b, in order to compare with Humphrey's [1977] data:

$$\text{Intensity} = \frac{\tilde{u}}{U_b}\cdot 100 \tag{5.1}$$

As in the straight duct turbulent calculations, the comparison of the calculated turbulent intensity is made with the experimental streamwise intensity profiles, measured by Humphrey. Here again, the symmetry about R^* = 0.5 is observable. The bulging of the $\tilde{u}/U_b$ profiles in the duct corners is due to the stress driven secondary motion mentioned previously, and is not reproduced in the calculations. The VDM formulation shows a flatter profile in the corner regions than the WFM formulation (Figure 5.7b) due to the corner treatment discussed in chapter 4. The levels of turbulence intensity predicted using either formulation are in the same range as was measured in the experimental study. However, the levels predicted using the VDM for the core of the flow are a little higher than those predicted using the WFM (7% vs. 6%). The peaks in the turbulence intensity profiles which occur near the walls in the WFM calculations are due to the wall function treatment of this region which gives a higher level of k-production than the VDM. This leads to gradients of $\tilde{u}/U_b$ in the wall region which are too high. On the other hand the gradients of $\tilde{u}/U_b$ predicted by the VDM calculations are lower than the experimental data.

Figure 5.8 compares the predicted contours of ε, the dissipation of turbulent kinetic energy using the two formulations. In the core of the flow the dissipation levels are very similar. The contour lines are more "rounded" in the corners using the VDM formulation (Figure 5.8b) due to the corner treatment used but the differences are small. It is in the wall region that the differences are most notable. Here the dissipation level is five times greater for the WFM calculations than for the VDM calculations. The peak in the ε-profile is similar to that in the k-profile predicted in the WFM calculations.

$\theta = 0°$ **plane.** At the inlet plane the bend has definitely influenced the flow structure development, both in the experiments and predictions. Figures 5.9-5.11 show an acceleration of the fluid near the inner radius wall (r_i) responding to the favorable streamwise pressure gradient in this region. At the same time the fluid near the outer radius wall is decelerated, responding to the unfavorable pressure gradient in this region. Both the model formulations show this shift of the maximum velocity towards the inner radius wall. The WFM formulation predicts a slightly larger value of the velocity maximum than the VDM formulation. This is shown further in Figure 5.15, the vector plot of the cross-stream velocities for both models. Here all the radial velocities in both cases are from the concave outer wall towards the convex inner wall. This streamwise pressure gradient distribution at the inlet plane is caused by the centrifugal force-radial pressure gradient imbalance set up in the flow downstream in the bend. The centrifugal forces acting on the fluid in the bend itself do not influence the flow at the inlet plane. The resulting acceleration near the inner radius wall is similar to what would happen to an inviscid flow in the bend.

The bulging of the velocity profile towards the corner at the inner radius wall, which is exhibited in the experiments, is a residual of the stress-driven secondary motion so it does not show up in the predictions. The same effect appears in Figure 5.11b as an underprediction of the maximum velocity in the region near r_i. The differences in the predictions of the mean velocity field by the two model formulations are small throughout the entire cross-section.

In Figures 5.12-5.14 contours and profiles of the turbulence intensity are given. The experimental results show small but noticeable changes in the $\tilde{u}/U_b$ profiles. The predictions of both model formulations show larger variations from the upstream tangent station, even at this early point in the bend. Both sets of calculations show a shift towards the inner radius wall of the intensity contours in response to the favorable pressure gradient near r_i and the unfavorable pressure gradient near r_o. The shift is similar to that displayed by the U_θ profiles in Figures 5.8-5.10 and can also be seen in the experimental profiles.

The WFM calculations show a large increase in the maximum turbulence intensity (26%) near the inner radius wall over the peak value in this region at the upstream tangent location (17%). There is a corresponding drop-off in the intensity peak near the outer radius wall. The WFM predictions correspond to a large increase in the production of turbulent kinetic energy near r_i and a drop-off in production near r_o. The VDM calculations show a much smaller change in the kinetic energy production in both regions. In the core of the flow, the $\tilde{u}/U_b$ profiles predicted by the VDM calculations is 1%-2% higher than those predicted by the WFM calculations (Figure 5.14).

The predicted contours of energy dissipation, ε due to both model formulations are compared in Figure 5.16. There is a small shift of the constant ε contours towards the inner radius wall shown by both sets of calculations. The dissipation contours show a similar asymmetry to that shown in the turbulence intensity profiles (see Figures 5.12 and 5.13). Since the regions of high turbulence intensity correspond to regions of increased energy dissipation, the contours of both quantities often show similar behavior. The WFM predictions show a higher dissipation level near r_i due to the higher production of k. In the core of the flow the predicted values show small variations depending on the model formulations.

$\theta = 45°$ plane. The acceleration of the flow near the inner radius wall is also noticeable at the 45° plane. This shows up in Figures 5.17-5.19 in the contours of U_θ which are displaced towards the convex inner wall. The predictions of both model formulations yield similar contour plots, shown in Figures 5.17 and 5.18. However, the predicted radial profiles of U_θ in Figure 5.19 show some quantitative variations between the results of the two models. In this figure the results of the WFM and VDM calculations of this study are compared with the numerical results of Humphrey et al. [1981] in addition to the experimental results of Humphrey [1977]. The calculations of Humphrey et al. used an elliptic procedure and a coarse grid, $11 \times 14 \times 19$ ($x \times r \times \theta$) with wall functions in the near wall region. In general, the results of the VDM and WFM calculations are in agreement with each other. The VDM formulation does a better job of predicting the velocity profile near the inner radius wall on the symmetry plane (Figure 5.19a) but both models as well as the elliptic calculations miss the velocity peak and drop-off near the outer radius wall. At the $z/D_h = 0.25$ position (Figure 5.19b) both WFM and VDM are in better agreement with the data (particularly in the region near r_o) than the elliptic calculations of Humphrey et al. [1981].

At the 45° plane, the secondary motion in the cross-stream plane begins to be noticeable. The predicted contours of U_θ in Figures 5.17 and 5.18 show the beginnings of the deformation due to the secondary flow which is already evident in the experimental results. Figure 5.23 shows the predicted cross-stream velocity vector plots. In the figure the longitudinal vortices characteristic of bend flow are clearly evident. Both sets of calculations show a relatively thin layer ($0.15D_h$) of fluid moving quickly along the side wall of the bend from the concave outer radius wall towards the inner radius wall. The slower moving fluid in the core of the flow moves from r_i to r_o forming a stagnation region on the symmetry plane at the outer wall. There are some distinct differences in the predictions of the streamwise vortices based on the two models. For example, the centers of the predicted vortices (where the cross-stream velocity is zero) have different radial locations. The VDM calculations predict the zero velocity location to be at $R^* = 0.55$ (Figure 5.23a) while the WFM predictions give $R^* = 0.35$, much closer to r_i. In addition, the maximum cross-stream velocity predicted by the WFM formulation was $U_r = 0.5U_b$ while the VDM formulation only gave cross-stream velocities as high as $U_r = 0.38U_b$. In both cases the maximum velocities occurred near the flat side walls in the pressure dominated side wall boundary layers.

Figures 5.20-5.22 show the contours and profiles of the turbulence intensity, $\tilde{u}/U_b$ compared with the experimental results. Although the details of the $\tilde{u}/U_b$ distribution are not reproduced by the predictions, many of the qualitative features emerge. Both sets of calculations show high levels of $\tilde{u}/U_b$ (12%-14%) near the outer concave wall and near the flat side wall compared to the inner convex wall (8%-9%). These values of turbulence intensity are similar to the values found in the experiments though the contour shapes are different. In comparing the predictions of the two model formulations in Figure 5.22, the peaks in the normal stress profiles predicted by the WFM appear near the inner and outer radius walls. In the core of the flow the VDM calculations predict slightly higher values of the intensity than the WFM calculations. As before, qualitative features in the dissipation profiles similar to the turbulence intensity profiles show up in Figure 5.24.

$\theta = 71°$ **plane.** At this position in the bend the influence of the centrifugal force on the fluid (through the cross-stream secondary motion) finally manifests itself in the streamwise velocity profiles. The contours of U_θ are shown for the two sets of calculations in Figures 5.25-5.27. The maximum velocity has been displaced to the outer radius wall on the symmetry plane (Figure 5.27a). Both model formulations predict a greater shift (to $R^* \approx 0.55$) than shows up in the experiments. The VDM calculations are in better agreement with the experimental profiles in Figure 5.27 in the region near the inner convex wall ($0 \le R^* \le 0.5$). Both models miss the drop-off in the velocity profile near r_o. The tendency of the U_θ contours to bend in the corners near r_i is more prevalent in the WFM calculations and is probably due to the different secondary flow patterns predicted there, shown in Figure 5.31. Differences in the predicted vector plots similar to those found at $\theta = 45°$ show up again. In particular, the location of the zero cross-stream velocity is closer to the flat side wall and convex inner wall in the WFM calculations (Figure 5.31b) than in the VDM calculations (Figure 5.31a). This is consistent with a higher radial velocity in the side wall boundary layers in the WFM results and leads to a greater deformation in the longitudinal velocity contours. In both sets of predictions the movement of the zero velocity point is towards r_i from the 45° plane to the 71° plane. The maximum cross-stream velocities predicted by the WFM formulation are $U_r \approx 0.5U_b$ in the region near the flat side walls and $U_r \approx 0.4U_b$ in the VDM formulation, also near the side walls.

Figures 5.28-5.30 show the predicted distribution of the turbulence intensity. Here again, there is qualitative agreement with the experiments although many details are not reproduced numerically. At this position in the bend the turbulence intensity is still highest near the concave outer wall and flat side walls (12%-14%). However, the intensity levels in the region of r_i have increased ($\approx$9%) compared to this region at $\theta = 45°$. The trend of increasing turbulence intensity near r_i is also noted in the experimental contours and profiles. The same peaks in the $\tilde{u}/U_b$ profiles near the walls in the WFM calculations again show up, as does the slightly higher turbulence level in the core of the flow, also predicted the VDM calculations.

Figure 5.32 shows the predicted contours of the energy dissipation ε, due to the two sets of calculations. The features in both cases are very similar. The relative peaks of ε near the bounding walls is in keeping with the fact that the maximum dissipation occurs in the regions of maximum k production. The higher relative values of ε in the very near wall region of the WFM calculations are due to the wall function boundary conditions employed in the WFM formulation.

$\theta = 90°$ plane. At the exit plane of the bend there are some fairly drastic differences between the predicted velocity fields and the experimentally measured one. Figures 5.33-5.35 compare the predictions with Humphrey's [1977] experimental results at this plane and also with the elliptic calculations of the flow by Humphrey et al. [1981]. The predicted location of the velocity maximum on the symmetry plane was $R^* \approx 0.9$ in both model calculations as compared with the experimental location of $R^* \approx 0.57$. The influence of the secondary motion on the streamwise velocity contours is more pronounced in the WFM results than in the VDM results. Both model formulations of the present study show the drop-off in U_θ near r_i on the symmetry plane. This feature is completely missed by the elliptic calculations of Humphrey et al. [1981].

The predicted cross-stream velocity fields shown in Figure 5.39 continue to exhibit the same qualitative differences which are dependent on the model formulation. The zero velocity point has moved towards the inner radius wall in both cases and has moved away from the side wall towards the symmetry plane in the WFM predictions. The maximum cross-stream velocities predicted by the WFM calculations are $U_r \approx 0.36U_b$ in the region near the flat side walls. Velocities of up to $U_r \approx 0.24U_b$ are predicted on the symmetry plane. The VDM calculations yield maximum radial velocities of $U_r \approx 0.3U_b$ near the side walls and

$U_r \approx 0.28U_b$ on the symmetry plane. In Humphrey's [1977] experimental study the maximum radial velocities occurred on the symmetry plane ($U_r \approx 0.28U_b$). The maximum radial velocities Humphrey measured near the side walls were $U_r \approx 0.14U_b$. Both models show evidence of small secondary longitudinal vortices near r_i, on the symmetry plane. These are induced by the primary vortices and much weaker in strength. These secondary vortices were not discussed in Humphrey's experimental investigation but may have been present.

Figures 5.36-5.38 show the predicted turbulence intensity ($\tilde{u}/U_b$) profiles compared with Humphrey's data. The effect of the strong cross-stream velocity field can be seen in the calculated $\tilde{u}/U_b$ distribution. There is a decrease in the predicted turbulence intensity near the outer concave wall (to 10%-12%) and a corresponding increase near the inner convex wall (9%-10%) relative to the 71° plane. The peak in turbulence intensity near the side wall has also moved from r_o towards r_i in both sets of calculations. These trends are similar to those found in the experiments, although the turbulence levels, particularly near r_i, are significantly higher than those predicted using either model formulation (12% vs. 8% in Figure 5.38a). The VDM calculations predict turbulence levels 2%-3% higher than the WFM calculations away from the walls. Neither model picks up the local minimum in the normal stress distribution. The predicted profiles tend to be flatter and show less variation in the radial direction than is experimentally observed (Figure 5.38).

The same trends in the predictions of $\tilde{u}/U_b$ are observable in the contour plots of the energy dissipation, ϵ in Figure 5.40. The dissipation peaks near those walls where the production of k is highest and decreases towards the core of the flow. Both models predict increasing dissipation levels near the inner radius wall as compared to the 71° plane (compare Figure 5.32 and 5.40). The contours also show the effect of the cross-stream velocity field in the bending of the contour lines near r_i. The high levels of energy dissipation very close to the walls predicted by the WFM formulation are not found in the VDM calculations.

Figure 5.41 shows the variation of the pressure coefficient c_p, on the duct symmetry plane at the inner and outer radius walls, where

$$c_p = \frac{\Delta p}{\frac{1}{2}\rho U_b^2}$$

Since there is no experimental data with which to compare the predictions, the results of the two model formulations are again compared with each other.

Qualitatively, the two models predict similar variations in the pressure coefficient. Both show the favorable pressure gradient at r_i and the adverse gradient at r_o near the bend entrance. This is responsible for the relative fluid acceleration in the region near r_i upstream of the bend. The pressure gradients predicted by both models near the bend exit are also in agreement with each other. On the inner radius wall, the largest variation between between the two models occurs at the minimum value of c_p at 25° in the bend. Here, the difference in the predicted values of the pressure coefficient is 5% of the dynamic pressure, $\frac{1}{2}\rho U_b^2$. On the outer radius wall, the largest variation occurs at the maximum value of c_p at 58° in the bend. The difference in the predicted values of c_p is also 5% of the dynamic pressure.

The maximum and minimum values of c_p do not occur at the same longitudinal (θ) position in the bend as was found in the experimental investigation of a 90° bend by Taylor et al. [1982]. This could be due to the different inlet conditions in the experiments which had thin boundary layers on the side walls upstream of the bend. Unfortunately, for the case modeled in the present work, Humphrey did not provide data for the pressure field variation in the bend.

The bend also apparently affects the pressure fields in the straight duct tangents. The influence of the bend on the pressure field in the upstream duct tangent extends $1.5D_h$ upstream of the bend entrance. In the downstream tangent, the effect of the bend is still noticeable $3D_h$ after the bend exit plane.

The variation of the friction coefficient c_f on the symmetry plane at the inner and outer radius walls is shown in Figure 5.42, where

$$c_f = \frac{\tau_w}{\frac{1}{2}\rho U_b^2}$$

Despite qualitative similarities, there are some fairly large differences in the predictions of the two model formulations. The initial differences in the friction coefficient upstream of the bend are due to the different near wall model formulations. This initial difference might be expected to persist through the bend, however, this is not the case. The differences are most pronounced near the bend entrance on the inner radius wall and near the bend exit on the outer radius wall. These are regions where the maximum shear stress occurs on the radial walls. A comparison with Figure 5.41 shows that these regions are where favorable pressure gradients exist, which cause the fluid to accelerate in the streamwise direction. The WFM formulation shows larger changes in the friction coefficient in these regions. The differences between the two models amounts to 10% of the dynamic pressure, $\frac{1}{2}\rho U_b^2$ at the bend inlet and 17% at the bend exit. Both model formulations agree on the streamwise locations of the local maxima in the friction coefficient profile. On the inner radius wall the maximum occurs at 1° into the bend, while at the outer radius wall it occurs $0.4D_h$ downstream of the bend exit in the downstream tangent.

The models are in closer agreement in predicting the location and magnitude of the minimum friction coefficient in the bend. At the outer radius wall, c_f reaches its minimum value at 10° into the bend. The difference in the predictions of the two models here is 1% of the dynamic pressure. Of more interest is the local minimum which occurs at r_i. Here the minimum value of c_f occurs in the downstream tangent, $0.3D_h$ beyond the bend exit, where it goes to zero. This indicates a potential at this location for streamwise recirculation which is not permitted in the semi-elliptic calculation scheme. The streamwise diffusion terms in the momentum and turbulence equations (underlined in equations 2.26-2.30) have been neglected, although in this region they are certainly important. To get an accurate description of the flow field in this region, a fully elliptic procedure would have to be used.

Downstream of the bend exit the two models predict a return to the straight duct values of c_f although at $3.5D_h$ in the downstream tangent the flow is still developing.

5.3. Discussion

A comparison of the predicted results with the experimental data for the turbulent flow in a 90° bend shows similar qualitative behavior throughout the bend. There are some quantitative differences which exist, particularly in the distribution of the turbulent kinetic energy, k. In general, both model formulations predicted the overall features of the flow, although the results differed in some details. The acceleration of the flow near r_i between the bend inlet and the 45° plane, and the onset of secondary motion in the cross-stream plane, were well predicted in both sets of calculations. The location of the velocity maximum near the center of the duct curvature up to the $\theta = 71°$ plane, followed by a shift to the outer concave wall was also predicted by both model formulations. The general development of the turbulence intensity $\tilde{u}/U_b$ field through the bend and its modification by the cross-stream velocity field can be seen in the figures for $\theta = 45°$, $71°$ and $90°$.

Some features of the flow do not show up at all in the calculations. The "bulging" of the velocity and turbulence intensity profiles towards the duct corners does not show up in the predictions of the upstream tangent and bend inlet plane positions. The bulging, due to the Reynolds stress driven secondary motion in straight duct, cannot be predicted with a model formulation which assumes an isotropic eddy diffusivity.

The development of the longitudinal vortices in both sets of calculations is slower than in the experiments. As a result there is less distortion of the U_θ profiles in the corners near r_i. The shift in the maximum turbulence intensity from r_o at $\theta = 45°$ to r_i at $\theta = 90°$ is also not complete in either set of predictions compared with the experiments. As a result, there is less slower moving fluid near the inner radius wall between $\theta = 45°$ and $\theta = 71°$ than is experimentally the case. This could be due to the predicted radial pressure gradients being weaker than in the experimental study. This in turn, would favor the centrifugal forces acting on the fluid and lead to a velocity maximum closer to the concave outer wall than is actually the case (Figures 5.27 and 5.35).

The maximum secondary velocities predicted by the WFM calculations tend to be higher than those predicted by the VDM formulation and higher than experimentally measured. In Humphrey's [1977] study the maximum radial velocity occurred at the outlet plane on the symmetry plane and was $U_r \approx 0.28U_b$. Both models predicted similar radial velocities at this position but also predicted radial velocities $U_r = 0.3U_b$ near the side walls as compared with Humphrey's measured values of $U_r \approx 0.14U_b$. The maximum calculated cross-stream velocities occurred upstream at the $\theta = 45°$ plane. The maximum predicted velocities occurred near the flat side walls and were $U_r \approx 0.4U_b$ and $U_r \approx 0.5U_b$ for the VDM and WFM formulations, respectively.

The WFM formulation tends to predict much higher levels of turbulence near the bounding walls than the VDM calculations due to the treatment of the wall region (see Figures 5.22, 5.30 and 5.38). In the WFM calculations the wall regions are treated using wall functions as explained in Chapter 2. This method essentially fixes the maximum values of k and ε at the point nearest the wall and places all of the wall influence on the flow in the determination of the boundary conditions for the dependent variables. The wall functions were originally derived for a fully developed two-dimensional shear flow based on simple equilibrium considerations. In the case of the flow in ducts and bends it leads to peaks in the k- and ε-profiles in the near wall region which have little experimental support.

The profiles of the pressure coefficient, c_p predicted by the two models at r_i and r_o, agree with each other quite well through the entire bend. In the predictions of the friction coefficient, c_f however, substantial differences exist. These are due to differences in the near wall treatment of the two models as well as how they react to changes in the global flow field. Both models show a minimum value of c_f approaching zero near the bend exit at the inner radius wall. This indicates the possibility of streamwise recirculation in this region which cannot be handled by the semi-elliptic procedure.

Both model calculations do a better job of predicting the flow than the fully elliptic calculations of Humphrey et al. [1981]. This is almost certainly due to the coarse grid $11 \times 14 \times 19$ ($x \times r \times \theta$), used in the latter calculations and the resulting numerical diffusion. An estimate of the magnitude of the numerical diffusion relative to turbulent diffusion is given by the authors:

$$\frac{\mu_{num}}{\mu_e} \approx 0.36\mathrm{Re}_c\left(\frac{\mu}{\mu_e}\right)\sin 2\xi \qquad (5.2)$$

where $\mathrm{Re}_c = \rho U\,\Delta x/\mu$ is the cell Reynolds number, based on the local velocity U and cell dimension Δx, and ξ is the angle the velocity vector makes with the coordinate system. Relative to the authors' elliptic calculations the numerical diffusion has been reduced by 50% in the present set of calculations. This is due to the increased grid size in all three coordinate directions. The semi-elliptic calculation scheme and the availability of a supercomputer (CRAY-XMP) allowed for 12 times as many grid nodes as were used for the elliptic calculations (36,000 vs. 3,000). Larger grids than those used in the present investigations would reduce the importance of numerical diffusion still further but are not practical. Higher order differencing schemes (such as QUICK) giving better accuracy would be a way of further reducing the numerical diffusion which occurs in such flows.

6. CONCLUSIONS

Calculations of turbulent flow developing in a 90° bend of square cross section performed using a semi-elliptic numerical procedure yield better results than earlier predictions of the same flow using an elliptic procedure and a turbulence model equivalent to the WFM of this work. This is attributed to the higher levels of grid refinement possible in the present work.

Of the two models used here, the VDM shows better overall conformity with the measurements of mean streamwise velocity. However, neither model reproduces well the corresponding component of stress. This is due to the assumption of an isotropic turbulence viscosity in a flow where the convective, diffusive and pressure redistributions of a stress field are important to resolve it properly. To improve upon this however, it would be necessary to solve modeled transport equations for six stress components and such a task was beyond the scope and resources available for this study. Notwithstanding, support for this approach is to be found in the study by Choi et al [1987], brought to our attention at the conclusion of the present work. These authors show that the use of an algebraic stress model of turbulence, in conjunction with a semi-elliptic numerical procedure, yields considerably improved predictions of the normal stresses for the flow in a 180° bend of square cross section. Notwithstanding, improvements to predictions of the mean flow were fairly minimal, substantiating the premise of this work, that the flow in a bend is dominated by secondary motion of the first kind as a result of pressure-centrifugal force imbalances. The correct calculation of the cross stream flow in a bend depends upon resolving accurately the effects of the bend on the wall boundary layers. Wall-flow interactions, in the presence of streamline curvature, represent the area of most pressing attention for the improved modeling of curved duct flows.

Appendix A

The QUICK scheme formulation

A.1 The problem of interest

To achieve a stable higher order finite difference approximation of the convective terms in the transport equations, that avoids the artificial numerical diffusion caused by upstream differencing and the unstable nature of central differencing, Leonard [1979] has devised the QUICK (Quadratic Upstream Interpolation for Convective Kinematics) scheme. This appendix outlines how the QUICK scheme is incorporated in the REBUFFS code with special consideration for the treatment required at boundaries.

A.2 Formulation

A.2.1 Grid arrangement

The current REBUFFS code was programmed with the option for implementing nonuniform grids. To simplify this outline, the grid arrangement for one direction only will be discussed. With reference to Fig. A.1 and A.2, for a nonuniform grid, passive properties are located at locations x_i, x_{i+1}, etc., and velocity nodes at $x_{i+1/2}$, and $x_{i-1/2}$, etc.. With this grid arrangement, nodes for passive properties are always located inside the calculation domain. A node surface will coincide with a boundary when the node is adjacent to the boundary. Velocity nodes are placed halfway between two passive property nodes. This kind of arrangement simplifies the coding process, especially for a multi-dimensional code. For passive properties there is only one type of boundary node to consider, as shown in Fig. A.3, while for velocities there are two, as shown in both Fig. A.3 and A.4, depending on the velocity component considered.

A.2.2 Finite difference approximation of the convective term(s)

The general convective term in the transport equations is represented by $\rho\vec{U}\cdot\nabla\phi$, where ϕ can be any passive property or velocity component. If the ϕ-transport equation is expressed in divergence (or conservative) form, the convection terms can be represented as $\nabla\cdot(\rho\vec{U}\phi)$. Integrating this expression over a one-dimensional finite control volume enclosing node P as shown in Fig. A.1, yields the finite difference expression for the convective term: $(\rho u\phi)_e A_e - (\rho u\phi)_w A_w$, where A represents the area at the subscripted interface, and u is the velocity component in the direction considered. Since the ϕ's are not defined on the interfaces, they have to be approximated by interpolation.

A.2.3 Quadratic upstream interpolation

Depending on the sign of the velocity component in question on each interface, the grid points needed for interpolation vary. For example, with reference to Fig. A.1, assume that both u_w and u_e are positive, i.e. directed in the positive x direction. In order to approximate ϕ_w, we need ϕ at P, W, and WW, and for ϕ_e we need ϕ at E, P, and W. After the interpolated values are found, they are substituted into the convective terms of the transport equations. The difference equations are then expressed in terms of ϕ's that are defined at the nodal locations. The interpolation equation used is $\phi=ax^2+bx+c$. It is straightforward to find the coefficients in this interpolation equation.

Unfortunately, a direct application of the interpolation results to the convective terms of the ϕ-transport equation will not always guarantee convergence. This is because the diagonal dominance of the resulting coefficient matrix is not necessarily guaranteed. In order to devise a scheme that converges, Han et al. [1981] proposed a remedy that relies on a "false transient" approach; i.e. placing some of the interpolation terms into the source term in the difference equations. An improvement by Freitas et al. [1984] ensures that the matrix of coefficients is diagonally dominant under all possible situations.

The procedure of Freitas et al. [1984] for setting up the finite difference expressions for the convective terms in a one-dimensional configuration is given below. The expressions for C's in this appendix are different from the expressions derived by them. Their expressions apply only to the nodal configuration corresponding to Fig. A.1, while the present expressions for the coefficients apply to both configurations; i.e. Figures A.1 and A.2. Of the four possible flux combinations through the e and w control volume surfaces, only one case is given in full detail. The remainder can be deduced with little added difficulty.

For $u_e > 0$ algebraic considerations yield,

$$\phi_e = C_1\phi_P - C_2\phi_E + C_3\phi_W + \frac{1}{2}\phi_E \tag{A.1}$$

where

$$C_1 = 1 + \frac{(x_{i+\frac{1}{2}} - x_i)(x_{i+1} - x_{i+\frac{1}{2}} - x_i + x_{i-1})}{(x_{i+1} - x_i)(x_i - x_{i-1})} \tag{A.1.a}$$

$$C_2 = \frac{1}{2} - \frac{(x_{i+\frac{1}{2}} - x_i)(x_{i+\frac{1}{2}} - x_{i-1})}{(x_{i+1} - x_i)(x_{i+1} - x_{i-1})} \tag{A.1.b}$$

$$C_3 = -\frac{(x_{i+\frac{1}{2}} - x_i)(x_{i+1} - x_{i+\frac{1}{2}})}{(x_i - x_{i-1})(x_{i+1} - x_{i-1})} \tag{A.1.c}$$

and $\frac{1}{2}\phi_E$ is designated as a source term.

For $u_e < 0$,

$$\phi_e = C_7\phi_P + C_8\phi_E + C_9\phi_{EE} \tag{A.2}$$

where

$$C_7 = \frac{(x_{i+1} - x_{i+\frac{1}{2}})(x_{i+2} - x_{i+\frac{1}{2}})}{(x_{i+1} - x_i)(x_{i+2} - x_i)} \tag{A.2.a}$$

$$C_8 = 1 - \frac{(x_{i+1} - x_{i+\frac{1}{2}})(x_{i+2} - x_{i+1} - x_{i+\frac{1}{2}} + x_i)}{(x_{i+1} - x_i)(x_{i+2} - x_{i+1})} \tag{A.2.b}$$

$$C_9 = - \frac{(x_{i+1} - x_{i+\frac{1}{2}})(x_{i+\frac{1}{2}} - x_i)}{(x_{i+2} - x_{i+1})(x_{i+2} - x_i)} \tag{A.2.c}$$

and $C_9\phi_{EE}$ is the source term.

For $\mathbf{u_w > 0}$,

$$\phi_w = C_4\phi_P + C_5\phi_W + C_6\phi_{WW} \tag{A.3}$$

For $\mathbf{u_w < 0}$,

$$\phi_w = C_{10}\phi_P + C_{11}\phi_E - C_{12}\phi_W + \frac{1}{2}\phi_W \tag{A.4}$$

As for u_e, the last term in both Equations (A.3) and (A.4) is designated as the source term. The coefficients in these equations are:

$$C_4 = \frac{(x_{i-\frac{1}{2}} - x_{i-1})(x_{i-\frac{1}{2}} - x_{i-2})}{(x_i - x_{i-1})(x_i - x_{i-2})} \tag{A.3.a}$$

$$C_5 = 1 + \frac{(x_{i-\frac{1}{2}} - x_{i-1})(x_i - x_{i-\frac{1}{2}} - x_{i-1} + x_{i-2})}{(x_i - x_{i-1})(x_{i-1} - x_{i-2})} \tag{A.3.b}$$

$$C_6 = - \frac{(x_{i-\frac{1}{2}} - x_{i-1})(x_i - x_{i-\frac{1}{2}})}{(x_{i-1} - x_{i-2})(x_i - x_{i-2})} \tag{A.3.c}$$

$$C_{10} = 1 - \frac{(x_i - x_{i-\frac{1}{2}})(x_{i+1} - x_i - x_{i-\frac{1}{2}} + x_{i-1})}{(x_i - x_{i-1})(x_{i+1} - x_i)} \tag{A.4.a}$$

$$C_{11} = - \frac{(x_i - x_{i-\frac{1}{2}})(x_{i-\frac{1}{2}} - x_{i-1})}{(x_{i+1} - x_i)(x_{i+1} - x_{i-1})} \tag{A.4.b}$$

$$C_{12} = \frac{1}{2} - \frac{(x_i - x_{i-\frac{1}{2}})(x_{i+1} - x_{i-\frac{1}{2}})}{(x_i - x_{i-1})(x_{i+1} - x_{i-1})} \tag{A.4.c}$$

Corresponding interpolations along the other two coordinate directions can be obtained by a direct substitution of the appropriately subscripted coordinate into the above formulae.

A.2.4 Implementation of QUICK scheme in variable density flows

To simulate buoyant flow, density variations must be considered in the implementation of the QUICK scheme. Consider a steady one-dimensional, variable density flow described by

$$\nabla \cdot (\rho \vec{u}) = 0 \qquad (A.5)$$

and

$$\nabla \cdot (\rho \vec{u} \phi) = 0 \qquad (A.6)$$

A difference approximation to (A.6) is obtained by integrating over the one-dimensional control volume surrounding node P in Fig. A.1. Thus,

$$(\rho u \phi)_e A_e - (\rho u \phi)_w A_w = 0 \qquad (A.7)$$

Likewise, for (A.5),

$$(\rho u)_e A_e - (\rho u)_w A_w = 0 \qquad (A.8)$$

Multiplying (A.8) by ϕ_P and subtracting the result from (A.7), yields, (assuming that A_e equals A_w)

$$[\ (\rho u \phi)_e - (\rho u)_e \phi_P\ ] - [\ (\rho u \phi)_w - (\rho u)_w \phi_P\ ] = 0 \qquad (A.9)$$

Note that the following relations among coefficients always apply:

$$C_1 - C_2 + C_3 + \frac{1}{2} = 1$$

$$C_4 + C_5 + C_6 = 1$$

$$C_7 + C_8 + C_9 = 1$$

$$C_{10} + C_{11} - C_{12} + \frac{1}{2} = 1$$

Therefore, for example, when $\mathbf{u_e > 0}$ **and** $\mathbf{u_w > 0}$, it follows that

$$(\rho u)_e \phi_P = (\rho u)_e\ [\ C_1 - C_2 + C_3 + \frac{1}{2}\ ]\ \phi_P$$

$$(\rho u)_w \phi_P = (\rho u)_w \; [\; C_4 + C_5 + C_6 \;] \; \phi_P$$

Utilizing the above results, and substituting Equations (A.1) and (A.3) for ϕ_e and ϕ_w in the first and second brackets in (A.9) respectively, yields

$$(\rho u \phi)_e - (\rho u)_e \phi_P$$

$$= (\rho u)_e \; [\; C_1 \phi_P - C_2 \phi_E + C_3 \phi_W + \frac{1}{2} \; \phi_E \;]$$

$$- (\rho u)_e \; [\; C_1 - C_2 + C_3 + \frac{1}{2} \;] \; \phi_P$$

$$= -(\rho u)_e C_2 \phi_E + (\rho u)_e C_3 \phi_W + [\; (\rho u)_e C_2 - (\rho u)_e C_3 \;] \; \phi_P$$

$$+ [\; \frac{1}{2} \; (\rho u)_e \phi_E - \frac{1}{2} \; (\rho u)_e \phi_P \;]$$

and

$$(\rho u \phi)_w - (\rho u)_w \phi_P = (\rho u)_w C_5 \phi_W - (\rho u)_w C_5 \phi_P$$

$$+ [\; (\rho u)_w C_6 \phi_{WW} - (\rho u)_w C_6 \phi_P \;]$$

Subtracting these expressions yields,

$$[\; (\rho u \phi)_e - (\rho u)_e \phi_P \;] - [\; (\rho u \phi)_w - (\rho u)_w \phi_P \;]$$

$$= [\; (\rho u)_e C_3 - (\rho u)_w C_5 \;] \; \phi_W - [\; (\rho u)_e C_2 \;] \; \phi_E$$

$$+ [\; (\rho u)_e C_2 - (\rho u)_e C_3 + (\rho u)_w C_5 \;] \; \phi_P$$

$$+ [\; \frac{1}{2} \; (\rho u)_e \phi_E - \frac{1}{2} \; (\rho u)_e \phi_P$$

$$- (\rho u)_w C_6 \phi_{WW} + (\rho u)_w C_6 \phi_P \;] = 0 \qquad \text{(A.10)}$$

For completeness, the other three possibilities are listed below

For $u_e < 0$ and $u_w > 0$

$$(A.9) = - [\; (\rho u)_w C_5 \;] \; \phi_W + [\; (\rho u)_e C_8 \;] \; \phi_E$$

$$+ [\; (\rho u)_w C_5 - (\rho u)_e C_8 \;] \; \phi_P$$

$$\begin{aligned} &+ [\ (\rho u)_e C_9 \phi_{EE} - (\rho u)_e C_9 \phi_P \\ &- (\rho u)_w C_6 \phi_{WW} + (\rho u)_w C_6 \phi_P\ ] = 0 \end{aligned} \tag{A.11}$$

For $u_e > 0$ and $u_w < 0$

$$\begin{aligned} (A.9) = &[\ (\rho u)_e C_3 + (\rho u)_w C_{12}\ ]\ \phi_W \\ &- [\ (\rho u)_e C_2 + (\rho u)_w C_{11}\ ]\ \phi_E \\ &+ [\ (\rho u)_e C_2 - (\rho u)_e C_3 + (\rho u)_w C_{11} - (\rho u)_w C_{12}\ ]\ \phi_P \\ &+ [\ \frac{1}{2}\ (\rho u)_e \phi_E - \frac{1}{2}\ (\rho u)_e \phi_P \\ &- \frac{1}{2}\ (\rho u)_w \phi_W + \frac{1}{2}\ (\rho u)_w \phi_P\ ] = 0 \end{aligned} \tag{A.12}$$

For $u_e < 0$ and $u_w < 0$

$$\begin{aligned} (A.9) = &[\ (\rho u)_w C_{12}\ ]\ \phi_W + [\ (\rho u)_e C_8 - (\rho u)_w C_{11}\ ]\ \phi_E \\ &+ [\ -(\rho u)_e C_8 + (\rho u)_w C_{11} - (\rho u)_w C_{12}\ ]\ \phi_P \\ &+ [\ (\rho u)_e C_9 \phi_{EE} - (\rho u)_e C_9 \phi_P \\ &- \frac{1}{2}\ (\rho u)_w \phi_W + \frac{1}{2}\ (\rho u)_w \phi_P\ ] \end{aligned} \tag{A.13}$$

Equations (A.10), (A.11), (A.12), (A.13) can all be represented by the general equation

$$a_P \phi_P + a_E \phi_E + a_W \phi_W + S_U = 0 \tag{A.14}$$

where a_E, a_W, and a_P are the coefficients for ϕ_E, ϕ_W, and ϕ_P respectively, and S_U is the source term composed of the last bracketed term in any one of the above mentioned equations. For multidimensional flows, one applies the same procedure in each coordinate direction to obtain similar expressions. To set up the multidimensional finite difference equation, one simply adds up the expressions derived for each dimension.

A.2.5 Treatment of boundary nodes

With the way the grids are arranged, all boundary nodes for passive properties have at least one control volume surface coincident with the boundary. For the velocity components two situations arise. If the velocity component is parallel to the boundary, one of its control volume surfaces coincides with the boundary, otherwise it does not; see Figures A.3 and A.4.

For the case shown in Fig. A.3, the value at w is given, so interpolation is not needed. However, the gradient at w and both the value and gradient at e must be approximated by interpolation. Leonard [1979] has suggested a way to treat this boundary nodal configuration. He used property values (such as velocity) at locations w, i, and i+1 to interpolate for the information required. To apply his approach directly complicates the coding. A simpler procedure, used here, requires the prescription of a node outside the calculation domain; i.e. at location i-1 in Fig. A.3. The value at i-1 is extrapolated from the quadratic fit to values at w, i, i+1. By doing this, the required values and gradients at w and e can be readily calculated in a manner consistent with the QUICK formulation.

As for the case shown in Fig. A.4, only surface w needs special treatment. To approximate the value (of, for example, velocity) at w, one averages the sum of the values at i and i-1. The difference between this approximation and that employing quadratic interpolation (using property values at i-1, i, i+1) is of order $O(\Delta x^2)$. When the grid is uniform, the gradient at w, calculated by taking the ratio between the difference of values at two neighboring nodes and the distance between them, is the same as that obtained by quadratic interpolation. When the grid is nonuniform, simple calculation shows that the difference is of the order $\Delta x(1-\varepsilon)$, where Δx is the larger of the two grid sizes in question, and ε is the ratio of the two grid sizes, with value between 1 and 0. If the node distribution is so arranged that w is of equal distance to nodes i and i-1, then ε equals 1, and the two approaches coincide.

References

1. Bergeles, G., Gosman, A. D. and Launder, B. E. [1978]. The turbulent jet in a cross stream at low injection rates: a three-dimensional numerical treatment. Num Heat Transfer 1, p 217.

2. Chang, S. M. and Humphrey, J. A. C. [1983]. Turbulent flow in a passage around 180° bend; an experimental and numerical study, Report F.M. 83-7, University of California, Berkeley.

3. Chang, S. M., Humphrey, J. A. C. and Modavi, A. [1983]. Turbulent flow in a strongly curved U-bend and downstream tangent of square cross-sections. PhysicoChemical Hydrodynamics 4, No. 3, p 243.

4. Choi, Y. D., Iacovides, H. and Launder, B. E. [1987]. Numerical computation of turbulent flow in a square-sectioned 180° bend, Internal report, Dept. of Mechanical Engineering, University of Manchester Institute of Science and Technology.

5. Coles, D. E. and Hirst, E. A. [1968]. Proc. Comput. Turbul. Boundary-Layers, vol. II, Department of Mechanical Engineering, Stanford University, Palo Alto, California.

6. Demuren, A. O. and Rodi, W. [1984]. Calculation of turbulence driven secondary motion in non-circular ducts, J. Fluid Mech., 140, p 189.

7. Freitas, C. J., Street, R. L., Findikakis, A. N. and Koseff, J. R. [1985]. Numerical simulation of three-dimensional flow in a cavity, Int. J. Num. Meth. in Fluids, 5, p 561.

8. Goldstein, R. J. and Kreid, D. K. [1967]. Measurement of laminar flow development in a square duct using a laser-Doppler flowmeter, J. of Appl. Mech., 34, p 813.

9. Gosman, A. D. and Ideriah, F. J. K. [1976]. TEACH-2E: A general computer program for two-dimensional, turbulent, recirculating flows, Department of Mechanical Engineering, Imperial College, University of London.

10. Han, T., Humphrey, J. A. C., and Launder, B. E. [1981]. A comparison of HYBRID and quadratic upstream differencing in high Reynolds number elliptic flows, Comp. Meth. Appl. Mech. Eng., 29, p 81.

11. Humphrey, J. A. C. [1977]. Flow in ducts with curvature and roughness, Ph.D. thesis, London University.

12. Humphrey, J. A. C., Whitelaw, J. H. and Yee, G. [1981]. Turbulent flow in a square duct with strong curvature. J. Fluid Mech. 103, p 433.

13. Iacovides, H. [1986]. Momentum and heat transport in flow through 180° bends of circular cross section, Ph.D. thesis, Victoria University of Manchester.

14. Kays, W. M. and Crawford, M. E. [1980]. **Convective Heat and Mass Transfer**, McGraw-Hill publishing, New York.

15. Laufer, J. [1950]. Investigation of turbulent flow in a two-dimensional channel, TN-2123, NACA, Washington, D. C.

16. Laufer, J. [1954]. The structure of turbulence in fully developed pipe flow, TN-1174, NACA, Washington, D. C.

17. Launder, B. E. and Spalding, D. B. [1974]. The numerical computation of turbulent flow, Comp. Meth. in Appl. Mech. and Eng., 3, p 269.

18. Leonard, B. P. [1979]. A stable and accurate convective modeling procedure based on quadratic upstream interpolation, Comput. Meths. Appl. Mech. Eng., 19, p 59.

19. McDonald, J. W., Denny, V. E. and Mills, A. F. [1972]. Numerical solutions of the Navier-Stokes equations in inlet regions, J. Appl. Mech., 39, p 873.

20. Patankar, S. V. [1980]. **Numerical Heat Transfer and Fluid Flow**, Hemisphere publishing Corporation, New York.

21. Patankar, S. V., Pratap, V. S. and Spalding, D. B. [1974]. Prediction of laminar flow and heat transfer in helically coiled pipes. J. Fluid Mech. 62, pt. 3, p 539.

22. Patankar, S. V., Pratap, V. S. and Spalding, D. B. [1975]. Prediction of turbulent flow in curved pipes. J. Fluid Mech. 67, pt. 3, p 583.

23. Patankar, S. V. and Spalding, D. B. [1972]. A calculation procedure for heat, mass and momentum transfer in three-dimensional parabolic flows, Int. J. Heat Mass Transfer, 15, p 1787.

24. Prandtl, L. [1925]. Bericht ueber Untersuchungen zur ausgebildeten Turbulenz, Zeit. Angew. Math. Mech., 5, p 136.

25. Pratap, V. S. [1975]. Flow and heat transfer in curved ducts, Ph.D. thesis, London University.

26. Pratap, V. S. and Spalding, D. B. [1976]. Fluid flow and heat transfer in three-dimensional duct flows. Int. J. Heat Mass Transfer 19, p 1183.

27. Reynolds, O. [1895]. On the dynamical theory of incompressible viscous fluids and the determination of the criterion, Phi. Trans. Royal Soc., series A, 186, p 123.

28. Rhie, C. M. [1983]. Basic calibration of a partially-parabolic procedure aimed at centrifugal impeller analysis. AIAA 21st Aerospace Sciences Meeting, January 10-13, 1983, Reno, Nevada.

29. Rodi, W. [1980]. **Turbulence Models and Their Application in Hydraulics,** International Association for Hydraulic Research, DELFT, The Netherlands.

30. Schlichting, H. [1979]. **Boundary layer theory,** McGraw-Hill publishing, New York.

31. Spalding, D. B. [1972]. A novel finite-difference formulation for differential expressions involving both first and second derivatives, Int. J. Num. Methods Eng., 4, p 551.

32. Taylor, A. M. K. P., Whitelaw, J. H. and Yianneskis, M. [1982]. Curved ducts with strong secondary motion: velocity measurements of developing laminar and turbulent flow, J. Fluids Eng., 104, p 350.

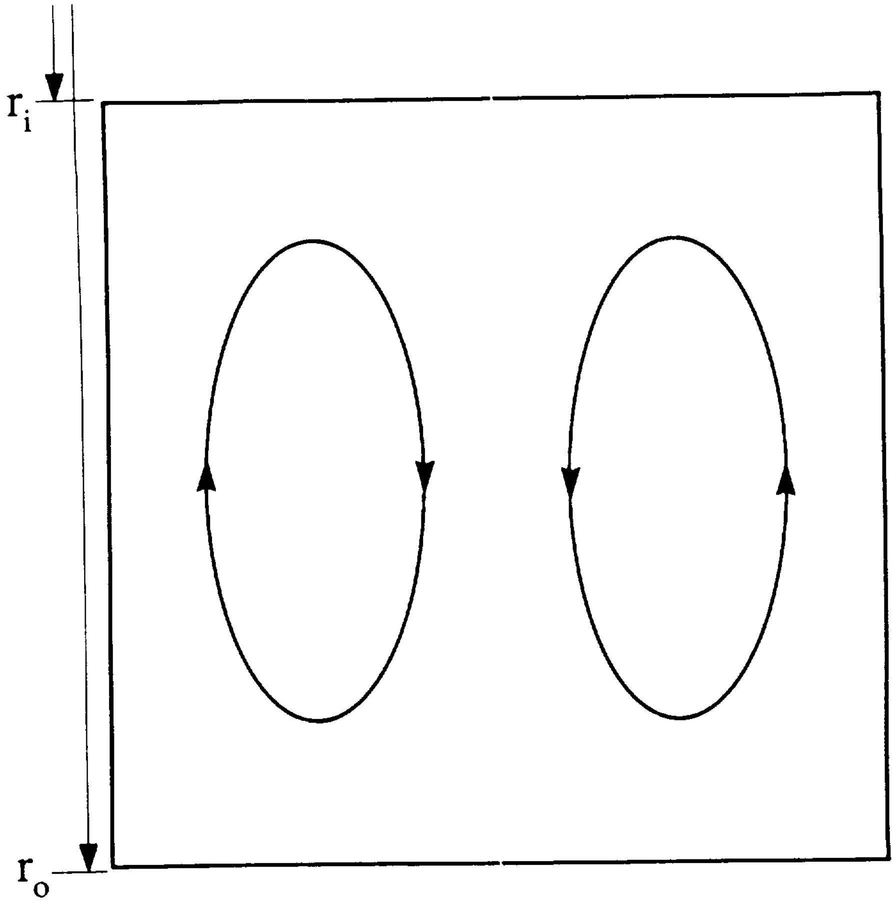

Figure 1.1. Flow pattern of the secondary motion in a curved duct of square cross-section, r_i and r_o are the inner- and outer- curved wall radii, respectively.

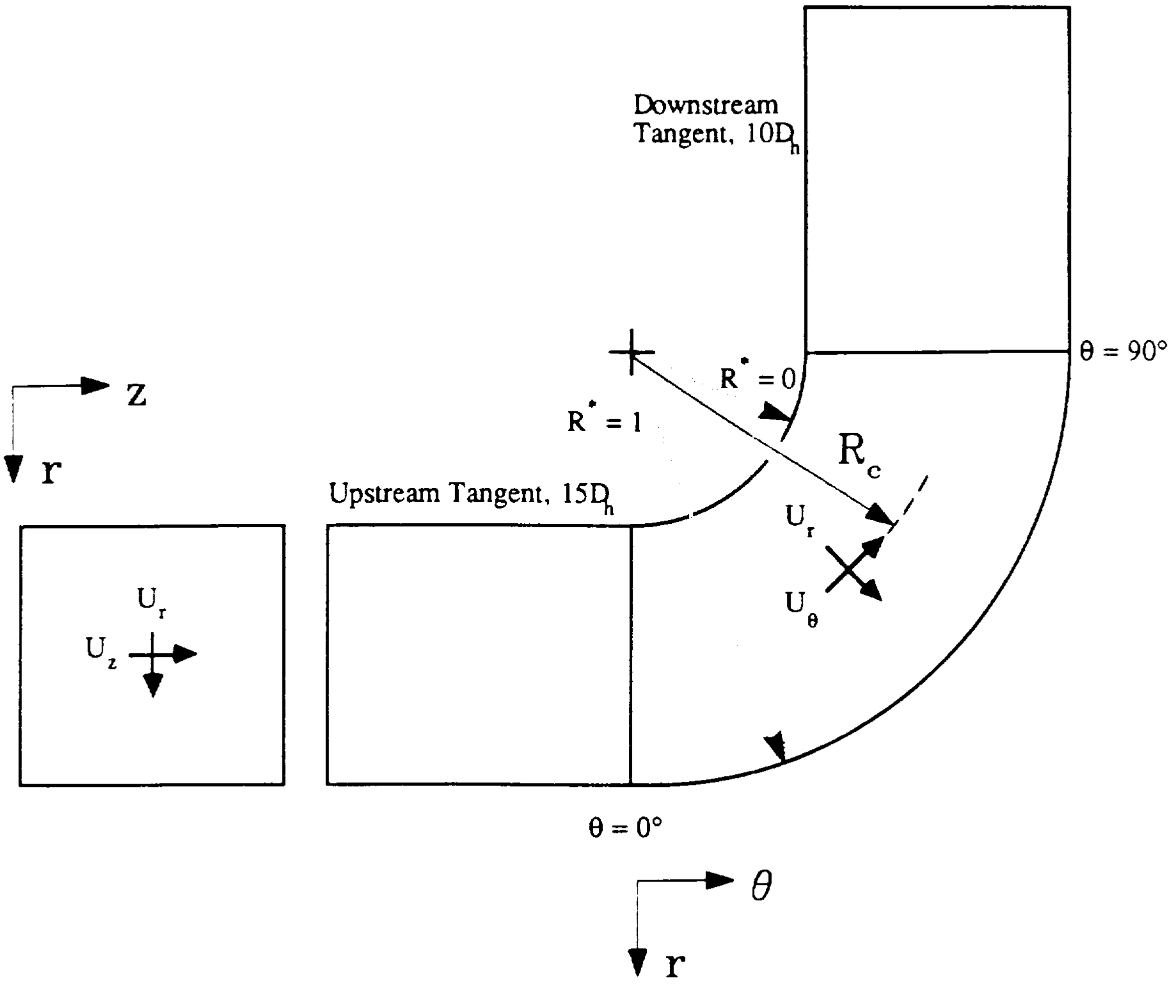
Downstream
Tangent, 10D_h
θ = 90°
R* = 0
z
r
R* = 1
R_c
Upstream Tangent, 15D_h
U_r
U_θ
U_r
U_z
θ = 0°
θ
r

Figure 1.2. Schematic of test section from Humphrey et al. [1981] showing dimensions, coordinate system and velocity components of the flow. $R^* = (r-r_i)/(r_o-r_i)$ is the non-dimensional radial position in the bend.

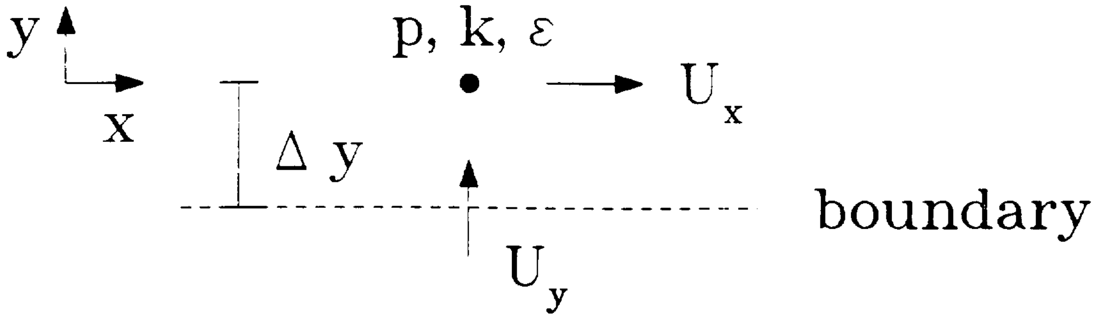
y
x
p, k, ε
U_x
Δ y
boundary
U_y

Figure 2.1. Coordinate system for boundary condition definitions. The boundary is either a wall or symmetry plane.

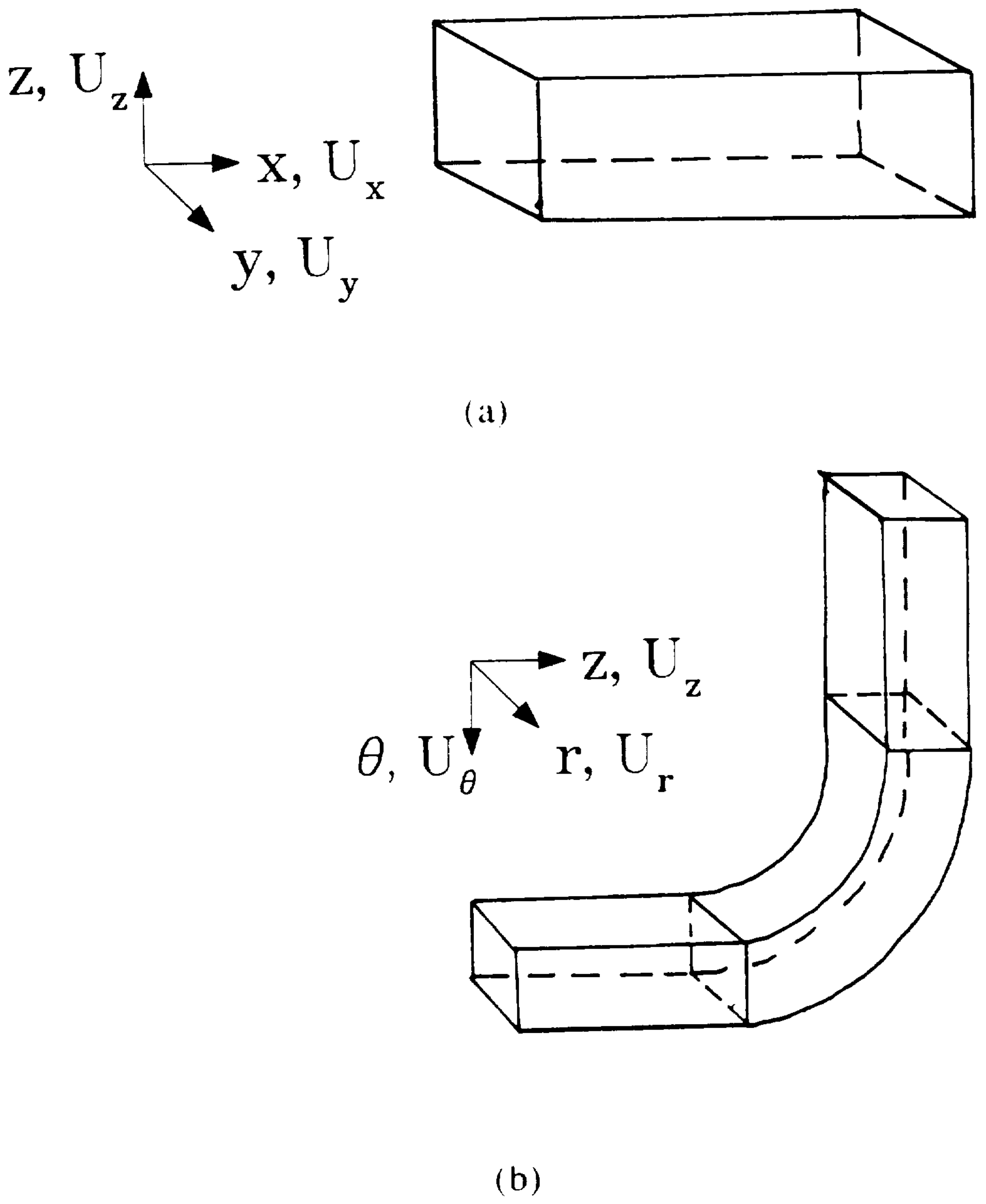
z, U_z
x, U_x
y, U_y
(a)
z, U_z
θ, U_θ
r, U_r
(b)

Figure 2.2. Duct geometry, showing coordinate system and velocity components. (a) Straight duct. (b) Curved duct.

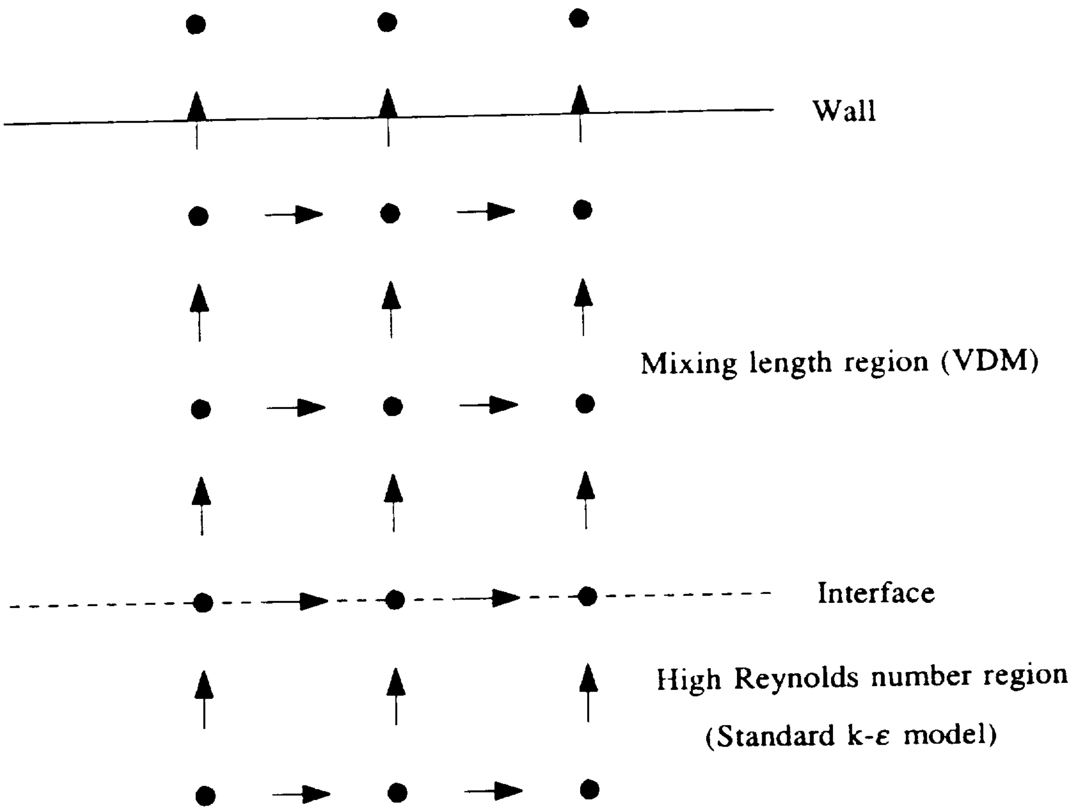
Wall
Mixing length region (VDM)
Interface
High Reynolds number region
(Standard k-ε model)

Figure 2.3. Illustration of the mixing length region, interface and core flow region in the VDM formulation.

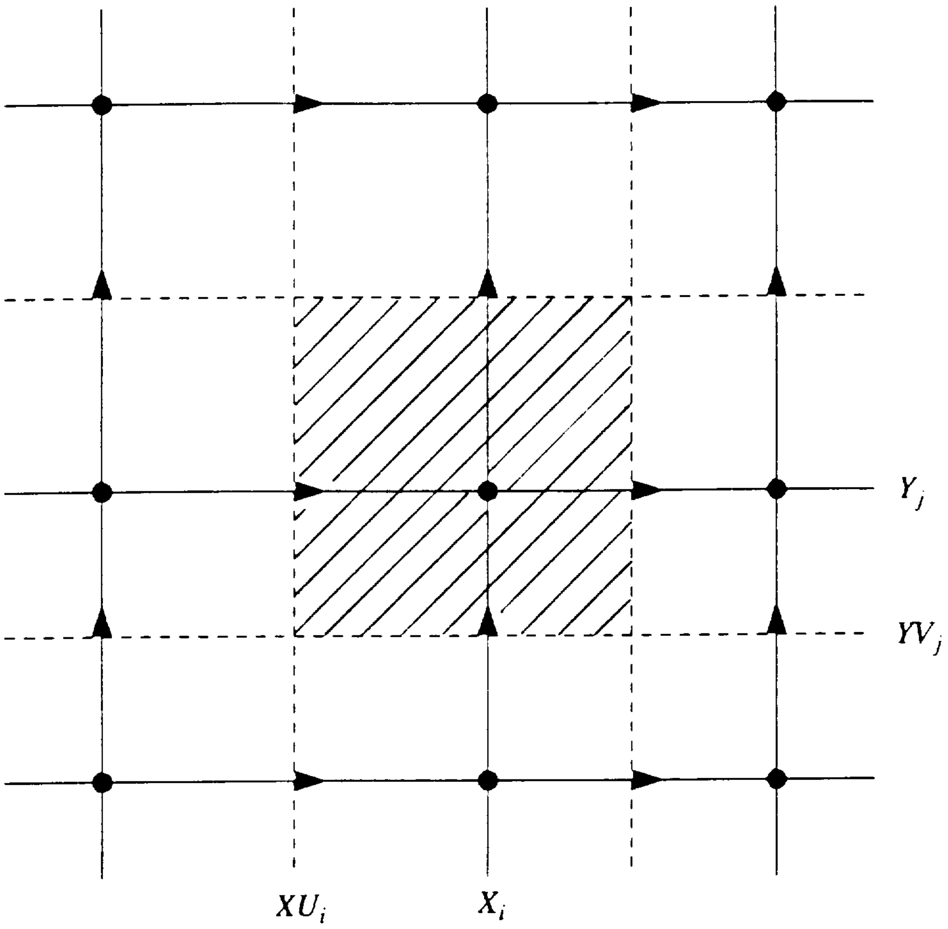
Y_j
YV_j
XU_i
X_i

Figure 3.1. Main grid node control volume.

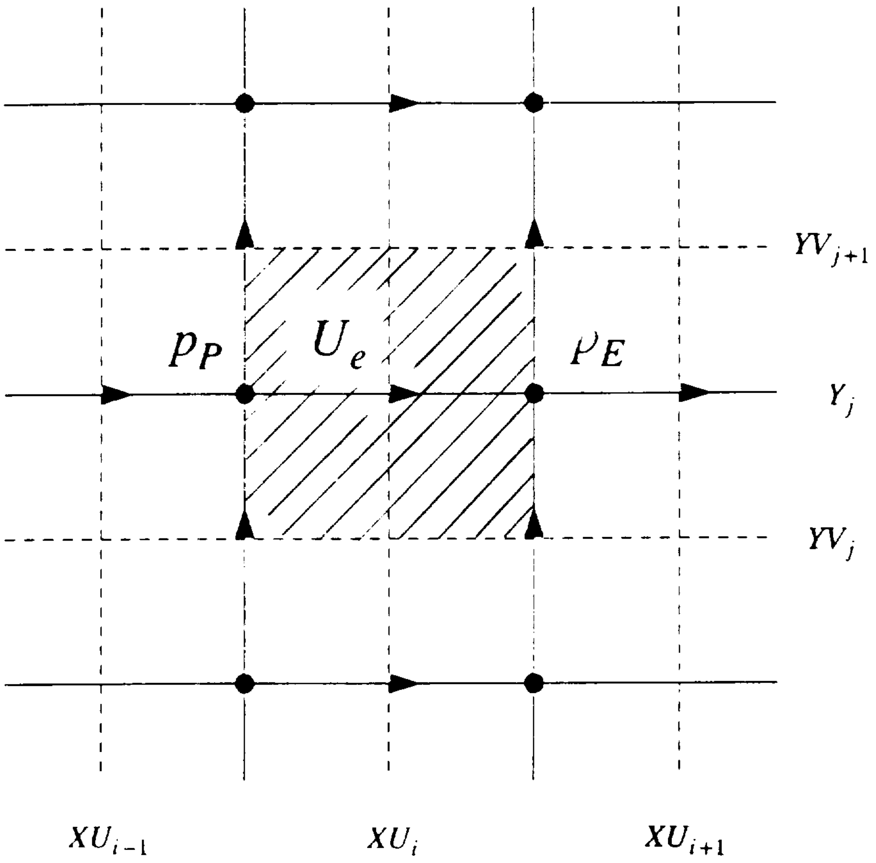
YV_{j+1}
p_P
U_e
p_E
Y_j
YV_j
XU_{i-1}
XU_i
XU_{i+1}

Figure 3.2. Velocity node control volume.

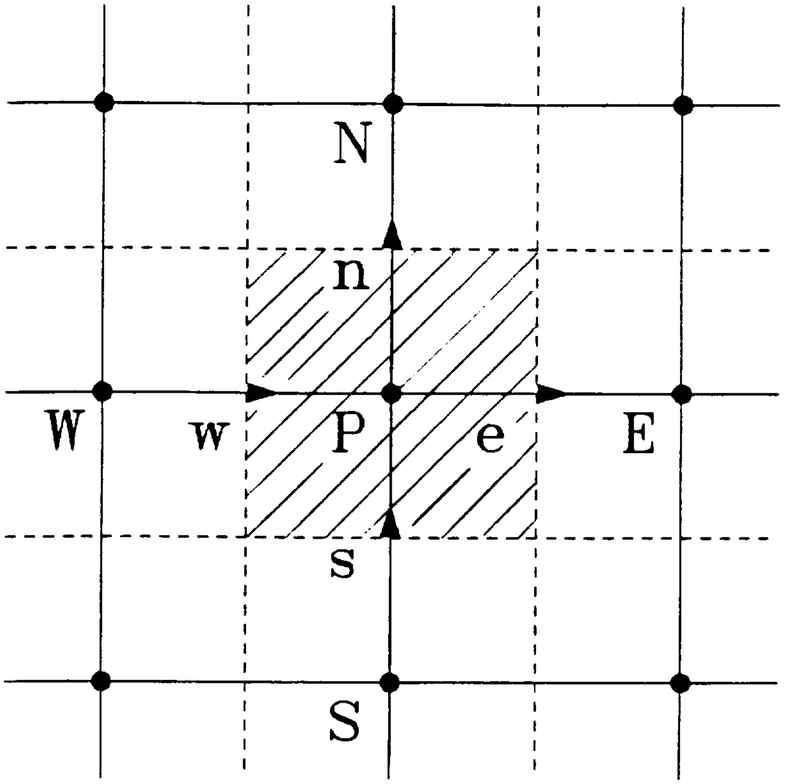

Figure 3.3. Control volume for intergration of the general ϕ-variable transport equation.

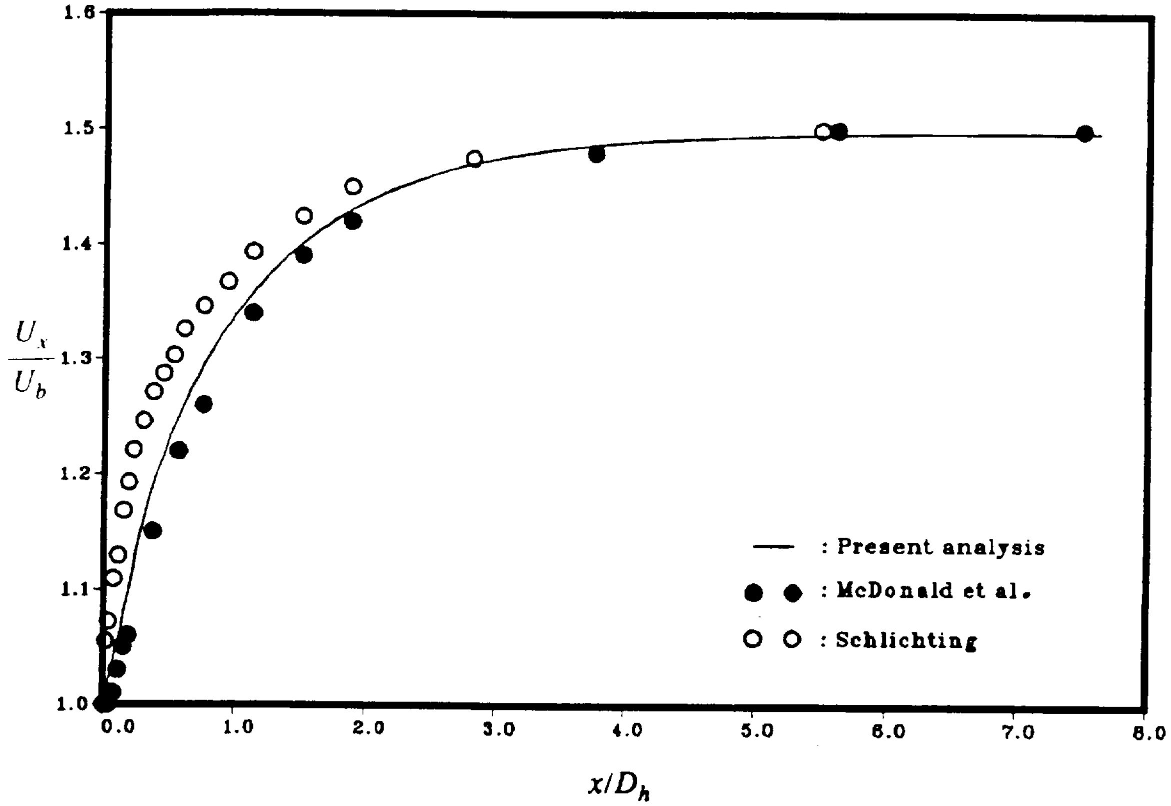

Figure 4.1. Centerline velocity for developing laminar flow in a 2D straight channel, Re=300. Comparison with Schlichting [1979] boundary layer predictions and McDonald et al. [1972] fully elliptic predictions.

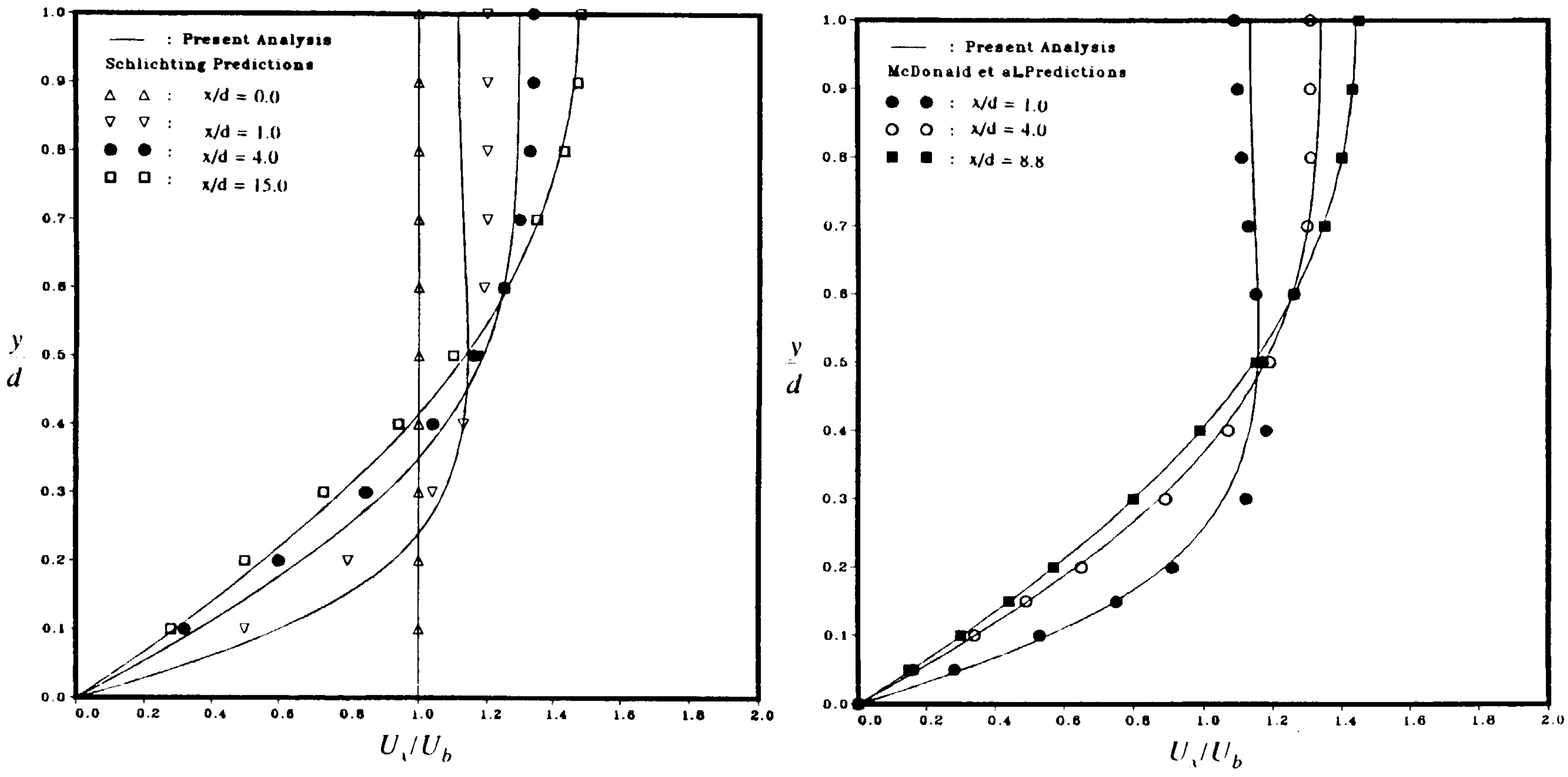

(a)

(b)

Figure 4.2. Velocity profiles for developing laminar flow in a 2D straight channel, Re=300. (a) Comparison with Schlichting [1979] boundary layer predictions. (b) Comparison with McDonald et al. [1972] fully elliptic predictions.

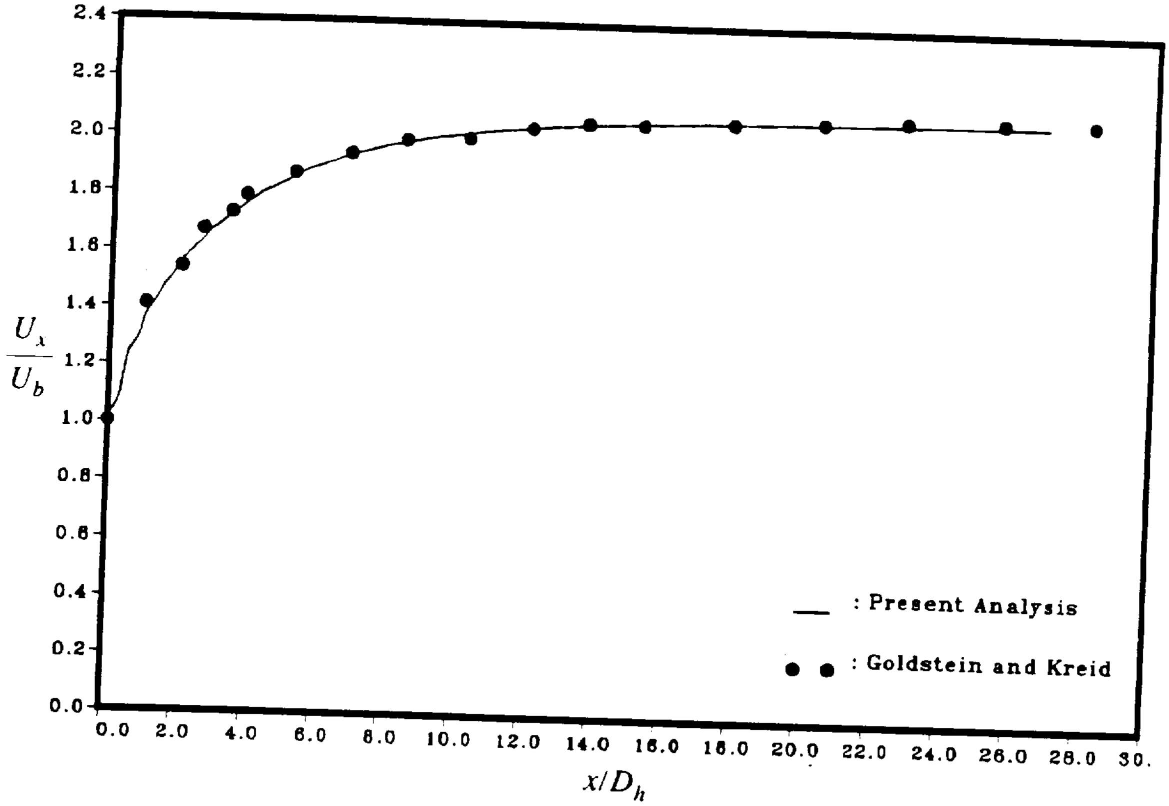

Figure 4.3. Centerline velocity for developing laminar flow in a square duct, Re=200. Comparison with data of Goldstein and Kreid [1967].

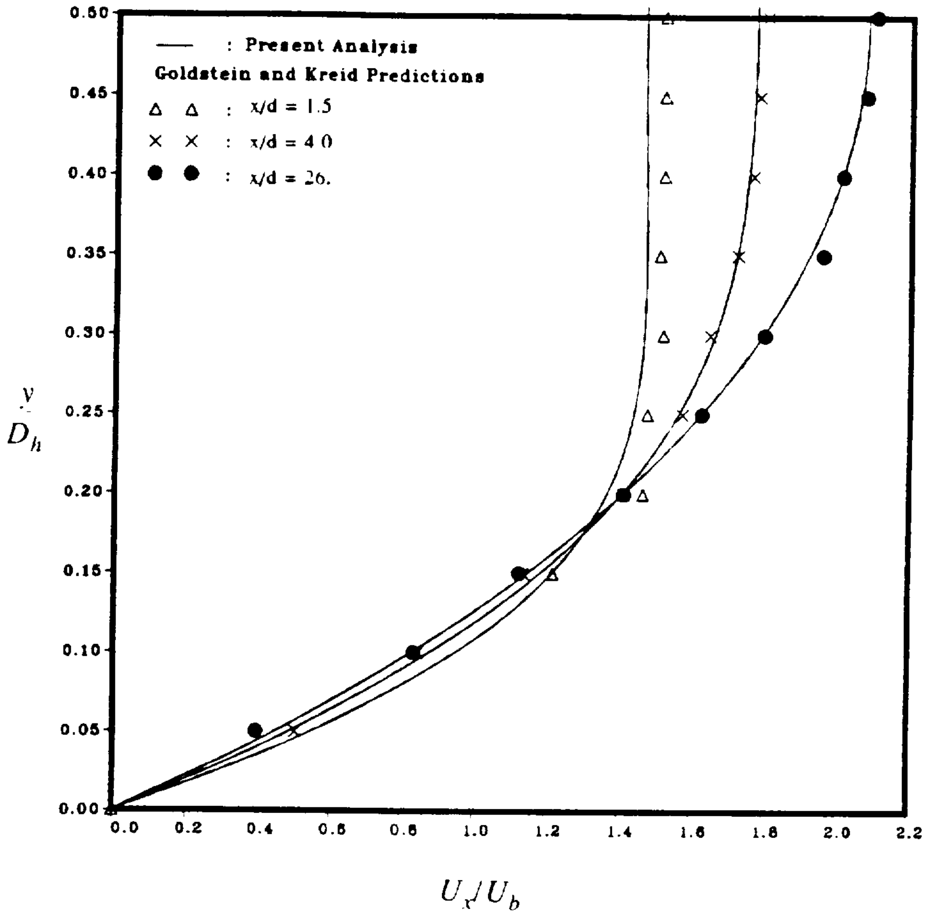

Figure 4.4. Velocity profiles for developing laminar flow in a square duct, Re=200. Comparison with data of Goldstein and Kreid [1967].

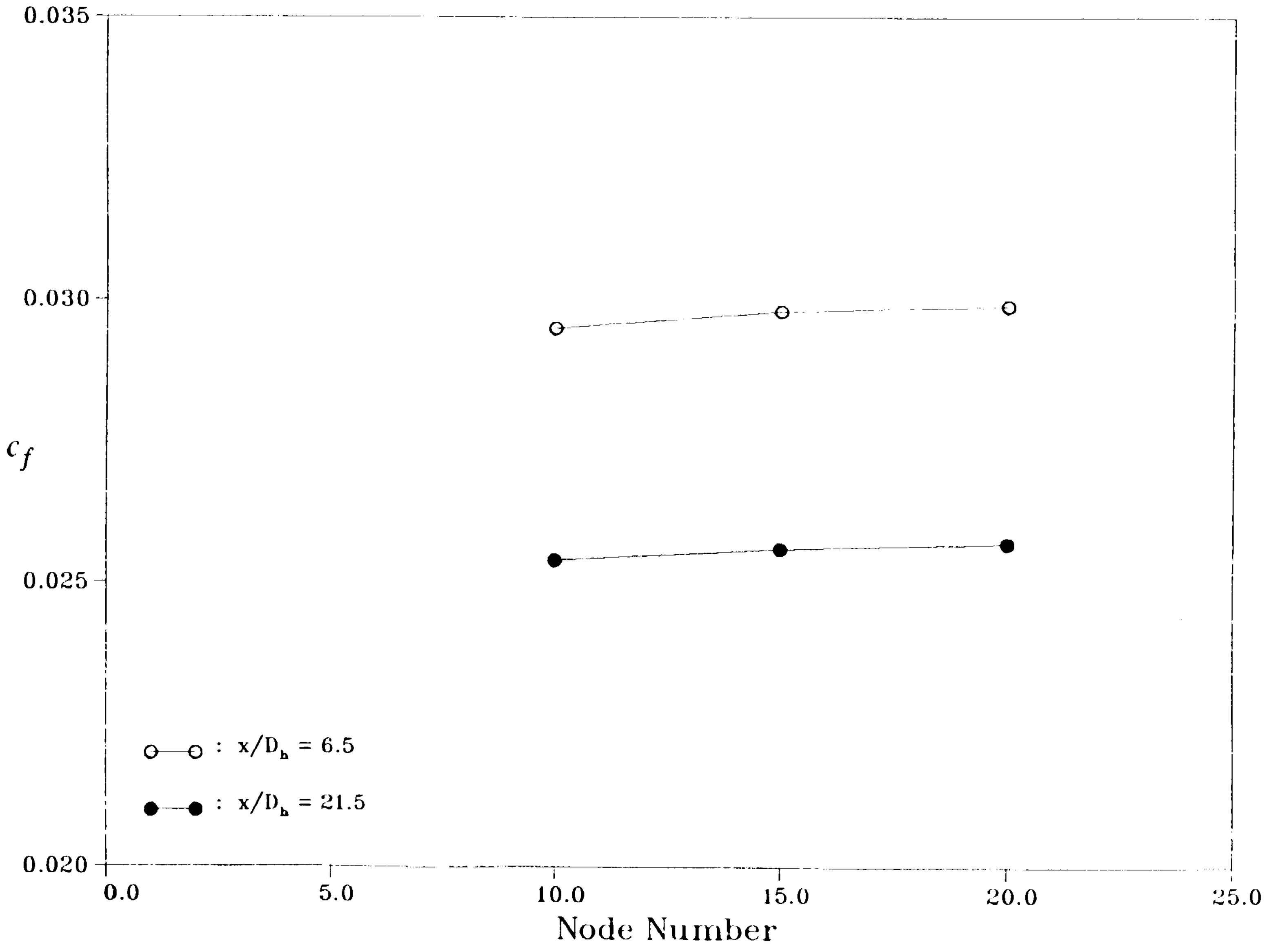

Figure 4.5. Variation of streamwise friction coefficient c_f, with number of nodes in a cross-stream direction. Straight duct laminar flow.

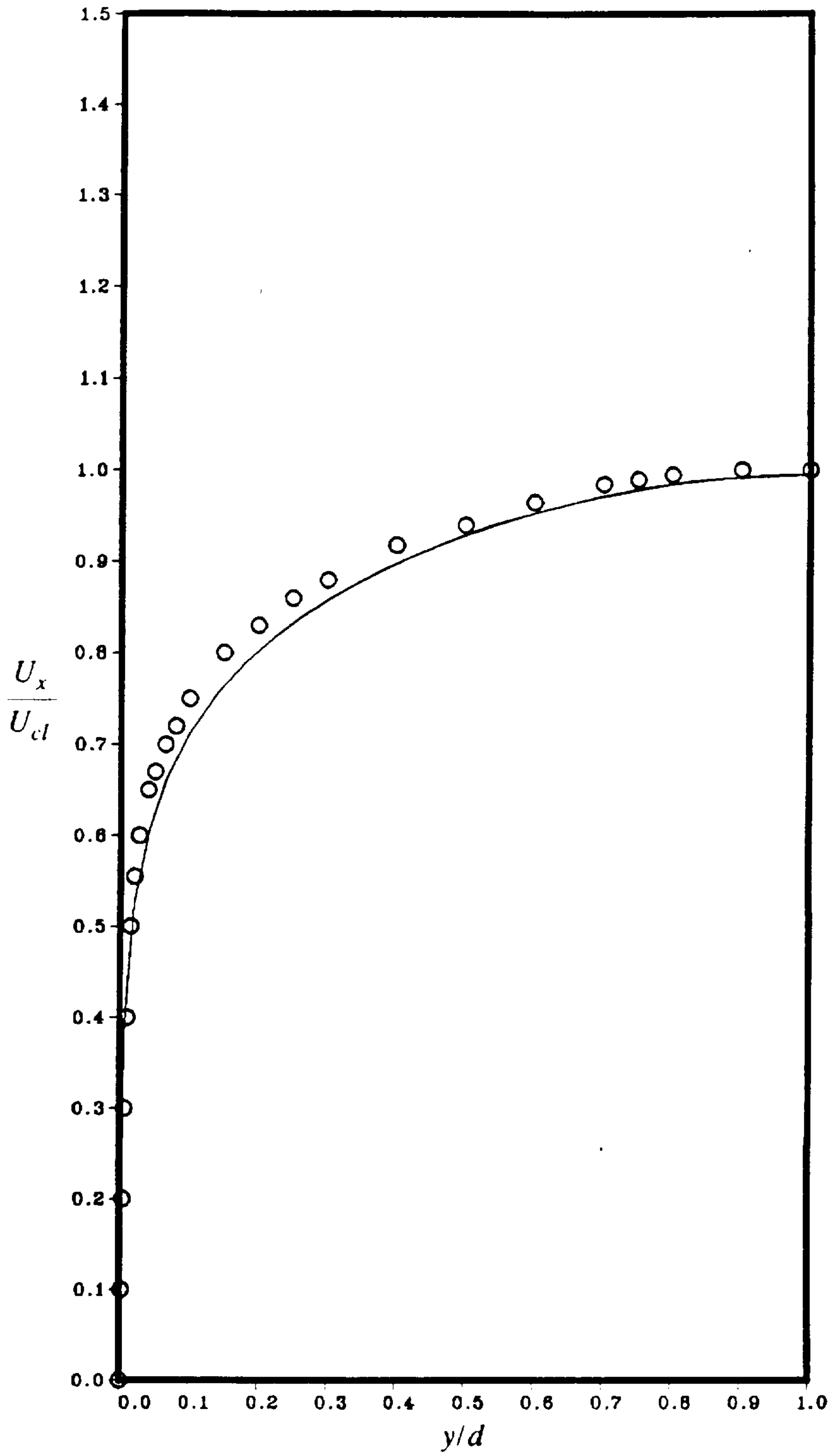

Figure 4.6. Mean velocity profile for fully developed turbulent channel flow, Re=110,000. Comparison of predictions using VDM with Laufer [1950] data.

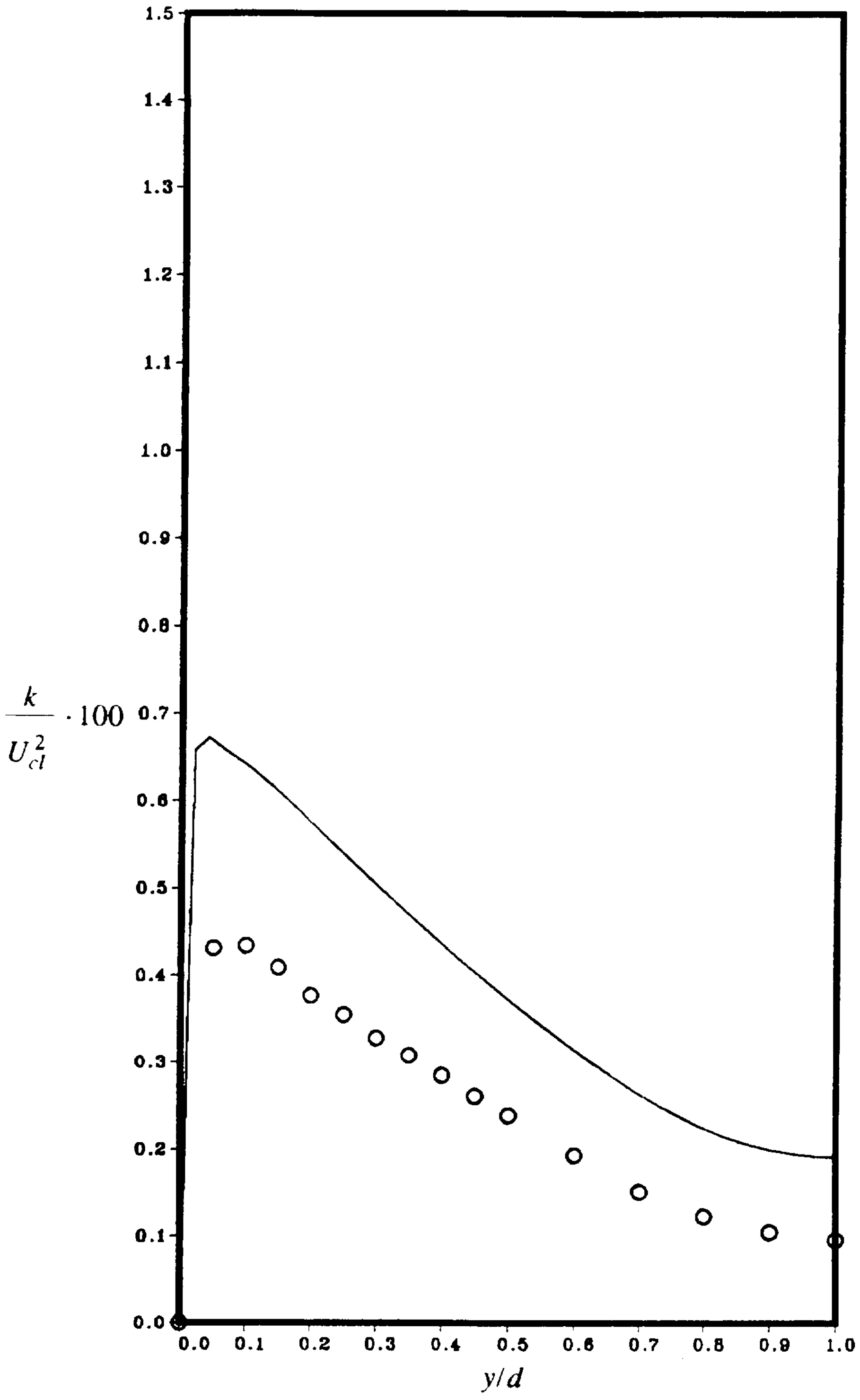

Figure 4.7. Turbulent kinetic energy profile for fully developed turbulent channel flow, Re=110,000. Comparison of predictions using VDM with Laufer [1950] data.

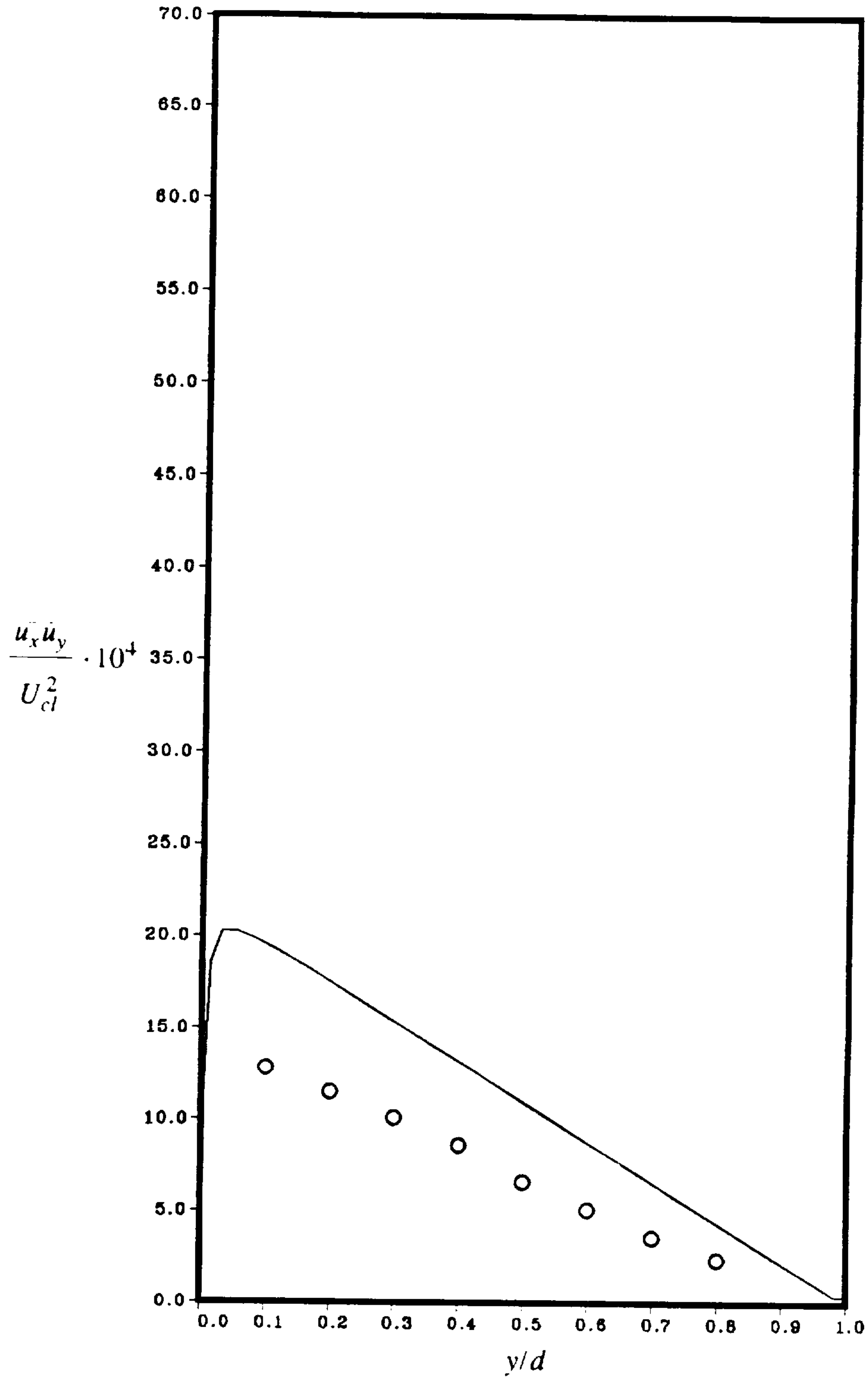

Figure 4.8. Turbulent shear stress profile for fully developed turbulent channel flow, Re=110,000. Comparison of predictions using VDM with Laufer [1950] data.

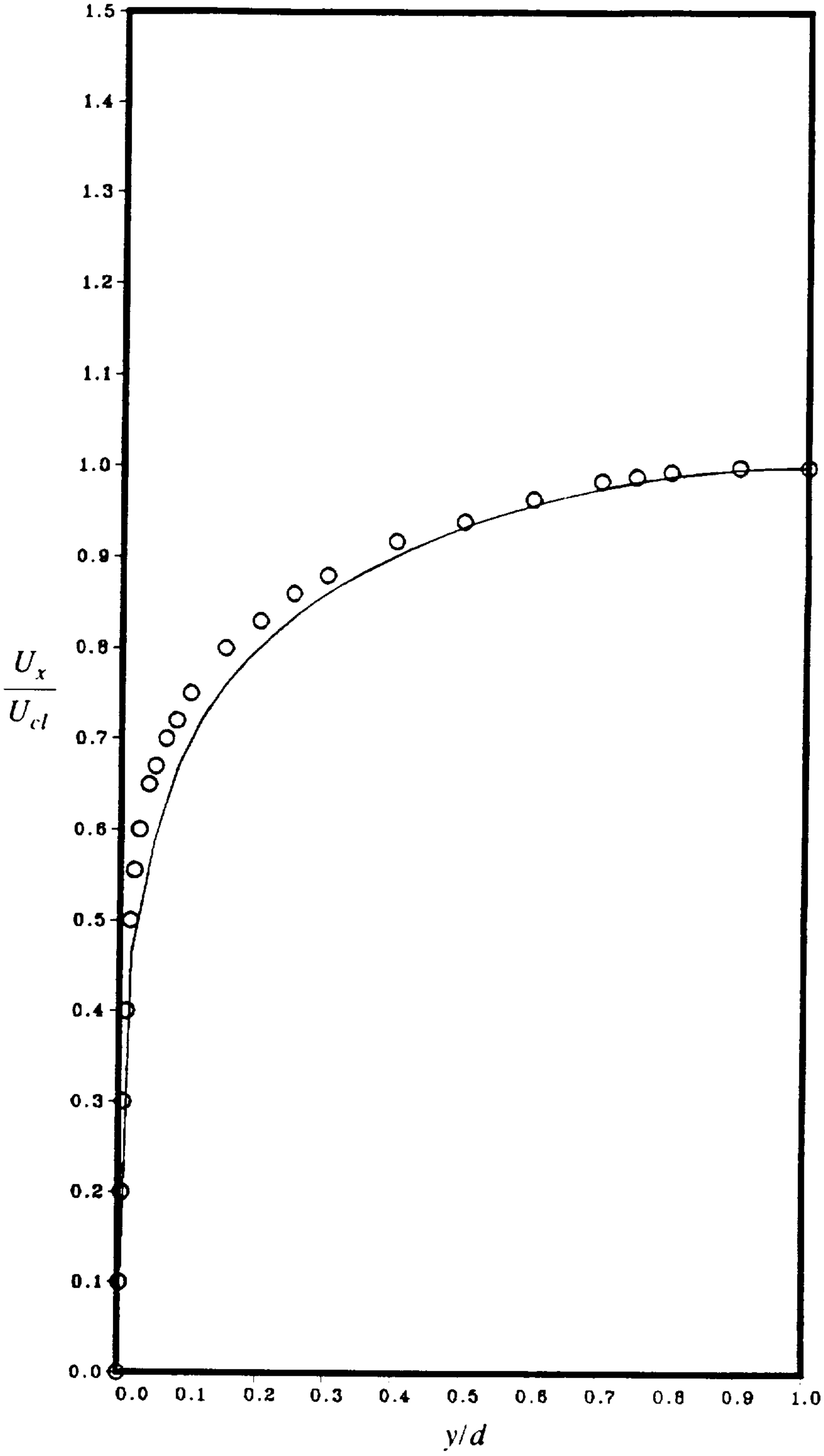

Figure 4.9. Mean velocity profile for fully developed turbulent channel flow, Re=110,000. Comparison of predictions using WFM (standard constants) with Laufer [1950] data.

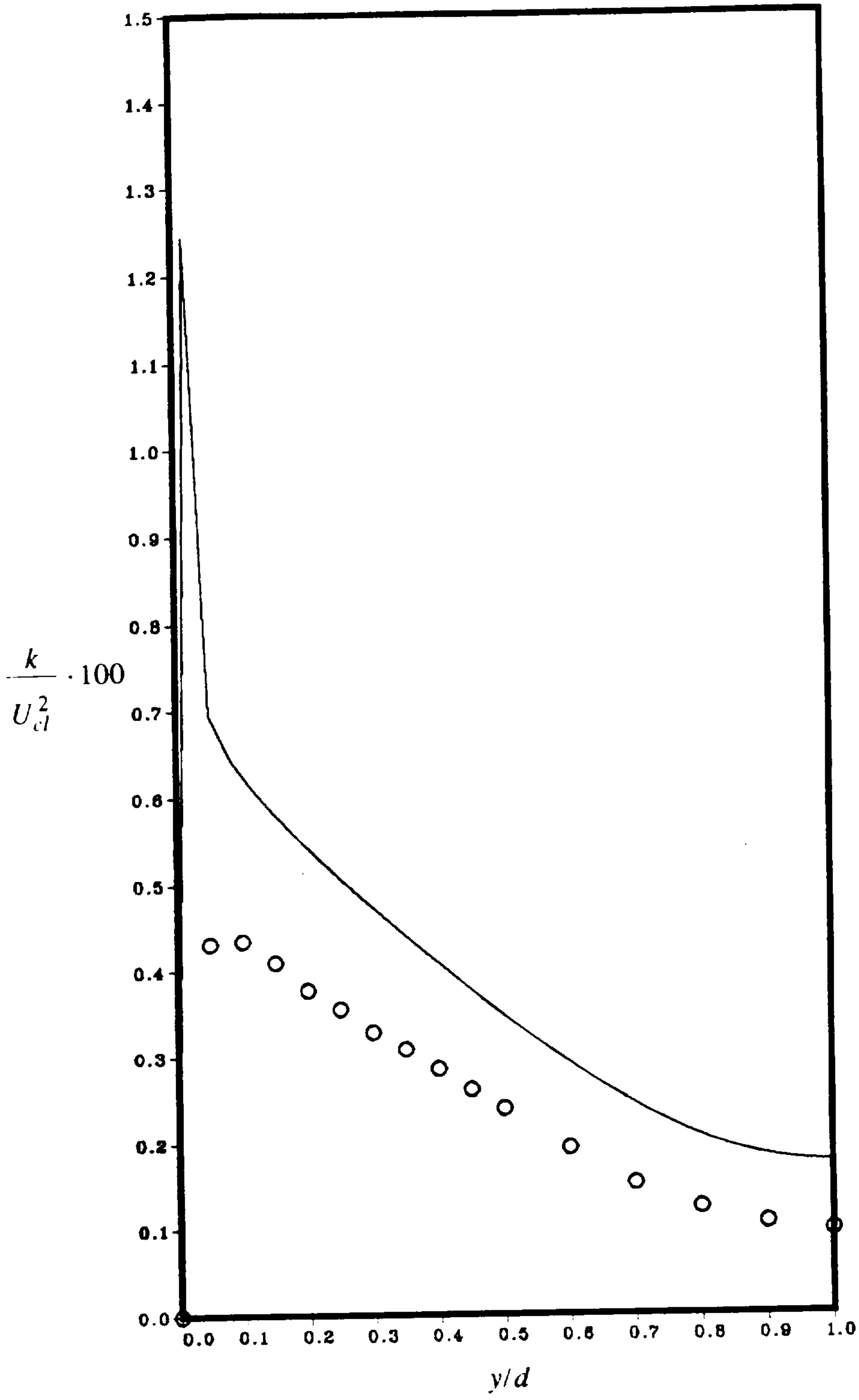

Figure 4.10. Turbulent kinetic energy profile for fully developed turbulent channel flow, Re=110,000. Comparison of predictions using WFM (standard constants) with Laufer [1950] data.

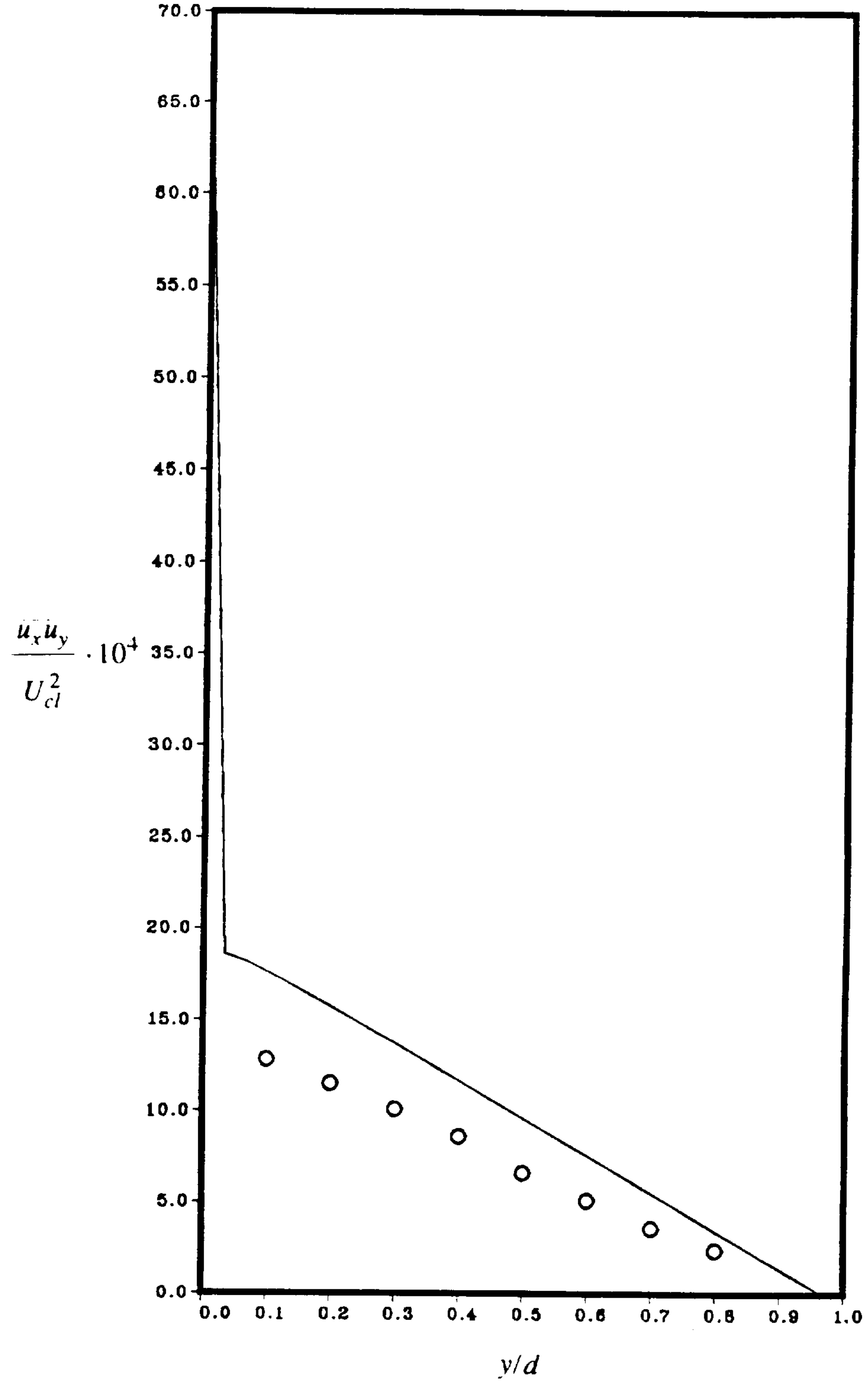

Figure 4.11. Turbulent shear stress profile for fully developed turbulent channel flow, Re=110,000. Comparison of predictions using WFM (standard constants) with Laufer [1950] data.

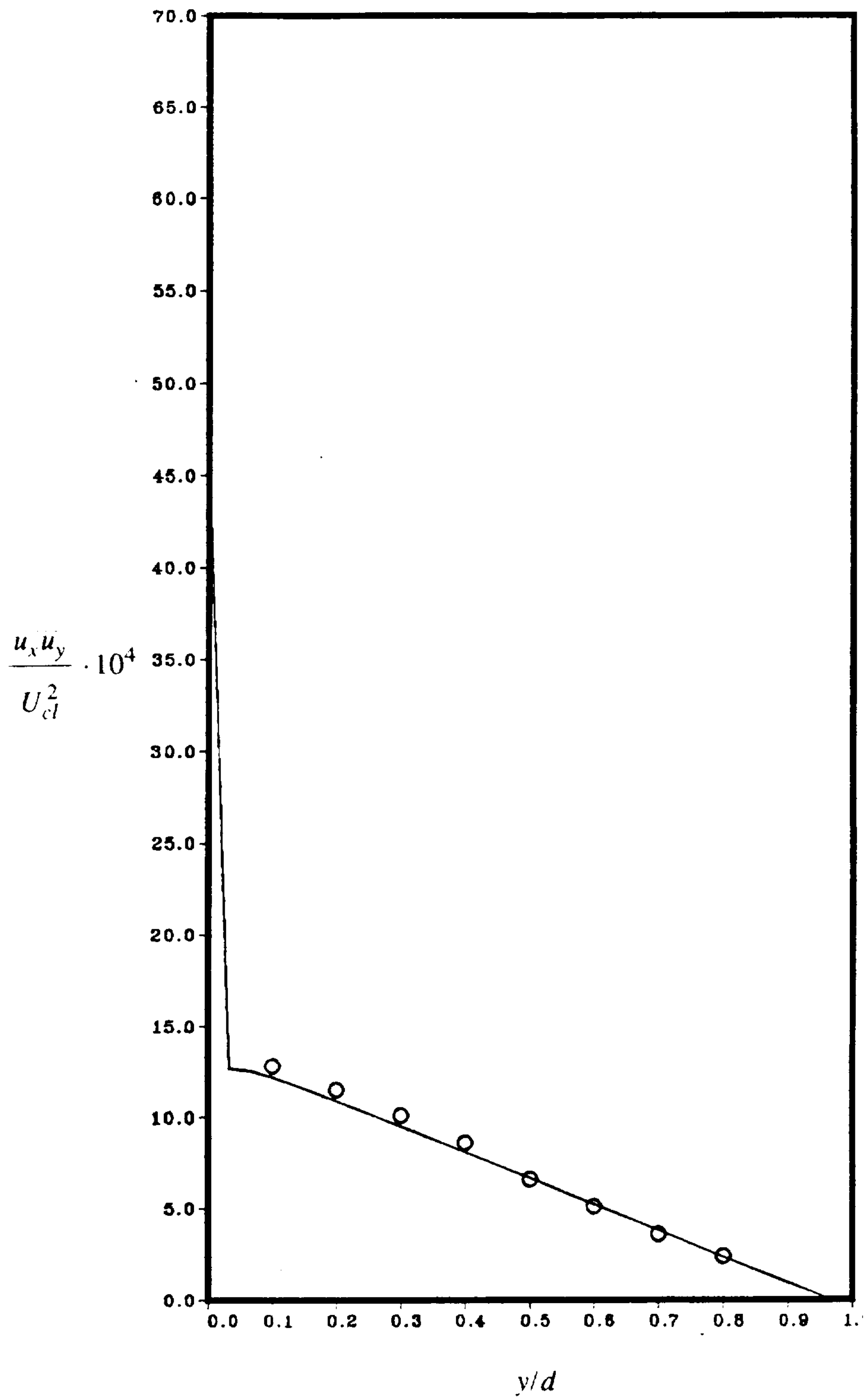

Figure 4.12. Turbulent shear stress profile for fully developed turbulent channel flow, Re=110,000. Comparison of predictions using WFM (Laufer's constants) with Laufer [1950] data.

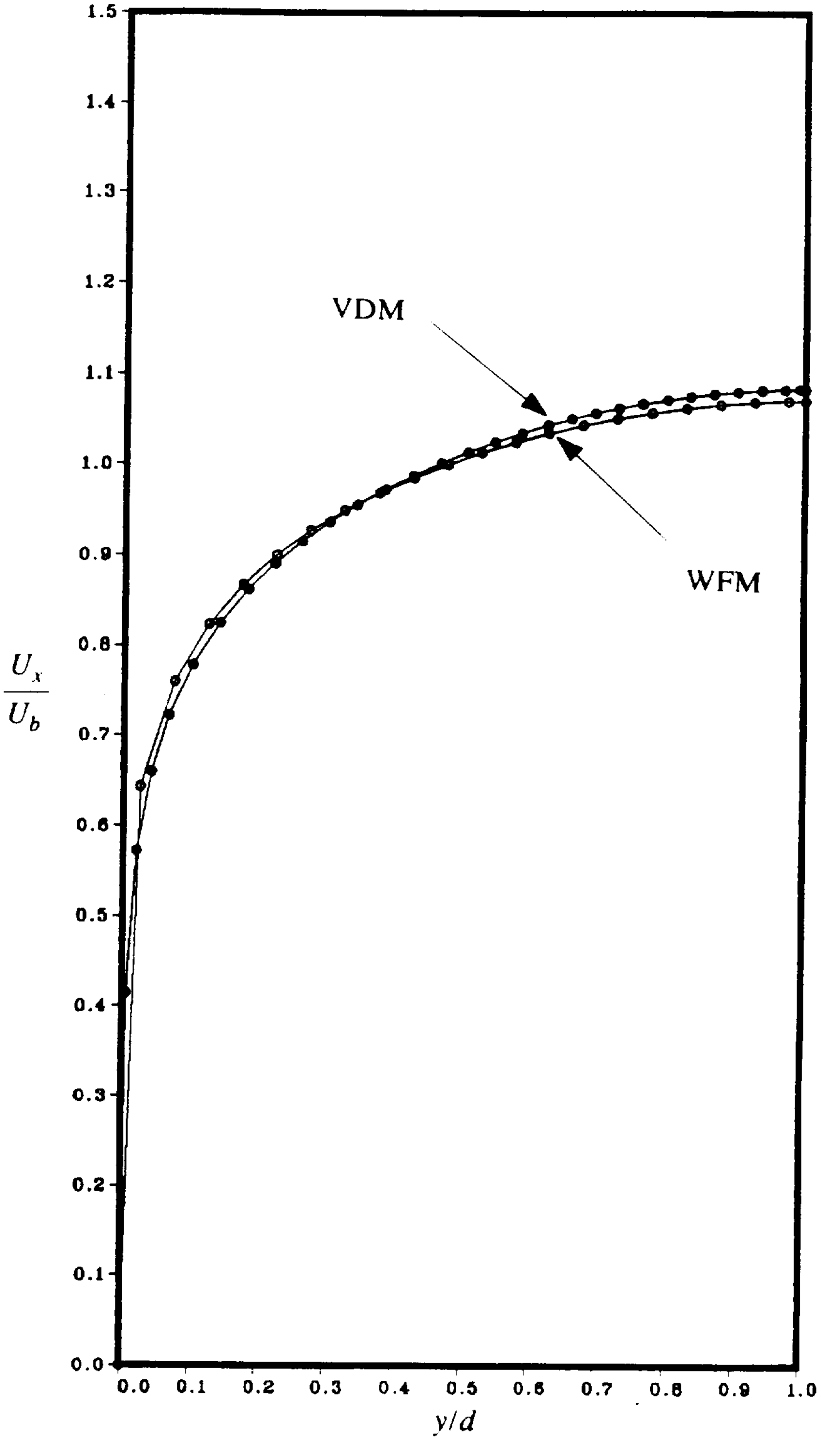

Figure 4.13. Mean velocity profile for fully developed turbulent channel flow, Re=110,000. Comparison of predictions using WFM (standard constants) and VDM with interface region at $y^+ \approx 10$.

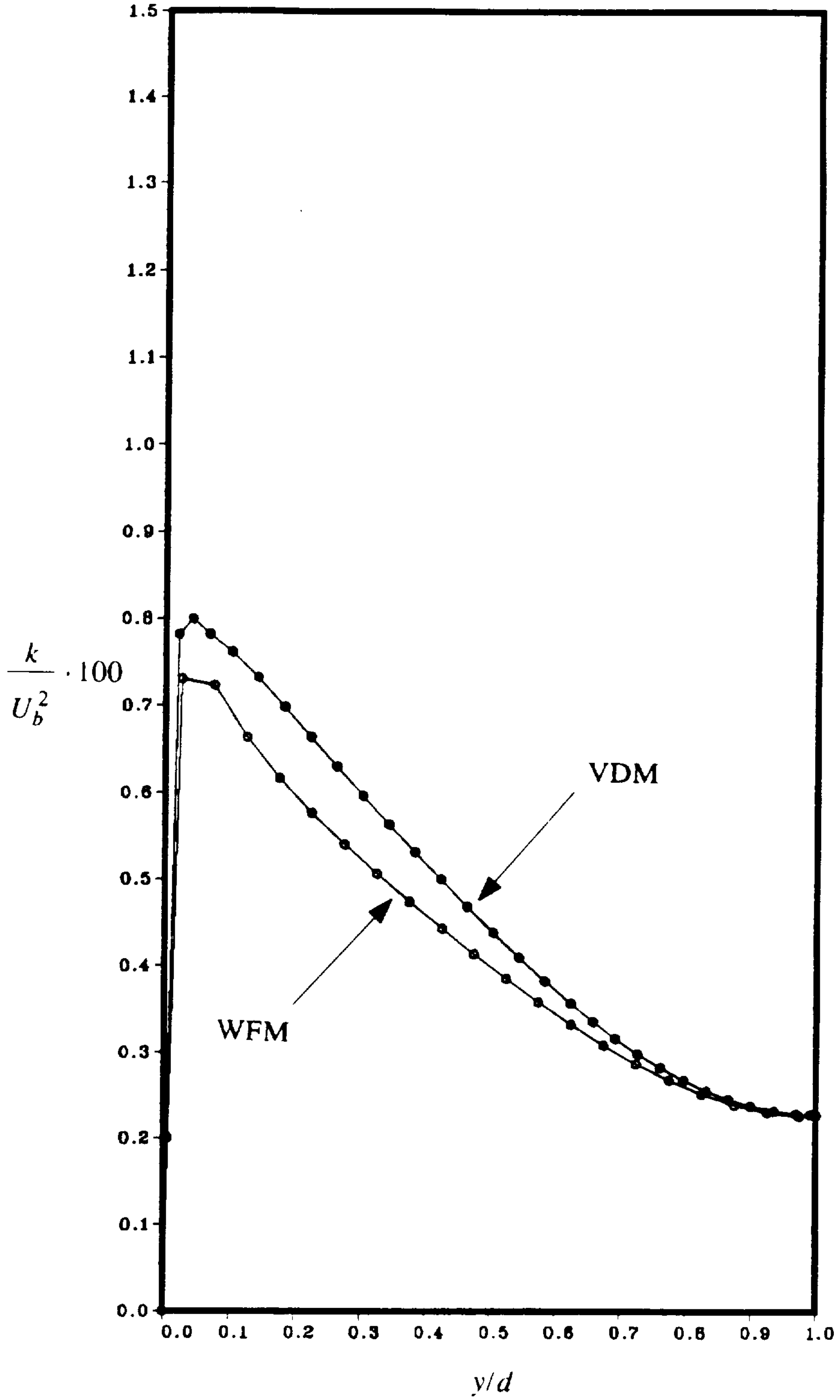

Figure 4.14. Turbulent kinetic energy profile for fully developed turbulent channel flow, Re=110,000. Comparison of predictions using WFM (standard constants) and VDM with interface region at $y^+ \approx 10$.

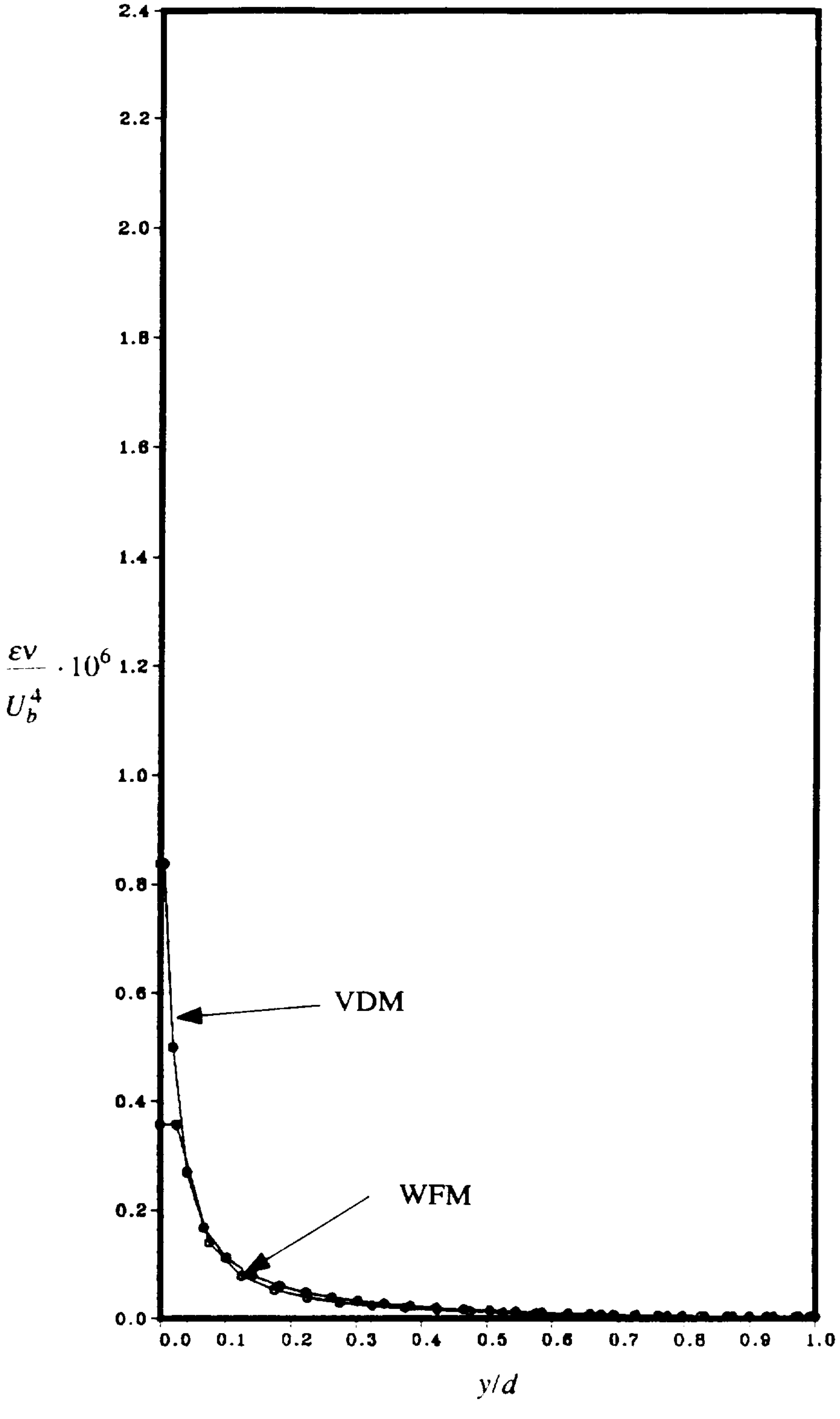

Figure 4.15. Energy dissipation profile for fully developed turbulent channel flow, Re=110,000. Comparison of predictions using WFM (standard constants) and VDM with interface region at $y^+ = 10$.

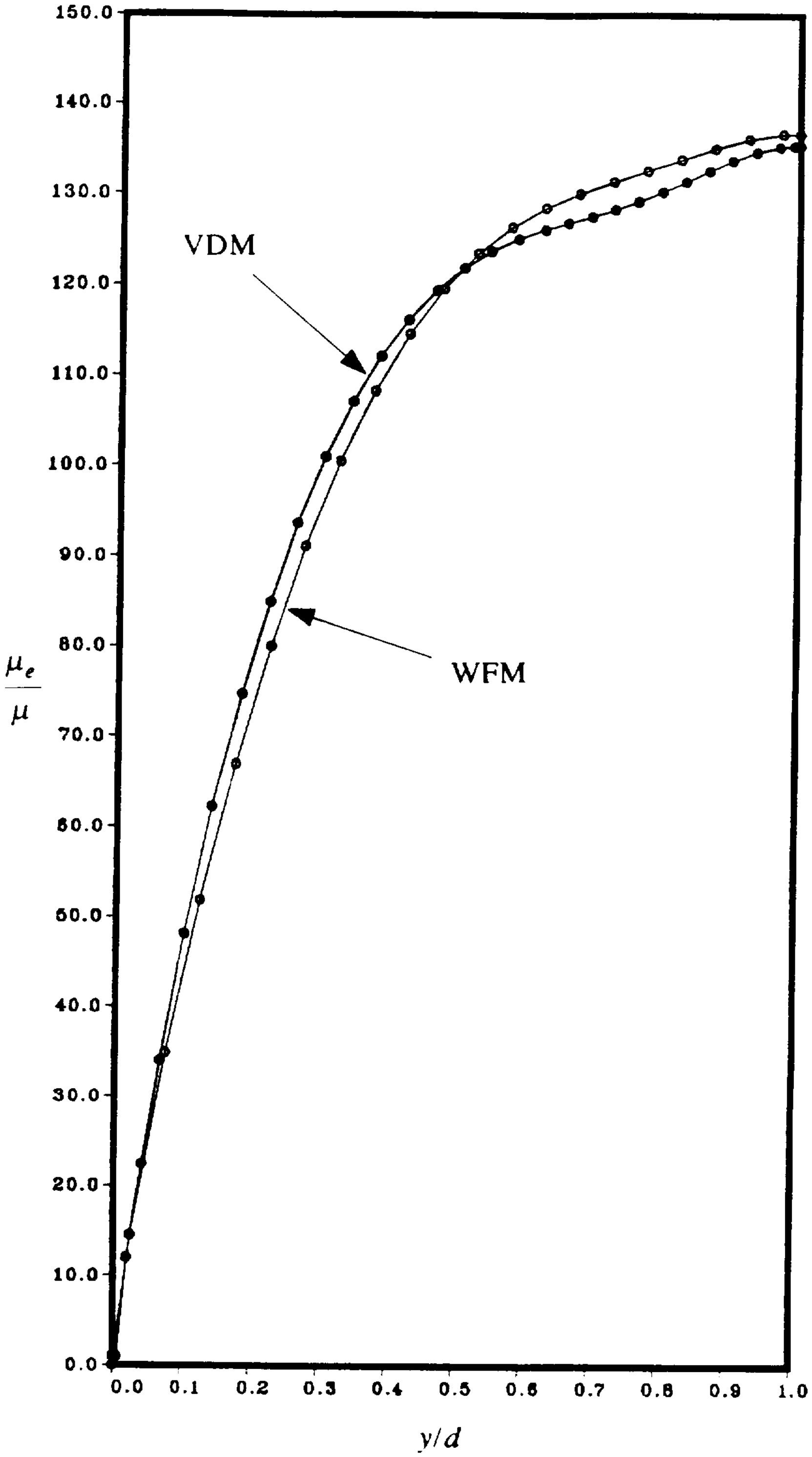

Figure 4.16. Eddy diffusivity (μ_e) profile for fully developed turbulent channel flow, Re=110,000. Comparison of predictions using WFM (standard constants) and VDM with interface region at $y^+ \approx 10$.

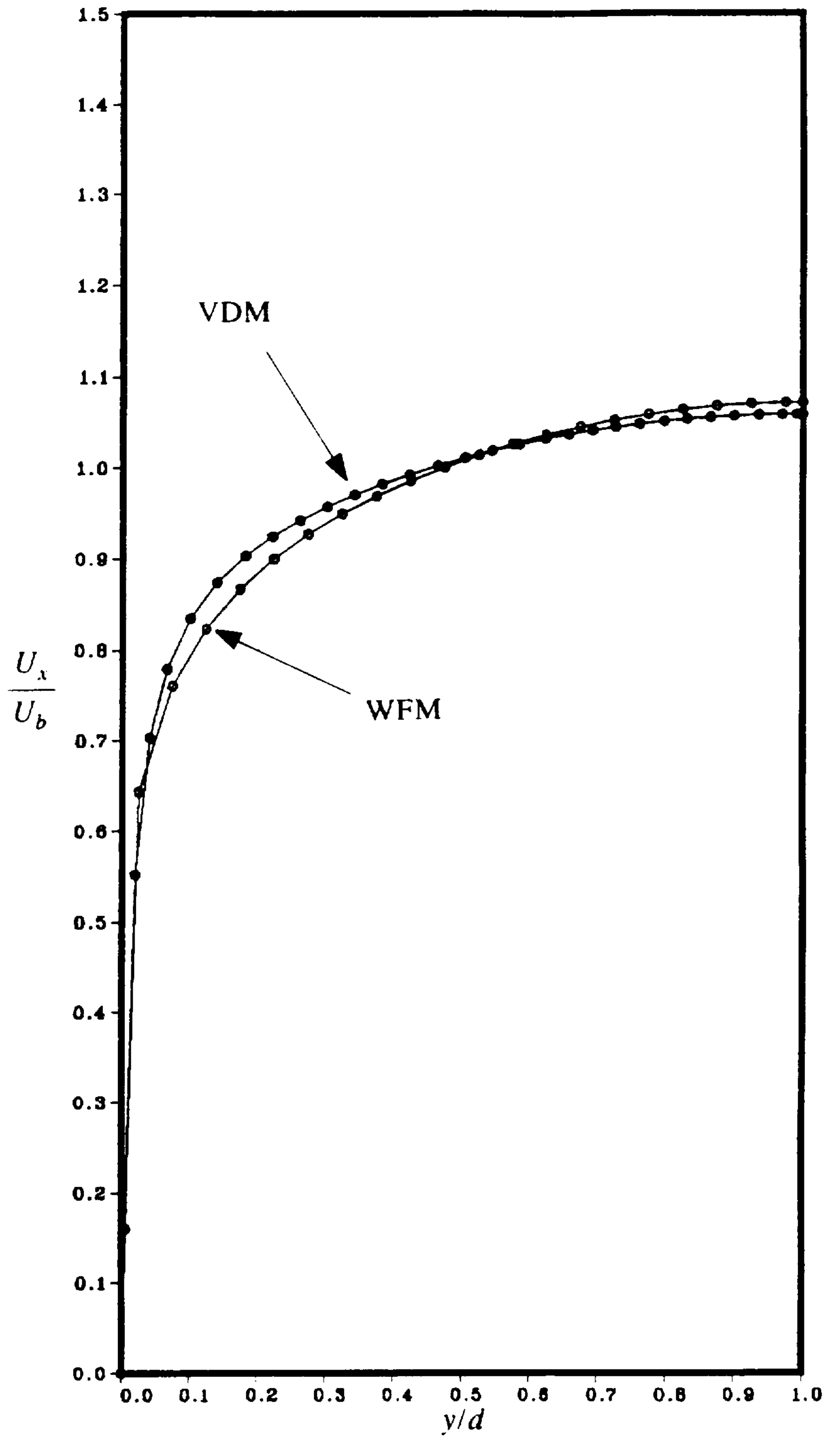

Figure 4.17. Mean velocity profile for fully developed turbulent channel flow, Re=110,000. Comparison of predictions using WFM (standard constants) and VDM with interface region at $y^+ \approx 25$.

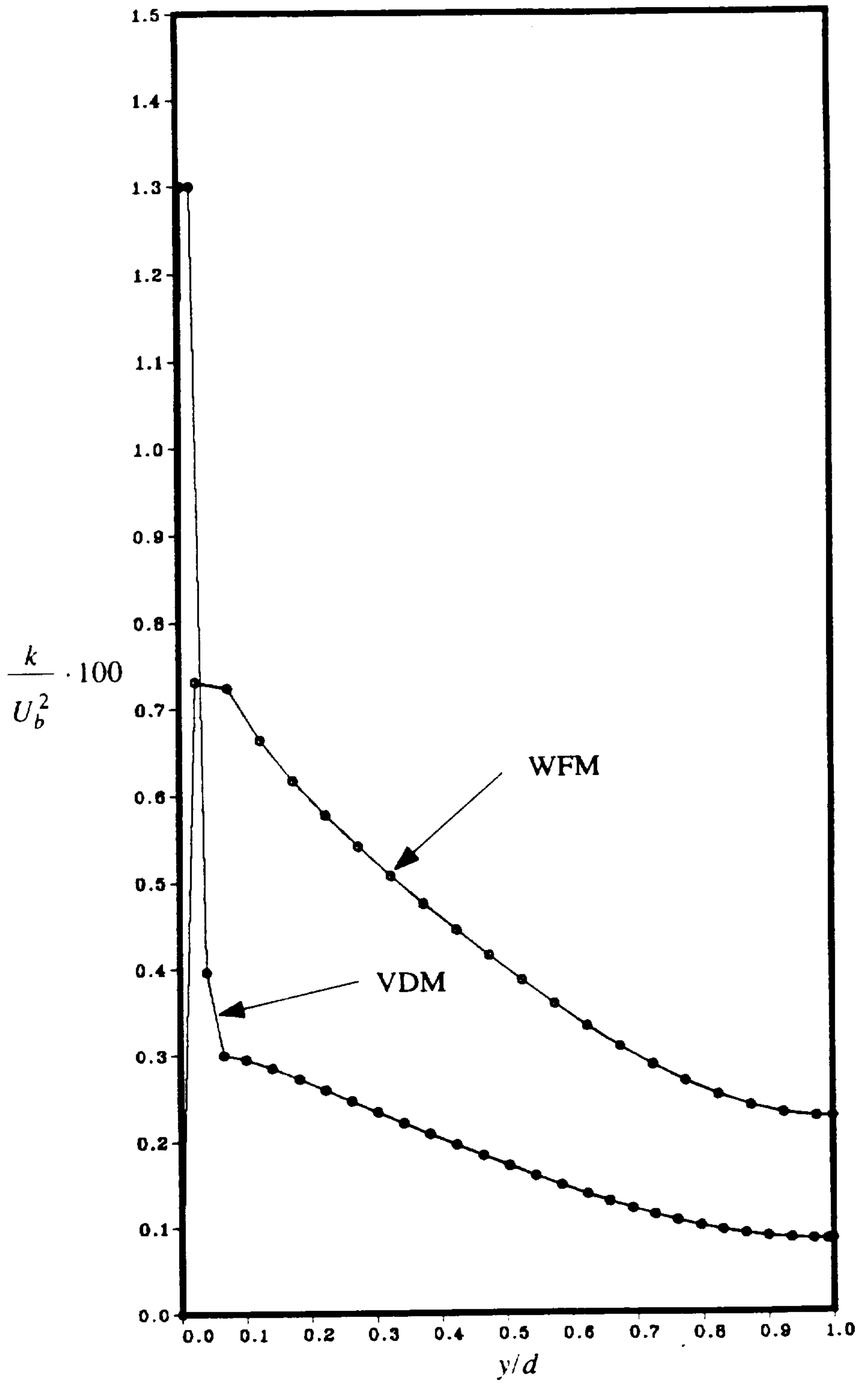

Figure 4.18. Turbulent kinetic energy profile for fully developed turbulent channel flow, Re=110,000. Comparison of predictions using WFM (standard constants) and VDM with interface region at $y^+ \approx 25$.

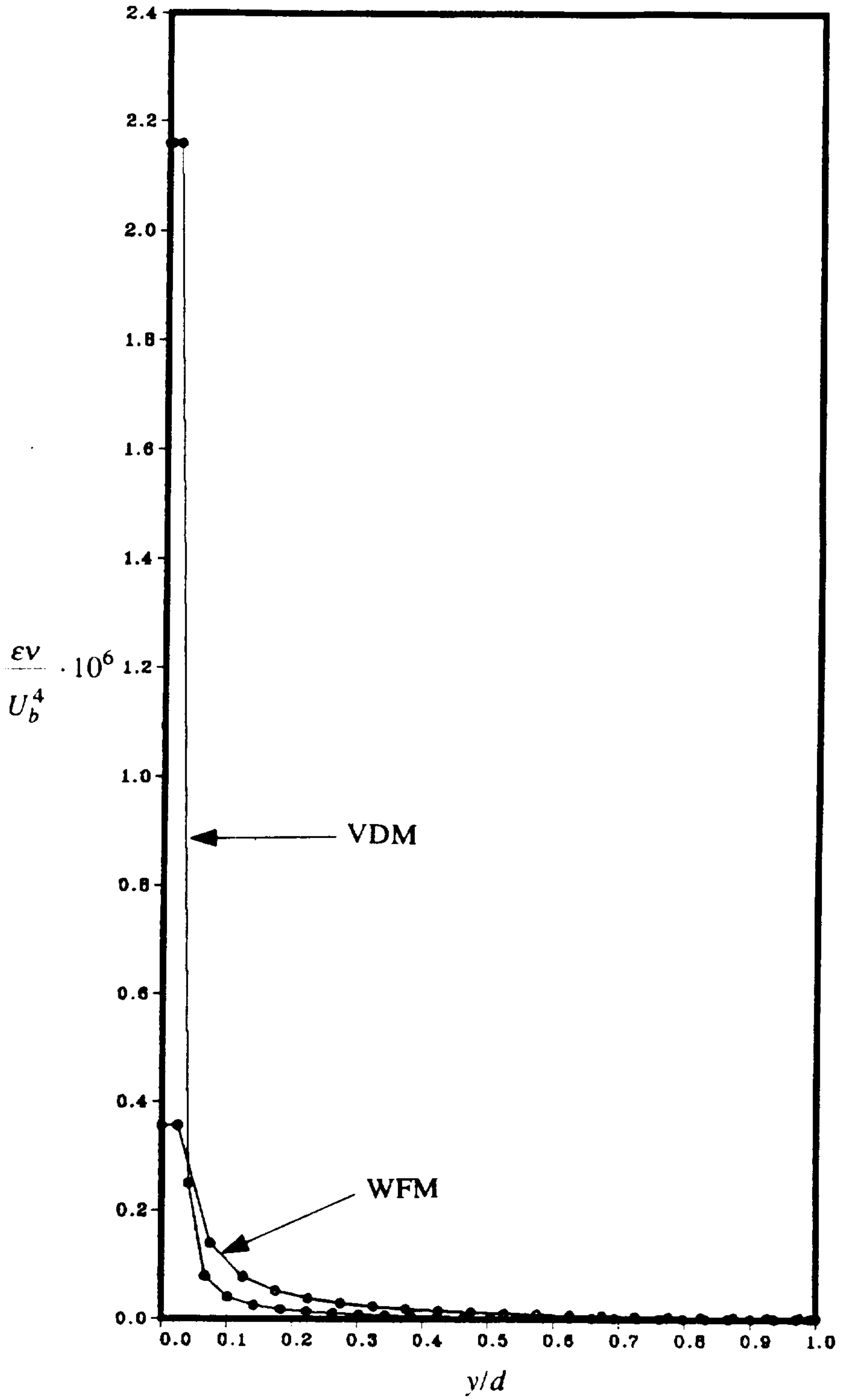

Figure 4.19. Energy dissipation profile for fully developed turbulent channel flow, Re=110,000. Comparison of predictions using WFM (standard constants) and VDM with interface region at $y^+ \approx 25$.

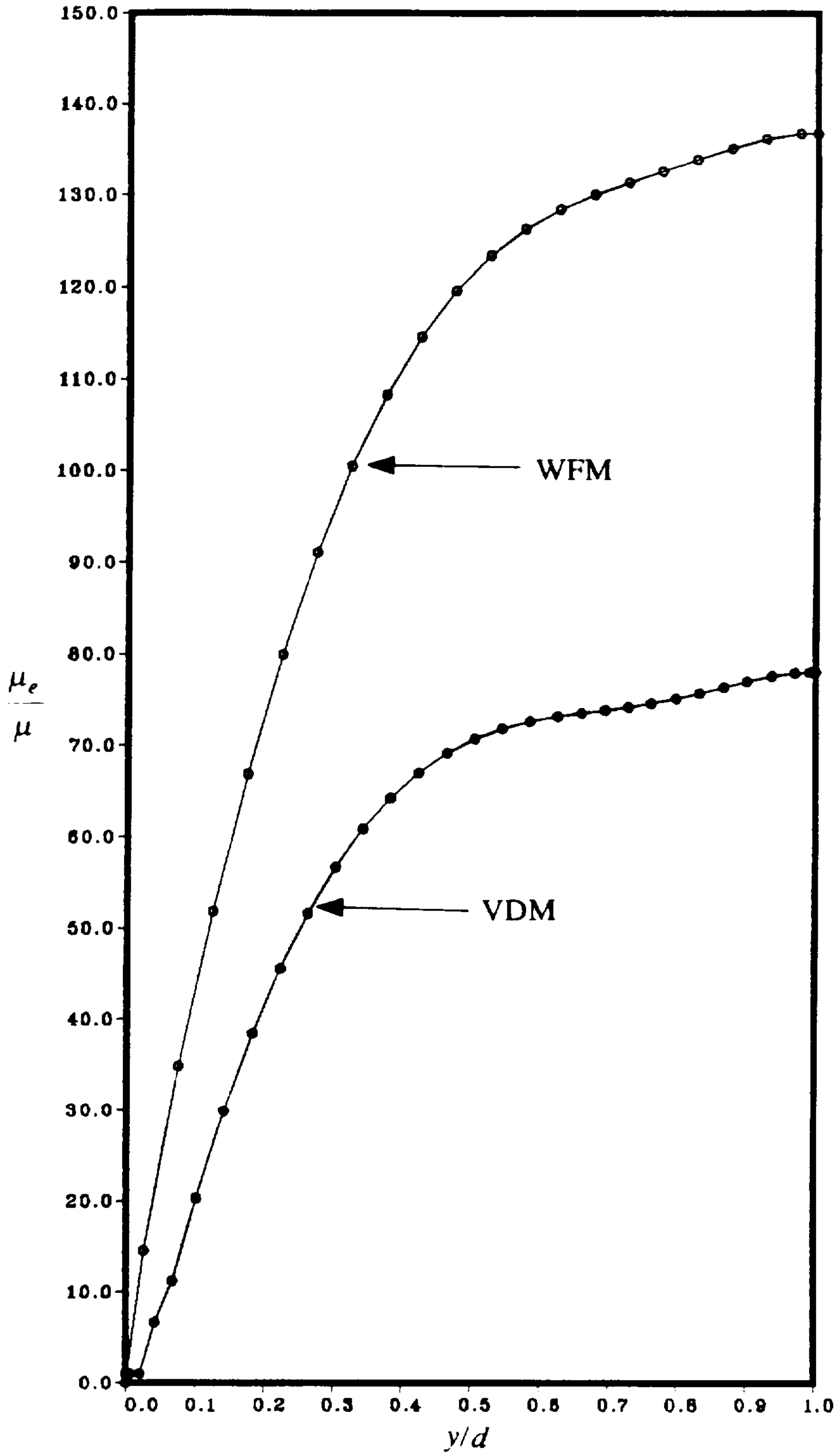

Figure 4.20. Eddy diffusivity (μ_e) profile for fully developed turbulent channel flow, Re=110,000. Comparison of predictions using WFM (standard constants) and VDM with interface region at $y^+ \approx 25$.

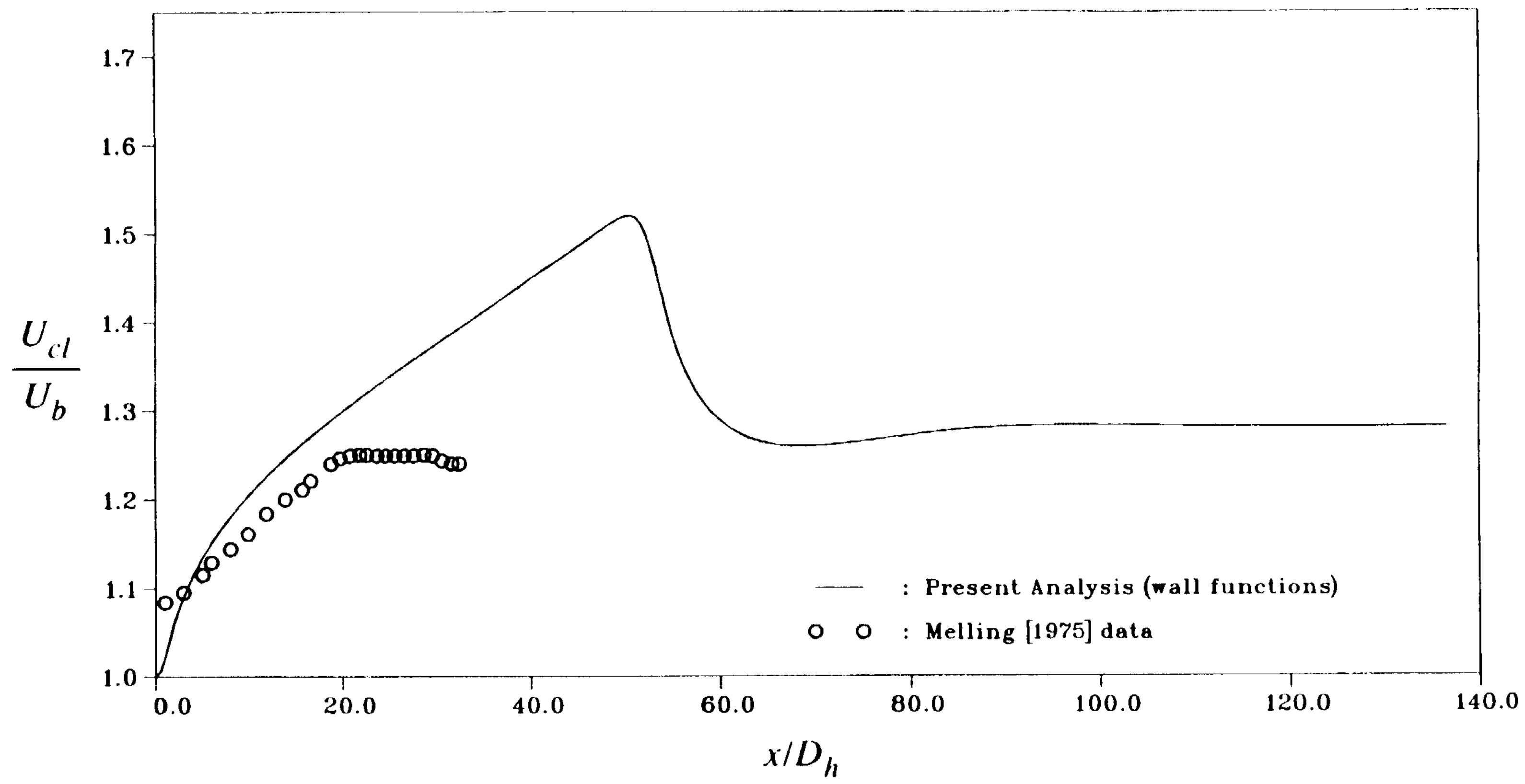

Figure 4.21. Centerline velocity for developing turbulent duct flow, Re=40,000. Comparison of predictions using WFM in the near wall region with Melling [1975] data.

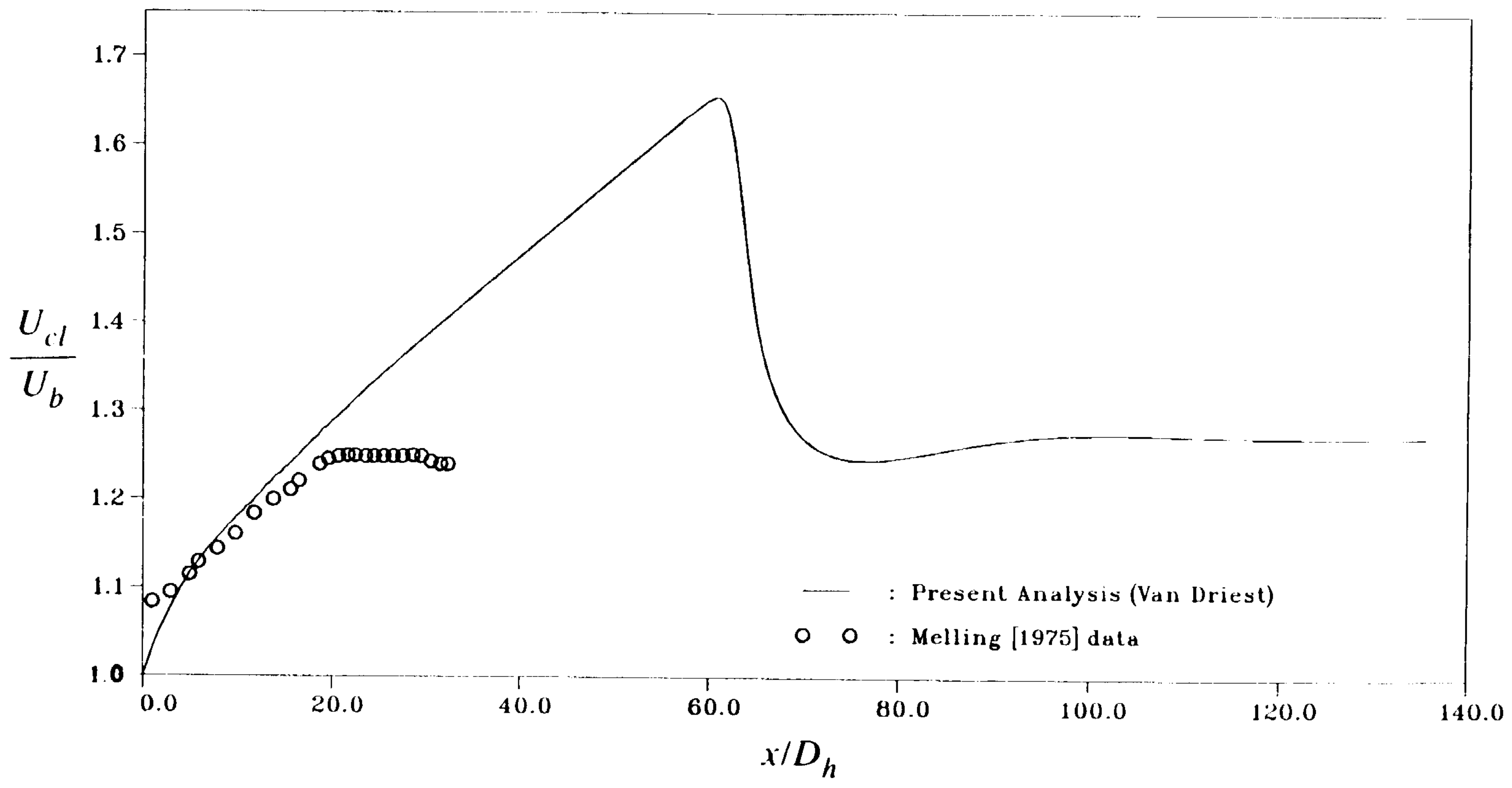

Figure 4.22. Centerline velocity for developing turbulent duct flow, Re=40,000. Comparison of predictions using VDM in the near wall region with Melling [1975] data.

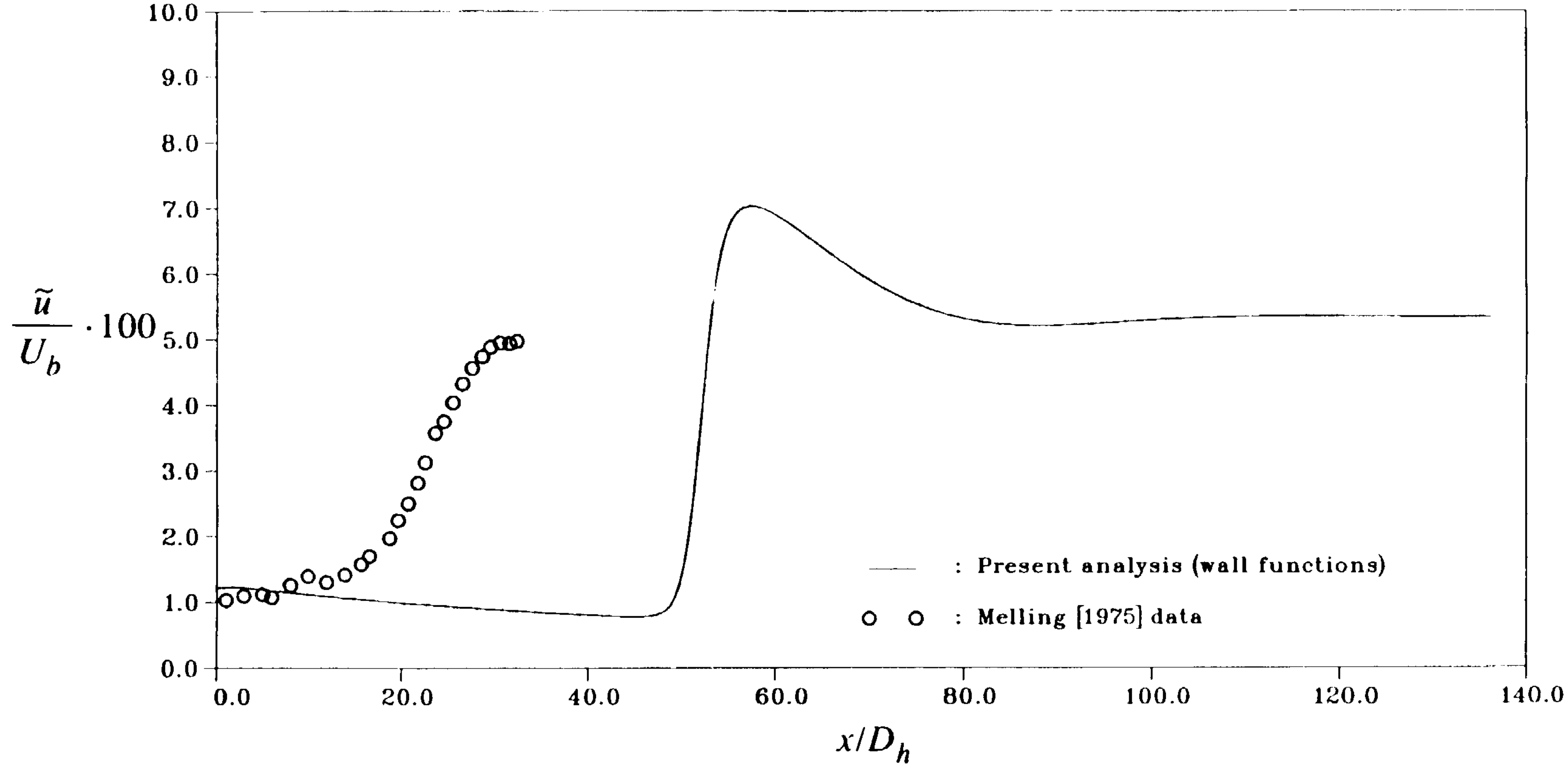

Figure 4.23. Centerline turbulence intensity for developing turbulent duct flow, Re=40,000. Comparison of predictions using WFM in the near wall region with Melling [1975] data.

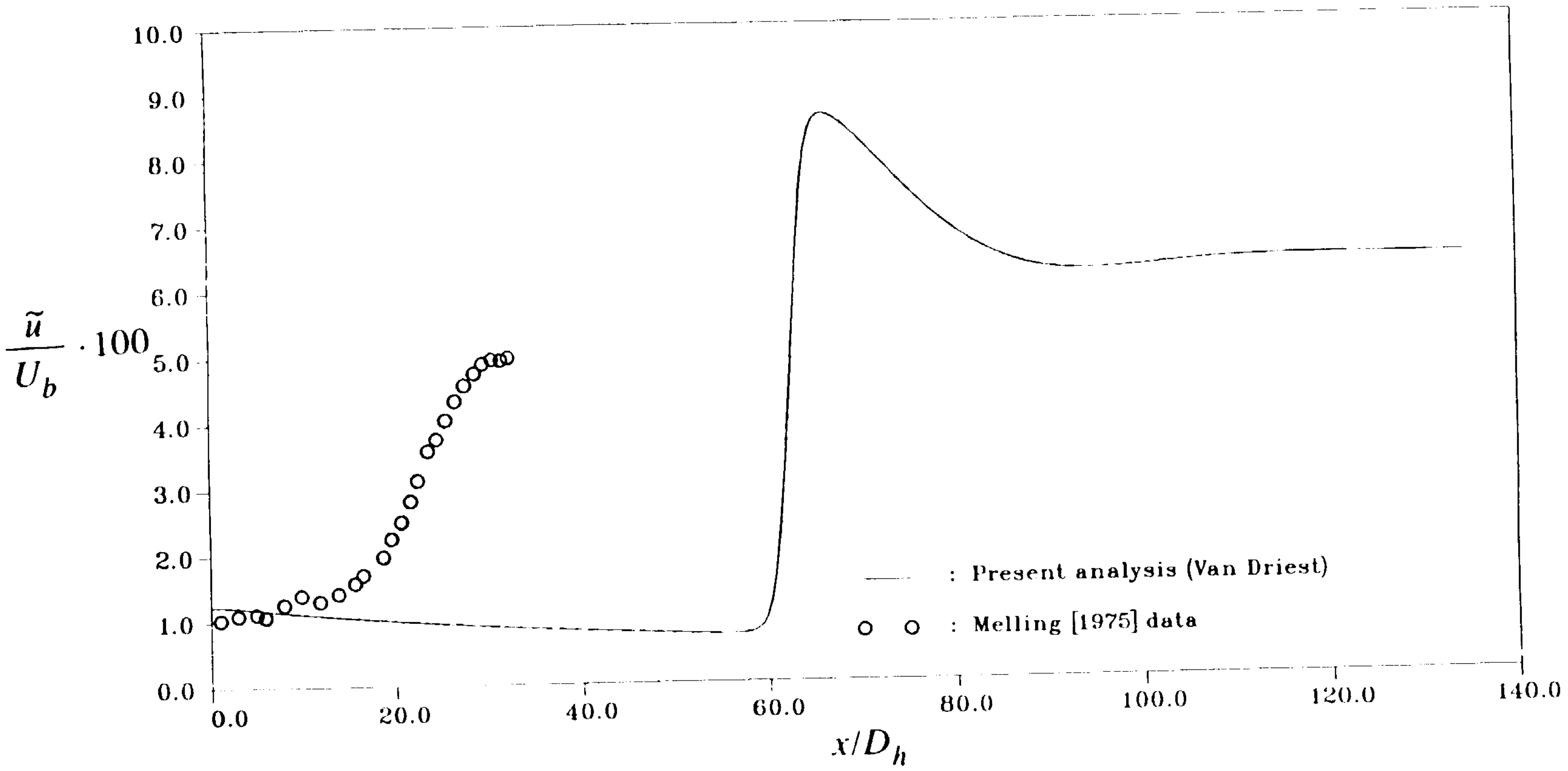

Figure 4.24. Centerline turbulence intensity for developing turbulent duct flow, Re=40,000. Comparison of predictions using VDM in the near wall region with Melling [1975] data.

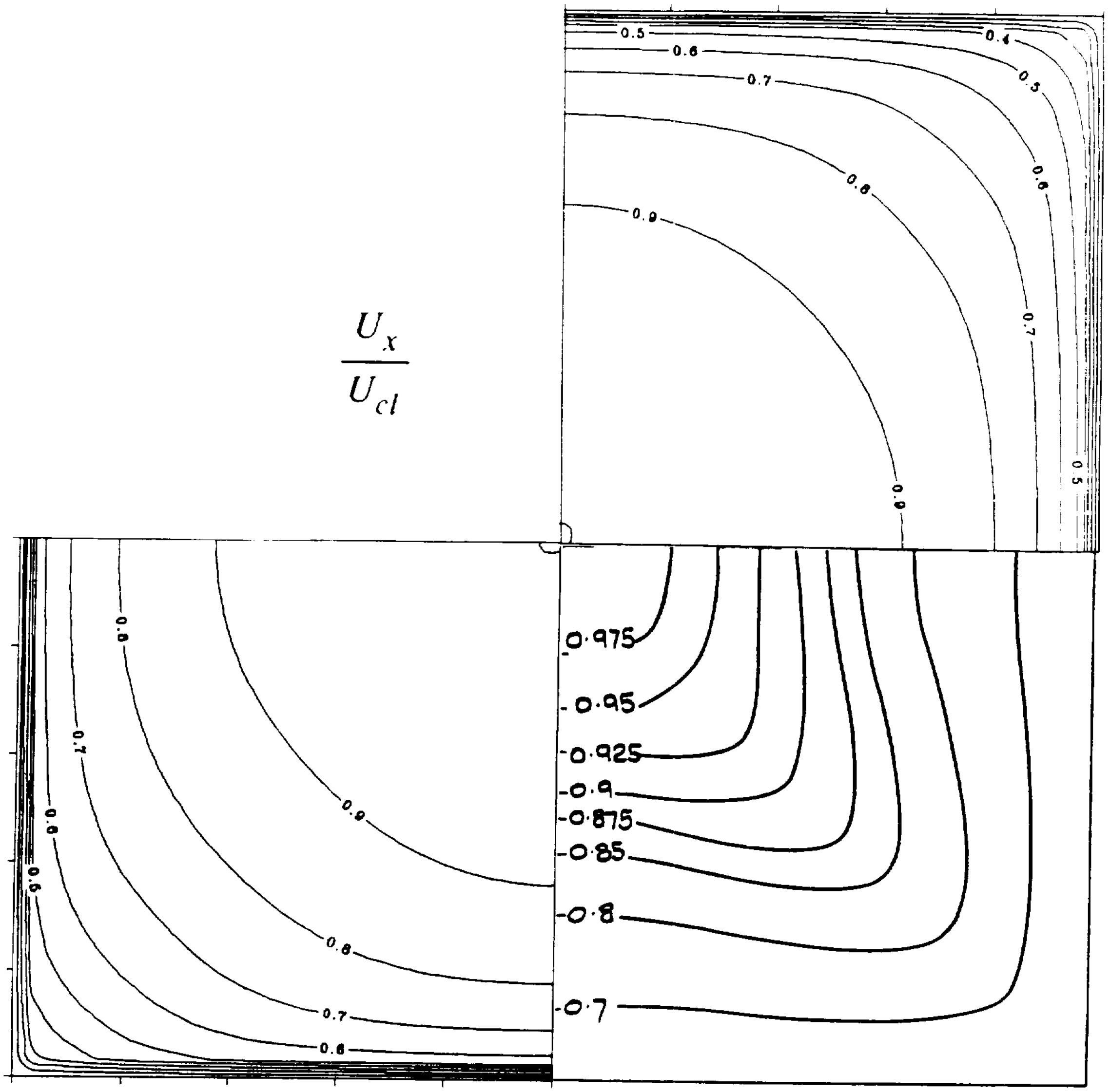

Figure 4.25. Contours of U_x/U_{cl} for fully developed turbulent duct flow, Re=40,000. Comparison of predictions using VDM (lower left) and WFM (upper right) with data of Melling [1975].

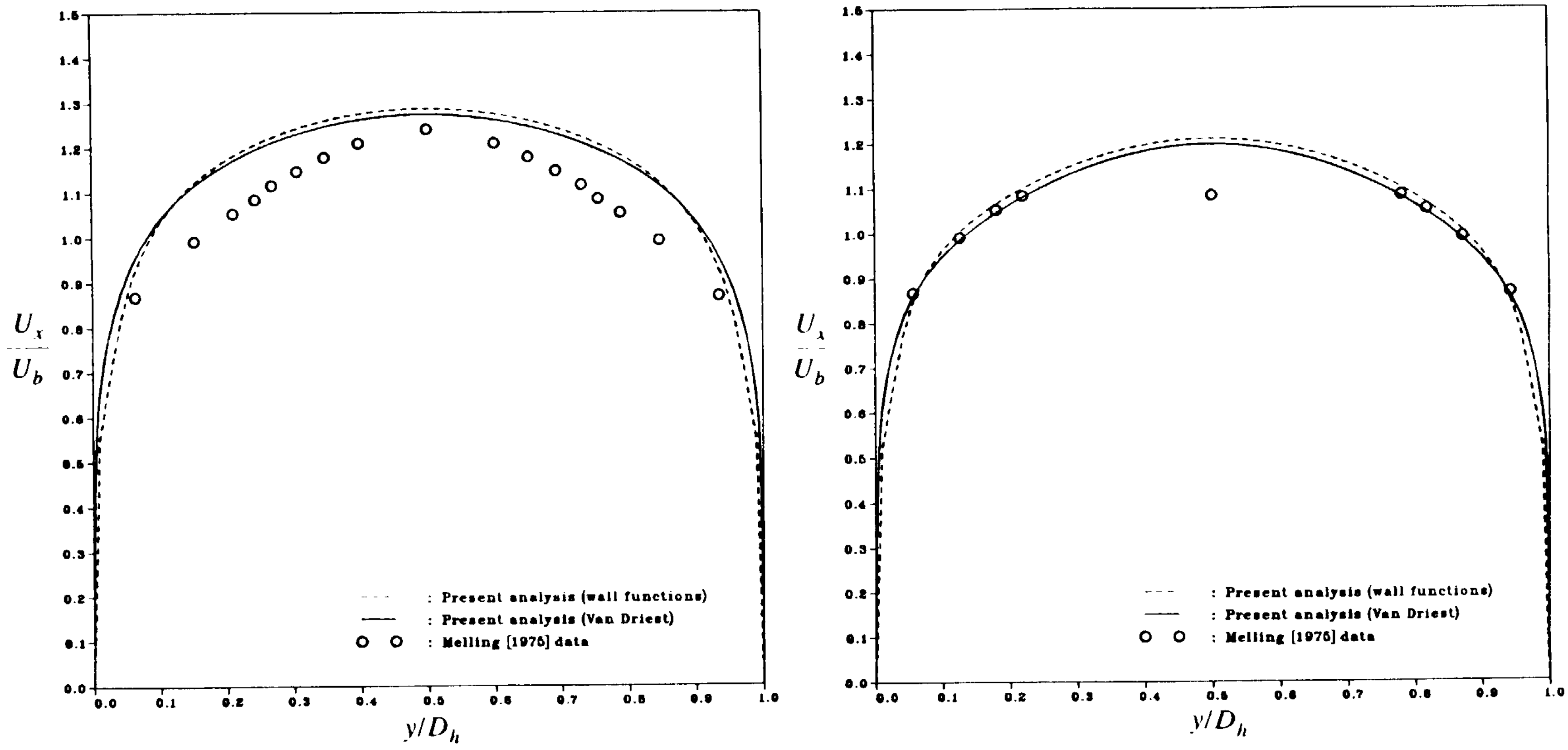

(a)

(b)

Figure 4.26. Cross-stream profiles of U_x/U_b for fully developed turbulent duct flow, Re=40,000. (a) $z/D_h = 0.5$. (b) $z/D_h = 0.25$. Comparison of predictions with data of Melling [1975].

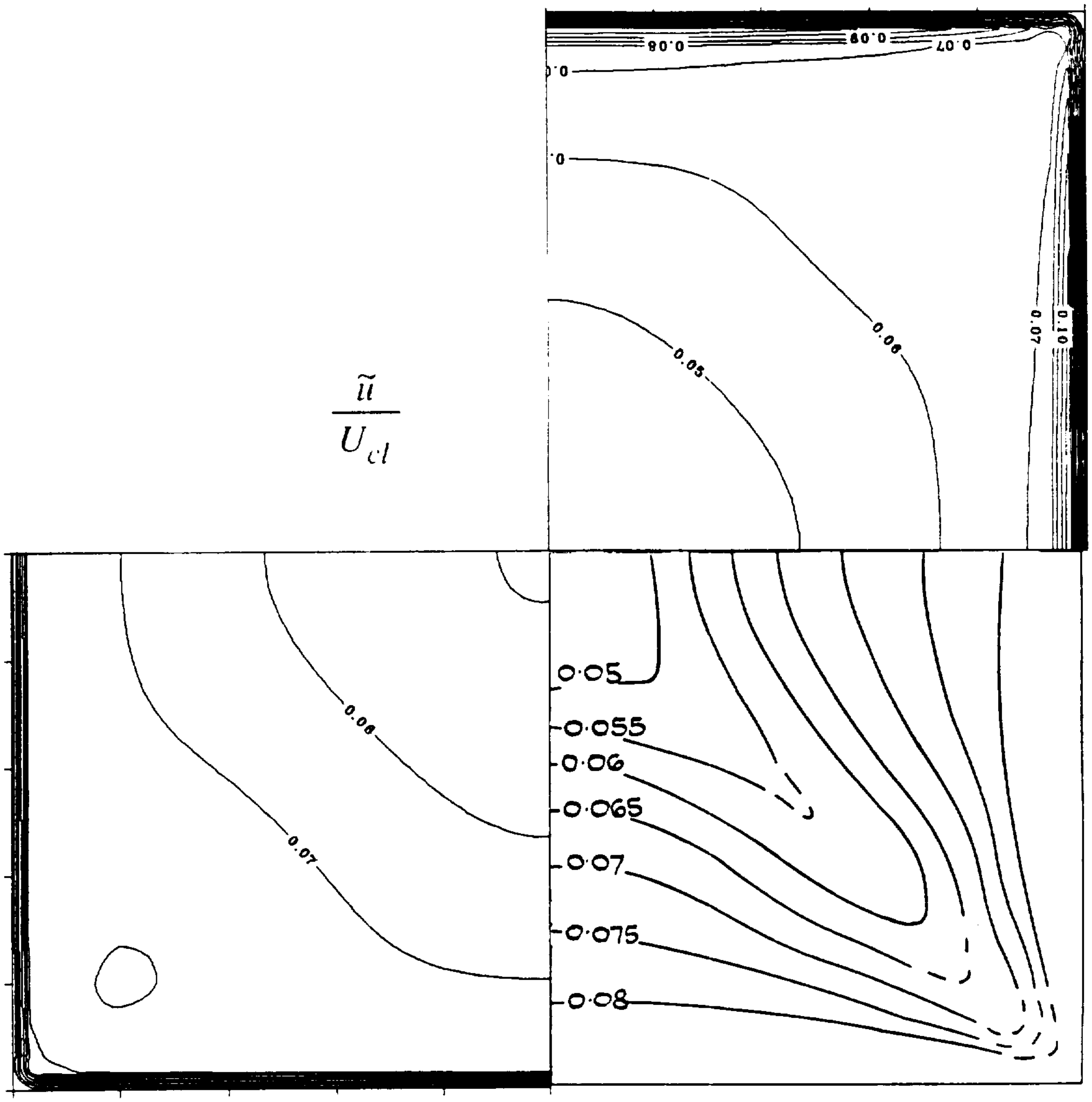

Figure 4.27. Contours of $\tilde{u}/U_{cl}$ for fully developed turbulent duct flow, Re=40,000. Comparison of predictions using VDM (lower left) and WFM (upper right) with data of Melling [1975].

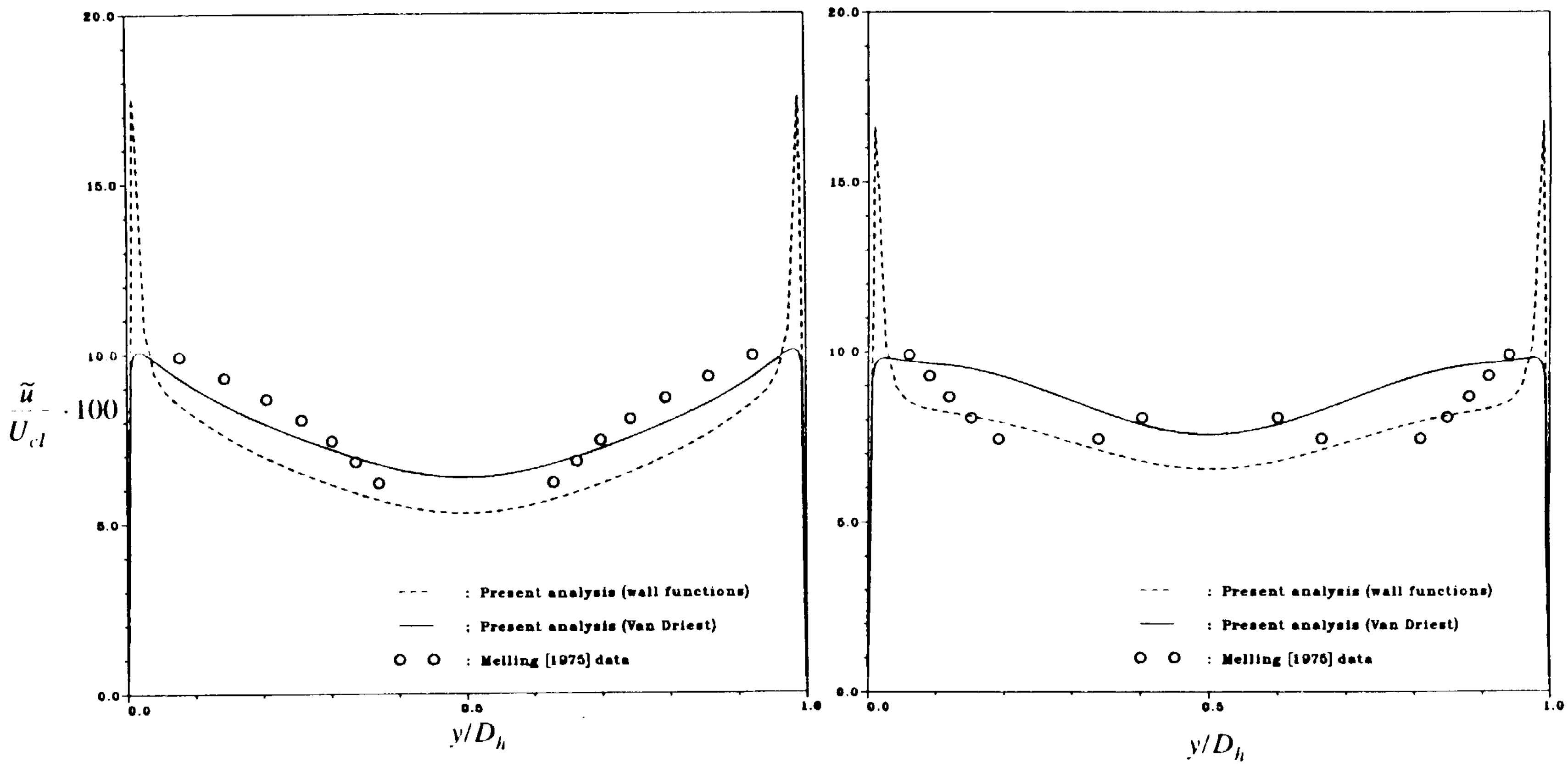

(a)

(b)

Figure 4.28. Cross-stream profiles of $\tilde{u}/U_{cl}\times10^2$ for fully developed turbulent duct flow, Re=40,000. (a) z/D_h = 0.5. (b) z/D_h = 0.25. Comparison of predictions with data of Melling [1975].

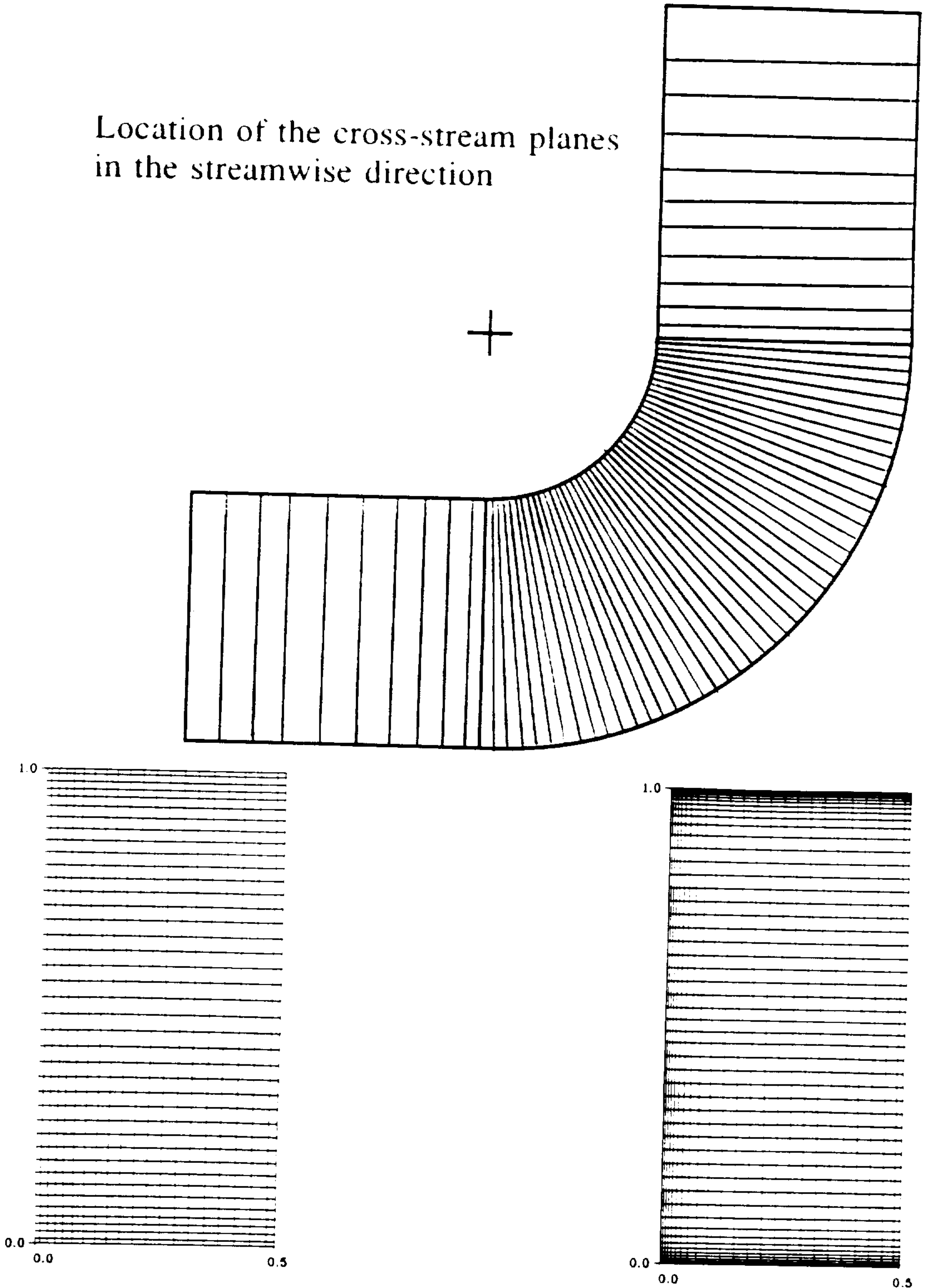
Location of the cross-stream planes in the streamwise direction
1.0
0.0
0.0
0.5
1.0
0.0
0.0
0.5

Cross-stream grid for WFM formulation

Cross-stream grid for VDM formulation

Figure 5.1. Grid arrangement for curved duct calculations.

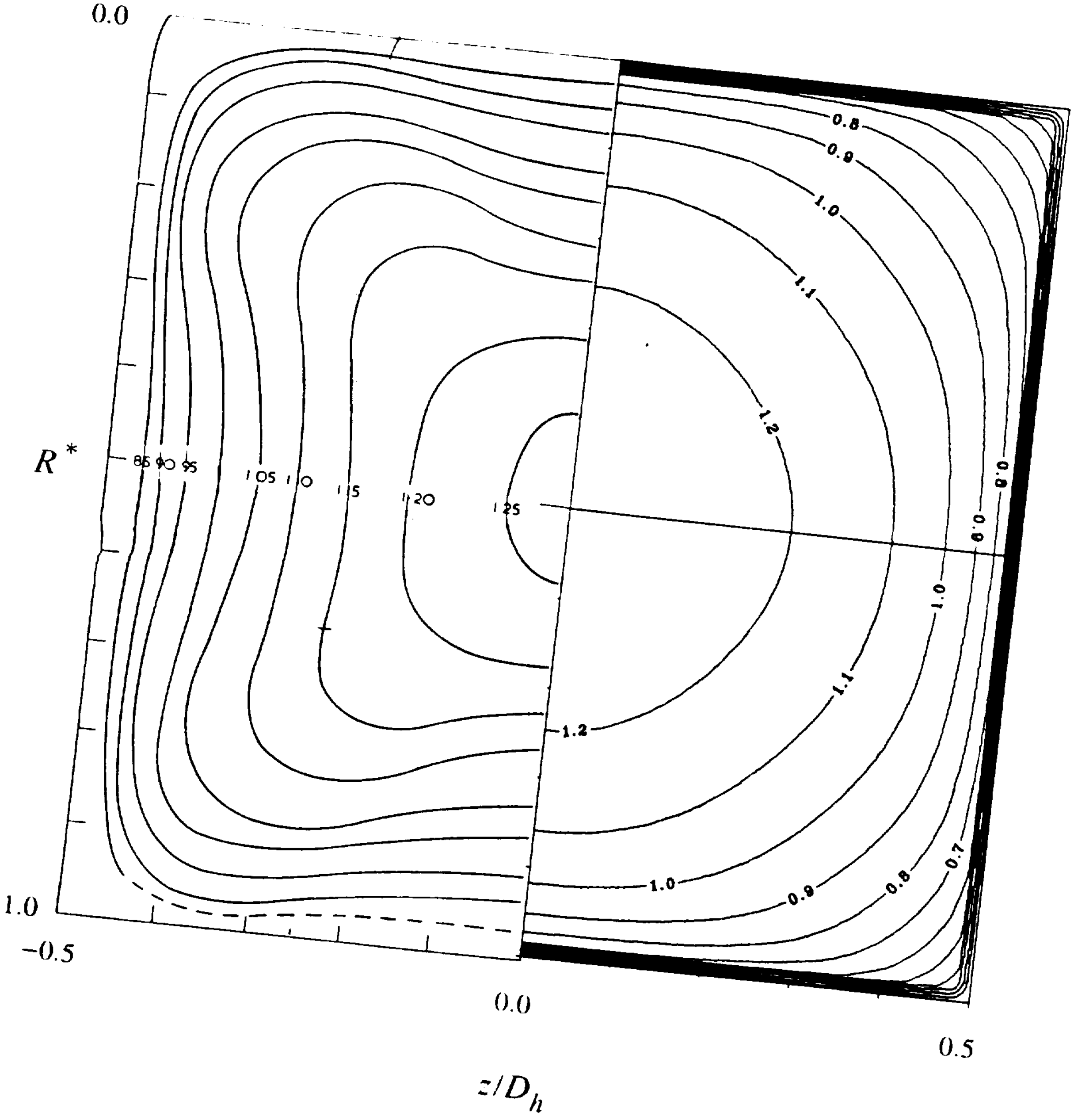

Figure 5.2. Contours of U_θ/U_b for turbulent bend flow, $x/D_h = -2.5$. Comparison of predictions using VDM with data of Humphrey [1977].

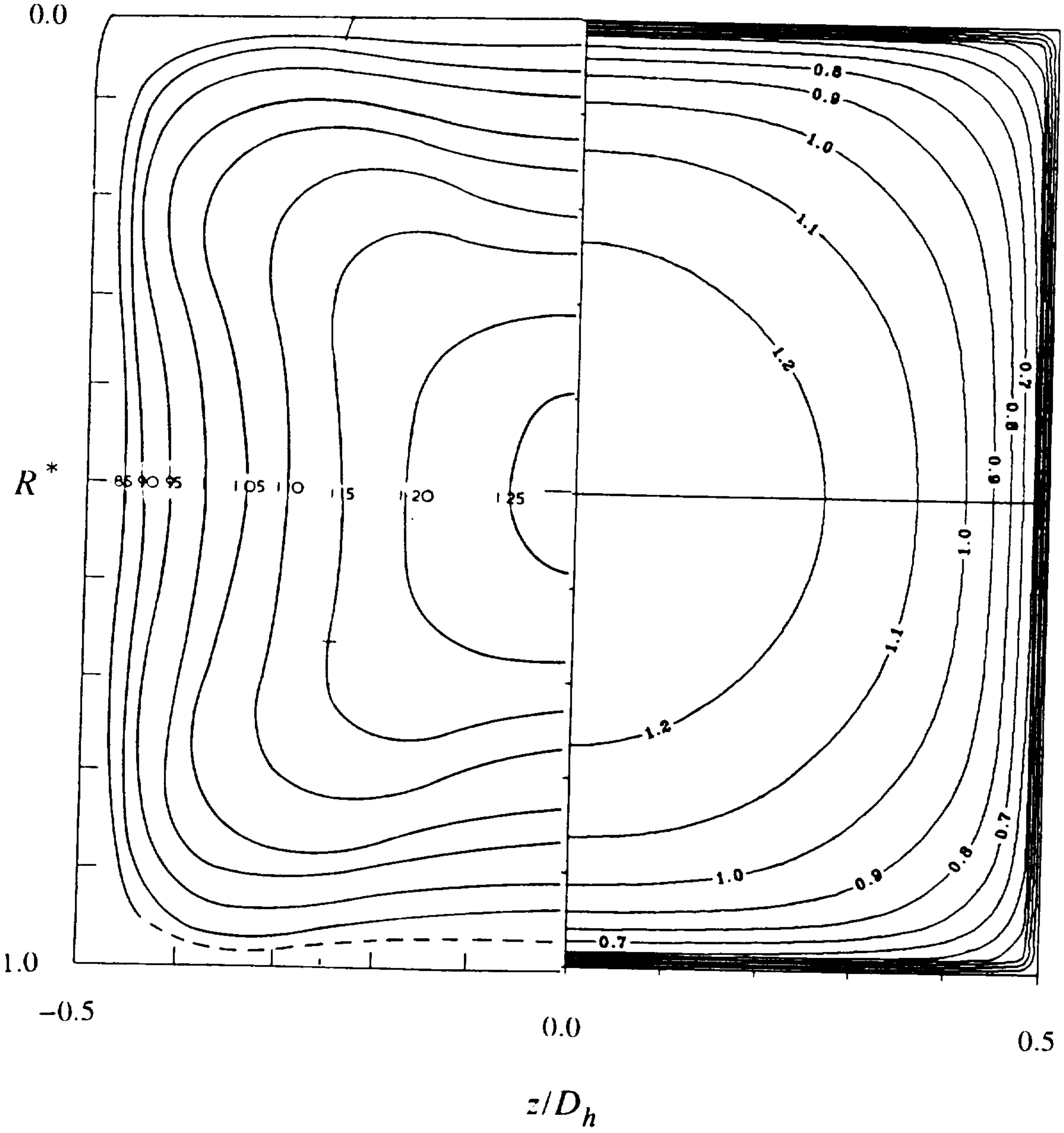

Figure 5.3. Contours of U_θ/U_b for turbulent bend flow, $x/D_h = -2.5$. Comparison of predictions using WFM with data of Humphrey [1977].

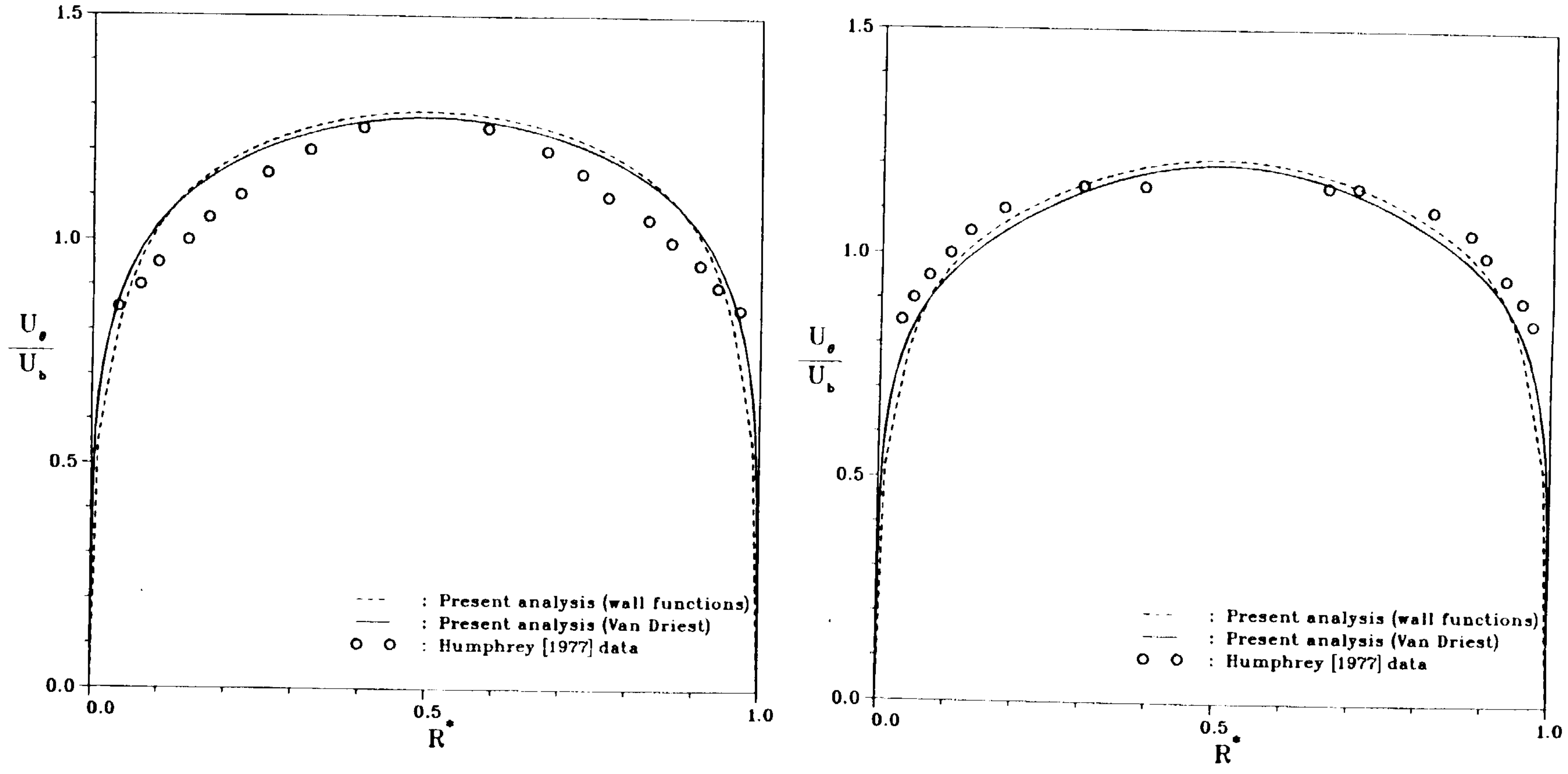

(a)

(b)

Figure 5.4. Radial profiles of U_θ/U_b for turbulent bend flow, $x/D_h = -2.5$. (a) $z/D_h = 0.5$. (b) $z/D_h = 0.25$. Comparison of predictions with data of Humphrey [1977].

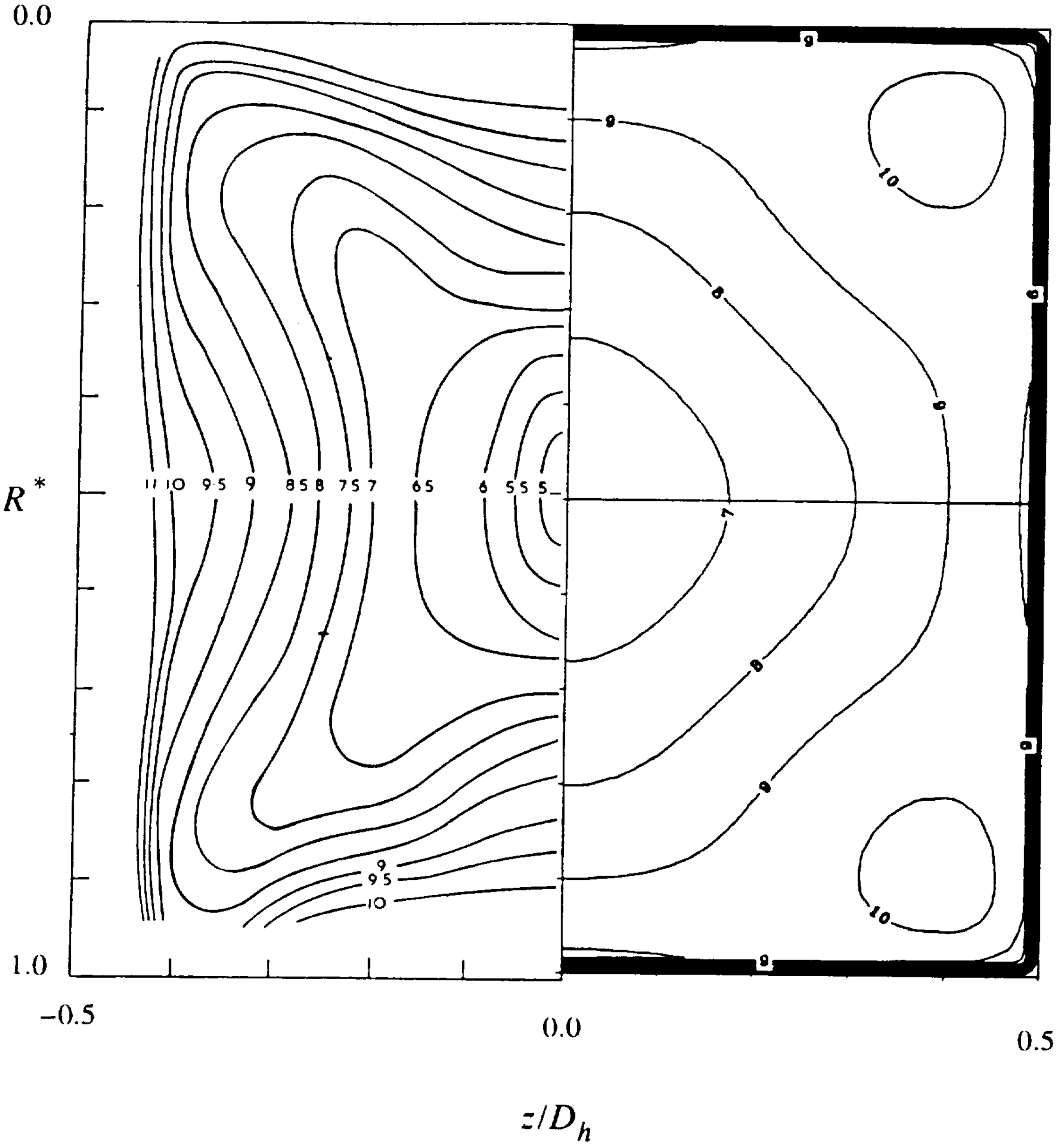

Figure 5.5. Contours of $\tilde{u}/U_b \times 10^2$ for turbulent bend flow, $x/D_h = -2.5$. Comparison of predictions using VDM with data of Humphrey [1977].

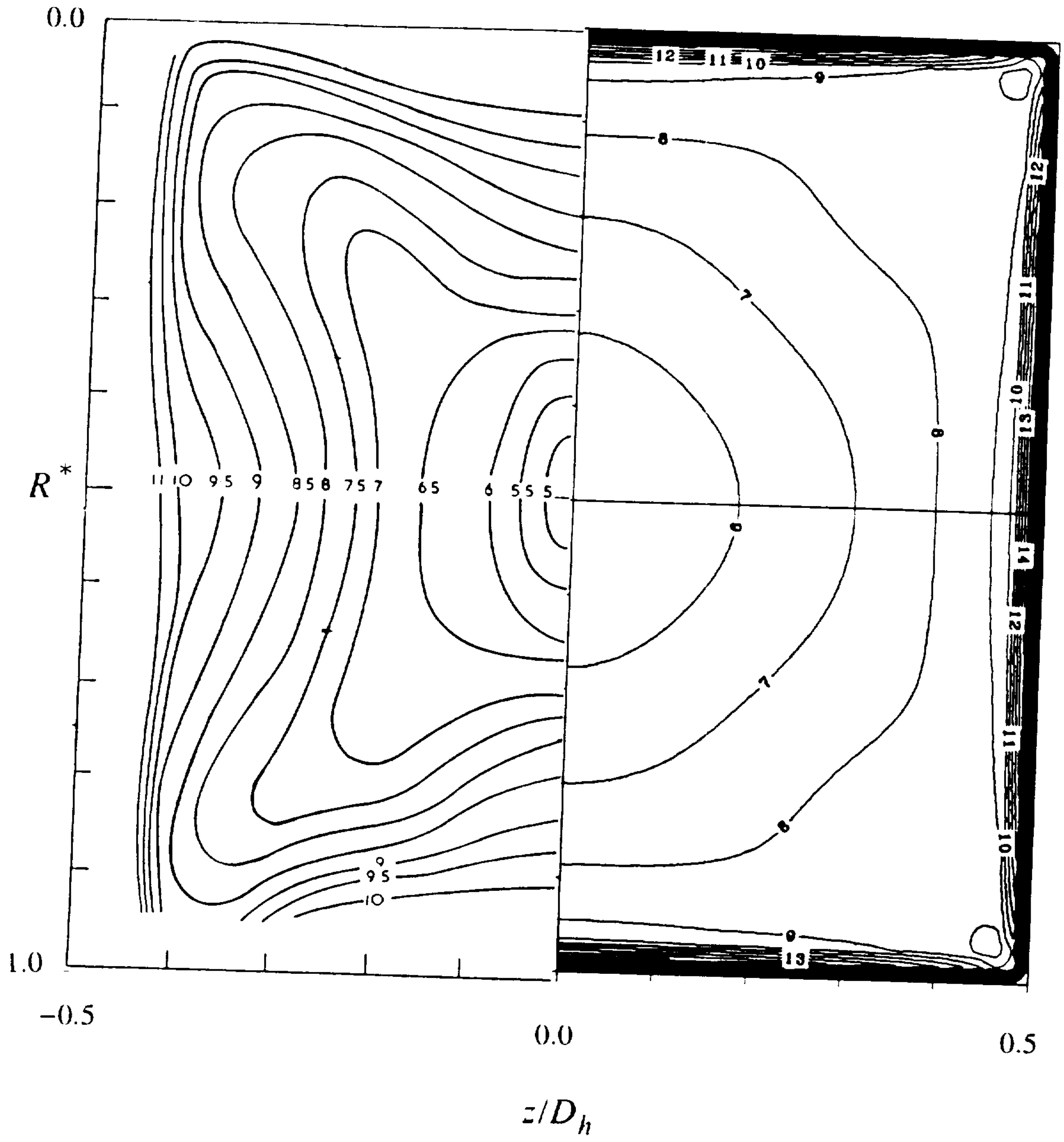

Figure 5.6. Contours of $\tilde{u}/U_b \times 10^2$ for turbulent bend flow, $x/D_h = -2.5$. Comparison of predictions using WFM with data of Humphrey [1977].

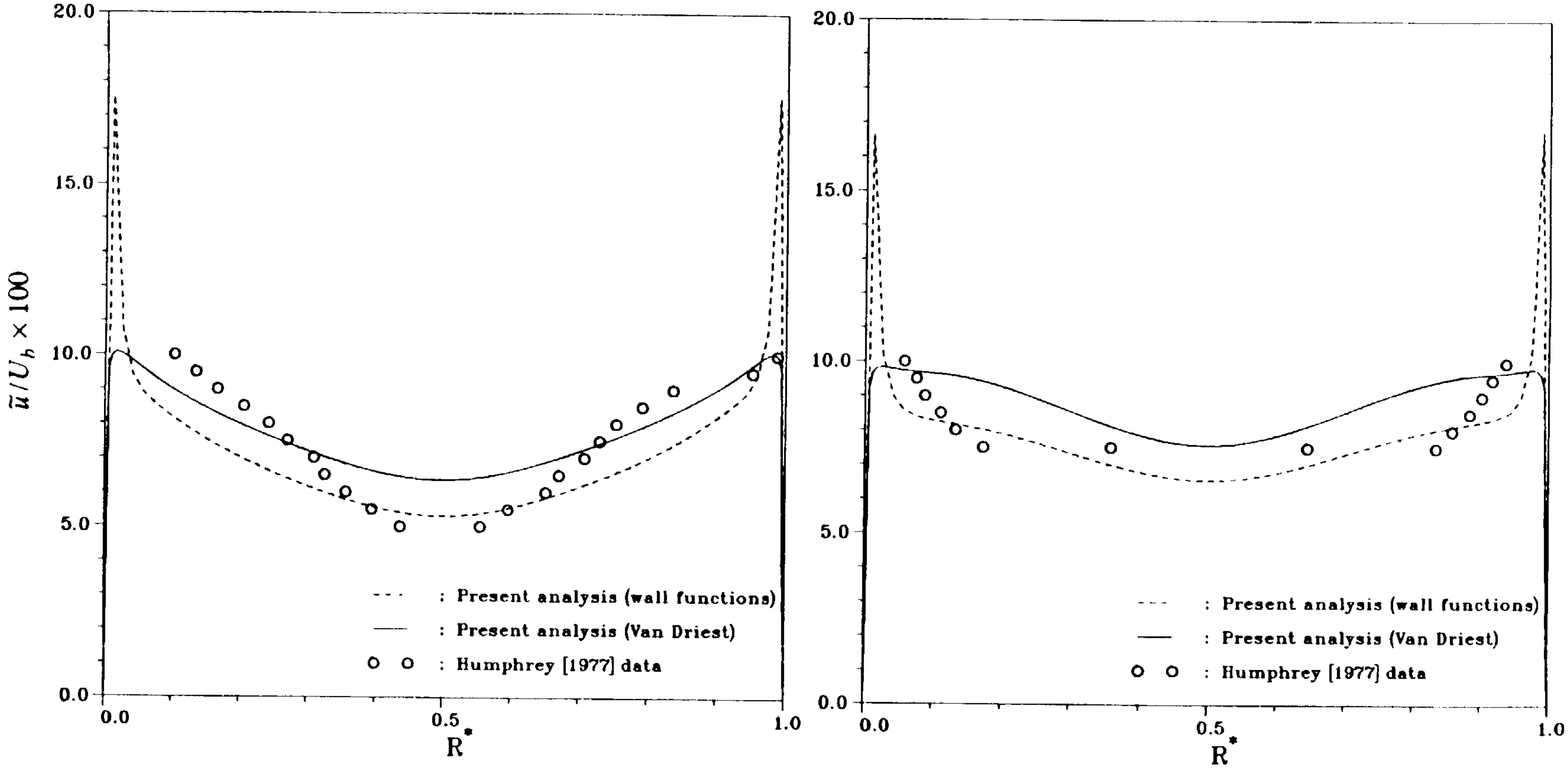

(a)

(b)

Figure 5.7. Radial profiles of $\tilde{u}/U_b{\times}10^2$ for turbulent bend flow, $x/D_h = -2.5$. (a) $z/D_h = 0.5$. (b) $z/D_h = 0.25$. Comparison of predictions with data of Humphrey [1977].

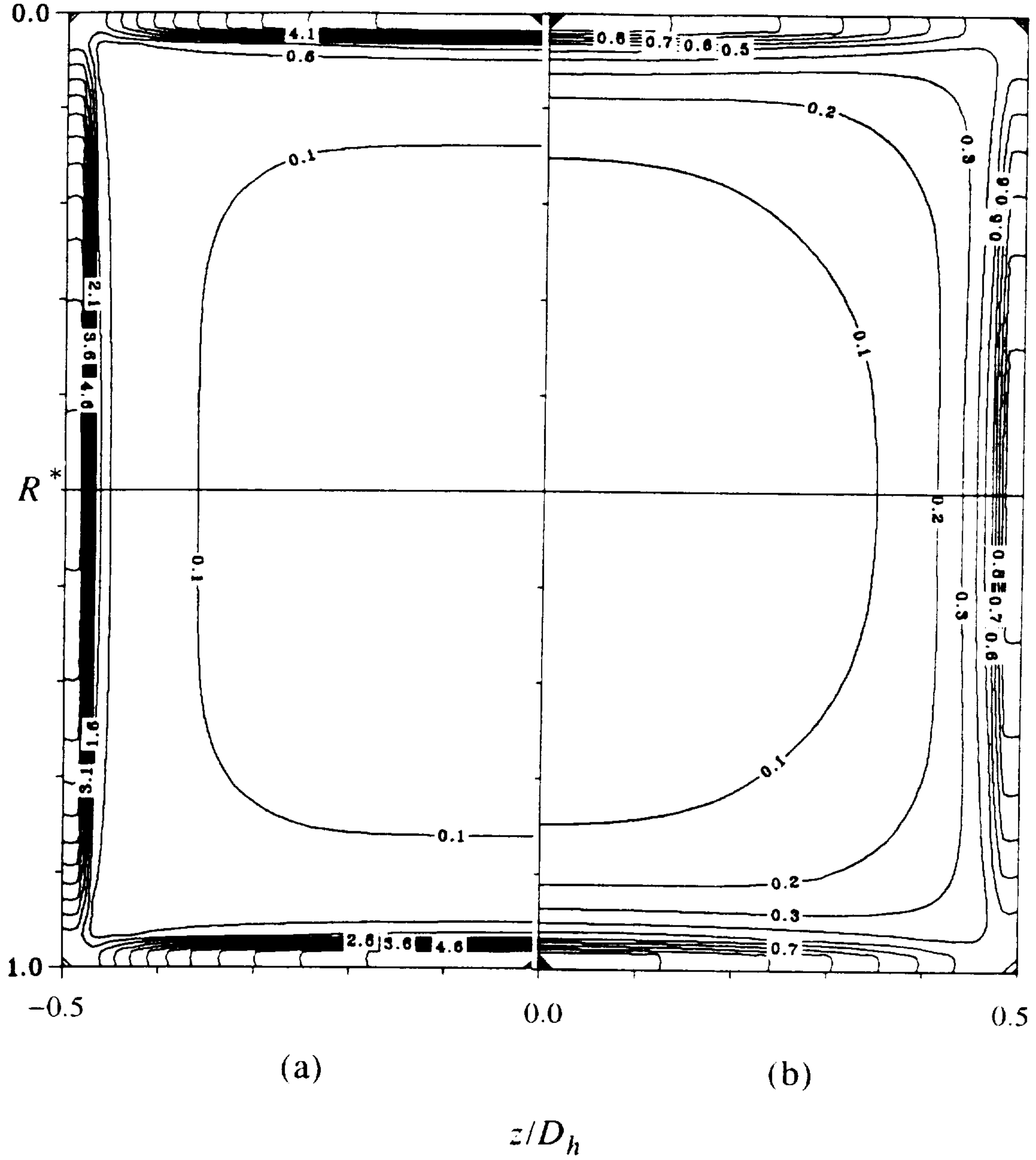

Figure 5.8. Contours of turbulent dissipation, $\varepsilon\nu/U_b^4\times10^6$ for turbulent bend flow, $x/D_h = -2.5$. Comparison of predictions using (a) WFM and (b) VDM.

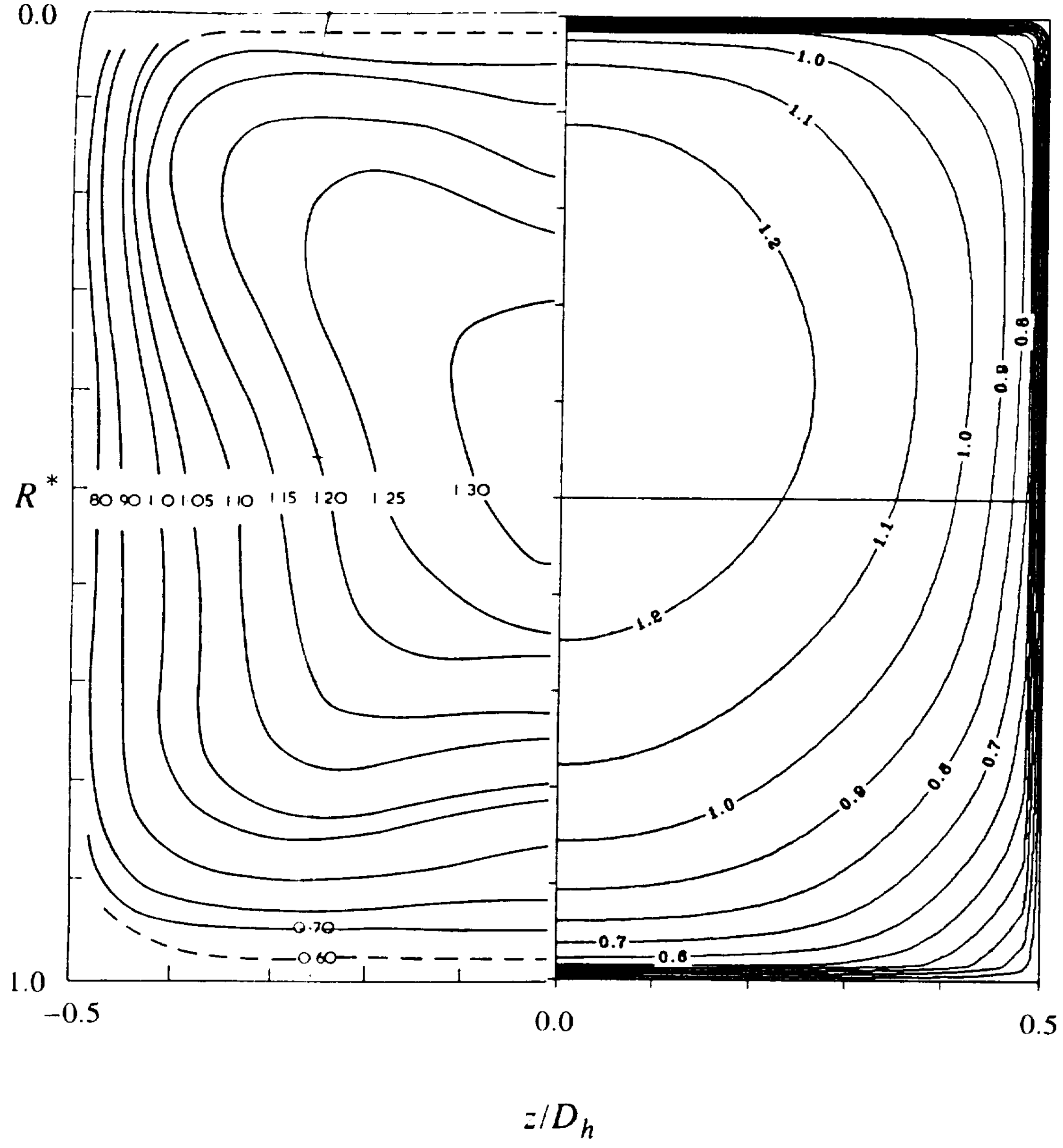

Figure 5.9. Contours of U_θ/U_b for turbulent bend flow, $\theta = 0°$. Comparison of predictions using VDM with data of Humphrey [1977].

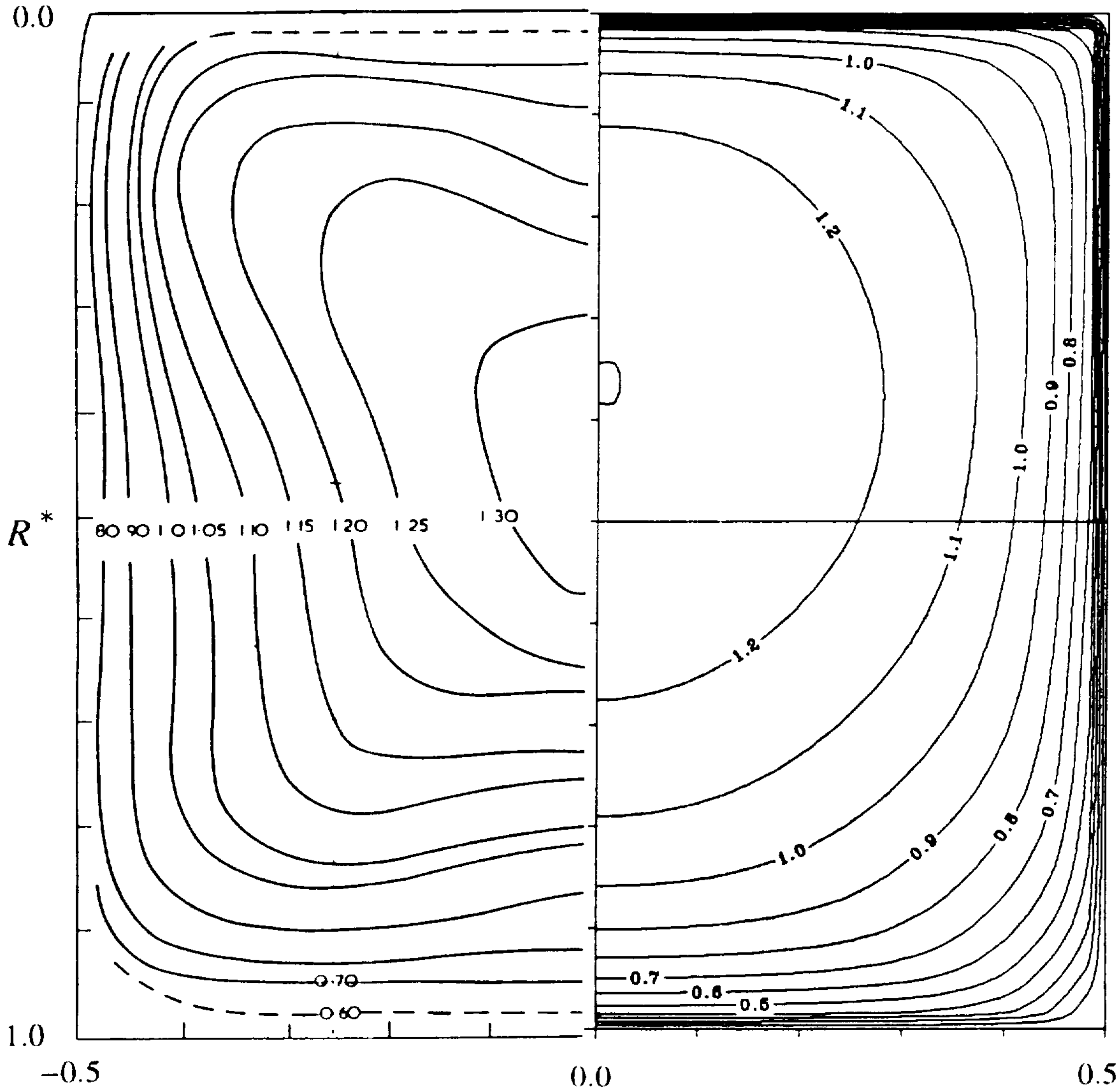

Figure 5.10. Contours of U_θ / U_b for turbulent bend flow, $\theta = 0°$. Comparison of predictions using WFM with data of Humphrey [1977].

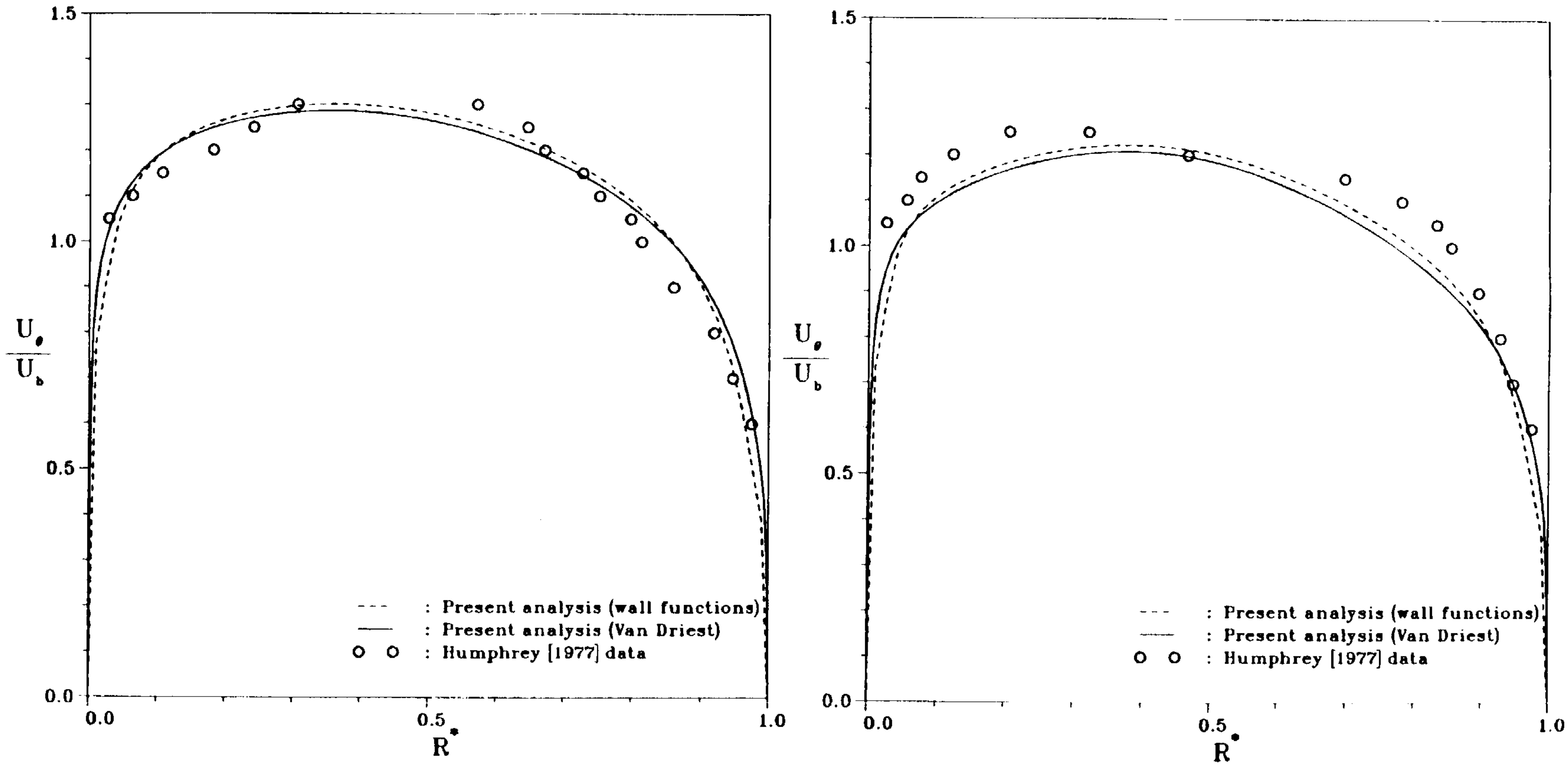

(a)

(b)

Figure 5.11. Radial profiles of U_θ/U_b for turbulent bend flow, $\theta = 0°$. (a) $z/D_h = 0.5$. (b) $z/D_h = 0.25$. Comparison of predictions with data of Humphrey [1977].

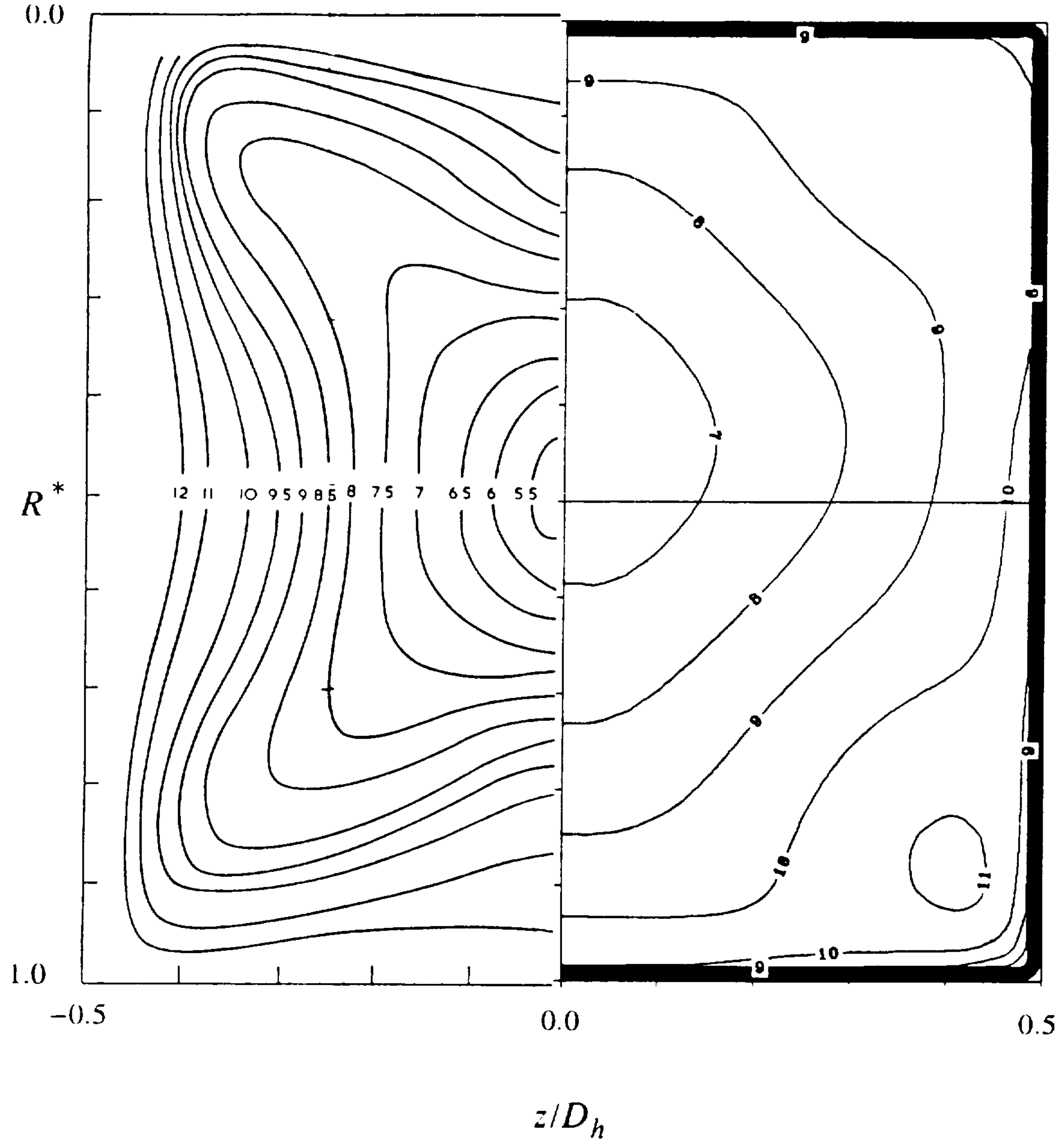

Figure 5.12. Contours of $\tilde{u}/U_b \times 10^2$ for turbulent bend flow, $\theta = 0°$. Comparison of predictions using VDM with data of Humphrey [1977].

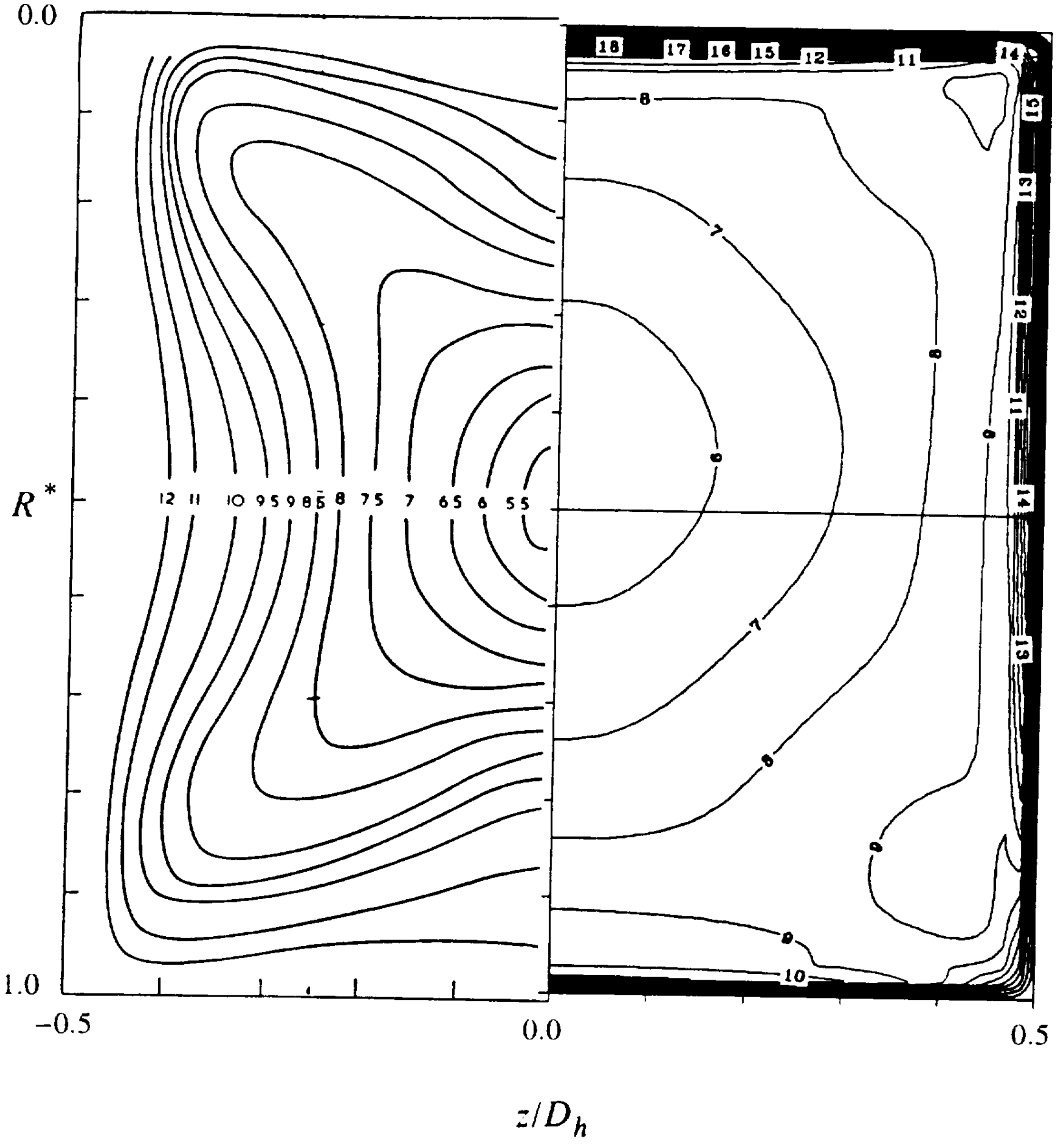

Figure 5.13. Contours of $\tilde{u}/U_b \times 10^2$ for turbulent bend flow, $\theta = 0°$. Comparison of predictions using WFM with data of Humphrey [1977].

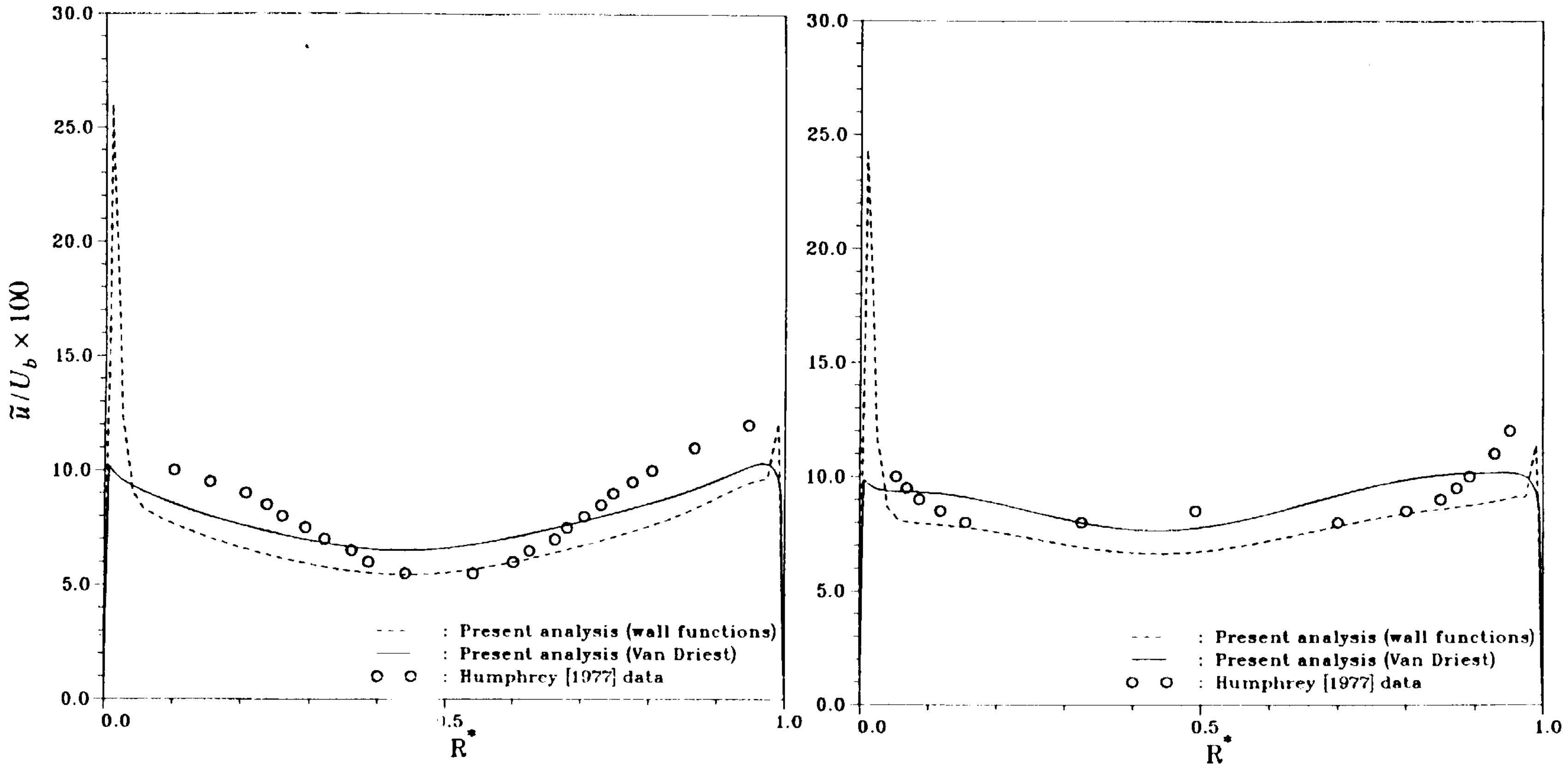

(a)

(b)

Figure 5.14. Radial profiles of $\tilde{u}/U_b{\times}10^2$ for turbulent bend flow, $\theta = 0°$. (a) $z/D_h = 0.5$. (b) $z/D_h = 0.25$. Comparison of predictions with data of Humphrey [1977].

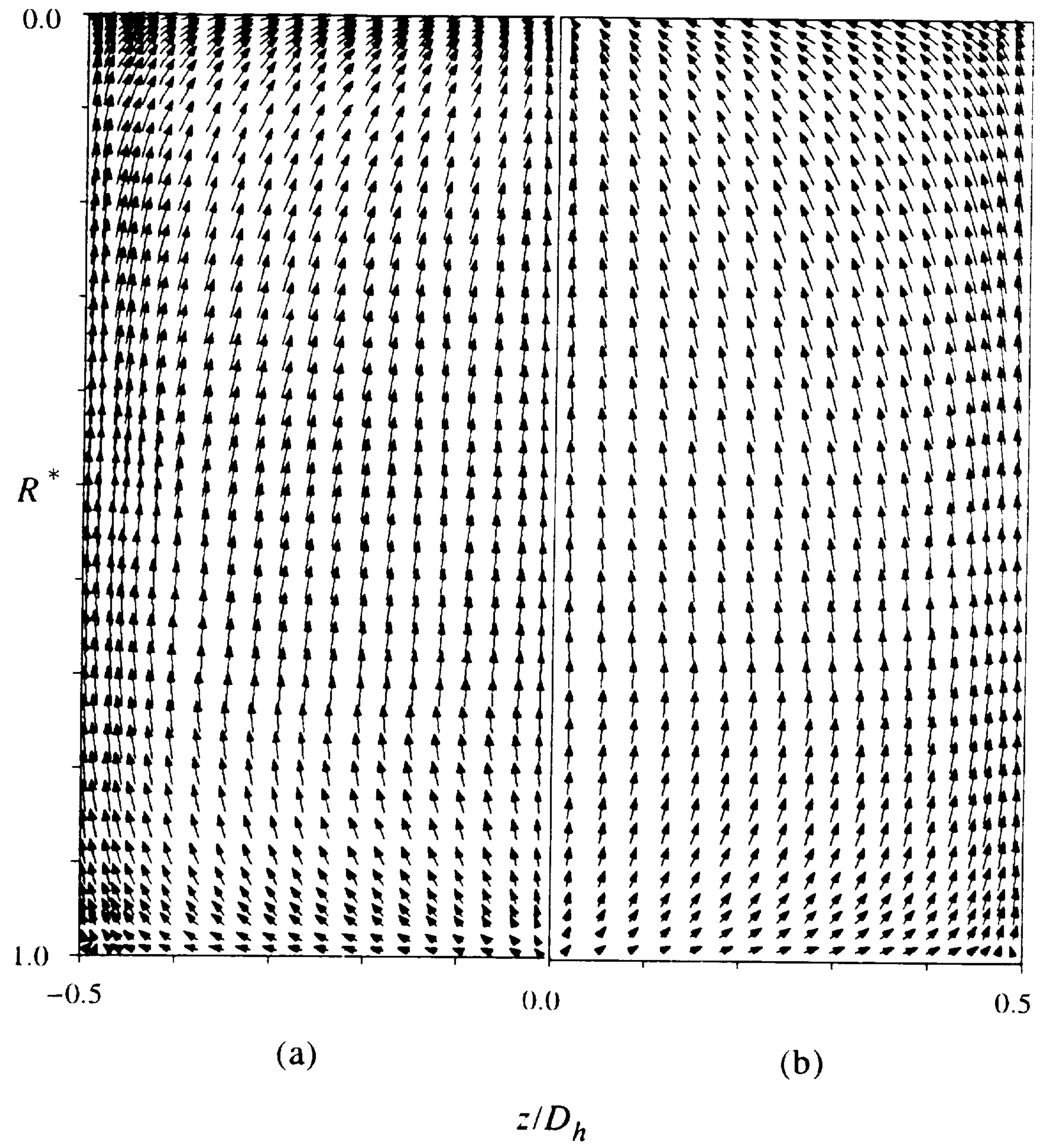

Figure 5.15. Cross-stream velocity vector plot for turbulent bend flow, $\theta = 0°$. Comparison of predictions using (a) VDM and (b) WFM.

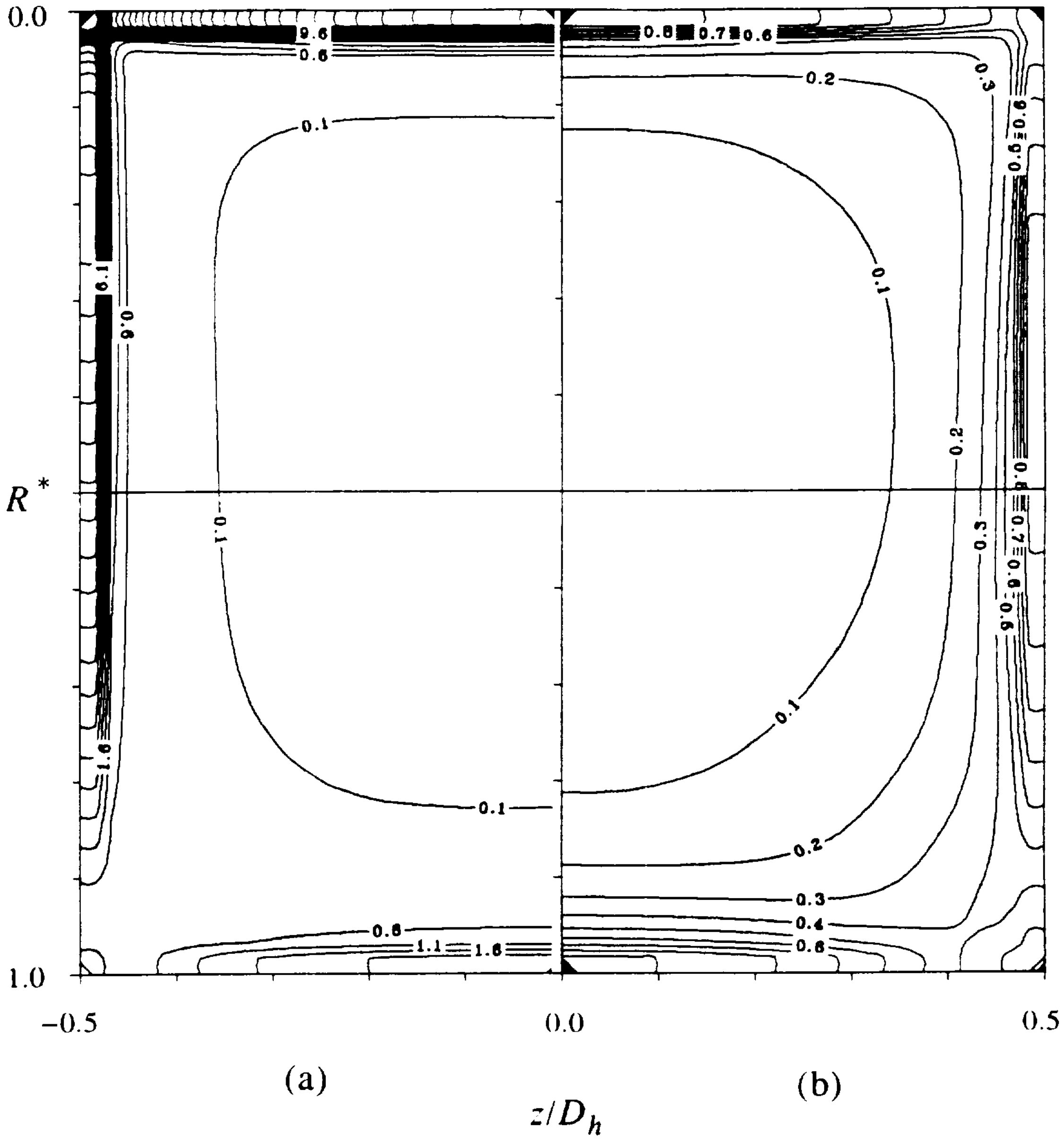

Figure 5.16. Contours of turbulent dissipation, $\epsilon\nu/U_b^4\times10^6$ for turbulent bend flow, θ = 0°. Comparison of predictions using (a) WFM and (b) VDM.

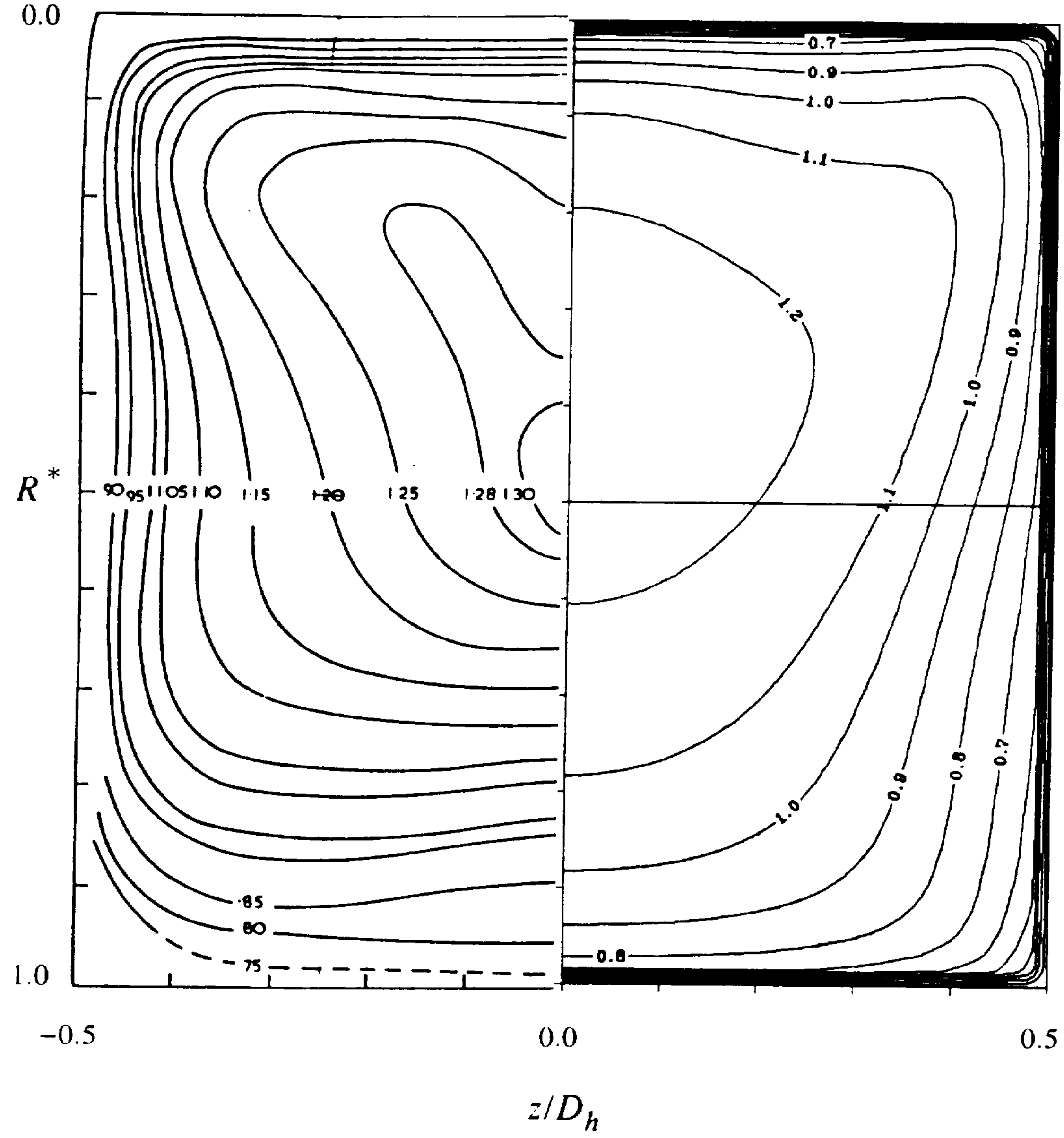

Figure 5.17. Contours of U_θ/U_b for turbulent bend flow, θ = 45°. Comparison of predictions using VDM with data of Humphrey [1977].

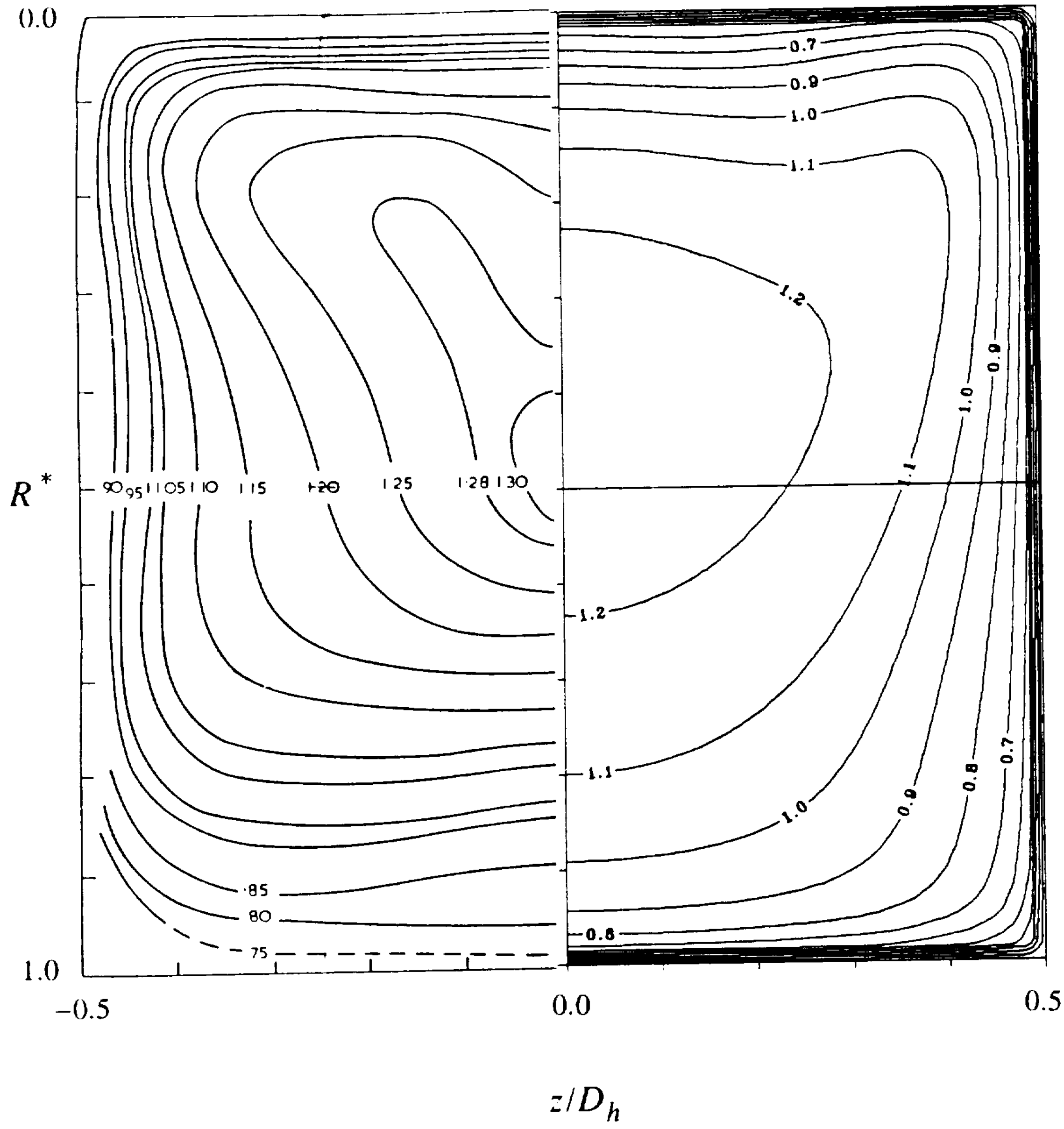

Figure 5.18. Contours of U_θ/U_b for turbulent bend flow, $\theta = 45°$. Comparison of predictions using WFM with data of Humphrey [1977].

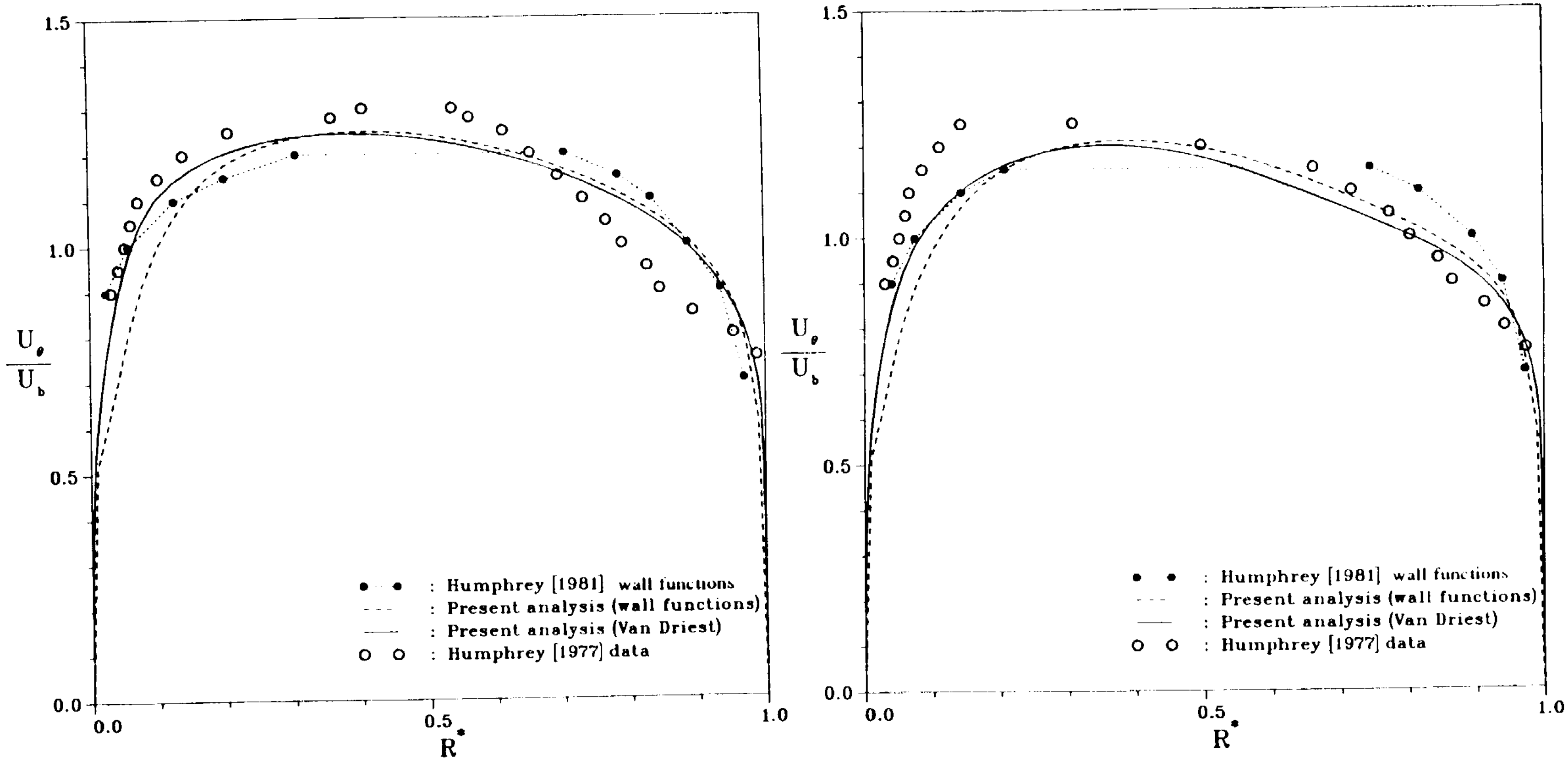

(a)

(b)

Figure 5.19. Radial profiles of U_θ/U_b for turbulent bend flow, $\theta = 45°$. (a) $z/D_h = 0.5$. (b) $z/D_h = 0.25$. Comparison of predictions with data of Humphrey [1977] and predictions of Humphrey et al. [1981].

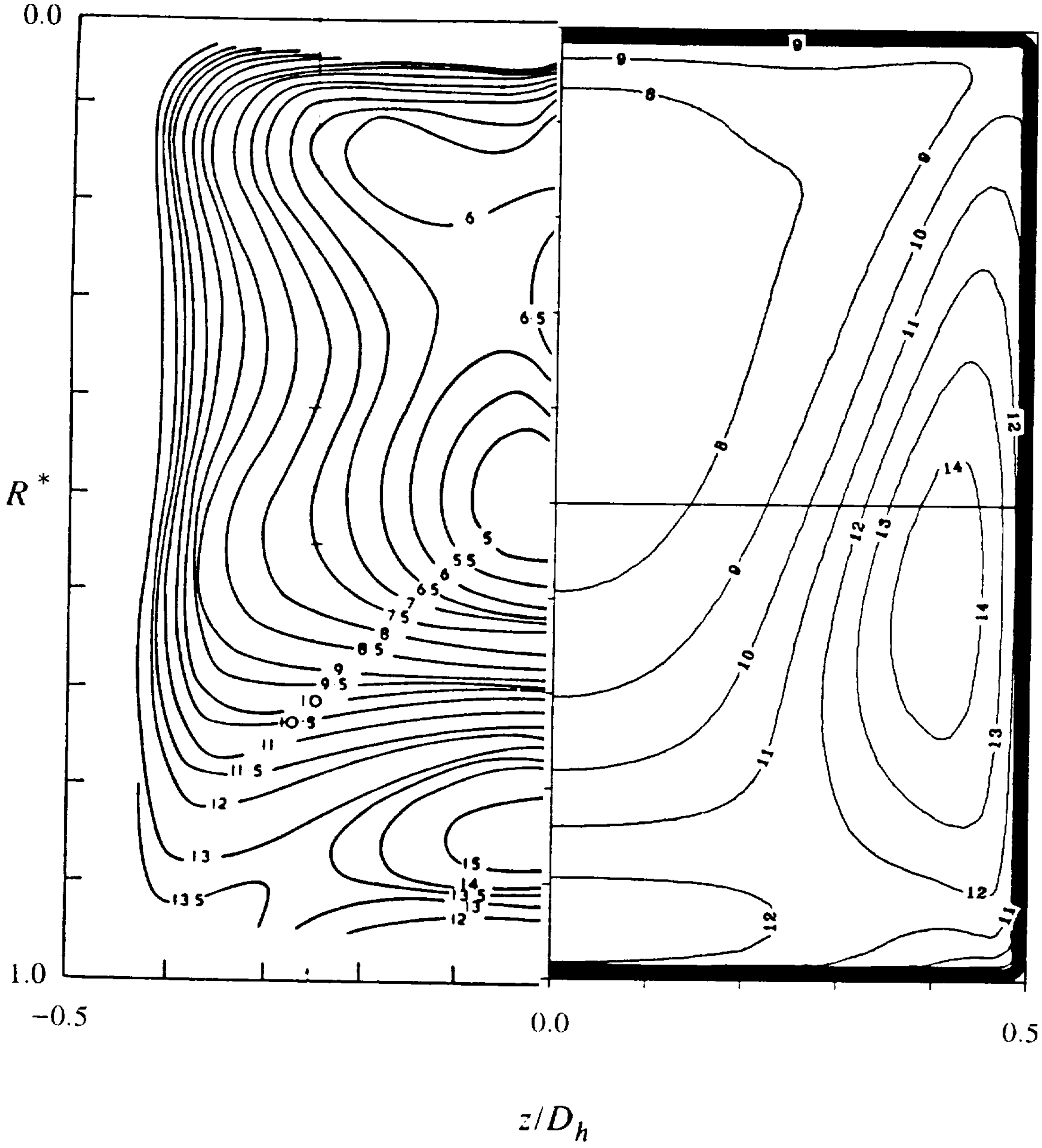

Figure 5.20. Contours of $\tilde{u}/U_b \times 10^2$ for turbulent bend flow, θ = 45°. Comparison of predictions using VDM with data of Humphrey [1977].

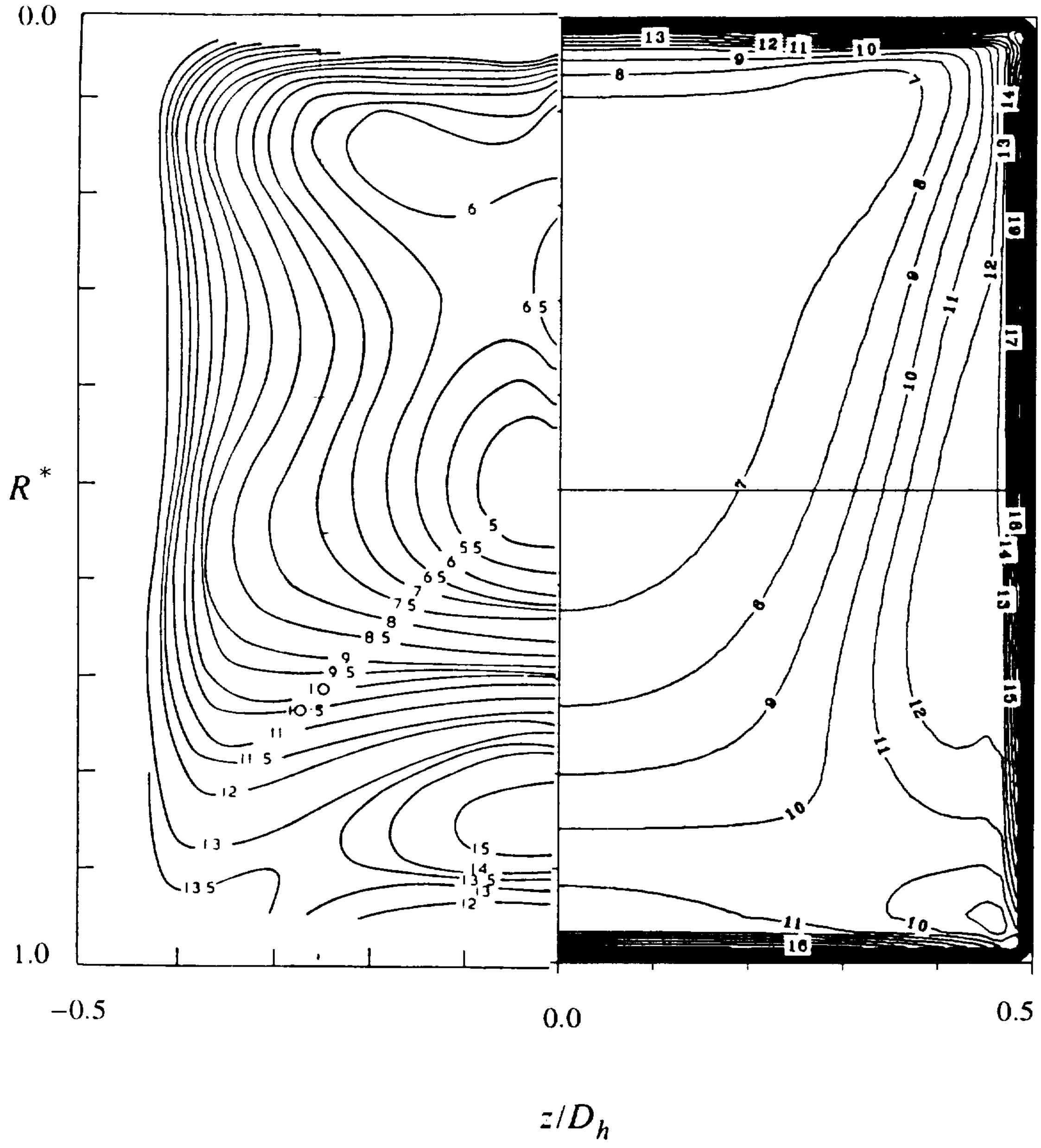

Figure 5.21. Contours of $\tilde{u}/U_b \times 10^2$ for turbulent bend flow, $\theta = 45°$. Comparison of predictions using WFM with data of Humphrey [1977].

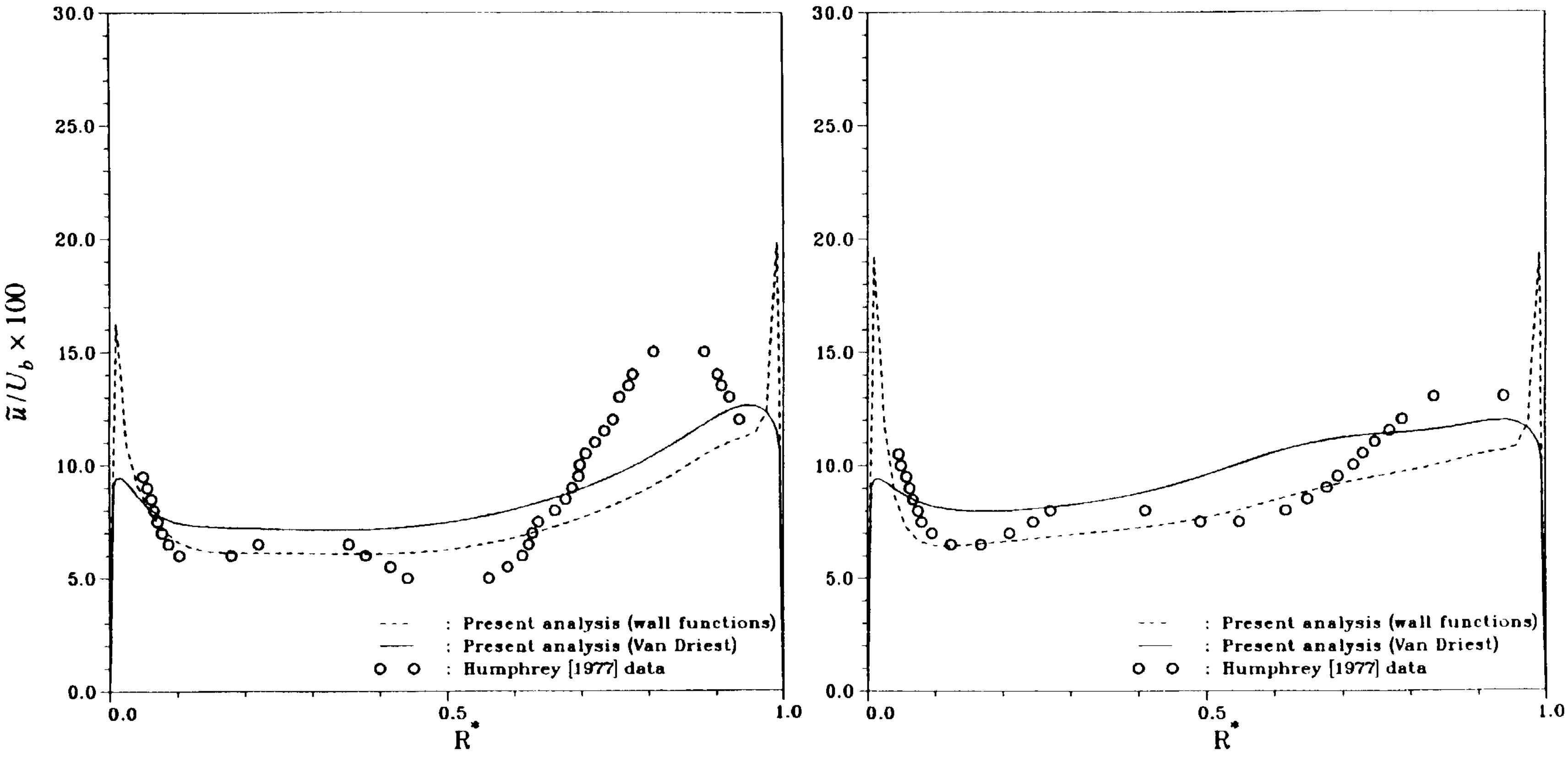

(a)

(b)

Figure 5.22. Radial profiles of $\tilde{u}/U_b \times 10^2$ for turbulent bend flow, $\theta = 45°$. (a) $z/D_h = 0.5$. (b) $z/D_h = 0.25$. Comparison of predictions with data of Humphrey [1977].

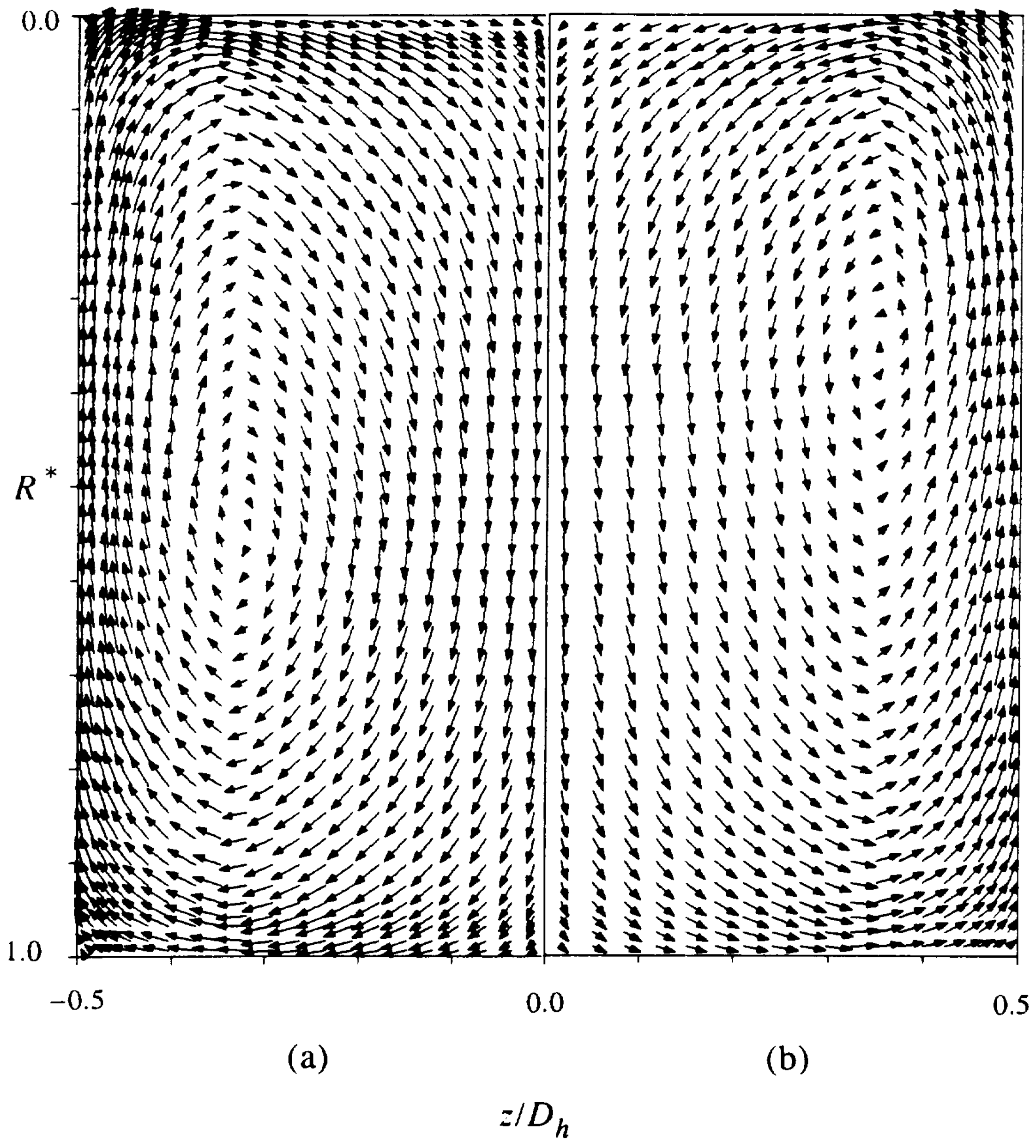

Figure 5.23. Cross-stream velocity vector plot for turbulent bend flow, $\theta = 45°$. Comparison of predictions using (a) VDM and (b) WFM.

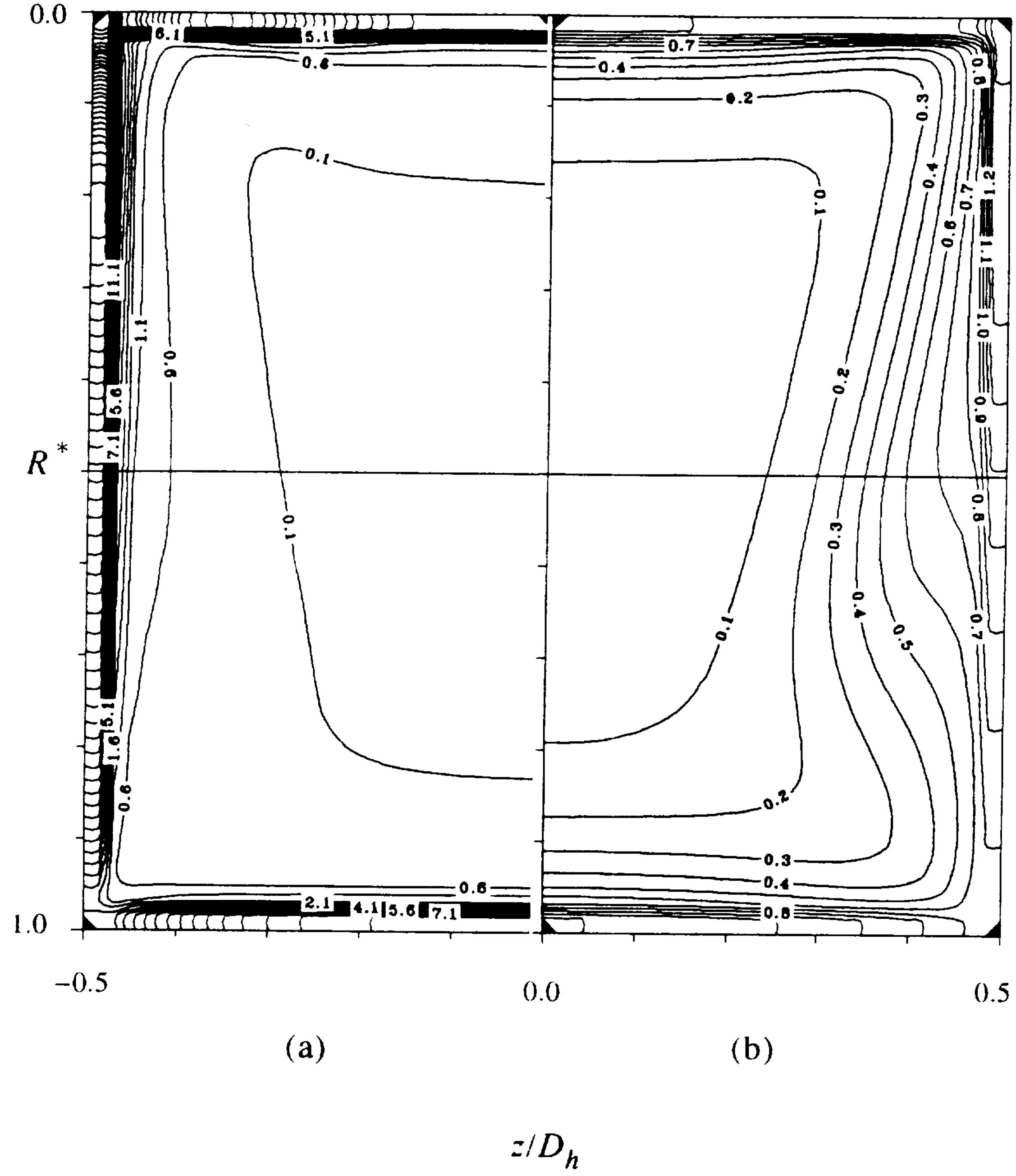

Figure 5.24. Contours of turbulent dissipation, $\varepsilon\nu/U_b^4\times10^6$ for turbulent bend flow, θ = 45°. Comparison of predictions using (a) WFM and (b) VDM.

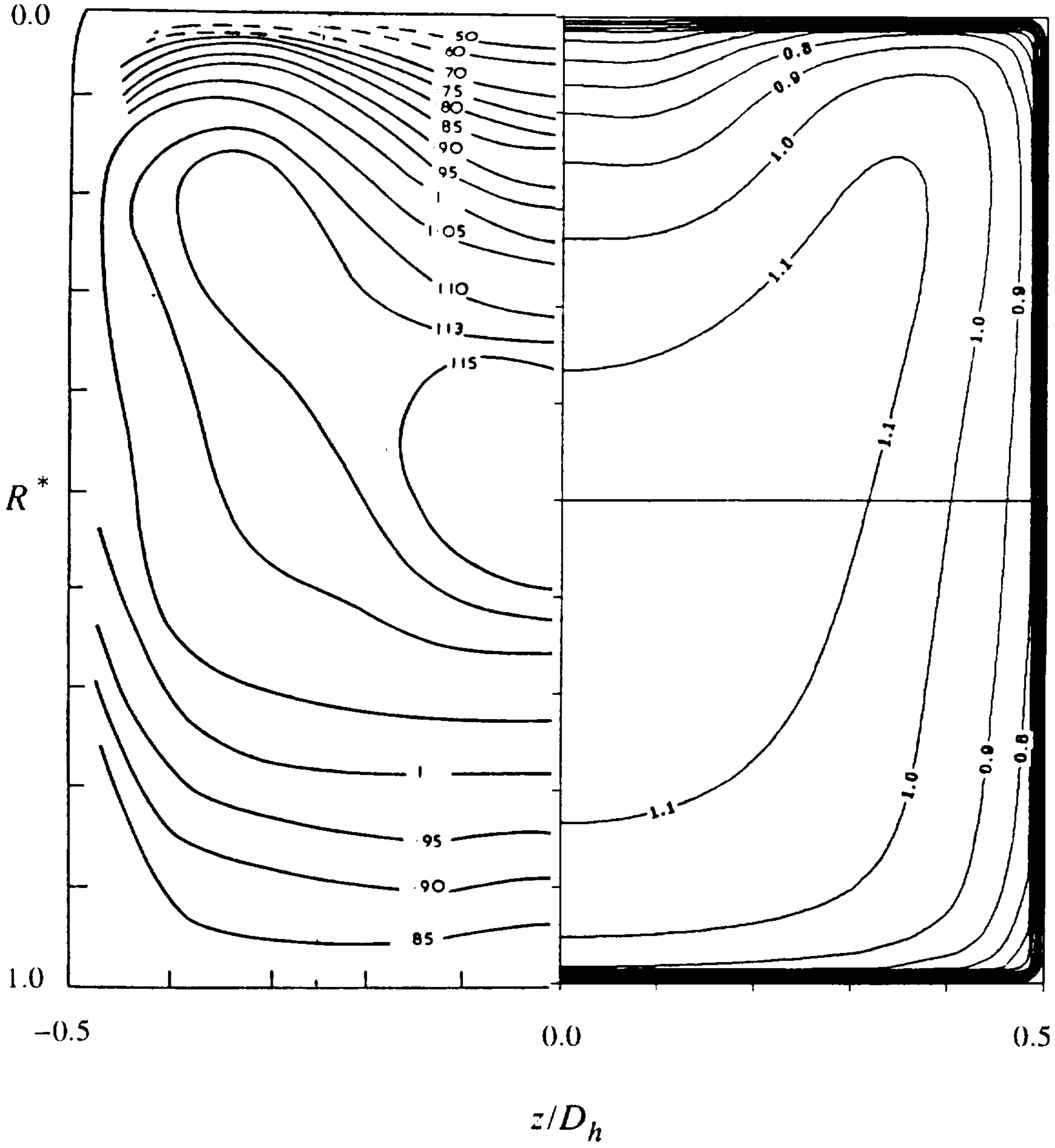

Figure 5.25. Contours of U_θ/U_b for turbulent bend flow, $\theta = 71°$. Comparison of predictions using VDM with data of Humphrey [1977].

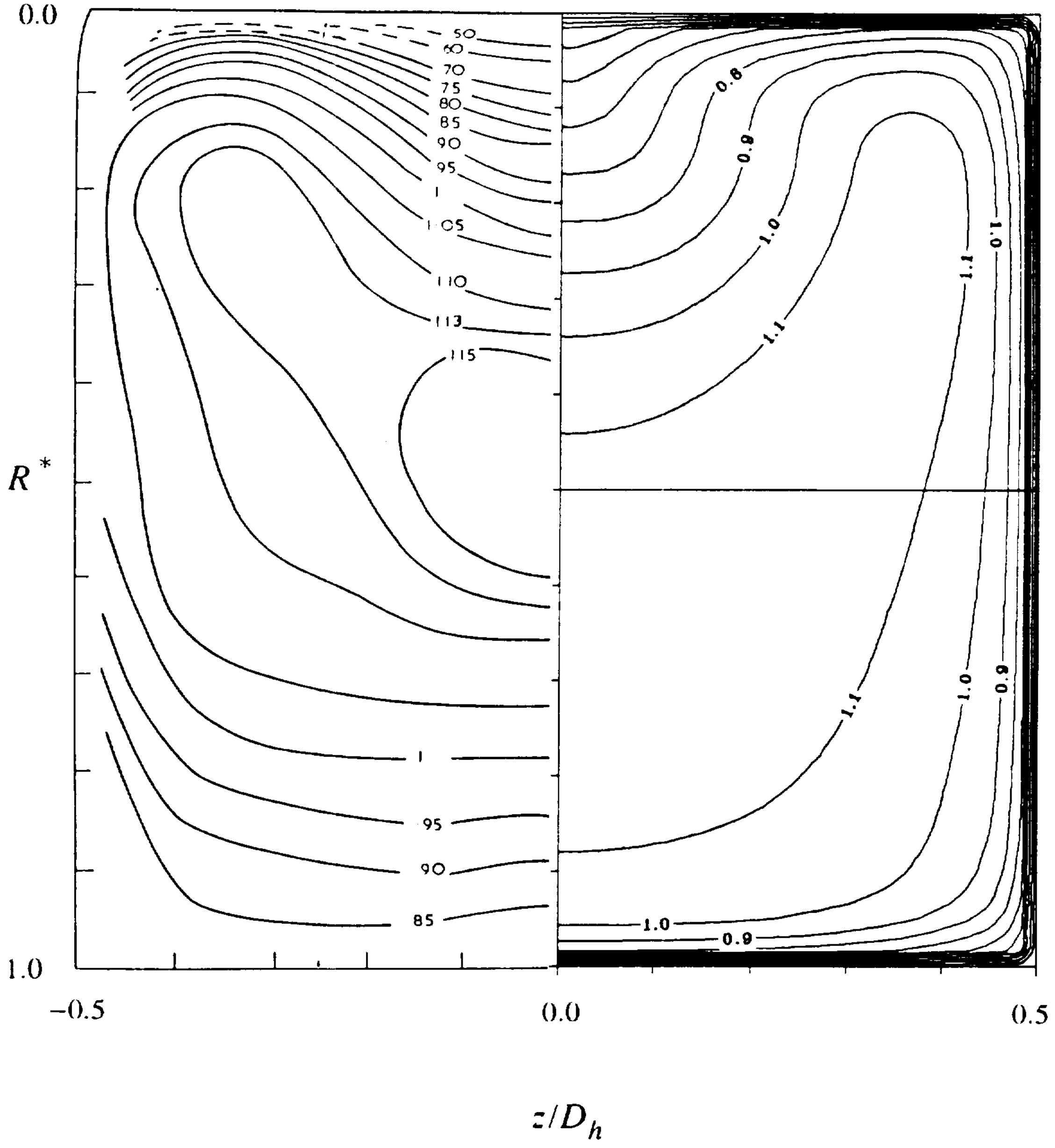

Figure 5.26. Contours of U_θ/U_b for turbulent bend flow, $\theta = 71°$. Comparison of predictions using WFM with data of Humphrey [1977].

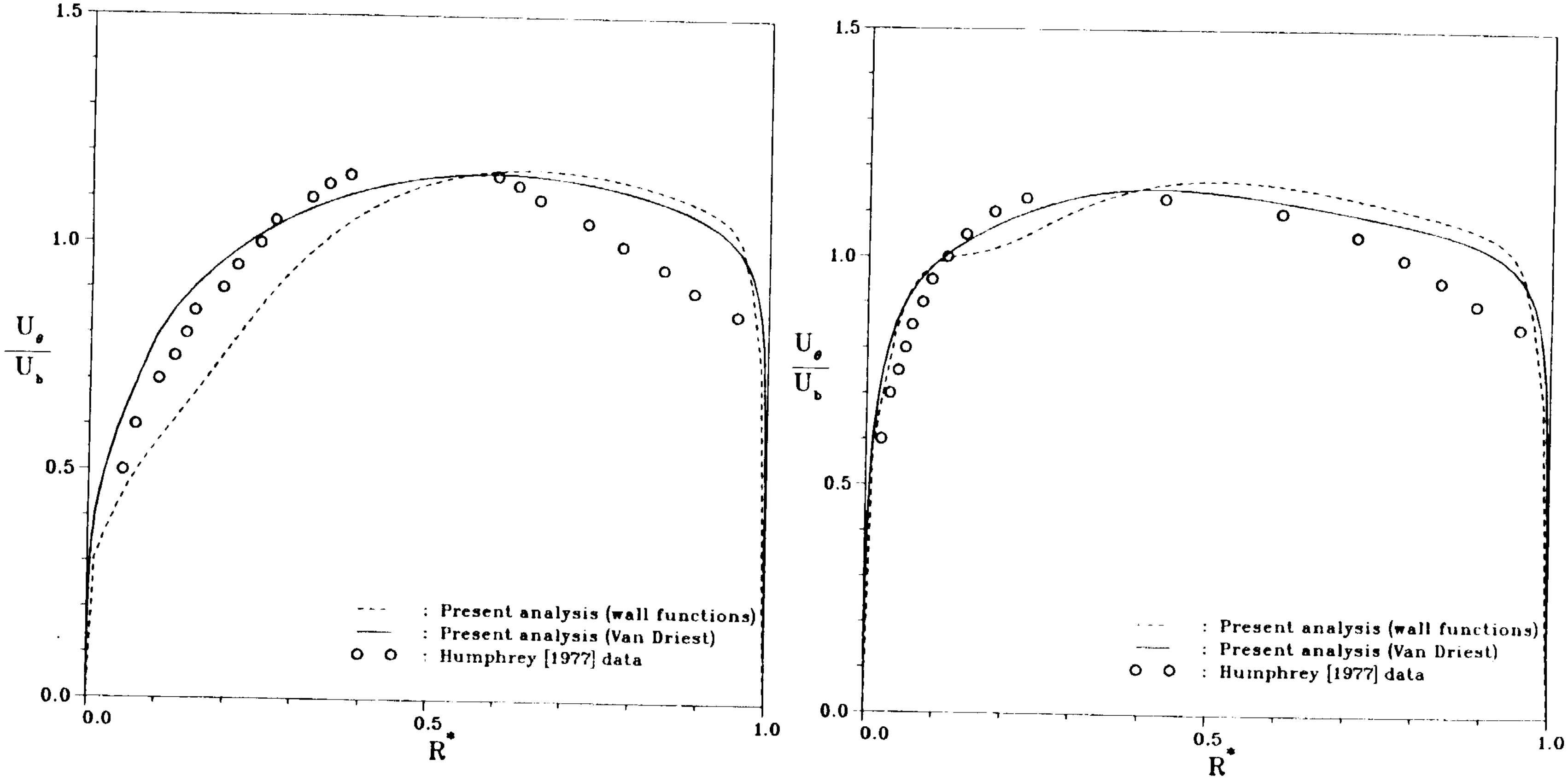

(a)

(b)

Figure 5.27. Radial profiles of U_θ/U_b for turbulent bend flow, $\theta = 71°$. (a) $z/D_h = 0.5$. (b) $z/D_h = 0.25$. Comparison of predictions with data of Humphrey [1977].

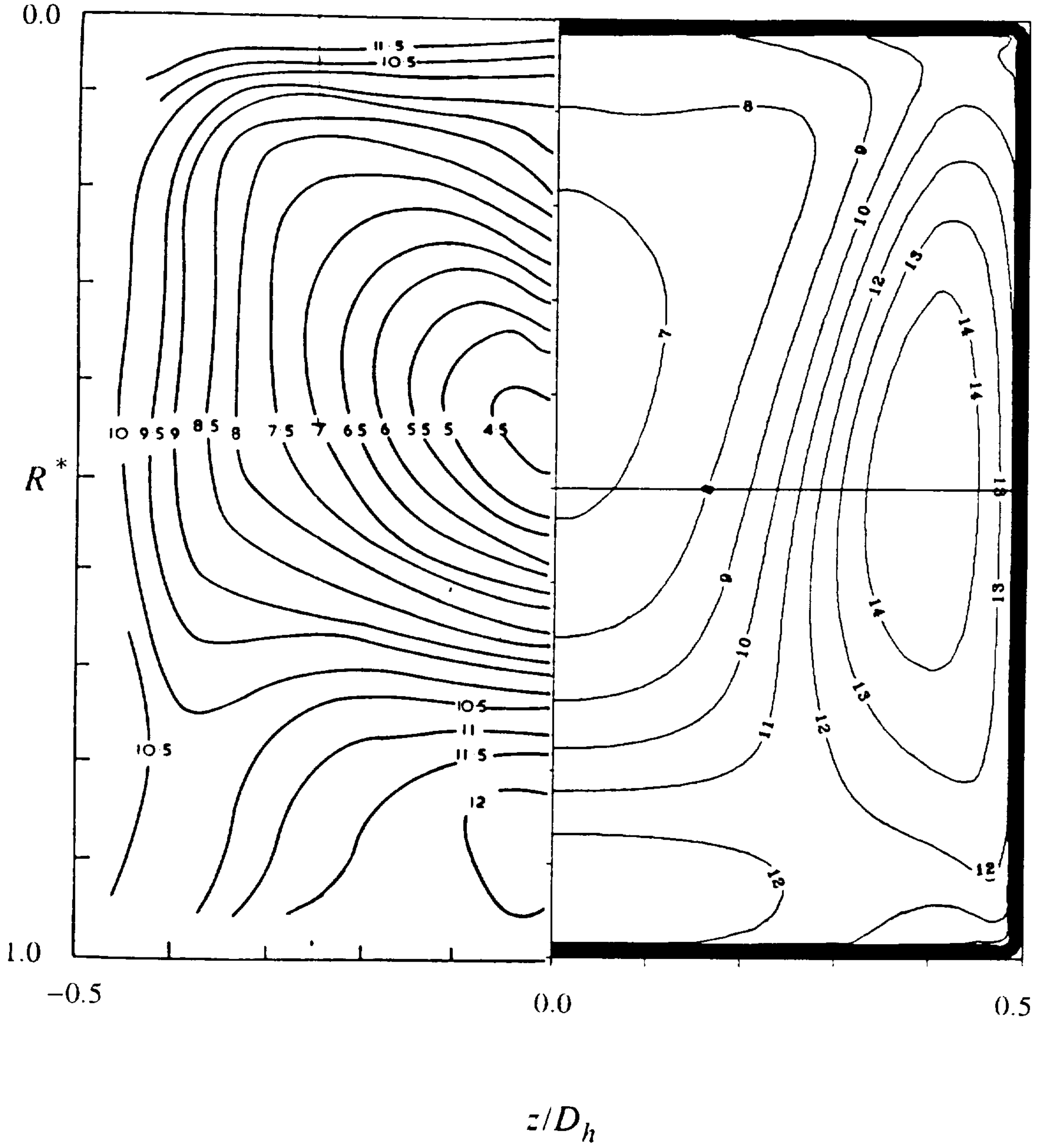

Figure 5.28. Contours of $\tilde{u}/U_b \times 10^2$ for turbulent bend flow, θ = 71°. Comparison of predictions using VDM with data of Humphrey [1977].

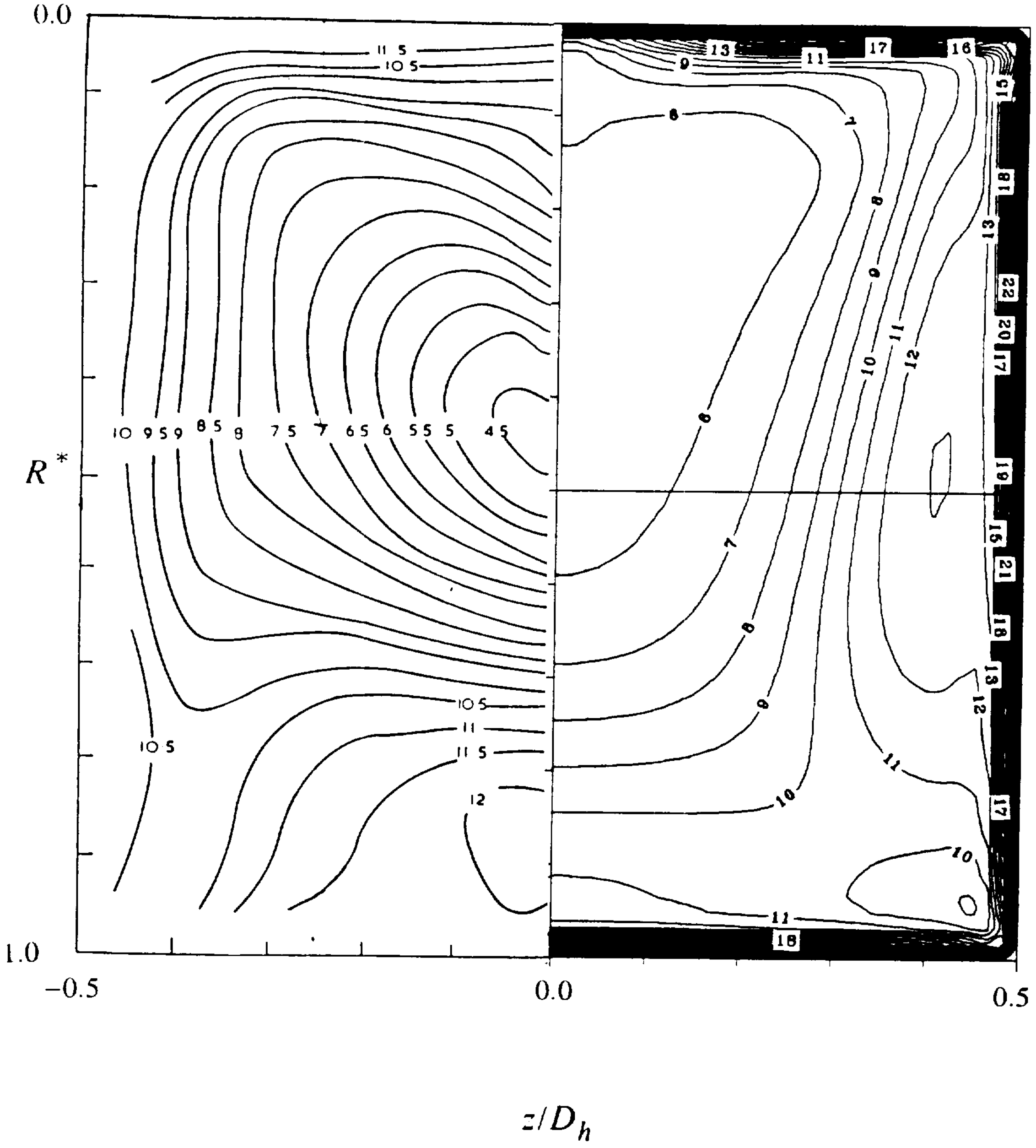

Figure 5.29. Contours of $\tilde{u}/U_b \times 10^2$ for turbulent bend flow, θ = 71°. Comparison of predictions using WFM with data of Humphrey [1977].

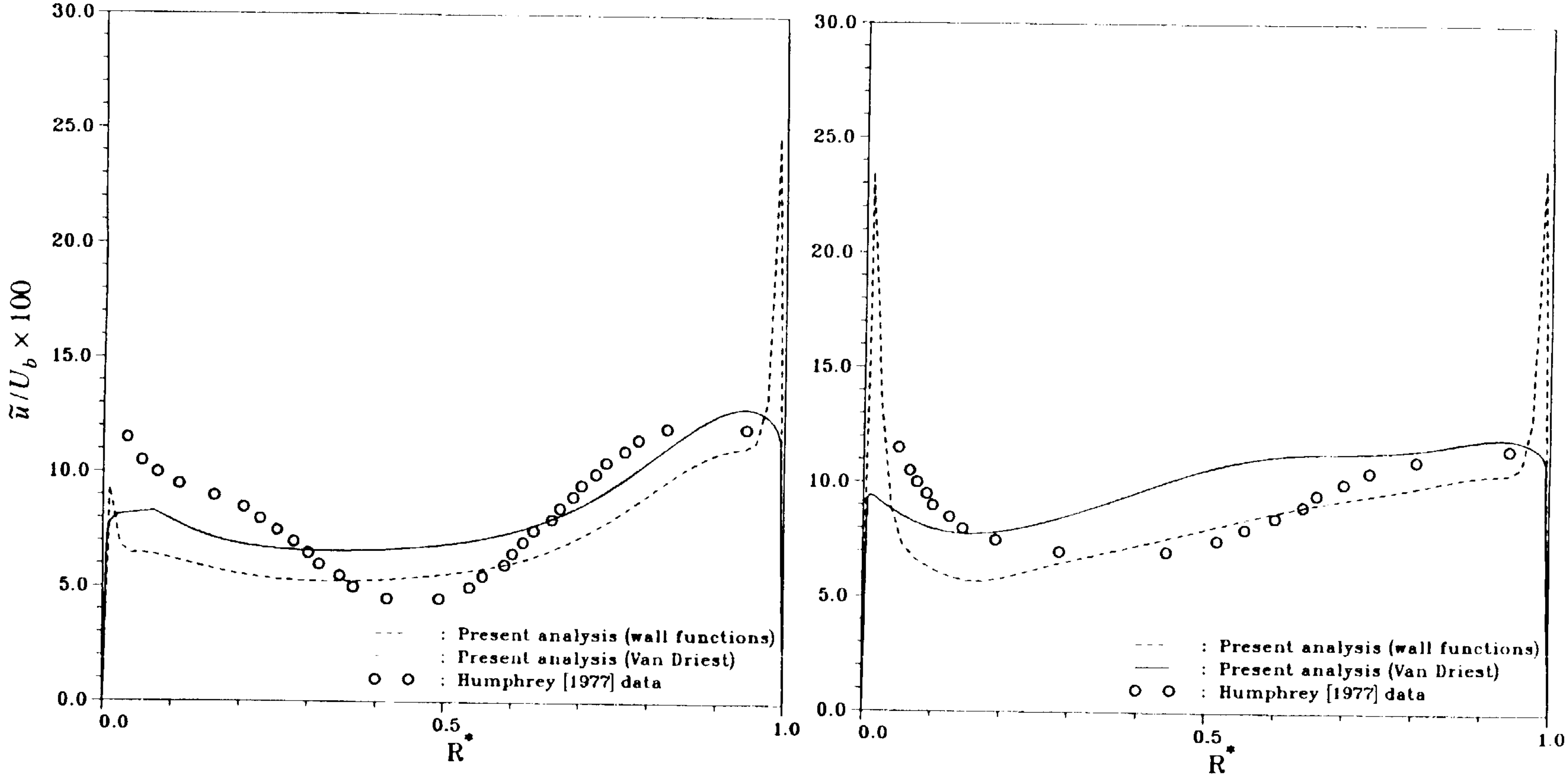

(a)

(b)

Figure 5.30. Radial profiles of $\tilde{u}/U_b \times 10^2$ for turbulent bend flow, $\theta = 71°$. (a) $z/D_h = 0.5$. (b) $z/D_h = 0.25$. Comparison of predictions with data of Humphrey [1977].

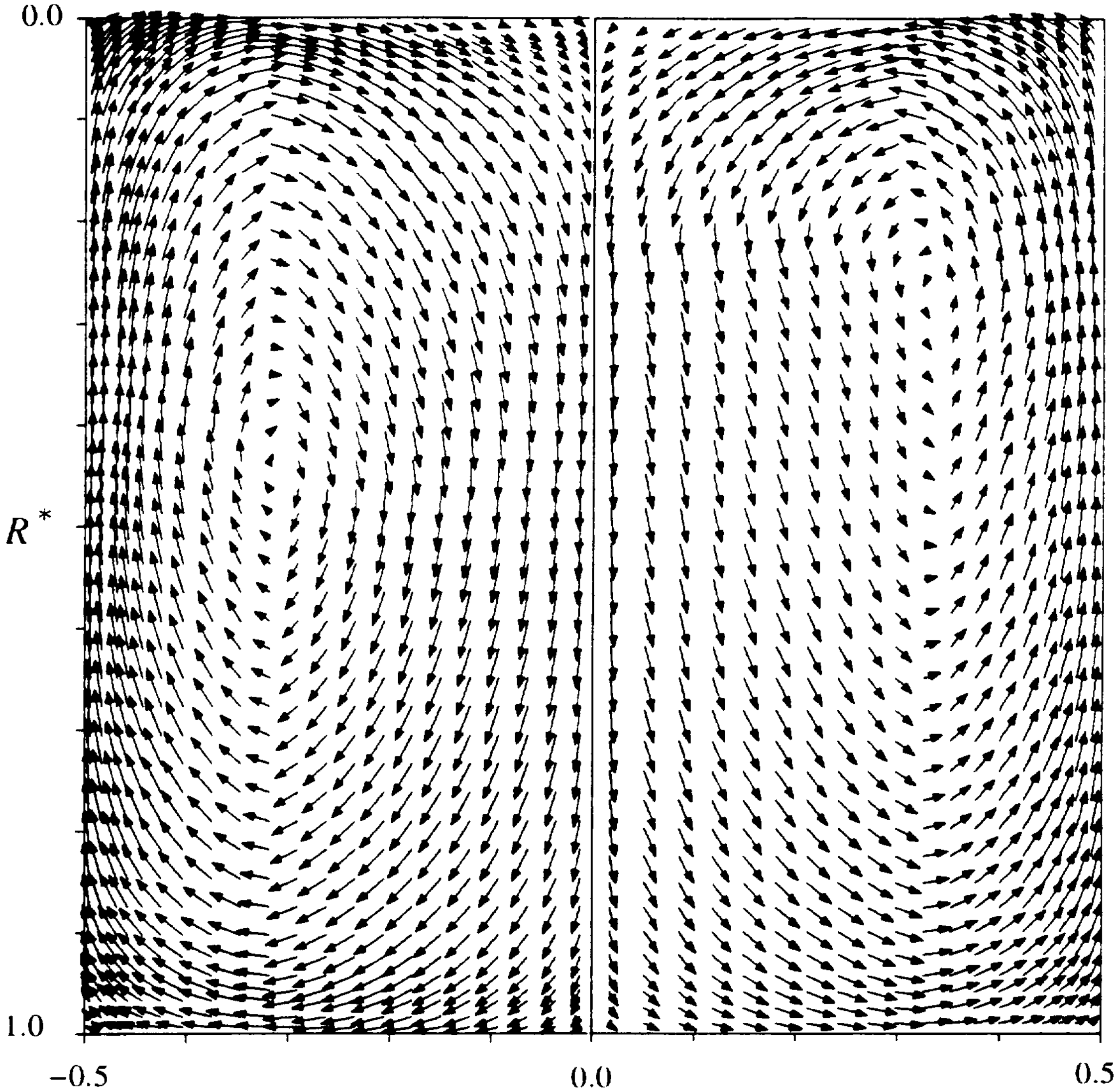

Figure 5.31. Cross-stream velocity vector plot for turbulent bend flow, $\theta = 71°$. Comparison of predictions using (a) VDM and (b) WFM.

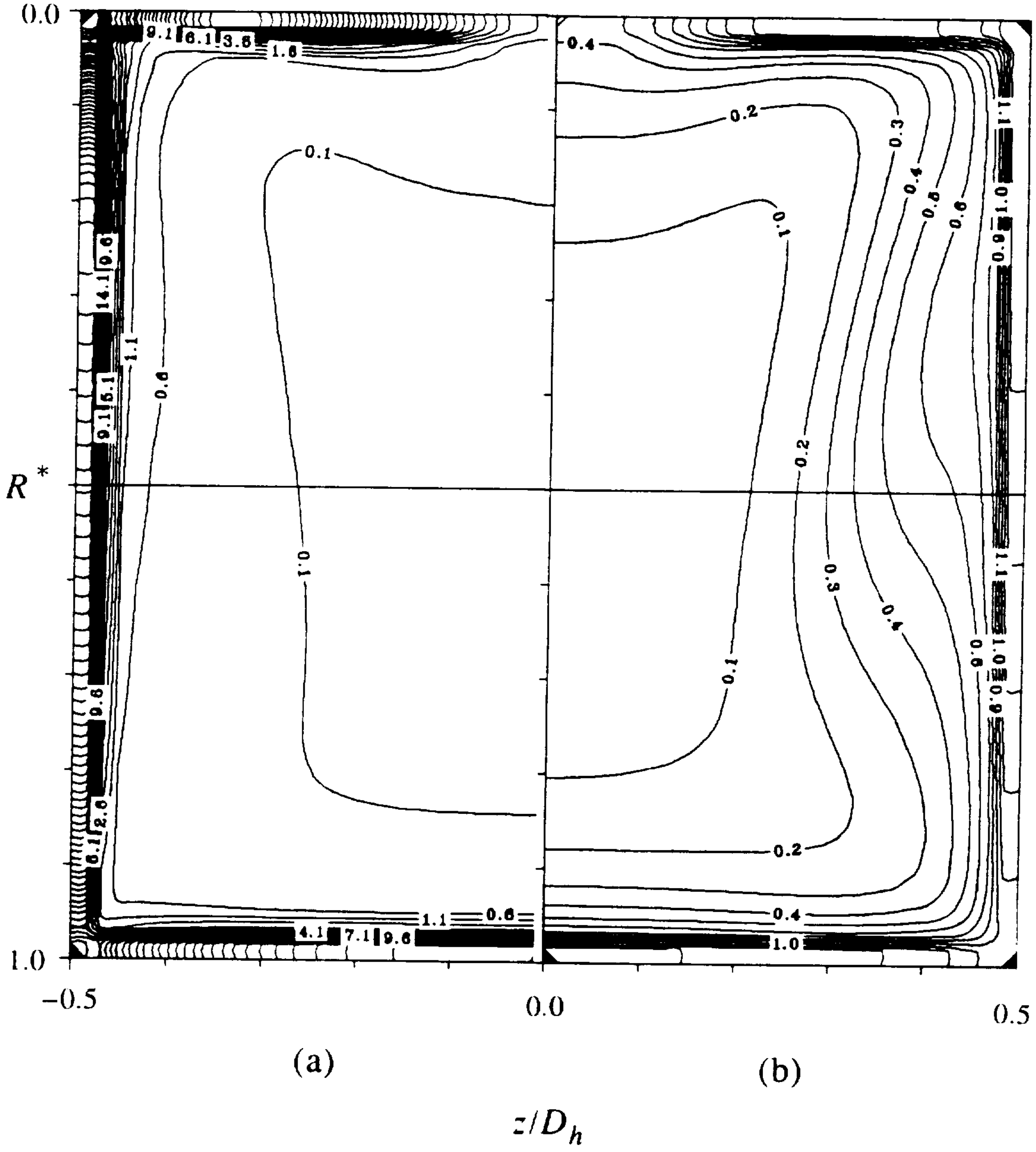

(a) (b)

Figure 5.32. Contours of turbulent dissipation, $\varepsilon\nu/U_b^4 \times 10^6$ for turbulent bend flow, $\theta = 71°$. Comparison of predictions using (a) WFM and (b) VDM.

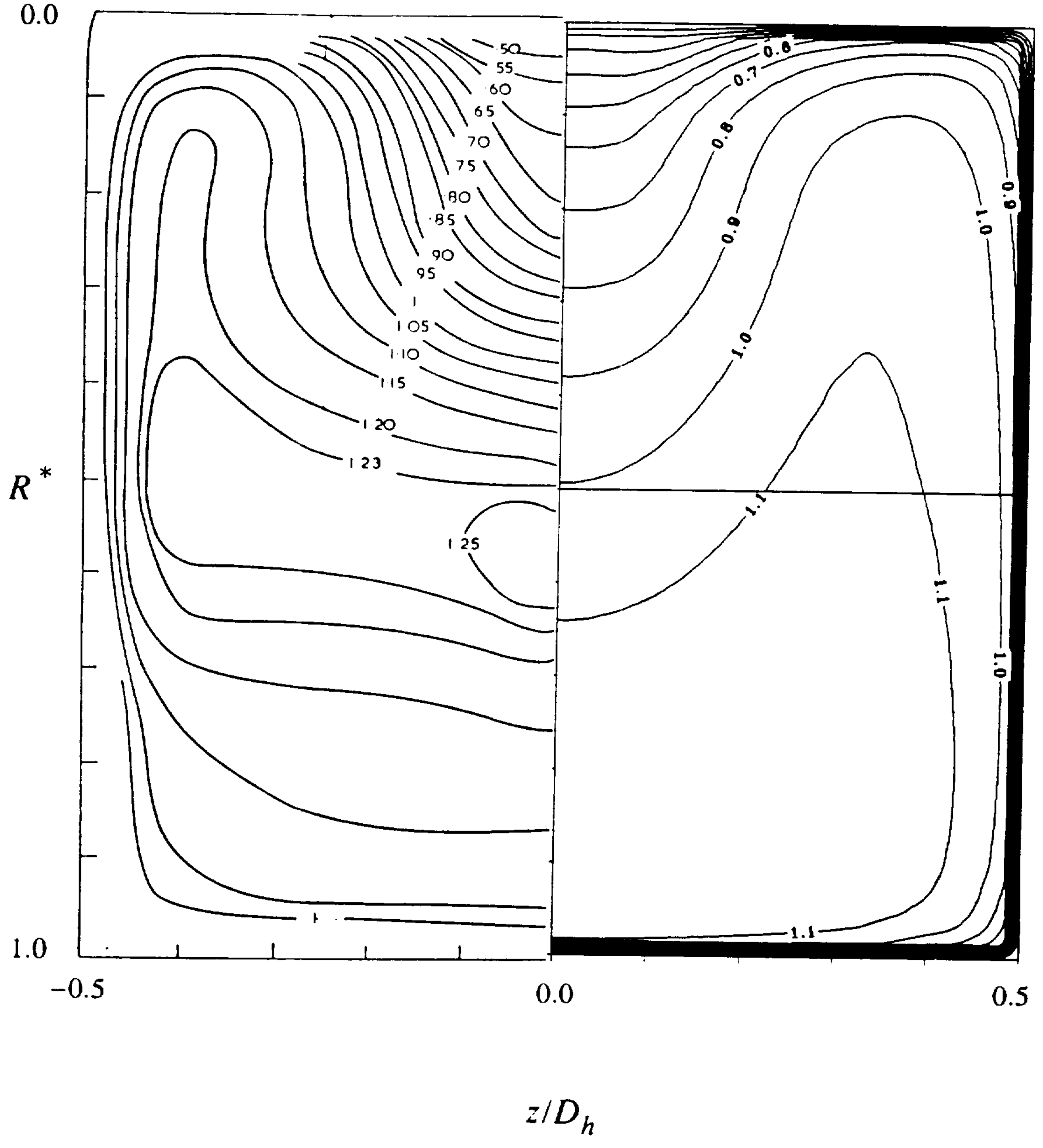

Figure 5.33. Contours of U_θ/U_b for turbulent bend flow, θ = 90°. Comparison of predictions using VDM with data of Humphrey [1977].

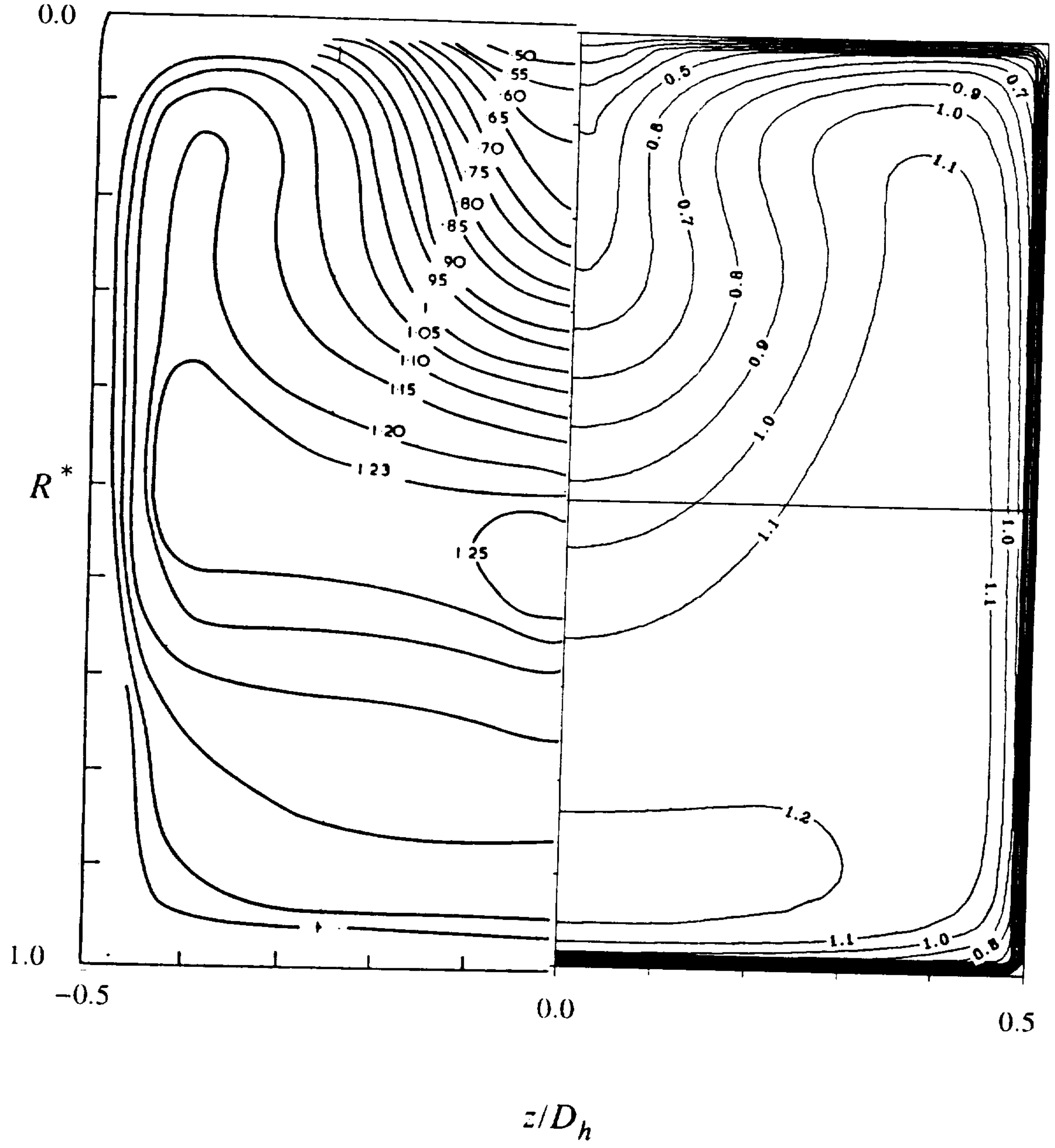

Figure 5.34. Contours of U_θ/U_b for turbulent bend flow, θ = 90°. Comparison of predictions using WFM with data of Humphrey [1977].

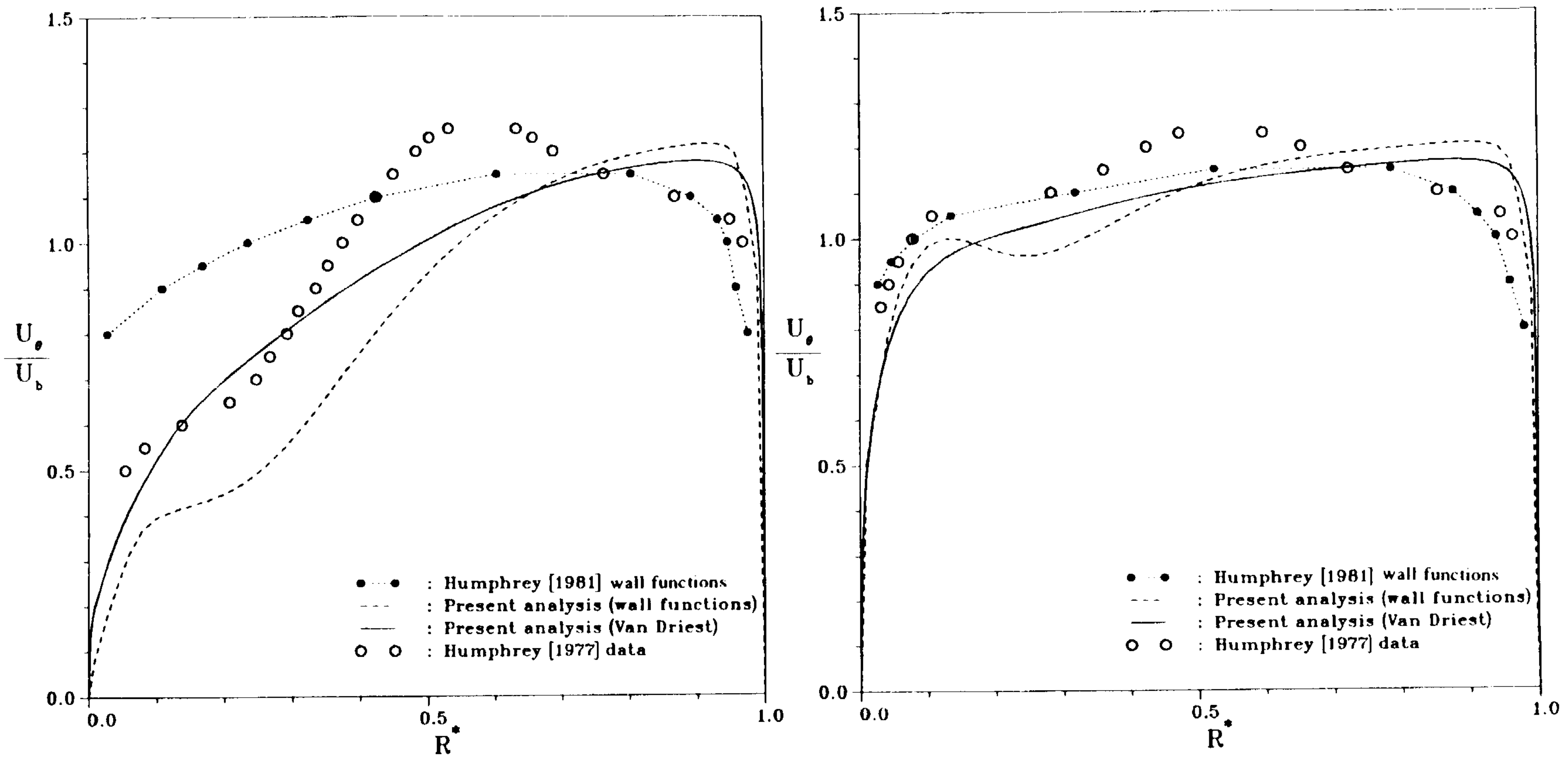

(a)

(b)

Figure 5.35. Radial profiles of U_θ/U_b for turbulent bend flow, $\theta = 90°$. (a) $z/D_h = 0.5$. (b) $z/D_h = 0.25$. Comparison of predictions with data of Humphrey [1977] and predictions of Humphrey et al. [1981].

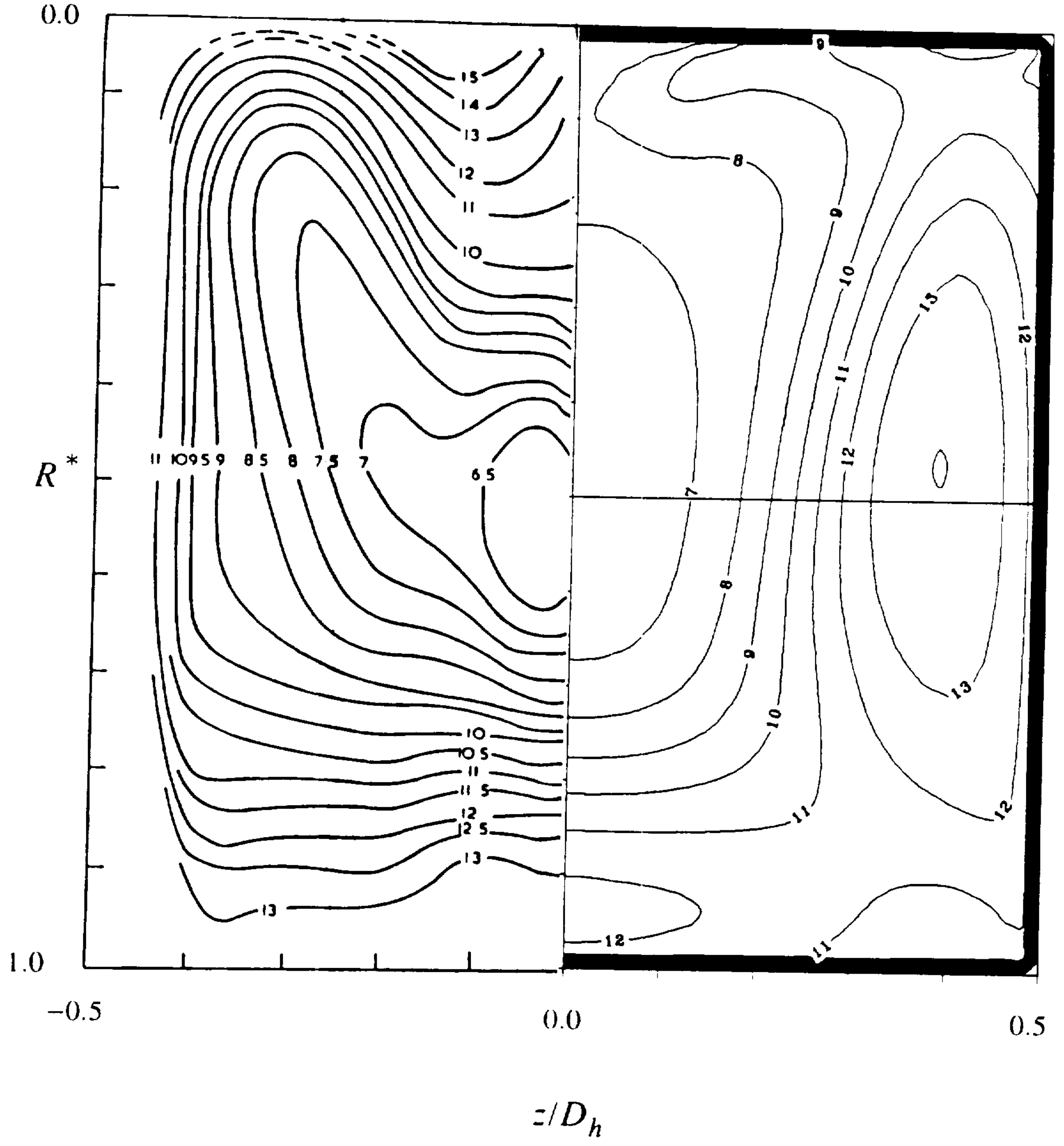

Figure 5.36. Contours of $\tilde{u}/U_b \times 10^2$ for turbulent bend flow, $\theta = 90°$. Comparison of predictions using VDM with data of Humphrey [1977].

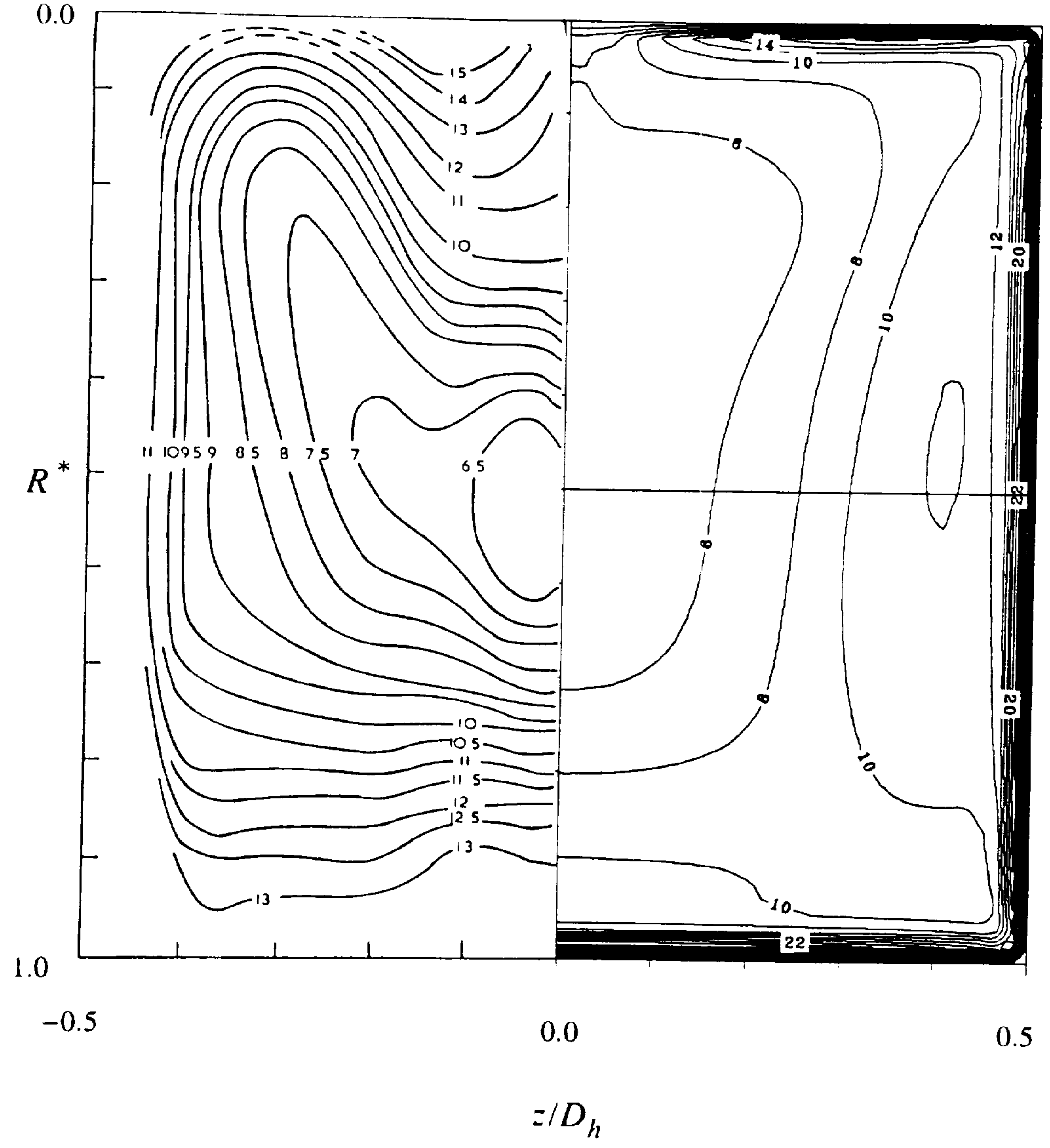

Figure 5.37. Contours of $\tilde{u}/U_b \times 10^2$ for turbulent bend flow, $\theta = 90°$. Comparison of predictions using WFM with data of Humphrey [1977].

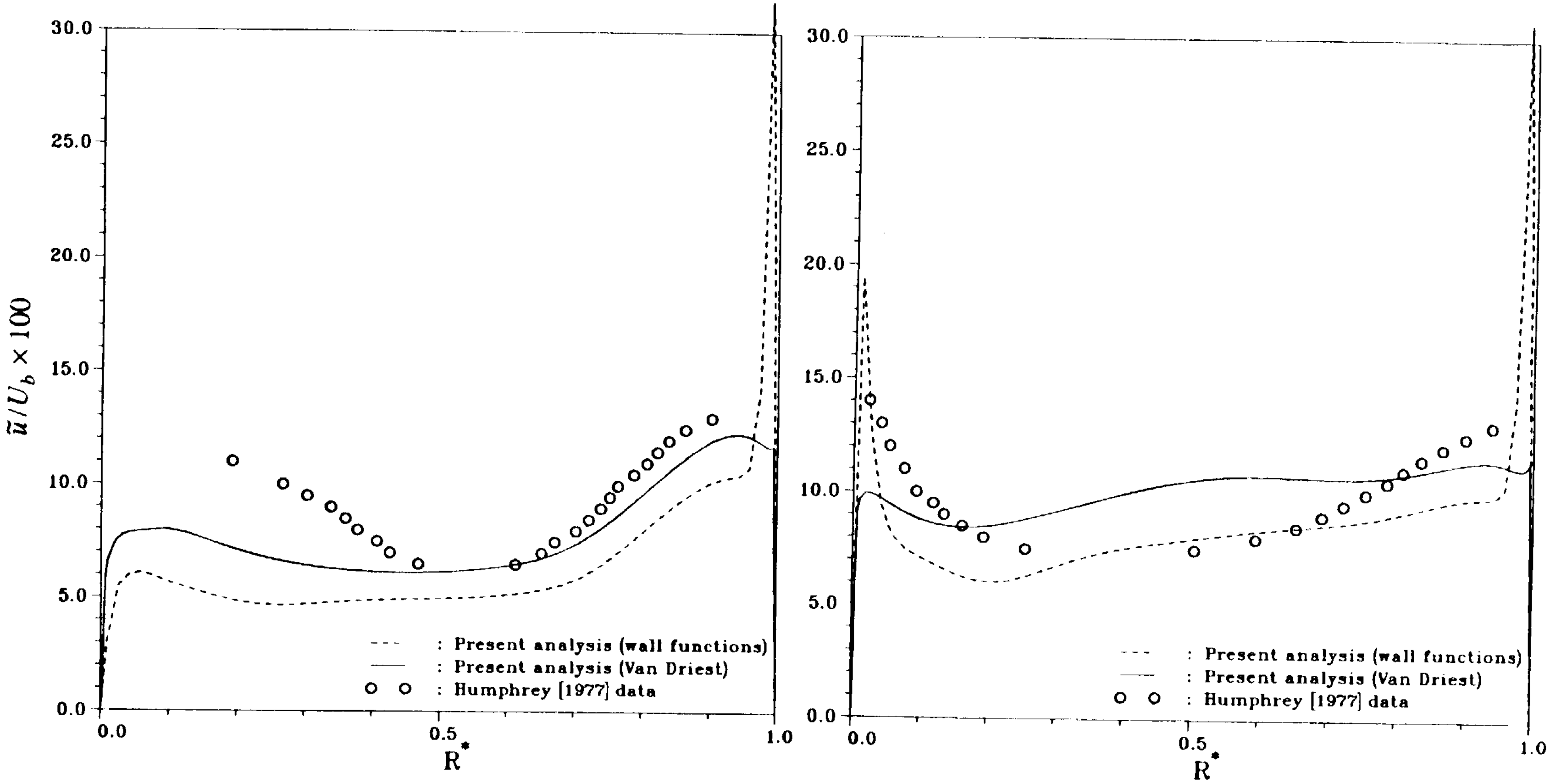

(a)

(b)

Figure 5.38. Radial profiles of $\tilde{u}/U_b \times 10^2$ for turbulent bend flow, $\theta = 90°$. (a) $z/D_h = 0.5$. (b) $z/D_h = 0.25$. Comparison of predictions with data of Humphrey [1977].

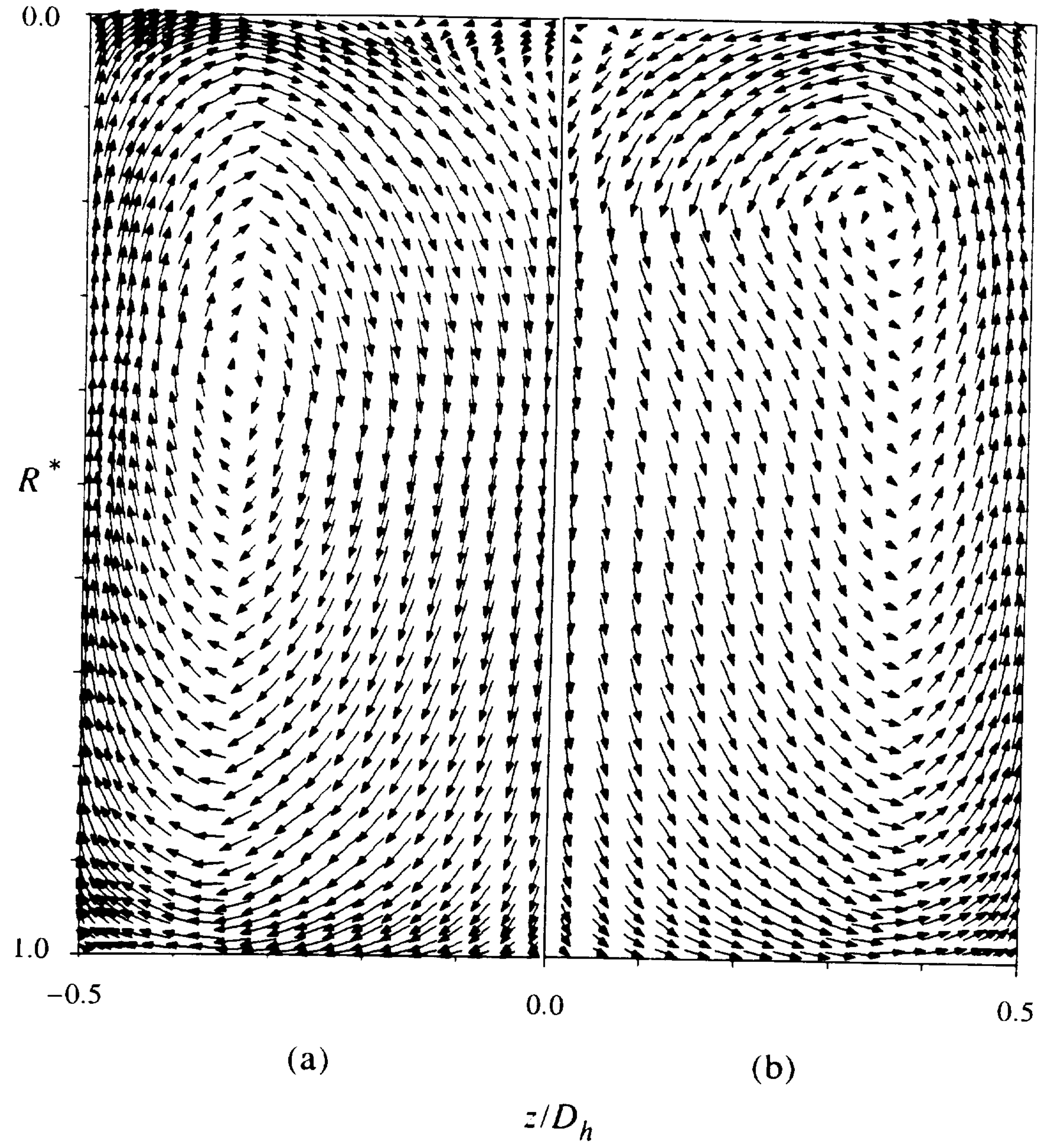

Figure 5.39. Cross-stream velocity vector plot for turbulent bend flow, $\theta = 90°$. Comparison of predictions using (a) VDM and (b) WFM.

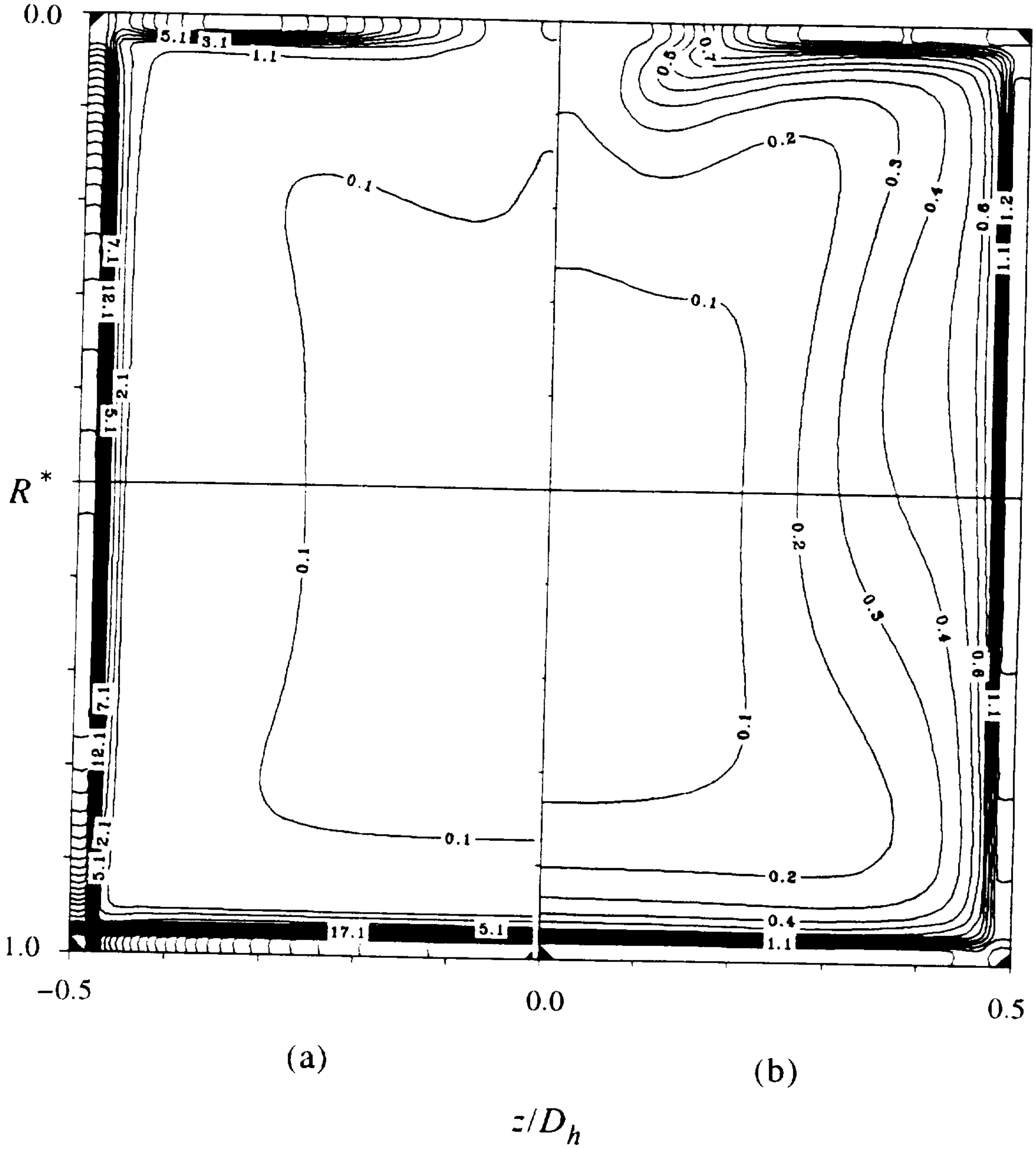

Figure 5.40. Contours of turbulent dissipation, $\varepsilon\nu/U_b^4\times10^6$ for turbulent bend flow, θ = 90°. Comparison of predictions using (a) WFM and (b) VDM.

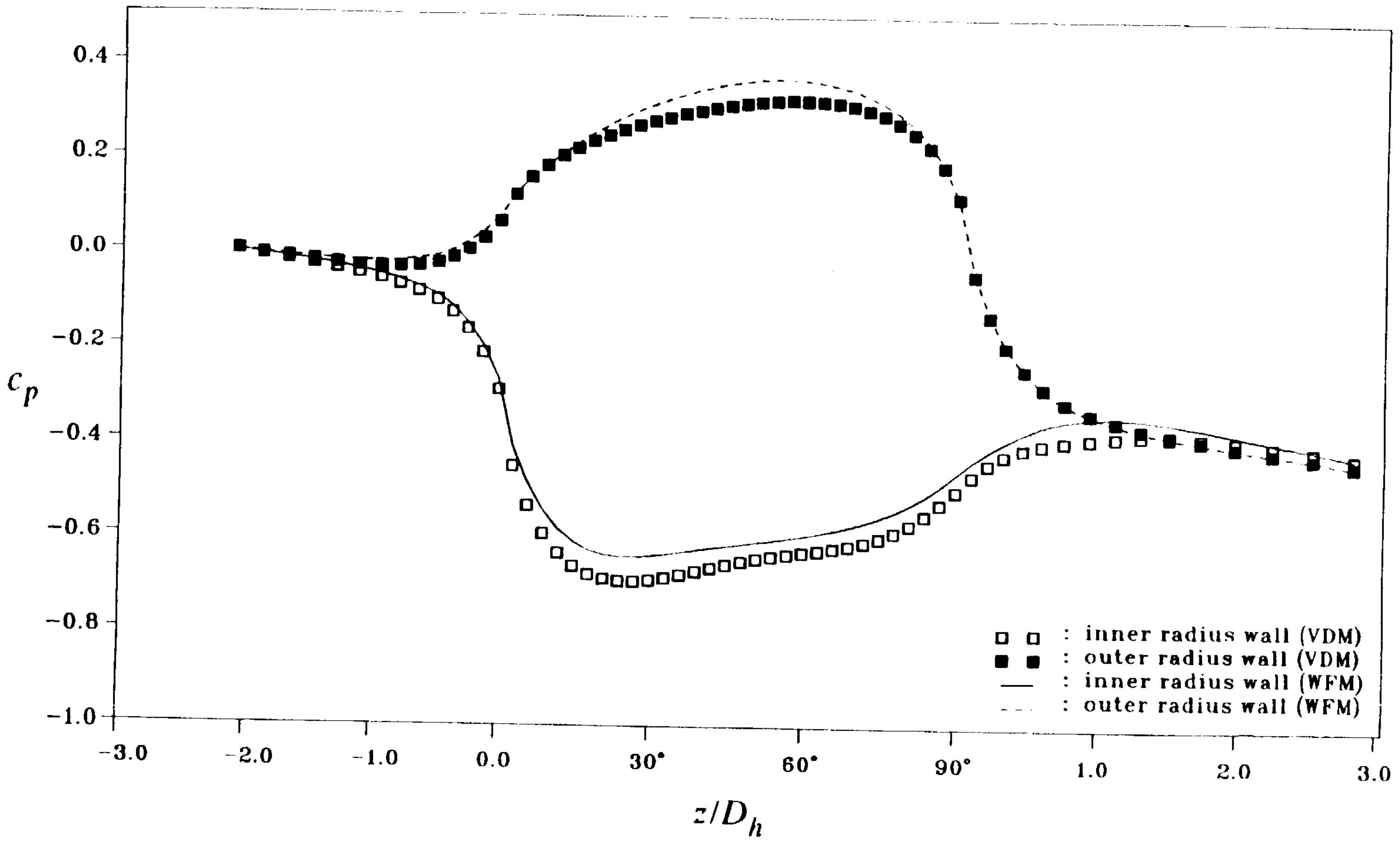

Figure 5.41. Wall pressure coefficient on the symmetry plane of a 90° curved duct, Re=40,000. Comparison of calculations using Van Driest model in the near wall region with wall function model.

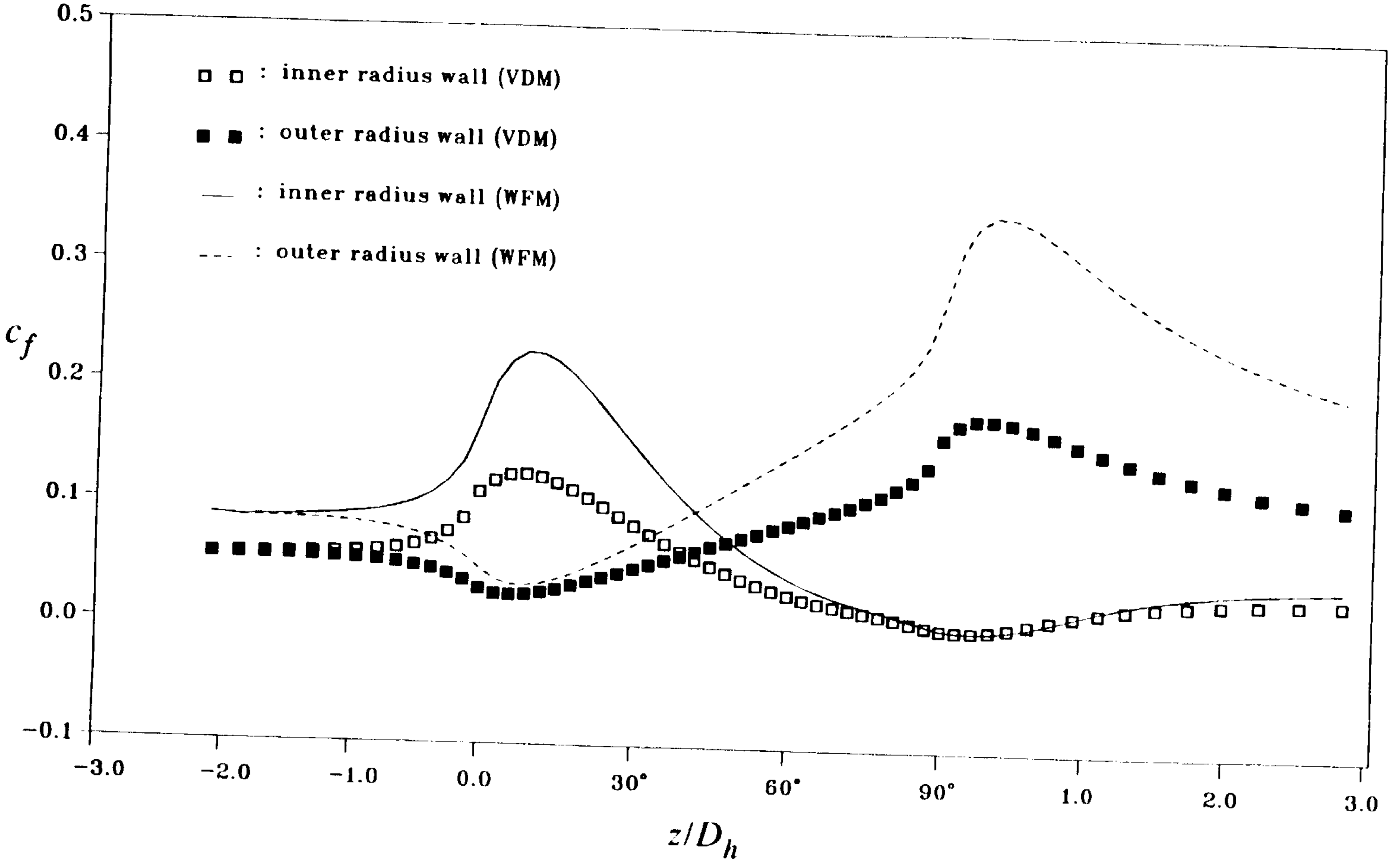

Figure 5.42. Friction coefficient on the symmetry plane of a 90° curved duct, Re=40,000. Comparison of calculations using Van Driest model in the near wall region with wall function model.

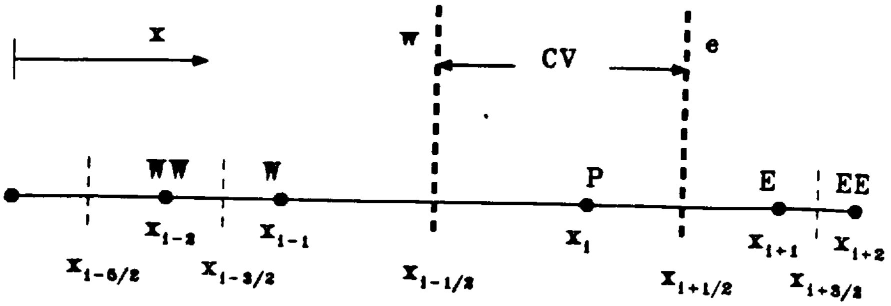
x
w
CV
e
WW
W
P
E
EE
x_{i-2}
x_{i-1}
x_i
x_{i+1}
x_{i+2}
$x_{i-5/2}$
$x_{i-3/2}$
$x_{i-1/2}$
$x_{i+1/2}$
$x_{i+3/2}$

Figure A.1. Control volume for the property node.

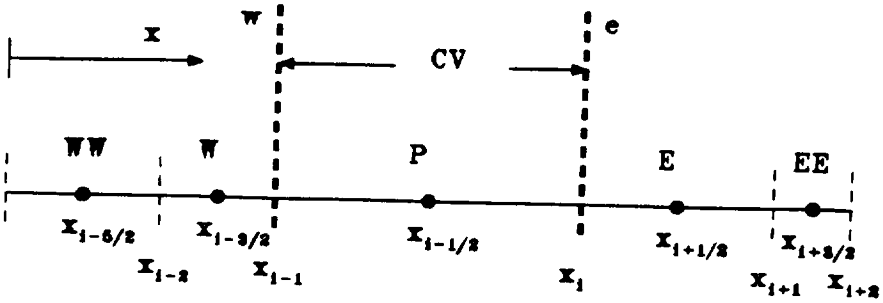
x
w
CV
e
WW
W
P
E
EE
$x_{i-5/2}$
$x_{i-3/2}$
$x_{i-1/2}$
$x_{i+1/2}$
$x_{i+3/2}$
x_{i-2}
x_{i-1}
x_i
x_{i+1}
x_{i+2}

Figure A.2. Control volume for the velocity node.

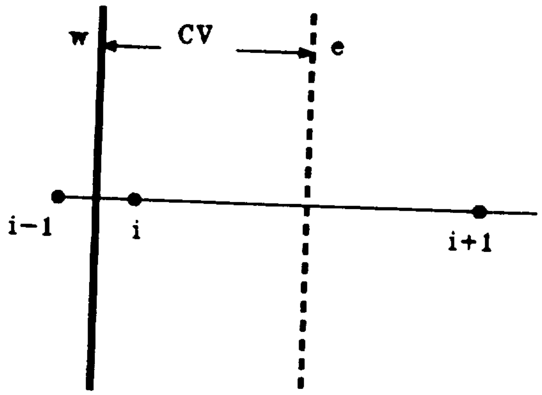

Figure A.3. Boundary node for a scalar or velocity component parallel to the boundary.

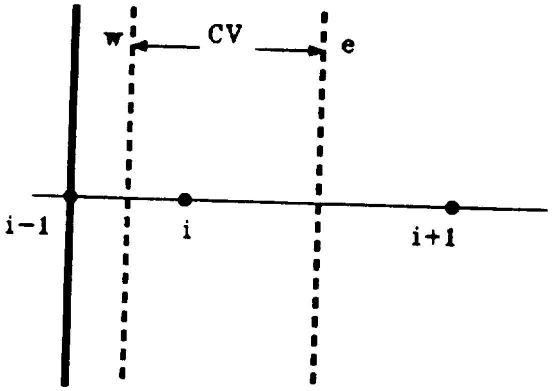

Figure A.4. Boundary node for a velocity component perpendicular to the boundary.